Technology Development For a Compact Rubidium Optical Frequency Reference

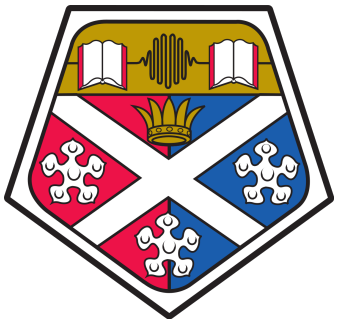

Brendan L. Keliehor

Experimental Quantum Optics and Photonics Group

Department of Physics and SUPA

University of Strathclyde

A thesis presented in the fulfilment of the requirements for the degree of

Doctor of Philosophy

September 2023

Declaration

This thesis is the result of the author's original research. It has been composed by the author and has not been previously submitted for examination which has led to the award of a degree.

Signed: Brendan Keliehor

Date: 15-09-2023

Abstract

The precision and accuracy of navigation and radar systems is typically limited by the stability of their internal frequency references. Currently, microwave atomic frequency references are close to the limits of what they can achieve in terms of short-term stability. Optical atomic frequency references have demonstrated several orders of magnitude improvement in both short-term as well as long-term stability. In the past decade, improvements in optical frequency comb (OFC) technology have enabled the precise measurement of optical frequencies with much smaller form-factors, spurring research to build a portable optical atomic clock referenced to the ^{87}Rb $5S_{1/2}, F = 2 \rightarrow 5D_{5/2}, F' = 4$ two-photon transition (TPT). Using a single laser source and simple Doppler-free spectroscopy in a heated Rb vapour cell one can generate an atomic reference signal with a linewidth approaching 334 kHz.

The research presented here, compares the suitability of a telecoms (1550-1560 nm) CW laser with a narrow bandwidth OFC laser of 10-20 modes spaced apart at 3-6 GHz f_{rep}. The OFC laser achieves more than double the second harmonic conversion efficiency compared with the CW laser, while delivering up to 30 mW of 778 nm light. The 778 nm OFC is then used to excite the reference transition and demonstrate coherent interaction of all OFC modes. Towards the aim of making the system compact, the research explores the use of micro-fabricated vapour cells, 3D printed oven designs and a chip-scale DFB (distributed feedback) laser with the prospects of integrating both the laser and spectroscopy on to a single micro-fabricated semiconductor platform.

Pre-stabilising a noisy laser to an optical cavity is commonly required for optical atomic clocks, in order to resolve narrow-linewidth transitions. Towards this application, a low-drift, all-metal optical cavity is developed and characterised using Allvar metal, which possesses a negative coefficient of thermal expansion (CTE). The overall cavity CTE can be temperature tuned to yield a CTE of < 0.001 ppm/°C at ~ 27 °C. The long-term cavity mode stability of the cavity was measured while referenced to one of the ^{87}Rb $5S_{1/2} \rightarrow 5P_{3/2}$ 780 nm transitions, residual drifts of 0.3 MHz/hr on time-scales up to 5 hrs (after subtracting off pressure-correlated frequency shifts). The all-metal cavity should be less sensitive to thermal gradients as well as more responsive temperature stabilisation than ultra-low expansion cavities.

Research Outputs

0.1 Publications and Conference Proceedings

- E. Di Gaetano, P. Griffin, B. Keliehor, M. Sorel, E. Riis, and D. J. Paul, "Single-mode distributed feedback lasers for ^{87}Rb two-photon quantum technology systems" in 2022 IEEE Photonics Conference (IPC), p. 1, IEEE, 2022.

- K. Gallacher, E. Di Gaetano, S. Dyer, B. Keliehor, J. P. McGilligan, M. Sinclair, U Hawley, A. S. Arnold, P. F. Griffin, M. Sorel, E. Riis and D. J. Paul, "Silicon-Nitride Photonic Integrated Circuits for Atomic Systems", IEEE Photonics Society Summer Topicals Meeting Series, IEEE, 2023.

0.2 Public Engagement

- Poster: "Towards a Compact Optical Rb Frequency Reference", Quantum Hub Annual Review, 2022

- Timelord Training Public Activity, Institute Of Physics: Big Bounce Festival, 2021 and 2022

Acknowledgements

The further down the trail of research I have ventured, the more I recognise the impact of my teachers at all stages of my education. I owe a huge gratitude to them all. Of all of the teachers I have had over the years, none have I worked more closely with than my PhD supervisors Prof. Erling Riis and Dr Paul Griffin. I would like to thank both of them for their patience, insights, and encouragement they have offered during my studies at Strathclyde University.

Second of all, I must thank my family, whom have supported me to attend university. They have always encouraged me to work productively towards any goal that I could imagine, regardless of how fanciful the goal was. From my Grandparents I have gathered my inspiration to study in the field of engineering and physical sciences, and from my parents, aunts and uncles I have learned to appreciate a lifestyle of creativity.

Especially I am thankful for the friends who I have always relied upon the most for support during challenging times. I would additionally like to thank my colleagues from the EQOP department, who have played a role in helping me develop the experiments for my research. Finally, I would like to extend my gratitude to Bob and Ewan in the mechanical workshop for the custom components they have built for our experiment.

Contents

Chapter 1

Introduction to Frequency References

1.1 Time-keeping Devices and Synchronisation

Frequency references are devices which generate a specific frequency, that is calibrated with a high precision and accuracy to that of an atomic transition or another naturally occurring stable frequency. The Earth itself has a remarkably stable rotation period [1], with just ±0.5 millisecond fluctuations during a year (31536000 seconds), and essentially constituted the reference of time for early human civilisations who relied upon observations of the stars and our sun's passage overhead to track the days of the year. However by 2300 BC, there are records of the Chinese and Egyptians using the sun's trajectory to measure time using gnomons and sundials with hourly divisions [2]. By 150 BC documentation of a hand-held time-keeping device named the astrolabe can be found [3, 4], which allowed the exact time of the year to be determined, during both the day and night, with a precision of hours, using astronomical observations. Portable devices like astrolabes and sundials were equally used for navigation as well as time measurement.

Mechanical clocks (for example sand timers, water clocks and later pendulum clocks) eventually replaced sun dials to measure time in steps of seconds, but still required calibration with astronomical observations. The development of radio communication in the early 1900's was quickly followed by computers, and the combination of these two technologies led to the development of quartz crystal oscillators by the 1920's [5]. In a relatively short span of years that followed this development, advances in both theoretical atomic physics and experimental spectroscopy led to the first demonstrations of a reliable caesium beam atomic clock in 1955 at the National Physics Laboratory (NPL) in the UK [5]. In the mid 1960's, the first portable atomic clocks were launched in to space [6] to begin forming what would later become the GNSS (global navigation

satellite system), allowing precise navigation and communication for anyone that can acquire a timing signal (10 MHz or 1 pps) from the satellites. This signal can be used to synchronise lab equipment and as a reference for other atomic clocks. Besides navigation applications, portable atomic clocks are used in tests of general relativity, gravitational wave detection in space and measuring fundamental physical constants [7, 8].

The experiments documented within this thesis aim to address the challenges faced in the process of scaling down optical frequency reference devices for applications in commercial portable optical atomic clocks and quantum sensing technology. The following chapters will address this aim by making use of robust and compact commercial-grade laser systems, new fabrication techniques for system components, and by referencing to a narrow linewidth, optical transition in rubidium atoms. The first chapter of this thesis aims to provide the necessary background knowledge to understand and measure frequency stability, as well as the requirements for a device with a high degree of frequency stability.

1.2 Atomic Frequency References

The central component of an atomic frequency reference (AFR) is a device that produces an oscillating signal, which is referred to as the local oscillator (much like the ticking second hand of an analogue clock). The local oscillator continually ticks, but the frequency at which it ticks will often speed up or slow down, causing it to lose or gain time relative to a fixed time reference. The frequency of an atomic transition however, is far less susceptible to fluctuations, and its also possible to calculate from theory, what their undisturbed natural frequencies should be. Since atoms are naturally occurring in the universe, their frequency in theory should measure the same no matter where or when their frequency is measured. This makes them a suitable candidate for using as a reliable reference frequency.

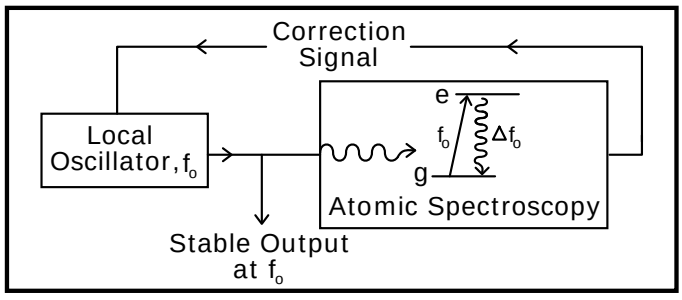

Figure 1.1: Basic process for creating an atomic frequency reference, which outputs a stable frequency at f_0.

In an AFR, a tuneable local oscillator generates a frequency, f_0 which can be fine-

tuned to excite an atomic transition, leading to a fluorescence or absorption signal which only occurs at the frequency of the transition (atomic spectroscopy). Corrections are then made to the local oscillator so as to maintain the maximum atomic signal strength, and hence stay matched with the frequency of the atomic transition. This cycle is illustrated in Fig. 1.1. Once the local oscillator is "locked" to the atomic frequency, then its accuracy and precision are improved to the stability level of the atomic transition, eliminating the long-term fluctuations of the oscillators frequency and making the frequency output much more reliable. An AFR can then be converted into an atomic clock by measuring the output frequency, and down-converting that frequency to an electronic timing signal at 10 MHz or 1 pps (pulse per second).

1.3 Measuring Frequency Stability

1.3.1 Precision and Accuracy

The frequency deviations of random frequency noise associated with an oscillator determines the precision of its frequency. Purely random frequency or phase fluctuations are termed white noise, and the ratio of the measured frequency, f_0 to its frequency fluctuations, Δf_0 on a 1 second timescale form one measure of a frequencies stability, known as the Q-factor:

$$Q = \frac{f_0}{\Delta f_0} \tag{1.1}$$

In the presence of random frequency noise, it is possible to continually take the average value of multiple measurements of an oscillators frequency to reduce frequency noise and increase the accuracy of the oscillator frequency. However, if the mean value of the oscillator frequency shifts around in between averages, then it is not possible to improve the accuracy beyond the size of the shifts. This type of long-term fluctuation, which does not appear to have a measurable period, is termed drift. Fig. 1.2 demonstrates the difference between fractional frequency measurements which possess different degrees of precision and accuracy. While a local oscillator, such as a quartz crystal oscillator can provide a very high precision, it quickly loses accuracy if it is not locked to a more stable frequency. Atomic transition frequencies, however, can be both precise and accurate, but primarily it is their accuracy that is valuable when locking an oscillator to their frequency.

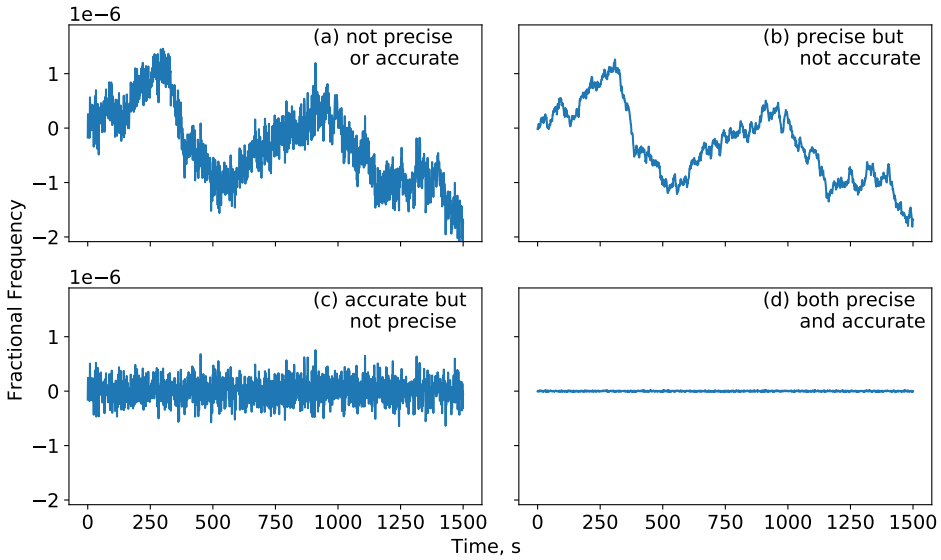

Figure 1.2: Randomly generated white frequency noise data, demonstrating the difference between a precise frequency and an accurate frequency.

1.3.2 The Allan Deviation

The Allan deviation (Adev) has become the standard method of comparing the long-term stability of different oscillators with one another [5]. The Allan deviation is calculated in terms of fractional frequency so as to allow comparison of the relative stability of frequency references operating at different frequencies. The Allan deviation algorithm extrapolates the long-term frequency stability by re-sampling a data set (like the one example shown in Fig. 1.2) at longer sampling periods. The algorithm generates a single data point per sampling period, which is the average of the measured data points within that period. It then calculates the standard deviation of the newly-averaged data set, which is then plotted against the sampling period, τ. In this way, high frequency noise within the sampling period is filtered out, and the total noise of the data set should continue to reduce as longer sampling periods are used. From the NIST handbook of frequency stability analysis [9], the Allan variance is defined as follows:

$$\sigma_y^2(\tau) = \frac{1}{2(M-1)} \sum_{i=1}^{M-1} [\bar{y}_{i+1} - \bar{y}_i]^2 \tag{1.2}$$

For which, M is the number of samples after the original data set has been re-sampled at intervals of τ, and $\bar{y}_i$ is the cumulative fractional frequency fluctuation over the sampling period, divided by the sampling period in seconds (essentially the integral of the original data set):

$$\bar{y}_i = \frac{1}{\tau}[y_{i+1} - y_i] \tag{1.3}$$

The Allan deviation, is then simply the square root of the Allan variance. In the normal Allan deviation (Eq. 1.2), the sampling period is imposed on to the original data set without allowing any of the original data points to be re-used for each consecutive sampling period. However this process quickly reduces the number of re-sampled data points in the series, and the largest value of τ that can be used is $1/3^{rd}$ of the original sample duration. The overlapping Allan deviation retains more data points for each sampling time, by allowing each sampling period to be overlapping as it is incremented (in steps equal to 1, instead of τ) over the original series to re-sample the data. The retention of extra data points in the series for each value of τ generates less noisy data as the deviation is calculated, and also allows the trend to be extended to 1/2 of the original sample length. The overlapping Allan variance formula is defined as follows:

$$\sigma_y^2(\tau) = \frac{1}{2m^2(M-2m+1)} \sum_{j=1}^{M-2m+1} \left[\sum_{i=j}^{j+m-1} [\bar{y}_{i+m} - \bar{y}_i] \right]^2 \tag{1.4}$$

In this case, M is again the length of the re-sampled series, and m is equal to τ, divided by the original sample period of the data. The overlapping Allan deviation (OAdev) is a bit more computationally intensive to calculate, due to the nested iterations. To reduce the computation time, typically the values of $\bar{y}_i$ from Eq. 1.3 should be calculated just once, outside the main loop for the algorithm. The trends of the Adev and the OADev are effectively the same (comparison shown in Fig. 1.3a), except that it is easier to identify smaller deviations from white frequency noise using the OAdev. For this reason, only the OAdev is used for analysis of data throughout this thesis. Note that the results of both the Adev and OAdev become less reliable toward longer averaging time scales (approaching $2/3^{rds}$ of the maximum τ value).

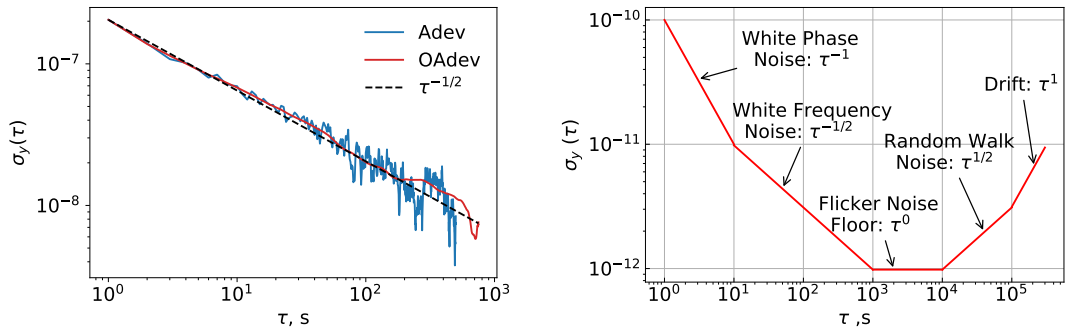

(a) *(b)*

Figure 1.3: (a) Example Adev analysis plot using the white frequency noise data from plot (c) in Fig. 1.2 to compare the results of using the Adev and OAdev functions. The close fit of the $\tau^{-1/2}$ to the OAdev plot confirms the prevalence of white frequency noise in the data. (b) Illustration of what type of frequency noise different Adev trends can reveal.

Several types of trends can be identified from the gradient of the plotted results

using ADev analysis. In Fig. 1.3a the trend line which is fitted is indicative of white frequency noise. A summary of the different trends are shown in Fig. 1.3b. The appearance of a white phase noise trend depends on if the local oscillator is phase-locked rather than frequency-locked to the frequency reference. If measurements are taken for long enough, there will almost always be a time scale on which a drift kicks in for one reason or another. Before reaching this point, the trend will reach a flicker noise floor, which is commonly associated with random electrical noise (e.g. from noisy amplifiers in the circuitry). The example frequency fluctuations plotted in (b) of Fig. 1.2 show traits of both random walk (brown noise), and frequency drift trends. To identify periodic components of noise in a data set, FFT (fast fourier transform) analysis provides a more useful analysis. Additionally, the FFT is the preferable method for analysing the stability of the frequency reference on short time-scales (< 1 s).

1.3.3 Frequency Stability of Atomic Frequency References

In the case where all other noise sources of noise for an optical AFR are negligible, the expected Adev stability trend (in terms of fractional frequency) will be limited by the photon shot noise [10, 11]:

$$\sigma_y(\tau) = \frac{1}{Q\sqrt{N\tau}} \tag{1.5}$$

In this case Q corresponds to the frequency of the atomic transition divided by its natural linewidth. N is the number of detected photons per second in the atomic signal. The $\tau^{-1/2}$ dependence indicates that white frequency noise will limit the stability of the frequency lock to the atomic reference. This is not to say that atomic frequency references are impervious to noise from the external environment which could cause drift, or random-walk noise. As will be discussed throughout Chapter 2, not only is the linewidth (precision) of an atomic transition temperature-dependent, but its accuracy is also sensitive to magnetic fields, local non-resonant electromagnetic fields, and relativistic shifts. However, this all typically occurs at a fractional frequency level much lower than that which affects the local oscillator devices.

Currently ground-based atomic clocks like the NIST-F1, and more recently the NIST-F2 [12] at the National Institute for Standards and Technology (NIST) in Colorado, U.S.A., operate as the primary frequency standard. Millions of clocks around the world (including other atomic clocks and navigation satellites) are synchronised with this primary standard to form the UTC (universal coordinated time) timing network. Currently, primary standard atomic clocks rely on measurements of the ground state hyperfine splitting frequency (9.192 GHz) from super-cooled (10's of micro-Kelvins) caesium atom fountains. This particular atomic clock achieves a fractional frequency stability of 1.7×10^{-13} at 1 second. On long averaging time scales ($> 10^3$ s) the stability

of this clock can reach 0.4×10^{-15} [12].

The most stable, state of the art atomic clocks are not used as primary frequency standards at present. One example is the strontium optical lattice clock, built by a Japanese team led by H. Katori [13]. These clocks are able to achieve a short-term fractional frequency stability (at a clock frequency of $\sim$ 429 THz) of 4×10^{-16} at 1 second, and can average down to $\sim 1 \times 10^{-17}$ at 1000 s, and have the ability to reach $\times 10^{-18}$ stability within two days of continually averaging measurements. Once the stability of a clock is higher than that of the primary frequency standard, such clocks must be compared to other clocks of equivalent or superior stability, to avoid limiting the measured stability to that of the measuring reference frequency. Optical clocks can easily gain a few orders of magnitude improvement to their stability, simply by referencing to optical atomic transitions instead of microwave transitions. In part, this is because the frequency of optical atomic transitions compared to microwave transitions are typically 4-5 orders of magnitude higher, increasing the Q-factor of the AFR by the same magnitude. Higher levels of stability are also related to an optical oscillators ability to achieve considerably higher fractional frequency stability (while pre-stabilised to a low-expansion optical cavity) than microwave oscillators. The level of stability provided by optical atomic clocks allows them to be sensitive to local gravitational shifts, like those related to the tides and increased flow of magma underground [14].

1.4 Portable Atomic Frequency References

Atomic clocks like those described above, are much too large and delicate to be taken to remote locations or launched into space. The GNSS was the first major use of portable atomic clocks, and is still the most extreme application for which portable AFR must be tested. A typical GNSS satellite such as those used in the U.S.A.'s GPS (global positioning system) constellation are relatively large, measuring around 2.5 m^3, and weighing 1000-2000 kg. Within this volume the satellite can be fitted with up to 3 different AFR units. Since the 80's, GPS satellites have typically used lamp-pumped Rb or Cs vapour cell AFR units like that described in [15], which stabilise an on-board quartz oscillator. The GPS-IIR satellites feature AFR units made by Perkin-Elmer, which specified a fractional frequency stability of 3.0×10^{-12} at 1 s [16]. However, the more recently deployed Galileo satellites are equipped with Passive Hydrogen Masers (PHMs) as well as Lamp-pumped Rb AFR. These PHMs are typically achieving fractional frequency stability of 9.4×10^{-13} at 1 s, during orbital operation [17], and long-term stability out to 1000 s which is comparable to an AFR.

Carrying several different types of AFR units per GPS satellite ensures technological diversity, i.e. to confirm each others readings by different methods and reducing the chance that all of the AFR units are made redundant due to the same failures. Whilst

the PHMs currently offer excellent stability on time-scales up to 1000 s, they are significantly bulkier than AFR units, and an AFR provides better accuracy on longer time-scales. The weight of the frequency reference is an equally important factor as their stability, due to the high price tag per kg of launch costs. Devices operating on board the GPS-IIR satellites share a total of roughly 1.9 kW of power on which to operate. This comes from a battery which is topped up by the solar panels of the satellite. In line with considerations for compact size and limited power supply, the devices on board have to be simplified as far as possible. This has the added advantage of making remote diagnosis easier in the event that something is not functioning properly.

Lasers are now being used instead of lamps in newer vapour cell AFR units, due to their higher amplitude stability and lower power consumption compared with lamps. This development is allowing the exploration of new variations of portable vapour cell AFR mechanisms such as coherent population trapping (CPT) clocks [18] and pulsed optical pumping (POP) clocks [19]. The development of CPT clocks have led to the demonstration of the world's first commercial chip-scale atomic clock (CSAC) [20], encouraging a new wave of miniaturised atomic frequency references [21], and quantum sensors [22]. Such chip-scale devices often cannot achieve as high stability as their desktop computer-sized competitors, because their small size limits the number of atoms that can be detected. However, their size and power demand are so small that they can be used across a very wide range of integrated and standalone applications.

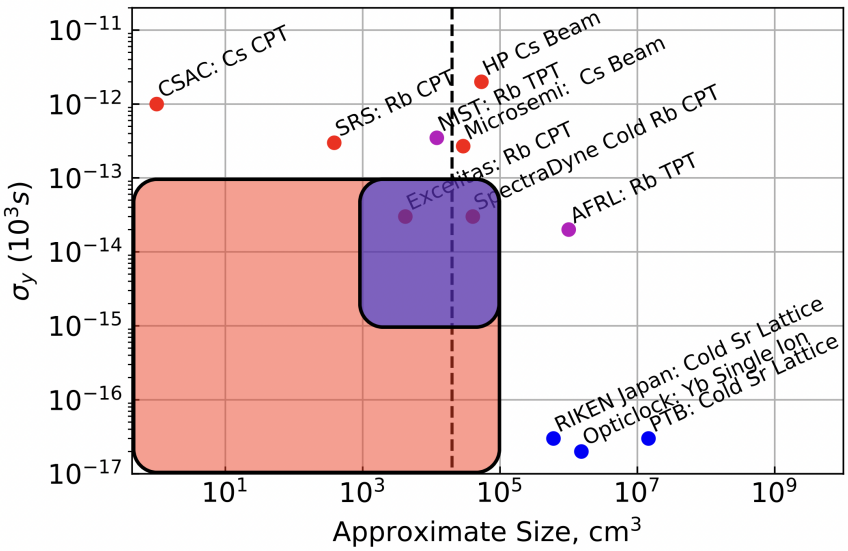

Figure 1.4: Long-term frequency stability plotted against the approximate size for a range of: commercial microwave atomic clocks (red dots) [20, 23–27], semi-portable optical atomic clocks (blue dots) [8, 28, 29] and Rb two-photon optical clocks (purple dots) [30, 31]. The red area marks a desirable region of stability which can be reached using optical clocks, provided their size fits within this region. The dotted vertical line marks the size of a 20 L backpack (or 10 cm tall 19" wide rack-mount case), and is a convenient size for a wide range of portable commercial applications. The aim of the research in this thesis is to develop a portable optical AFR with long-term stability and size fitting within the purple shaded region.

There are many commercial portable AFR and atomic clocks (e.g. MicroSemi 5071A and Spectra Dynamics cRb) of the type used on the GNSS which are also used in labs, radar stations and industrial settings as a local frequency standard. Several more examples of portable AFR and atomic clocks, comparing their stability and size, are shown in Fig. 1.4. The precision and accuracy of navigation and radar systems is limited by the stability of their internal frequency references. Optical AFR, can provide increased on-board clock stability for satellites in the GNSS as well as ground-based radar systems [6, 32].

The size of the optical atomic clocks shown in Fig. 1.4 is representative of their current state of progress toward portable: transportable, but not yet integrated with control electronics and streamlined for commercial applications. Several groups have recently been investigating the rubidium two-photon transition (Rb TPT) at 778 nm (384 THz) as an atomic reference for a portable optical atomic clock. Using relatively simple and compact equipment (compared to optical lattice clocks) it is possible to detect a narrow signal, from a large atomic sample (N $\sim 1\times 10^9$). ($\sim$ 334 kHz natural linewidth) from the transition. The characteristics of an Rb TPT reference described above yield a shot noise limited (Eq. 1.5), short-term stability of $\sigma_y = 3 \times 10^{-14}$. An atomic frequency reference of this type is the research focus of the work presented in this thesis. Using the Rb TPT reference, one group from NIST has already demonstrated a miniaturised optical AFR [30], while another group from the Air Force Research Laboratory (AFRL) has demonstrated high levels of long-term stability that out-compete current commercial microwave AFR [31]. These results confirm that it is realistic to aim to create a commercial AFR using this technique with stability and size that can easily fall within the range of the purple shaded area shown in Fig. 1.4.

Up until recently [33], optical atomic clocks have not been considered for portable applications, owing to their typically larger architecture and complexity than microwave AFRs. Measuring the exact frequency of optical atomic transitions has so far required the simultaneous locking of a several lasers and different atomic frequency references, to eventually down-convert the optical frequency to the range of comparison with a primary frequency standard. Such a frequency chain had to be used by F. Nez et. al. to originally measure the frequencies of the rubidium two-photon transitions [34]. With the development of self-referencing optical frequency combs which can be used to measure optical reference frequencies with a single laser system, a portable optical atomic clock is much more feasible.

1.5 Optical Frequency Combs: The Frequency Gearbox

In recent years the optical frequency comb (OFC) has been referred to as the frequency gearbox of science tools [35] in the field of spectroscopy and meteorology. This is due to the unique way in which the frequency spacing between optical modes, f_{rep}, and the optical frequency of the modes, f_m are linked in the OFC spectrum:

$$f_m = f_{ceo} + m \times f_{rep} \tag{1.6}$$

Where m is the mode number, starting at a value of 1, in a series of integers, which eventually multiply f_m to reach the optical frequency domain. f_{ceo} is termed the carrier-envelope offset and arises as a result of the difference between the group and phase velocity of the OFC pulses within the OFC laser cavity. Chapter 5.2 will discuss the details of OFC lasers in more depth, but at this point it is important to establish what makes an OFC self-referenced, and thus able to measure optical frequencies.

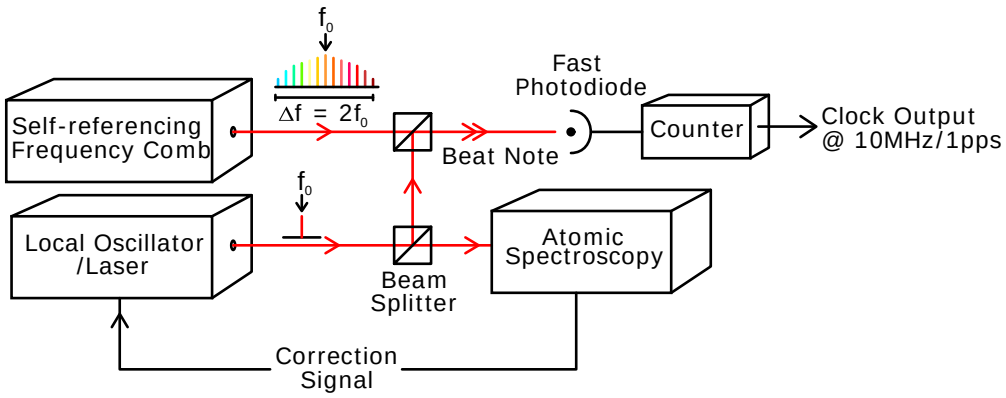

Figure 1.5: Generating a clock signal from an optical AFR through the use of a self-referencing OFC. The optical output of the laser, once locked to an atomic transition, forms the AFR. This output is then combined with the optical path of the OFC output using a beam splitter. The difference frequency between the two optical sources, generates an optical beat-note at the frequency of f_{rep}, which is detected on a fast photodiode. An electronic or microwave counter then generates a clock timing signal which is referenced to the AFR, while the wide spanning OFC modes are also simultaneously stabilised to the AFR.

Stabilising the optical frequency of an OFC mode to an optical AFR, effectively transfers the stability of the AFR to that mode and additionally to the rest of the laser modes, and consequently f_{rep}. The OFC generates a beat-note between the optical modes, occurring at f_{rep}, which can be measured, along with higher harmonics of f_{rep} on a fast photodiode, and used for an electronic timing signal. Hence, 5the link between the optical and microwave regime is established. This process of acquiring the beat-note is illustrated in Fig. 1.5. As long as the OFC modes are widely enough spaced, and the frequency of the optical transition that a comb mode is resonant with ($< \pm f_{rep}$)

is known, then there should be little ambiguity about the value of m. From Eq. 1.6 one can see that f_{ceo} must also be known alongside m and f_{rep} to determine the exact frequency of the AFR. However, f_{ceo} is not as easy to measure and is not necessarily stable.

OFC lasers such as the Ti:Sapphire laser have been capable of producing mode-locked pulses, with stable and measurable f_{rep} since the 1970's [36], but it was not until the year 2000 that T.W. Hansch et. al. were able to demonstrate a direct measurement of f_{ceo} from an OFC laser [37]. The measurement was made possible by the development of techniques which could extend the range of measurable modes within the OFC spectrum to span one octave. This allows, for f_{ceo} to be measured and stabilised by producing the second harmonic of the OFC, and measuring the beat-note of the same frequency at the fundamental and second harmonic, yielding the value of f_{ceo} [38]. There are a few different measurement schemes which allow self-referencing using the OFC second harmonic, one of which is demonstrated in [39], where they measure an f_{ceo} value of several GHz. Even just 100 MHz would be a significant offset on the frequency of an AFR to leave unaccounted for.

One particular application in space for a wide spectrum of precise optical frequencies all referenced to a known AFR, is for astronomical spectrographs [35]. Spectrographs for astronomical observations can detect significantly cleaner spectra outside the Earth's atmosphere, but will be much more prone to frequency shifts, compared to operation on ground. The atomic frequency-referenced OFC modes could be used to automatically re-calibrate the measured spectrum, in much narrower segments than are currently possible without manual intervention.

Chapter 2

The Rb Two-Photon Transition (TPT): Excitation Theory and Detection

2.1 Introduction

In the case of the AFR in this work, the reference transition will be the ^{87}Rb $5S_{1/2}, F = 2 \rightarrow 5D_{5/2}, F' = 4$ two-photon transition (TPT). This chapter will discuss the details of how the transition is excited, both in terms of the apparatus and the excitation theory. The discussion aims to lead the reader to an understanding of what factors affect the frequency accuracy, precision, and SNR (signal to Noise Ratio) of the AFR.

During the 1990's the Rb TPT transitions were added to the Comite International des Poids et Mesures (CIPM) list of recommended frequency references for the definition of the metre [40]. Following this, there was a rise in demonstrations of Rb TPT optical frequency standards over the next 20 years [10, 41, 42]. Many research groups have opted to excite the Rb TPT with a frequency-doubled telecoms laser [43–46]. These systems not only benefit from the advanced spectral quality and reliability of telecoms lasers, but yield additional applications at 1556 nm. Such an application might include the calibration of Dense Wavelength Division Multiplexing (DWDM) systems [47]. Additionally, the frequency-doubled laser can be used to provide a more accurate reference for calibrating optical spectrum analysers (OSAs) simultaneously at both 1556 and 778 nm [48]. The transition can then be excited using Doppler-free spectroscopy at $\simeq$ 778 nm, which is easily accessible using readily available infra-red laser diodes, or frequency-doubled telecoms lasers. The natural linewidth, Δf_0 of this transition is 667 kHz, which reduces to 334 kHz when both photons are simultaneously detuned from the same source, as in the case of Doppler-free spectroscopy. This is about 18 times narrower than the Rb D2 $5S_{1/2} \rightarrow 5P_{3/2}$ hyperfine transitions at 780

nm. As discussed in section 1.5 the recent improvements in OFC technology opens up the options for using an Rb TPT reference for a portable optical atomic clock.

Several groups are testing the Rb D2 TPT as a clock transition for a compact optical atomic clock, including Z. L. Newman et al. from NIST [30, 33] and K.W. Martin et al. with the Air Force Research Laboratory (AFRL) [31]. The NIST group are focused on developing a miniaturised optical atomic clock, demonstrating a short-term Adev stability of 2.9 $\times 10^{-12}/\sqrt{\tau}$ and reaching a noise floor of 1 $\times 10^{-13}$ at 1000 seconds [49]. The AFRL group have demonstrated a lab-based Rb TPT clock, with a short-term frequency stability of 3 $\times 10^{-13}/\sqrt{\tau}$, reaching an even lower noise floor of $\simeq$ 4.6 $\times 10^{-15}$ at 16,000 seconds averaging time intervals.

2.2 Excitation Scheme

The energy levels invloved in excitation and detection of the ^{87}Rb $5S_{1/2} \rightarrow 5D_{5/2}$ TPT are shown in diagram Fig. 2.1a. The $5D_{5/2}$ can by excited using two separate lasers matching the intermediate transitions at 780 nm and 776 nm (dichroic excitation), or else by using a single laser of 778 nm (monochromatic excitation) while detuned by Δ = 1.056 THz (2.131 nm) from the intermediate $5P_{3/2}$ state. The ground-state and excited-state both have several hyperfine components as shown in Fig. 2.1b. For this particular transition, the strongest excitation occurs between the $5S_{1/2}$, F = 2 and $5D_{5/2}$, F' = 4 hyperfine states. This is because the atoms in this excited state can only return to the F = 2 hyperfine level of the ground state, when they decay from the F' = 4 hyperfine level of the excited state, making it a "closed transition".

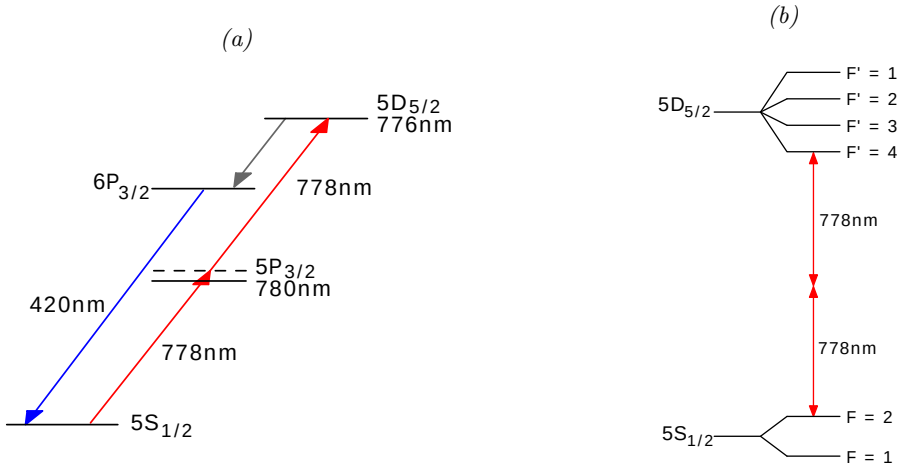

Figure 2.1: (a) Monochromatic excitation (778 nm), and emission (420 nm) of the ^{87}Rb 2-photon transition, with 1 THz detuning from the intermediate 5P energy level. (b) Excitation to the F' = 4 excited hyperfine level enables a closed transition cycle, preventing atoms falling in to the 5S, F = 1 dark ground state.

In terms of building a compact system, there are clear advantages to using a single

778 nm source, rather than two individual lasers. The first advantage being a reduction in equipment, and the second being the common noise between both of the photons absorbed. The downside however, is that the large detuning of the probe laser from the intermediate transitions greatly reduces the excitation rate of the 2-photon transition. Dichroic excitation is implemented by some groups working toward an Rb optical reference [10, 50]. However the more commonly used method is to excite directly to the upper state by the simultaneous absorption of two 778 nm photons.

The natural linewidth of the TPT is set by the upper-most excited state lifetime of the two-level transition, which in this case is the $5D_{5/2}$ level:

$$\Delta f_0 = \frac{1}{2\ \tau_{5D}} \tag{2.1}$$

The measured natural linewidth is reduced by a factor of 2, corresponding to the simultaneous detuning of the two photons which excite the transition. A paper from 2008 by D. Sheng et al. performs measurements of the 5D state lifetimes in ^{87}Rb, yielding 238.5 ± 2.3 ns [51] which agree closely with theoretical predictions of 235 ns, made by M. S. Safronova et al. [52]. Using $\tau_{5D} = 238.5 \pm 2.3$ ns yields a natural linewidth of 334 ± 3 kHz which equals the value typically quoted by other groups working towards an atomic clock using this transition [31, 33, 50].

One of the most comprehensive spectroscopic measurements of this transition and the neighbouring Rb TPTs, was carried out in 1993 by F. Nez et al. They measured a frequency (in vacuum) of 385.284566371 THz (778.107 nm) with an accuracy of ±8 kHz and a measured linewidth of $\simeq$ 500 kHz [34]. In recent years, more accurate measurements have been made by J.E. Bernard et al. [44] and by C.S. Edwards et al. [42] with lower uncertainties down to ±2 kHz.

Without requiring any changes to the experimental apparatus, one can easily perform spectroscopy of all of the Rb D2 TPTs from both ground hyperfine states in ^{87}Rb and ^{85}Rb, resulting in 4 sets of TPTs. The two strongest sets of hyperfine TPTs are the ^{87}Rb $5S_{1/2}, F = 2 \rightarrow 5D_{5/2}, F' = 4$ and the ^{85}Rb $5S_{1/2}, F = 3 \rightarrow 5D_{5/2}, F' = 5$ TPTs, which occur within 600 MHz of each other. In Rb vapour cells containing samples of naturally occurring Rb, such as are used in this work, the ^{85}Rb isotopes generate stronger fluorescence. However, the ^{87}Rb TPT is chosen to work with due to its lower second order Zeeman shift [31] as well as reduced linewidth-broadening, in the presence of magnetic fields, which will be discussed in Chapters 2.6 and 2.7. This is an important factor when considering the applications of such a frequency reference to be integrated in to a portable atomic clock.

2.3 Doppler-Free Spectroscopy Theory

Doppler-free spectroscopy of two-photon transitions has been extensively documented since the 1970's [53–55]. This method of spectroscopy is free of temperature-dependent Doppler-broadening, allowing one to resolve the natural linewidth of the 2-photon transitions with a heated Rb sample and relatively compact apparatus. Two-photon Doppler-free Spectroscopy has been used to map out narrowly-spaced hyperfine states [34] and precisely measure other atomic properties such as the Rydberg constant and Lamb-shift [56, 57] as well as Einstein-A coefficients [58]. Early applications of this technique were conducted with sodium [59], and eventually the rest of the alkali metals [58].

At room temperature, the natural linewidth of a transition is typically obscured by Doppler-broadening. Doppler-broadening occurs as a result of atoms in a sample having a distribution of velocities when they interact with photons at some excitation frequency, f_0. From the atoms perspective, f_0 is Doppler-shifted higher or lower according to their velocity, v relative to the direction of the propagating photons:

$$f = f_0(1 - \frac{v}{c}) \tag{2.2}$$

This is similar to the effect which can be heard when a car passes, and sounds high frequency (blue-shifted) as it approaches and low frequency (red-shifted) as it travels away from you. Relative to any single axis (e.g. x-axis) along which the propagating photons interact with the atoms, the range of atomic velocities (v_x) are centred around 0 ms^{-1}, with a Gaussian profile. The shape of this profile is determined by the 1D Boltzmann velocity distribution, which gives the probability density of the atoms having a particular velocity relative to a single axis using the formula:

$$f(v_x) = \sqrt{\frac{m}{2\pi k_B T}} e^{\frac{-m v_x^2}{2k_B T}} \tag{2.3}$$

In the equation above, k_B is the Boltzmann constant, m is the mass of a single atom, T is in Kelvin, and v_x is the 1D component of the atoms velocity in ms^{-1}. For most symmetrical distributions, e.g. Gaussian or Lorentzian, the peak amplitude varies inversely proportionally to the FWHM. When the Boltzmann distribution is plotted for a range of temperatures, as shown in Fig. 2.2, it becomes clear that lowering the atomic temperature leads to a higher probability of finding atoms with $\mathrm{v}_x = 0$ ms^{-1}. This is because the same number of atoms in the sample are now distributed between a narrower velocity range.

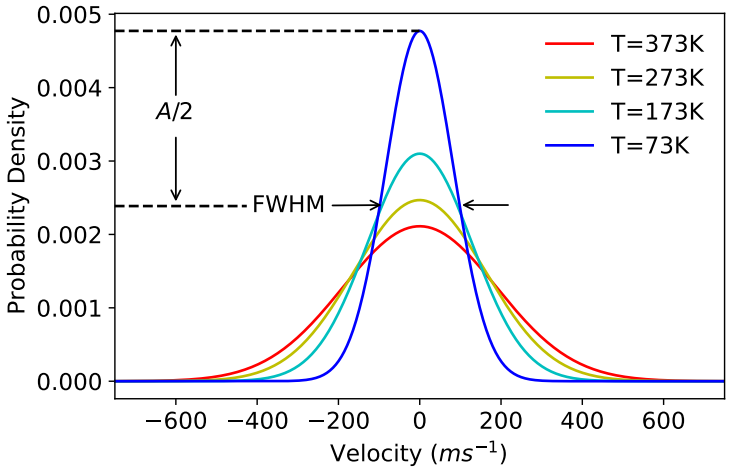

Figure 2.2: The 1D Boltzmann velocity distribution for ^{87}Rb atoms, plotted for a range of temperatures.

If the x-axis of Fig. 2.2 is then converted to Doppler-shifted frequencies, using Eq. 2.2, one can attain the Doppler-Broadened transition profile. The FWHM (full-width half-maximum) of the transition profile in terms of frequency, is given by the Doppler-width Δf_D:

$$\Delta f_D = 2\sqrt{ln2}\frac{v_p}{c} f_0 \tag{2.4}$$

Where c is the speed of light in a vacuum, and, v_p (the most probable velocity of the atoms) is calculated as a function of the temperature. In the case of a heated ^{87}Rb sample at 100 °C, $v_p = 267$ ms^{-1} and therefore $\Delta f_D = 572$ MHz. Fig. 2.2 demonstrates how the velocity distribution and hence Doppler-width, become narrower at lower temperatures. One way to achieve a Doppler-free signal is to bring the atomic temperature down as close to zero Kelvin as possible. This is one of the benefits of preparing the atoms in a magneto-optical trap (MOT). However, Doppler-free spectroscopy can also eliminate the Doppler-broadening using far less apparatus than a MOT. The simple trick to this method is to excite the two-photon transition with counter-propagating beams, as shown in Fig. 2.3. When the atom excites to its upper state, while absorbing a photon from both directions, the Doppler shifts of the photons will cancel out to allow the excitation to occur perfectly on resonance as shown below:

$$f_0(1 + \frac{v_x}{c}) + f_0(1 - \frac{v_x}{c}) = 2f_0 \tag{2.5}$$

From inspection of Eq. 2.5, it should be noted that one can use any velocity and still maintain the resonance condition of $2f_0$, which means that all of the atoms, regardless of their temperature or velocity, will contribute to a Doppler-free signal. It is worth

noting that saturable absorption spectroscopy [60] also provides a Doppler-free signal using single-photon transitions, but it is limited to interacting only with atoms of a specific velocity. Doppler-free spectroscopy often takes advantage of this aspect of the signals insensitivity to temperature by using a heated vapour cell to increase the atom density in the beam path.

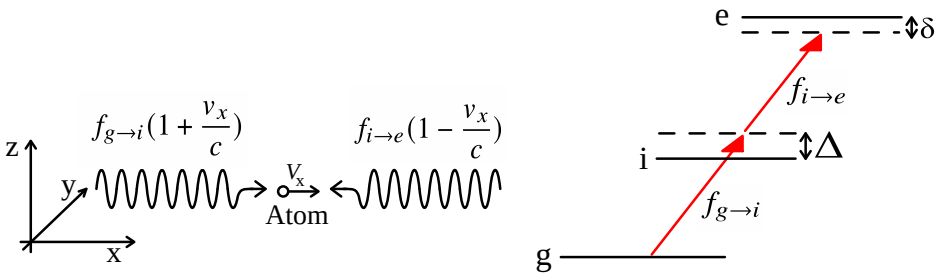

Figure 2.3: When the atoms absorb both photons from opposite directions, they may excite directly from ground, g to the upper state, e via a virtual intermediate level, which is detuned from level i, by Δ. Complete Doppler cancellation is achieved when $f_{g\to i} = f_{i\to e}$, but some degree of Doppler cancellation is also possible while the counter-propagating photons are both resonant with level i. δ is a small detuning of the photons, which allows us to scan over the transition resonance.

Due to the fact that two photons may still be absorbed from the same direction, as well as opposite directions, the lineshape of a typical Doppler-free TPT signal is the convolution of the Doppler-broadened Gaussian profile and a Doppler-free Lorentzian profile. However, the Doppler-width of 572 MHz compared with $\Delta\nu_{778} = 0.334$ MHz, means the relative amplitude of the Gaussian component is ∼1000x lower. Therefore the Doppler-free spectroscopy signal is essentially a Lorentzian profile which sits on top of a Doppler-broadened background, sometimes referred to as a Doppler pedestal. The beams must be perfectly anti-parallel, for this to work well. The effects of misalignment from anti-parallel are addressed further on in section 2.8.1.

There is however, never an exact cancellation of the Doppler-broadening, and some residual Doppler-broadening is present owing to a second order Doppler shift [53]. This shift arises, as the atoms are technically heavier in the excited state than in the ground state, owing to the absorption of the momentum of the two photons. This leads to the atoms acquiring a small velocity relative to the frame in which the atoms velocity was previously zero. The resulting shift, determined in [53], can be estimated using:

$$\Delta f_{D2} \simeq -f_0 \left(\frac{v_p^2}{2c^2}\right) \tag{2.6}$$

This yields a shift of -112 Hz at 0 °C and -153 Hz at 100 °C. The fractional shift relative to the transition frequency is about -1×10^{-15}/K.

2.4 Excitation Rate Theory

Monochromatic excitation at 778 nm occurs via a virtual intermediate level and is possible since the energy of the two 778 nm photons adds up to the same value as the sum of the 780 and 776 nm photons. The virtual intermediate level is detuned from the $5P_{3/2}$ state by $\Delta = +1.056$ THz (2.131 nm), which is also referred to as the energy defect. The two-photon transition probability may be calculated using perturbation theory to second order. According to the 1977 paper by Cagnac and Grynberg [54], the excitation rate of an atom from the ground state, g to an excited state, e via an intermediate state, i, is equal to:

$$\Gamma_{g\to e} = \frac{\Delta\nu_e}{(2\delta)^2 + \Delta\nu_e^2/4}\left|\sum_i \frac{< e|H_1|i >< i|H_2|g > + < e|H_2|i >< i|H_1|g >}{\Delta}\right|^2 \quad (2.7)$$

H_1 and H_2 are the interaction Hamiltonians, Δ, is the energy defect, and $\Delta\nu_e$ is the excited state linewidth. Assuming that both beams from either direction are equal intensity, and the detuning, δ of the individual photons from the TPT resonance is zero then the formula simplifies to:

$$\Gamma_{g\to e} = \frac{16}{\Delta\nu_e}\left|\sum_i \frac{< e|H_1|i >< i|H_2|g >}{\Delta}\right|^2 \quad (2.8)$$

This approach is considered accurate under the assumptions that the intermediate transitions are non-resonant with the laser. Upon the substitution of expressions for the Hamiltonians, the authors of [54] derive a more specific expression for the 778 nm TPT excitation rate, Γ_{778}:

$$\Gamma_{778} = \frac{1}{\Delta\nu_{5D}}\left(\frac{3\times r_0\times\lambda_{780}\lambda_{776}}{\pi\hbar c}\right)^2 I^2\frac{\omega_{780}\omega_{776}}{\Delta^2}f_{780}f_{776} \times|< j_g\ m_g; j_i\ m_i|J\ M >< j_i\ m_i; j_e\ m_e|J\ M >|^2 \quad (2.9)$$

In equation 2.9, $\Delta\nu_{5D} = 4192872$ s^{-1} [51], $r_0 = e^2/(4\pi\epsilon_0 m_e c^2) = 2.8\times10^{-15}$ m (the classical radius of the electron). I is the average intensity of both counter-propagating beams, in W/m^2, and the quadratic relationship of the excitation rate with the intensity, defines the non-linear behaviour of this excitation. The values used for the oscillator strengths, f_{780} and f_{776} are discussed below. The final term is the squared product of the Clebsch-Gordon (CG) coefficients for the intermediate transitions. This term is equal to 1, assuming only light source is only exciting the F = 2 $\rightarrow$ F' = 4 hyperfine TPT.

In the M. Safronova paper [52], updated dipole matrix elements are calculated for $D_{780} = 5.956$ and $D_{776} = 1.821$ (in units of a_0 - the Bohr radius), which they use to calculate the oscillator strengths of these transitions. The calculated oscillator strengths are $f_{780} = 0.691$ and $f_{776} = 0.053$. However, in [34], Biraben et al. quote using the oscillator strengths $f_{780} = 1$ and $f_{776} = 0.003440$, but without discussing how they attain these numbers. If the values from the Dirac-Hartree-Fock estimation of the dipole matrix elements (also quoted in [52]) is used, then one attains: $D_{780} = 6.807$ and $D_{776} = 0.493$, $f_{780} = 0.902$ and $f_{776} = 0.002379$. In this case, it seems appropriate to go with the values which Biraben et al. have quoted, as they correspond to the specific hyperfine transition used in this work. Calculating Γ_{778} from Eq. 2.9, using the same intensity of 1 W/cm^2, and oscillator strengths quoted in [34], yields a value of 27.8 s^{-1}, which agrees to within 7% of the value which they obtain. Using the relative transition intensities which have been calculated in this same paper, its also possible to model the spectrum which can be observed while scanning over all 4 of the TPT hyperfine transitions for ^{87}Rb, which is shown in Fig. 2.4.

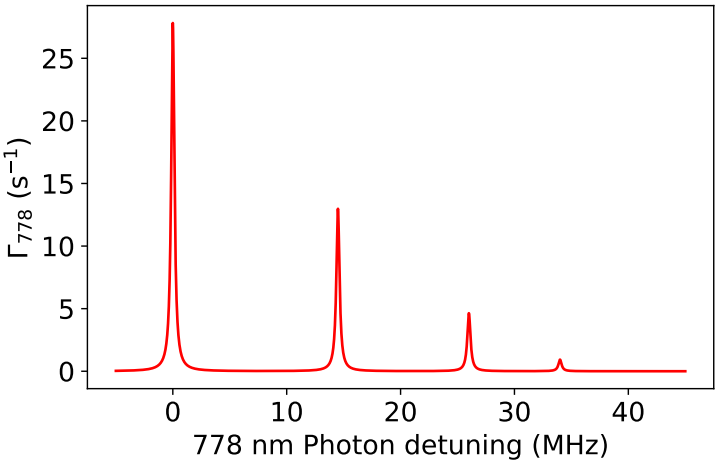

Figure 2.4: Estimation of the resonant excitation rate per atom for each of the hyperfine features of the ^{87}Rb $5S_{1/2}$, F=2 and $5D_{5/2}$, F'=4,3,2,1 under a 1 W/cm^2 linearly polarised illumination, using relative feature spacing and transition intensities quoted in [34].

There are several possible routes for atoms to decay from the $5D_{5/2}$ state, with a certain probability associated for each route. This means that not all atoms decaying from the excited state will result in 420 nm fluorescence. Branching ratios give the probability of decay to each of the neighbouring lower energy states. In this case, the branching ratios must be considered during the decay route from $5D_{5/2} \rightarrow 6P_{3/2} \rightarrow 5S_{1/2}$ (Fig. 2.1a), resulting in the emission of a 420 nm photon (as well as a 5.232-μm photon in the first step). Using the branching ratios from the 5D level quoted in [61], the $5D_{5/2} \rightarrow 6P_{3/2}$ decay has a 35% probability and the $6P_{3/2} \rightarrow 5S_{1/2}$ has a 31% probability. Hence the fluorescence scattering rate is related to the excitation rate as follows:

$$\Gamma_{420} = 0.35 \times 0.31 \times \Gamma_{778} = 0.123 \times \Gamma_{778} \tag{2.10}$$

Using the calculated fluorescence rate per atom, combined with the number of illuminated atoms in the cell and the power of a 420 nm photon, it is then possible to calculate how much power is radiated during excitation. This will be discussed further in Chapter 2.8.

2.5 Light Shift Sensitivity

The light shift, Δf_{LS} is also known as the A.C. Stark shift and denotes the atomic energy level shift caused by the presence of an an external oscillating electric field. The effect causes an offset on the transition frequency which is proportional to the intensity of the electric field, and if there are fluctuations in the fields intensity, then this leads to frequency noise. As noted in publications employing the Rb TPT for an optical atomic clock system [10, 31], the light shift is one of the largest contributing factors which limits the long-term stability of the clock frequency. The issue is worse for the Rb TPT than for single photon transitions because of the high 778 nm intensity ($\geq$ 10 W/cm^2 compared with $\sim$ 1 mW/cm^2 for $5S_{1/2} \rightarrow 5P_{3/2}$) required to achieve an equivalently strong signal from the weakly exciting Rb TPT. In C. Foot's Atomic Physics textbook, Chapter 7.7 [62], the A.C. Stark shift, Δf_{LS} is given as:

$$\Delta f_{LS} = \frac{\Omega_R^2}{4\Delta} \tag{2.11}$$

For the equation above, Δ is the detuning of a perturbing electromagnetic field from the transition frequency, and the Rabi frequency, Ω_R determines the strength of the interaction between an electromagnetic field and the atoms. In Chapter 7.1 of [62], the Rabi frequency is defined as:

$$\Omega_R = \frac{e < g|x|e > |E_0|}{\hbar} = \frac{e|D_{g\rightarrow e}||E_0|}{\sqrt{3}\hbar} \tag{2.12}$$

In the above equation e is the charge of an electron and $< g|x|e >= |D_{g\rightarrow e}|/\sqrt{3}$, with $D_{g\rightarrow e}$ equal to the matrix element for the transition between ground and excited states. The electric field amplitude $E_0 \propto \sqrt{I}$ (see Eq. 4.8). In the case of the Rb TPT, $\Delta = 1.05$ THz. The two-photon transition may be assigned an effective Rabi frequency, Ω_{eff} combining the response of both involved transitions, which is defined in appendix E1 of [62] as follows:

$$\Omega_{eff} = \frac{\Omega_{R,g\rightarrow i} \times \Omega_{R,i\rightarrow e}}{2\Delta} \tag{2.13}$$

In the case of the Rb TPT, $\Delta = 1.05$ THz for both Eq. 2.11 and 2.13. Once Ω_{eff} is substituted in to Eq. 2.11, the calculation for Δf_{LS} in the case of a TPT is therefore:

$$\Delta f_{LS} \propto I^2/\Delta^3 \tag{2.14}$$

rather than just I/Δ for a single-photon transition. Many publications have measured and calculated this shift in the past, and for now it will suffice to quote the sensitivity for the Rb TPT, measured in [31], as a fractional frequency (at 385.285 THz) of -6.6$\times 10^{-15}$/(mW/cm^2). Telecoms lasers, like those described in this thesis, often have built-in feedback to stabilise the optical output power, achieving peak-peak fluctuations which are less than 1% of the output power. Assuming a 778 nm intensity of 10 W/cm^2, the overall light shift is calculated to be Δf_{LS} = -25.5 kHz, with typical power fluctuations leading to a maximum fractional frequency noise of 6.64 $\times 10^{-13}$.

The light shift, becomes more problematic for AFR operating on satellites in orbit, as noted in [15]. Higher levels of solar and cosmic radiation are present outside the Earth's atmosphere, leading to higher chances of light-shifts from local radiation. Additionally, gradual ageing of the laser and intense daily temperature fluctuations of an orbiting satellite can lead to optical misalignment and changes in optical power, which then contribute to light shift, potentially resulting in long time scale frequency drifts.

2.6 Magnetic Sensitivity

In atomic spectroscopy for frequency references and especially for atomic clocks, the effects of magnetic fields are typically minimised by placing the atomic vapour cell in a Mu-metal shield or by using Helmholtz coils to cancel external magnetic fields. For portable frequency references this is especially necessary, due to changes in the local magnetic field depending on the location of the device. For the majority of the results in this thesis there was no magnetic shielding, owing to the focus being on other aspects of the spectroscopy apparatus and laser systems. This section and the following section will discuss the sensitivity of the reference TPT to magnetic fields, and estimate the broadening of the measured Rb TPT spectra which can be attributed to local background magnetic fields.

In the presence of a static magnetic field, the structure of the hyperfine levels becomes non-degenerate, by the splitting of each hyperfine level in to 2F+1 sub-levels. This effect is known as Zeeman splitting, and generates a series of Zeeman levels, (denoted m_F) with integers in the range:

$$m_F = -F ... + F \tag{2.15}$$

The Zeeman effect leads to a broadening of the transition linewidth, and can also lead to a shift in the resonant frequency of the transition. In the relatively low background magnetic field of Earth ($\simeq$ 0.5 Gauss or 50 μTesla), the Zeeman level splitting is too small ($<$ 1 MHz) to lead to any coupling between neighbouring hyperfine states. In this range the frequency shift of the Zeeman levels, $\Delta f_{|F,m_F>}$ varies linearly with the background magnetic field according to the normal Zeeman effect:

$$\Delta f_{|F,m_F>} = \frac{g_F m_F \mu_B B_0}{h} \tag{2.16}$$

Where h is planck's constant, B_0 is the magnetic field in Tesla and μ_B is the Bohr magneton. The m_F number of the Zeeman level affects the direction as well as the magnitude of the shift from its unperturbed energy. When comparing the sensitivity of different hyperfine transitions, the hyperfine Landé g-factor, g_F can make one transition more magnetically sensitive than another. This factor can be calculated using the following relationship from Chapter 7.4.1 of [63]:

$$g_F \approx g_J \frac{F(F+1) - I(I+1) + J(J+1)}{2F(F+1)} \tag{2.17}$$

In the above equation, F is the total atomic angular momentum (or hyperfine number), I is the nuclear spin of the atom (I = 3/2 for ^{87}Rb), J is the total electron angular momentum and g_J is the fine structure g-factor, which can be calculated using the formula (Chapter 7.4.1 of [63]):

$$g_J = 1 + \frac{J(J+1) + S(S+1) - L(L+1)}{2J(J+1)} \tag{2.18}$$

Where L is the orbital angular momentum, and S is the spin angular momentum. While the value of I must be attained from an appropriate reference such as [64], the values for L, S, F and J may be extracted from the spectroscopic energy level notation in the form below:

$$n^{2S+1}L_J \tag{2.19}$$

For the spectroscopic notation outlined in [63], n is the principal quantum number and the orbital angular momentum, L is an integer value in the set 0,1,2,3... each of which are represented by the letters, S,P,D,F respectively. The number in superscript tells us the multiplicity of the atomic state, which is always 2 for the alkali atoms (making S = 1/2) due to having only a single electron in their outermost electron shell. The superscript number is often omitted when there is no change in its value for the considered transition. Possible values of J occur in increments of 1 within the following range:

$$J = |L - S|...|L + S| \tag{2.20}$$

Using the values J and I, one can find the values of the hyperfine levels associated with an atomic state. These occur in increments of 1 within the following range:

$$F = |J - I|...|J + I| \tag{2.21}$$

To summarise the spectroscopic notation, Fig. 2.5 shows an example of the determination of the quantum numbers of the ^{87}Rb $5D_{5/2}$ energy level and its associated hyperfine and Zeeman level structure.

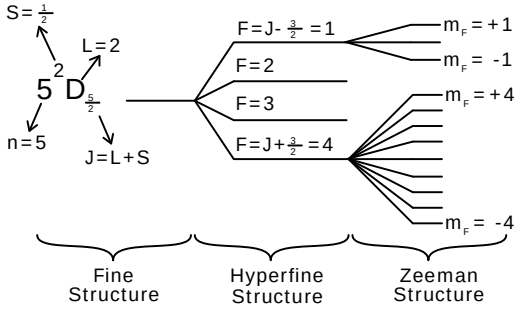

Figure 2.5: Example diagram of the hyperfine and Zeeman level structure associated with the ^{87}Rb $5D_{5/2}$ fine structure level.

The tables below summarise the contributing factors to the first order magnetic sensitivity associated with each level of the strongest TPTs for both Rb isotopes.

Transition Level	$5S_{1/2}, F = 2$	$5P_{3/2}, F = 3$	$5D_{5/2}, F = 4$
g_J	2.002	1.334	1.200
g_F	0.500	0.666	0.750
$\Delta f_{\|F,m_F=\pm1>}$ (MHz/Gauss)	± 0.699	± 0.934	± 1.049

Table 2.1: Calculated values for determining the magnetic sensitivity of the levels involved in the ^{87}Rb $5S_{1/2}, F = 2 \rightarrow 5D_{5/2}, F' = 4$ transition.

Transition Level	$5S_{1/2}, F = 3$	$5P_{3/2}, F = 4$	$5D_{5/2}, F = 5$
g_J	2.002	1.334	1.200
g_F	0.333	0.500	0.600
$\Delta f_{\|F,m_F=\pm1>}$ (MHz/Gauss)	± 0.466	± 0.699	± 0.839

Table 2.2: Calculated values for determining the magnetic sensitivity of the levels involved in the ^{85}Rb $5S_{1/2}, F = 3 \rightarrow 5D_{5/2}, F' = 5$ transition.

The overall shift of the TPTs between the Zeeman levels can be obtained by subtracting the excited level sensitivity from the ground level sensitivity. The intermediate level does not play a role in the overall shift of the frequency of the TPT Zeeman transitions. Therefore, in the case of the ^{87}Rb reference TPT this leads to 0.350 MHz/Gauss, and for the ^{85}Rb reference TPT, this leads to 0.373 MHz/Gauss.

In Fig. 2.6 the shift of the TPTs between the Zeeman levels of both Rb isotopes are plotted across a range of magnetic field strengths. In this case one assumes that only π transitions (i.e. $\Delta m_F = 0$) are occurring, by using a linearly polarised laser with the imposing magnetic field direction parallel to the angle of linear polarisation. Using this combination of magnetic field and polarisation ensures the Zeeman levels are symmetrically populated either side of $m_F = 0$. Hence there is no overall shift (to first order approximations) of the transition in the magnetic field, and the dominant effect is a uniform broadening of the transition linewidth. For this reason most frequency references and atomic clocks will ultimately choose to excite the clock transition in this way. The outermost Zeeman levels of both isotopes will not be populated in this case, as they cannot be reached during the transition while satisfying $\Delta m_F = 0$ (see Fig. 2.7 for more details).

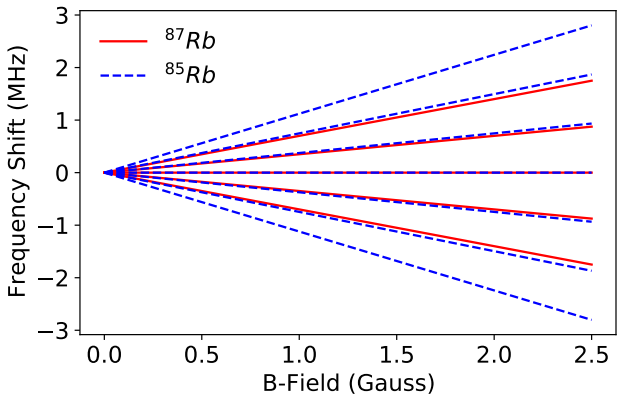

Figure 2.6: Zeeman level splitting for ^{87}Rb $5S_{1/2}, F = 2 \rightarrow 5D_{5/2}, F' = 4$ and ^{85}Rb $5S_{1/2}, F = 3 \rightarrow 5D_{5/2}, F' = 5$ $\Delta m_F = 0$ TPTs in the presence of a magnetic field.

Primarily owing to the higher F-number for the states in the ground and excited levels of the ^{85}Rb TPT, the overall broadening of the transition as the Zeeman levels split apart will be larger than for ^{87}Rb. In [31], K.W. Martin et al. calculate that the ^{85}Rb TPT possesses a second-order Zeeman shift of 190 kHz/Gauss^2, which is almost 4 times larger than the calculated 50 kHz/Gauss^2 for the ^{87}Rb TPT. For these reasons, again the ^{87}Rb TPT is a reasonable isotope choice as a reference transition. Circular polarisation is chosen rather than linear polarisation for the experiments presented here, and this changes the magnetic sensitivity of the TPT. The next section will discuss the differences arising from using different polarisation in the presence of a magnetic field.

2.7 Comparing Pump Polarisation Schemes

As previously mentioned with regards to Fig. 2.6, optical polarisation plays a role in determining how the Zeeman sub-levels within each hyperfine F-state become populated. In the presence of linearly polarised pump light, π transitions can occur, resulting in $\Delta m_F = 0$ transitions between the ground and excited state. Whereas in the presence of circularly polarised light, σ transitions can occur, inducing $\Delta m_F = \pm 1$ per hyperfine level to which the atoms are excited. Right-handed circular polarisation will be considered as rotating clockwise around the direction of propagation of the beam, leading to excite σ^+ transitions where $\Delta m_F = +1$. Therefore the opposite will apply for left-handed polarisation, exciting σ^- transitions where $\Delta m_F = -1$.

For a two-photon excitation, $\Delta m_F = -2, 0, +2$ are the allowed change in Zeeman states, corresponding to the 2 photons absorbed in the excitation. There are 3 possible polarisation schemes for driving the two-photon transition, including $\sigma^+ + \sigma^+$, $\pi + \pi$ and $\sigma^+ + \sigma^-$. Fig. 2.7 shows how the excited Zeeman states become populated as a result of each of the 3 polarisation schemes.

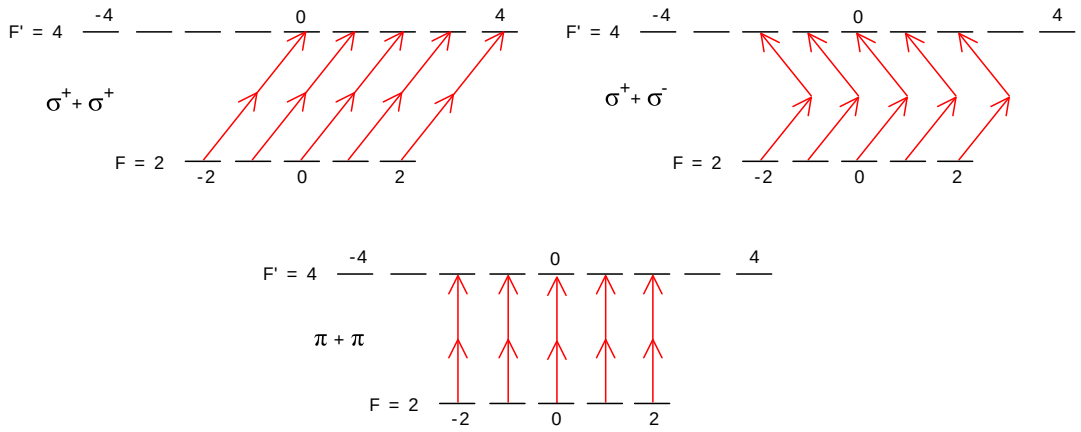

Figure 2.7: Different excitation paths to populate the excited Zeeman levels of the ^{87}Rb $5S_{1/2}, F = 2 \rightarrow 5D_{5/2}, F' = 4$, during a 2-photon excitation, using the 3 polarisation schemes that are discussed above. In the case of $\sigma^+ + \sigma^+$, the handedness of the polarisation as well as the direction of the magnetic field affect wether the population is biased toward + or - m_F levels.

In order to drive σ and π Zeeman transitions, the local magnetic field must be correctly oriented with the axis of polarisation for the propagating electromagnetic field. For linear polarisation this axis is parallel to the axis of polarisation, and for circular this is the axis along which the beam propagates (indicated in Fig. 2.8). When a magnetic field is not aligned correctly with the polarisation of the light, the atoms are excited with a mixture of π and σ transitions.

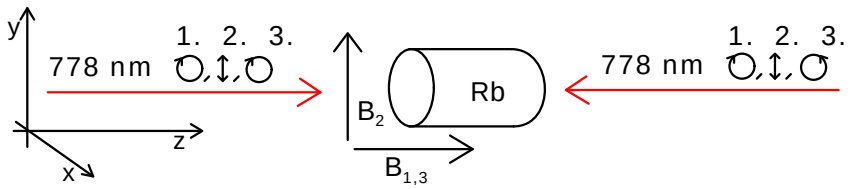

Figure 2.8: A vapour cell (rubidium) with an applied magnetic field along the beams propagation axis causes Zeeman splitting. The polarisation of the counter-propagating beams will alter the population distribution of the excited state Zeeman levels, if aligned with particular directions of magnetic field. Key: 1. right-circular + right-circular polarisation combined with magnetic field ($B_{1,3}$), 2. linear + linear polarisation combined with magnetic field (B_2), 3. right-circular + left-circular polarisation combined with magnetic field ($B_{1,3}$).

In all of the spectroscopy data presented in this thesis, the $\sigma^+ + \sigma^+$ polarisation scheme was chosen because it resulted in the narrowest TPT linewidth compared to the other schemes while there was no magnetic shielding. However, the local magnetic field was not necessarily oriented along a single axis, and hence it is difficult to be sure that only π or σ transitions are being driven. Instead it is likely that a combination of both are being driven, with a bias to one type or the other, depending on the orientation of the magnetic field w.r.t. the beams axis. When a mixture of the transitions are being driven, all of the excited state m_F levels could be populated simultaneously. In the best case scenario, only as many Zeeman levels as the ground state are populated.

To provide upper and lower bounds on the amount of linewidth broadening which can be attributed to local magnetic fields, it is first assumed that there is no optical pumping occurring for a thermal vapour cell. This prevents the biasing of the population toward any particular upper state Zeeman level. If the population is equal in each level, then the broadening is directly proportional to how many Zeeman levels are populated. The next step is to multiply the TPT Zeeman splitting sensitivity per m_F level by the number of populated excited state levels (minus the $m_F = 0$ level) to yield the upper and lower estimations of the Zeeman broadening, Δf_B as shown below.

Using the values given in table 2.1, the ^{87}Rb upper and lower estimate will be:

$$\Delta f_B = 8 \times (\Delta f_{|F=4,m_F=1>} - \Delta f_{|F=2,m_F=1>}) = 2.80\ MHz/Gauss$$
$$\Delta f_B = 4 \times (\Delta f_{|F=4,m_F=1>} - \Delta f_{|F=2,m_F=1>}) = 1.40\ MHz/Gauss$$

And again, using the values given in table 2.2, the ^{85}Rb upper and lower estimate will be:

$$\Delta f_B = 10 \times (\Delta f_{|F=5,m_F=1>} - \Delta f_{|F=3,m_F=1>}) = 3.73\ MHz/Gauss$$
$$\Delta f_B = 6 \times (\Delta f_{|F=5,m_F=1>} - \Delta f_{|F=3,m_F=1>}) = 2.24\ MHz/Gauss$$

Taking the average of the upper and lower estimates for both isotopes yields a value of 2.10 MHz/Gauss for ^{87}Rb, and 2.99 MHz/Gauss for ^{85}Rb.

Due to the magnetically-broadened lineshape resulting from the overlapping profiles of each of the individually offset Zeeman transitions, there is a limited range of field strengths where it is appropriate to assume the broadening increases linearly. In very low field strengths ($<$ 0.25 Gauss) or with excess broadening from other mechanisms (e.g. Δf_{tt}) a high degree of overlap of the Zeeman transitions reduces the rate of broadening. Fig. 2.9 shows simulations of the lineshape of the ^{87}Rb reference TPT in different magnetic field strengths and depicts how the lineshape changes and the amplitude is reduced as the magnetic field increases. When the atomic population is split between extra excited state m_F levels the amplitude is further reduced. Once the field is larger than 2 Gauss, it is possible to resolve the individual Zeeman transitions and these will not be broadened by the magnetic field.

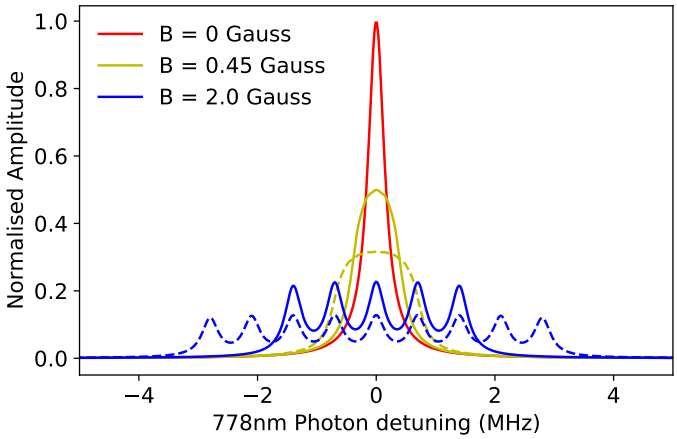

Figure 2.9: Simulated lineshapes of the $^{87}RbF = 2 \rightarrow F' = 4$ TPT at different strengths of magnetic field assuming no additional broadening mechanisms. The solid line profiles are the result of occupying the minimum number of excited state m_F levels, while dashed line profiles result from occupying the maximum number of m_F levels.

As mentioned already, due to the lack of magnetic shielding, the $\sigma^+ + \sigma^+$ is used for the time being, to allow characterisation of the detection apparatus and lasers, with less sensitivity to external magnetic fields such as Earth's prevailing background field. The reduced sensitivity of $\sigma^+ + \sigma^+$ over $\pi + \pi$ polarisation scheme is likely because the local field is oriented to more cleanly drive the $\sigma^+ + \sigma^+$ transitions. It should be noted the $\sigma^+ + \sigma^+$ polarisation scheme results in a shift in the overall line centre of the transition because the excited state population becomes centred around the $m_F = \pm 2$ level. For the ^{87}Rb reference transition, this results in a shift of:

$$\Delta f = \Delta f_{|F=4,m_F=2>} = \pm 2.1\ MHz/Gauss$$

2.8 Spectroscopy and Detection Apparatus

The apparatus used to excite and detect the fluorescence signal from the Rb TPTs requires no more than a pair of sufficiently intense counter-propagating beams crossing through an Rb vapour cell and a detector positioned at the side of that cell to detect the fluorescence at 420 nm. Some variations include:

1. Use of focused beams in to the centre of the cell, to increase the pump intensity [46, 65, 66].
2. Placement of the Rb cell within an optical cavity to increase the pump intensity [42, 44, 45].
3. Detection in-line with the retro-reflected beam through the Rb cell instead of from the side [33].
4. Excitation using a mode-locked, pulsed laser [67–69]. Such lasers typically possess narrow linewidth and high peak intensity, which are advantageous for the TPT excitation.

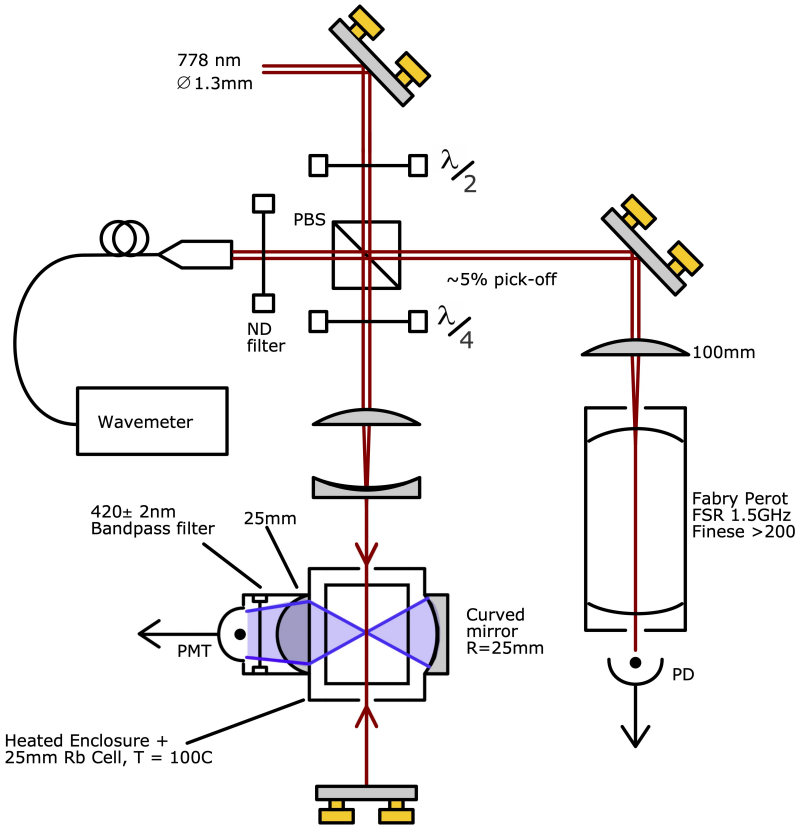

Figure 2.10: Apparatus used to carry out and detect Doppler-free spectroscopy of the Rb TPTs. The wavemeter and scanning Fabry-Perot help to make sure the laser is scanning properly and at the correct frequency when searching for the Rb TPT signal.

The apparatus employs a similar set up to that used by K.W. Martin et. al. [31]. This uses a collimated retro-reflected beam through the Rb cell, and side-on fluorescence detection from the using a PMT (Photo-Multiplier Tube), however with an additional curved mirror to boost fluoresce collection. Fig. 2.10 shows the layout of the excitation and detection apparatus. After the 778 nm beam exits the fibre collimator, a half-wave plate and PBS (polarising beam splitter) allows an adjustable amount of power to be picked off toward a Thorlabs SA200-5B scanning Fabry-Perot to help calibrate the pump laser scan range and make sure of its spectral quality. The transmitted beam is retro-reflected through a 25 mm length, natural abundance Rb vapour cell to carry out Doppler-free spectroscopy. As the beam returns to the PBS from spectroscopy, the majority of the return power can be coupled to a wavemeter to make sure the laser frequency is in the correct range to excite the Rb TPT reference transition. This arrangement of apparatus was planned out primarily as a test bed to ensure the chosen lasers worked properly for spectroscopy of the transition. Therefore, this version of the apparatus favours considerations allowing a large signal to be detected. However, in this version a 3D-printed oven is tested for enclosing the vapour cell, and securing the detection optics in place. In later chapters a more compact vapour cell oven, and detection scheme is developed for a micro-fabricated vapour cell.

2.8.1 Beam Preparation

Of the experiments mentioned so far, the typical laser power incident on the vapour cell can be anywhere between 1 and 30 mW [31, 33, 44, 70], depending on the capability of the laser used. Around 40±2 mW is typically used as the standard power at which to compare the Rb TPT spectra for different versions of the apparatus and the different lasers used. The beam suffers $\simeq 8\%$ power loss in reflections at each glass-air interface of the Rb vapour cell, which reduce the return beam intensity by 0.78x. This makes the typical average pump power in the cell 35.6 mW.

A quarter-wave plate sets the pump to a circular polarisation for driving the Rb TPT. This allows the TPT to be driven by σ^+, σ^+ transitions, which is shown in Chapter 2.7 to yield the strongest signal amplitude of the considered polarisation schemes. At later stages of the systems characterisation, outwith the scope of this work, linearly polarised pumping would enable more accurate measurements of the absolute frequency of the transition.

Perfect alignment of the beams play both a role in achieving the largest possible Doppler-free signal, and also for ensuring full cancellation of the Doppler-broadening. The Doppler-broadening is only fully cancelled out when both of the absorbed forward and counter-propagating photons observe an equal but opposite velocity for the atom they interact with. Assuming the forward propagating beam sets the Doppler-free axis, and hence sets the velocity of the atoms it interacts with. The counter-propagating

beam is then misaligned with this axis by a certain amount, θ (indicated in Fig. 2.11), which then generates a velocity differential between the counter-propagating beams equal to $v_p(1 - cos(\theta))$. The most probable velocity, v_p, is used to calculate the average amount of residual Doppler broadening. Using this relationship, combined with Eq. 2.5,one can then derive an expression for the residual Doppler broadening, Δf_{RD} resulting from a misalignment of θ:

$$\Delta f_{RD} = \left| \frac{v_p f_0}{c} (1 - cos(\theta)) \right| \tag{2.22}$$

The returning beam through the Rb vapour cell is aligned with the forward-propagating beam, by adjusting the angles of the mirror before the beam splitter, and after the Rb cell, to ensure that the retro-reflected beam profile overlaps the 0.65 mm $1/e^2$ radius input beam profile where it hits the first mirror of the optics. The distance between the two mirrors is about 30 cm, and allows the beams to be aligned with $\leq$ 2 mRads ($\tan^{-1}(0.065/30)$) misalignment angle (θ) between the beams. At 2 mRads of misalignment, $\Delta f_{RD} \simeq 686$ Hz, which rather insignificant compared with the other broadening mechanisms which are present (e.g. Zeeman and transit-time broadening). By 10 mRads, $\Delta f_{RD} \simeq 17$ kHz, but the reduction in signal amplitude resulting from the reduction in intensity along the Doppler-free axis will already result in a much bigger issue than Δf_{RD} by this point.

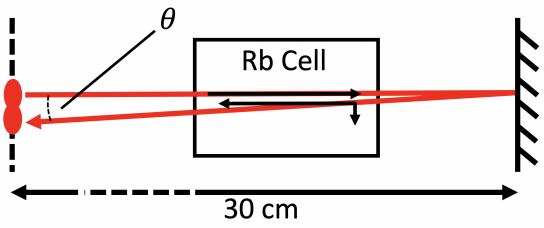

Figure 2.11: In this arrangement, the strength of the Doppler-free signal is determined by both overlap of the counter-propagating beams and the angle of misalignment of the return beam from the forward propagating beam. Both the return beam intensity and perceived differential velocity, may be calculated as vectors w.r.t. the axis of the forward-propagating beam.

Collimated beams are used for exciting the Rb TPT within the Rb vapour cell rather than focused beams, to ensure uniform intensity along the beams axis through the vapour cell. A Galilean style telescope is used in front of the Rb cell (see Fig. 2.10), to reduce the width of the pump beam in order to boost the intensity. There is a total return distance of approximately 140 mm from the telescope to the retro-reflecting mirror and back, and the beam will eventually begin to diverge as it propagates away from the telescope. The distance after which the beam has become $\sqrt{2}\times$ the width at the collimated waist of the beam, is known as the Rayleigh range, z_0:

$$z_0 = \frac{n\pi w_0^2}{\lambda} \tag{2.23}$$

Where n is the refractive index, w_0 is the $1/e^2$ beam radius at the collimated waist, and λ is the wavelength of the beam. There is a trade-off between creating sufficiently high pump intensity to achieve a measurable signal and maintaining beam collimation. Starting from a $1/e^2$ radius of 0.65 mm before the telescope, the beam radius is reduced no further than 0.22 mm, using a convex and concave lens pair. This would achieve a minimum Rayleigh range of 195 mm > the return distance, ensuring the beam intensity is not significantly reduced on its return through the cell.

Another factor to consider regarding the beam width is transit-time broadening, Δf_{tt} [54]. If the beam is too narrow, then the average velocity of the atoms carries them across the beam in a shorter interaction time than their excited state lifetime. This results in the measurement of a wider linewidth than the transitions natural linewidth. The amount by which the linewidth of a single-photon transition is broadened when crossing a Gaussian beam profile is given in Chapter 8 of [62] as well as Chapter 3.4 of [71]:

$$\Delta f_{tt} = \frac{2\sqrt{2\ln 2}}{2\pi}\frac{v_p}{2w_0} \tag{2.24}$$

Where w_0 is the same as for Eq. 2.23, and v_p is the most probable atomic speed, and the factor of 2π is simply required to convert from units of s^{-1} to Hz. However, for a two-photon transition the excitation results from the squared-intensity of the counter-propagating beams. Therefore the effective intensity that drives the transition can be thought of as resulting from a beam of the same physical width but with an intensity profile which is narrower by $1/\sqrt{2}\times$ the FWHM. This leads to the following expression for the transit-time broadening of a two-photon transition, and agrees with the relationship derived by Biraben et. al. [72]:

$$\Delta f_{tt} = \frac{\sqrt{\ln 2}v_p}{\pi w_0} \tag{2.25}$$

Assuming the atoms are at a temperature of 100 °C, then they have a speed of v_p = 267 ms^{-1}, and then using the minimum considered $1/e^2$ beam waist of w_0 = 0.22 mm, then a transit-time broadening of Δf_{tt} = 322 kHz may be expected.

2.8.2 Heated Vapour Cell Design

The majority of Rb TPT reference systems carry out spectroscopy in heated vapour cells at temperatures between 80 and 100 °C (e.g. [31, 33, 44, 70]). The purpose of heating the Rb cell is to increase the density of atoms in the beam, and hence yield a stronger

fluorescence signal at resonance. Using Doppler-free spectroscopy, the signal linewidth is insensitive to the temperature of the atoms (to first order approximations), and the main limitation in how hot the cell is operated, is owing to power and temperature handling of the apparatus. The 25 mm length, Rb vapour cell is housed in a $\simeq$ 40 mm cubic oven (pictured in Fig. 2.12), which is created in a bench-top 3D resin printer, using a high-temperature compound (High Temp Resin V2). After printing, the structure is UV cured in an oven for approximately 60 mins, at 60 °C. This allows the material to withstand temperatures between 100 and 238 °C (depending on the load it bears)[73] without loosing its rigidity. Therefore allowing the resin material to safely and continuously operate at the target Rb cell temperature of $\simeq$ 100 °C.

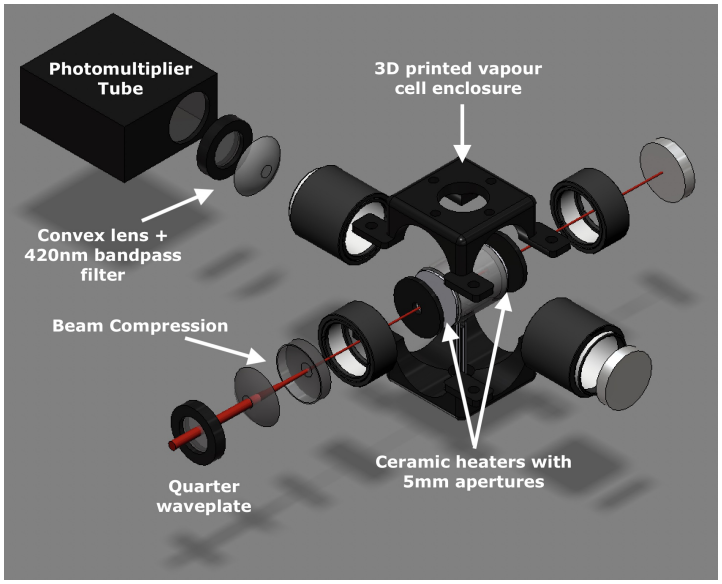

Figure 2.12: Exploded diagram showing all essential parts of the spectroscopy apparatus, including the Rb cell, ceramic heaters, 3D printed oven, beam preparation, and fluorescence detection.

The oven was designed with five 25 mm wide, circular ports to allow lens tubes to slot in to the structure, supporting the 25 mm wide Rb cell, and holding the telescope and fluorescence collection optics in place. There is an additional hole above the cell to allow observation of the 420 nm fluorescence in the beam path through the cell when an Rb TPT is excited on resonance. The Rb cell is heated using two Thorlabs circular ceramic heating elements (HT19R) in contact with either end of the cell. These heaters have 5 mm wide apertures to allow the beam to propagate in and out of the cell. Layers of solid and flexible insulation are fitted outside the heaters at either end of the cell. The insulation allows the cell to reach higher temperatures, and hence reach equilibrium temperature faster, as well as reducing thermal gradients within the Rb cell.

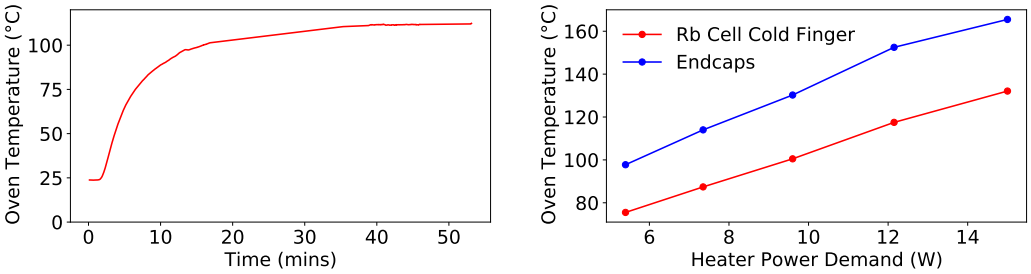

(a) *(b)*

Figure 2.13: (a) Typical vapour cell oven warm up time to reach 112 °C without active temperature feedback. (b) The oven can achieve higher temperatures, but at the cost of drawing more power. The cold finger temperature is the average of two separately calibrated thermistors, while the end-cap temperature (hottest part of cell) is the average of thermistor readings from both end-caps.

In Fig. 2.13, the oven reaches up to 165 °C, measured at the heaters at either end of the cell. However, normally the temperature at the coldest point of the cell is quoted (132 °C at max. power). The cold finger temperature is used to determine the Rb pressure and hence estimate the atom number in the cell using the following equations:

$$P_{Rb} = 10^{(2.881+4.312-(4040/T))} \tag{2.26}$$

Equation 2.26 converts the cell temperature in K to a pressure in Torr, and has been sourced from D.A. Steck's rubidium-87 reference notes [64]. Using the Rb pressure, and the Ideal gas law we can estimate the number of ^{87}Rb atoms lying within the cross-sectional volume of the pump beam (V_{beam}):

$$N_{Rb} = \frac{133.31 P_{Rb} V_{beam}}{k_B T} \times 0.2785 \tag{2.27}$$

A factor of 133.31 converts the Rb pressure from Torr to units of Pascal. The temperature is that of the coldest part of the vapour cell in K and V_{beam} should be in m^3. The number of 0.2785 is the fraction of the atoms in naturally occurring rubidium samples, which are ^{87}Rb. At a temperature of 100 °C and using the beam radius of 0.22 mm, as well as a path length of $\simeq$ 22 mm through the inner volume of the cell, we arrive at an estimation of $N_{Rb} = 5.55 \times 10^9$ atoms.

2.8.3 Fluorescence Detection

One of the advantages to spectroscopy of the Rb TPT is to allow for resonance detection using the fluorescence signal emitted at 420 nm when the excited $5D_{5/2}$ state decays via the $6P_{3/2}$ level (see Fig. 2.1a) rather than the weak absorption signal at 778 nm. A Hamamatsu photo-multiplier tube (PMT) with an internal trans-impedance amplifier

(H7827-002) offers a peak radiant sensitivity of 85 mA/W at 420 nm, with a bandwidth of up to 200 kHz, and was chosen for use in this version of the spectroscopy apparatus. Future versions aim to use a smaller version of this PMT (H12404), which offers 32x higher gain by its internal amplifier, but only $1/58^{th}$ of the detection area and $1/10^{th}$ the bandwidth. The gain of the PMT is adjustable via a control voltage, which has been set to 0.6 V to provide sufficient signal amplification without raising the background noise levels too high to reduce the signal quality (e.g. owing to detector dark current and ambient light pollution). At this amplification level the PMT detection noise floor owing to dark current is no greater than 6 fW. Ambient light pollution, scattered light from the pump beam, and oscilloscope resolution will all likely play a more significant role in setting the detection noise floor.

By placing a bandpass filter (BPF) in front of the signal detector, one can easily cut out the background detection noise-floor resulting from the strong pump power at 778 nm required to generate a signal from the atoms. Several different bandpass filters were used during the various experiments documented in this thesis. Their characteristics and usage are summarised in the table below:

Filter	420 nm Transmission	778 nm Transmission	Transmission range	Usage
Thorlabs BPF (FB420-10)	>45%	0.1×10^{-3}%	10 nm	1.
Semrock BPF (FF01-420/5-25)	>97%	0.2×10^{-3}%	5 nm	2.
Thorlabs Hot Mirror (FM01)	>85%	0.6%	<700 nm	3.

Table 2.3: Summary of different filters used to enhance fluorescence detection SNR. Usage key: 1. TPT Spectroscopy with ECDL and Pure Photonics Laser, 2. TPT Spectroscopy with Ti:Saph Laser and Pilot Laser, 3. TPT Spectroscopy with Microfab Rb Cell.

A 1-inch diameter plano-convex lens of focal length 25 mm is placed at approximately the working distance of 17.6 mm from the atoms in the beam, to collect the fluorescence propagating towards the PMT. Owing to the 15 mm wide detection area of the PMT, the spacing between the plano-convex lens and PMT may be shorter than the working distance. To enhance the detection efficiency, a spherical concave mirror with the same focal length is placed on the opposite side of the cell to collect fluorescence propagating away from the PMT. Fluorescence reflected back toward the detector from the concave mirror will reach the detector as a collimated beam along the horizontal axis after passing through the plano-convex lens (illustrated by the solid ray lines in Fig. 2.14). However, along the vertical axis of the collected fluorescence, the light via

the plano-convex lens will instead be collimated, while the light collected from the concave mirror will reach the detector in a focused beam after the plano-convex lens. The lens which is built in to the PMT ensures that any light reaching the 18 mm aperture of the PMT unit is focused on to the 15 mm detector area.

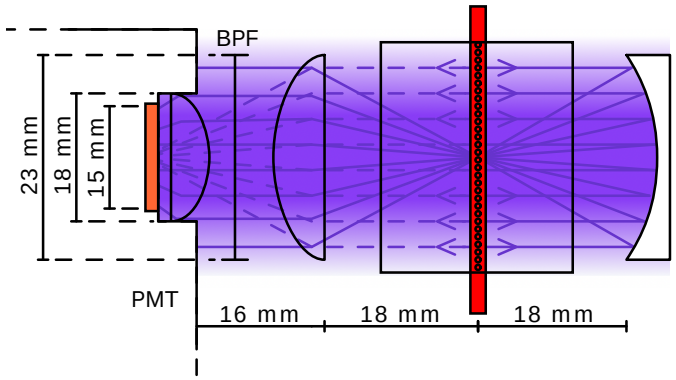

Figure 2.14: Horizontal cross-section of the fluorescence collection optics and Rb cell, with rays propagating from the beam path toward the PMT indicated by dashed lines, and rays propagating away from the PMT indicated by solid lines. The purple colouring represents the combined strength of fluorescence from the "string" of atoms in the beam.

We can estimate the total radiated fluorescence power by all of the atoms within the beam using the number of atoms, fluorescence scattering rate, and energy per photon:

$$P_{420} = E_{420} \times t = N_{Rb} \times \Gamma_{420}(I_{pump}) \times h \times f_{420} \times 1 \tag{2.28}$$

In the above equation h is Planck's constant, f_{420} is the frequency of a 420 nm photon ($\simeq$ 713.8 THz) and t is set to 1 second.

Estimating the fraction of the total radiated fluorescence which is collected by the PMT is a bit more challenging. First of all we can crudely approximate that all of the light in the beam originates from a single point, allowing us to use the fractional solid angle to determine how much light the lens picks up:

$$\Omega = \frac{A}{4\pi R^2} \tag{2.29}$$

In the above equation A is the effective area of the collection lens (23 mm), and R is the distance from the beam to that lens (17.6 mm). The fractional solid angle for both the convex lens and concave mirror is approximately 0.107, giving a total maximum of 0.214. However, all the light is not radiated from the middle of the beam within the cell and the collection efficiency of the lens will decrease for the atoms fluorescing at either end of the cell. To account for this, we have chosen to assume there is a Gaussian

variation in the fractional solid angle, reaching a maximum of 0.107 in the middle of the cell and with a FWHM equal to the radius of the collection lens. By integrating across the Gaussian distribution we find that the fractional solid angle is further reduced by $0.513\times\Omega$. Furthermore, the 25 mm Rb cell does not have anti-reflection coatings and based on the measured transmission losses of 8% at 778 nm we can assume at least 8% losses or more at 420 nm. Fluorescence reflected back from the concave mirror will suffer 3× higher transmission losses, resulting in a fluorescence collection fraction of:

$$\Phi_{lens} = (0.513 \times 0.107 \times 0.92) + (0.513 \times 0.107 \times 0.92^3) \tag{2.30}$$

This yields a collection fraction at the convex lens of 0.049 without the concave mirror and 0.089 with the concave mirror (under ideal conditions). Losses at the convex lens and concave mirror are assumed to be negligible. However, further losses will be incurred depending on which BPF is used, and finally some of the light will be cut off by the smaller aperture of the 18 mm dia. PMT collection lens, yielding further factor of 0.55 to the fraction of light collected. Therefore, the final fraction of the fluorescence collected is:

$$\Phi_{total} = \Phi_{lens} \times T_{BPF} \times 0.55 \tag{2.31}$$

As an example of the signal amplitude we can expect in the absence of any broadening mechanisms. Let us consider a 0.22 mm radius beam of 35.6 mW average power, providing an intensity of 23.4 W/cm^2. According to Eq. 2.9, this would yield an excitation rate per atom of 15,248 s^{-1}, and a fluorescence scattering rate of 1,654 s^{-1}. The beam path through the 100 °C Rb cell will illuminate approximately 5.8 $\times 10^9$ atoms. In this case, the total radiated 420 nm power estimated from Eq. 2.28 is 4.5 μW. Of this power, approximately 100 nW will reach the PMT for detection. Under these conditions, the total radiated fluorescence should be visible enough to help verify when the laser is on resonance with the Rb TPT. The PMT detection noise floor, is far below the detected fluorescence, providing a signal which should be easy enough to lock to. Transit-time broadening (Δf_{tt}) and magnetic field broadening (Δf_B) will both play a significant role to reduce the signal amplitude.

Chapter 3

Rb TPT Spectroscopy With CW 778 nm Lasers

3.1 Introduction

Rb TPT spectroscopy requires low-drift rate, narrow-linewidth lasers to resolve the transition at its natural linewidth, and avoid degrading the achievable stability of a frequency lock to the reference transition. There are a few single-frequency narrow linewidth laser which can offer this, including external cavity diode lasers (ECDLs), distributed feedback (DFB) lasers, DBR (distributed Bragg reflector) lasers and Ti:Sapphire lasers. In this chapter we will compare the suitability of several of the lasers mentioned, while also evaluating the TPT spectroscopy apparatus. With considerations toward creating a miniaturised Rb TPT optical frequency reference using micro-fabricated components, we also present the results of TPT spectroscopy in a micro-fabricated Rb vapour cell. Such considerations are particularly necessary for transitioning from a lab demonstration device to a commercially viable device.

3.2 Rb TPT Spectroscopy and Frequency Lock With an ECDL

3.2.1 ECDL Characterisation

An External Cavity Diode Laser (ECDL) is typically able to achieve a linewidth of less than 1 MHz, down to a few 100 kHz [74] (for measurement timescales of 1 second). If the laser noise is only limited by white frequency noise, then the laser linewidth becomes narrower when measured on shorter timescales. For characterisation of the Rb TPT spectroscopy, a narrow laser linewidth will enable easier resolution of other broadening mechanisms in the spectral profile. The light source in the ECDL is an inexpensive IR

(776 - 780 nm) laser diode, which has been temperature-stabilised to a temperature where it can output light at 778 nm. The laser diode is mounted in an aluminium, heat-sinking mount, which holds together a tuneable external cavity in the Littrow configuration (see figure 3.1). The design and functionality of this laser is very similar to what is demonstrated in [74] and [75]. In the Littrow configuration, a diffraction grating forms one end of the laser cavity, providing frequency-selective feedback to the cavity, and greatly reducing the linewidth of the laser diode. By adjusting the angle of the grating, one can tune the frequency of the laser across a range of up to a few GHz without any mode-hopping. A screw at the back of the module adjusts the grating angle, and hence the wavelength of light reflected back in to the laser from the 1^{st} order of the diffraction grating. This screw provides coarse tunability of the wavelength, while an internal piezo-electric transducer (PZT) allows fine-tuning of the laser frequency.

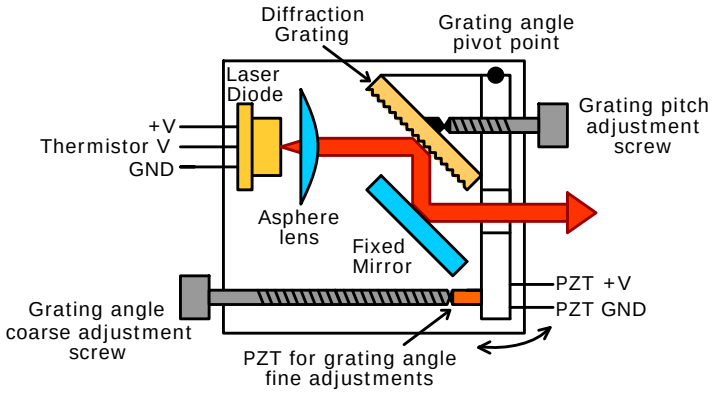

Figure 3.1: Design of the tuneable external cavity diode laser in the Littrow configuration.

A Thorlabs laser diode controller supplies the current to the laser, which typically draws $\simeq$ 120 mA when the ECDL runs at its maximum output of 54 mW. When the beam emerges from the ECDL it is already collimated via an internal lens, however it is horizontally elongated with a height to width ratio of about 1:3. To correct the beam to a symmetrical Gaussian profile, it is passed through an anamorphic prism pair, as shown in figure 3.2. Optical feedback from the spectroscopy apparatus, such as the retro-reflected beam after the vapour cell, can cause cause the laser frequency to become unstable. To avoid this, the beam passes through an optical isolator, which transmits 85% of the input power while providing $\geq$ 32 dB isolation for any beams passing the wrong direction through the isolator. Acoustic and mechanical vibrations also contribute to laser FM (frequency modulation) noise at modulation frequencies in the range of 1 kHz up to tens of kHz. This type of noise couples in through a vibrationally sensitive grating mount within the ECDL. This noise was reduced by placing some vibration-dampening rubber underneath the optics board. There was also an FM noise component at about 50 Hz, which is likely electrical mains noise being

picked up on the ECDL piezo or current control. This noise is potentially low-frequency enough to be able to compensate for within the frequency-lock feedback.

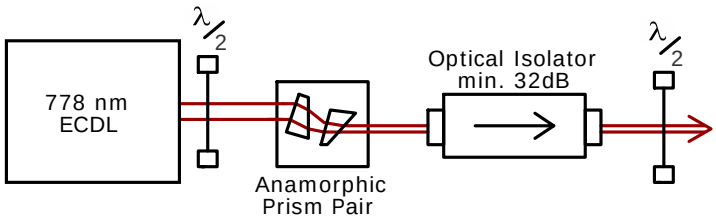

Figure 3.2: Beam preparation of the ECDL output, setting correct polarisation angle, correcting beam shape with an anamorphic prism pair, and an optical isolator to prevent laser frequency noise generated by optical feedback from the spectroscopy apparatus.

After the 778 nm ECDL output is directed to the spectroscopy apparatus. An additional optical isolation ≥ 20 dB is provided by a PBS (see Fig. 2.10) and quarter-wave plate combination in the beam path to the Rb vapour cell, causing the return beam to be reflected at the PBS instead of transmitted back toward the laser. The PBS diverts some of the optical power to a scanning Fabry-Perot cavity and also to a wavemeter (Coherent Wavemaster), where the laser frequency and spectral quality can be accurately monitored while it scans over the features. This is essential for identifying laser frequency noise, and ensuring the laser scans continually over the atomic transitions without mode-hopping during scans.

3.2.2 Initial Rb TPT Spectroscopy

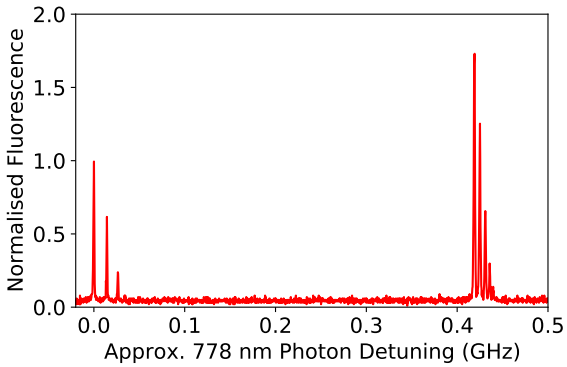

Figure 3.3: Scan of the ECDL frequency over the ^{87}Rb $5S_{1/2}, F = 2 \rightarrow 5D_{5/2}, F' = 4, 3, 2, 1$ (left) and ^{85}Rb $5S_{1/2}, F = 3 \rightarrow 5D_{5/2}, F' = 5, 4, 3, 2, 1$ (right) TPTs. While the data shows a comparison of both the strongest ^{87}Rb and ^{85}Rb TPTs within the same scan, the spacing between the two sets of TPTs is inaccurate owing to laser drift during the scan.

The wavemeter was used to set the laser frequency as close as possible to the ^{87}Rb $5S_{1/2}, F = 2 \rightarrow 5D_{5/2}, F' = 4$ TPT reference transition at 385.285 THz, with an

accuracy of ± 100 MHz. To help navigate to the correct TPT, it is useful to perform a wide scan of the laser frequency. Once the ^{85}Rb $5S_{1/2}, F = 3 \rightarrow 5D_{5/2}, F' = 5, 4, 3, 2, 1$ hyperfine TPT signal is observed, further reducing the laser frequency leads to a similar, but more widely-spaced set of hyperfine transitions, which include the ^{87}Rb reference hyperfine transition, as shown in Fig. 3.3. The reference transition actually occurs at the lowest frequency of all of the Rb D2 TPTs.

By scanning the ECDL grating angle over a wide range, the spectrum in Fig. 3.3 shows both of the tallest ^{85}Rb and ^{87}Rb TPTs under the exact same spectroscopy conditions. Based on the ratio of the two isotopes in natural rubidium, and also the relative transition strengths from [34], we expect to measure a ratio of 2 between the tallest hyperfine peaks of the ^{85}Rb and ^{87}Rb TPTs. However, in Fig. 3.3 the ratio between the tallest hyperfine peaks of the isotopes measures 1.7. The apparatus was not magnetically shielded for this measurement, and the reduction in the relative amplitude of the isotopes is likely a result of the more sensitive ^{85}Rb Zeeman levels splitting further apart in the presence of Earth's background magnetic field. It should also be noted that a jump in the laser frequency during the scan has artificially reduced the separation between the two sets of TPTs, for which their tallest hyperfine peaks should be 576 MHz apart. However the separation of the individual hyperfine features within both sets of TPTs accurately matches (± 1-2 MHz) those measured in [34]. The naturally wider spacing of the hyperfine peaks of the ^{87}Rb TPT reduces the likelihood of the laser locking to a lower amplitude feature nearby when noise disrupts the frequency lock to the reference TPT.

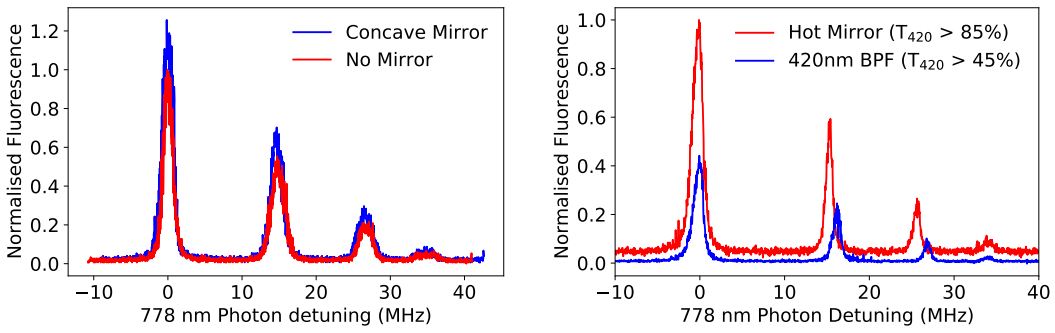

(a) *(b)*

Figure 3.4: (a) A direct comparison of the fluorescence signal amplitude before and after adding the concave mirror to the apparatus yields an enhancement of 1.28x. (b) The hot mirror used as a filter in front on the PMT yields a signal roughly twice that of the 420 nm BPF. However the BPF yields stronger suppression of ambient room light and 778 nm laser scatter, reducing the noise floor by six times yielding a better detection SNR.

The signal amplitude of the reference transition was used to characterise the detection apparatus described in Section 2.8. A direct comparison of the fluorescence signal amplitude before and after adding the concave mirror is shown in Fig. 3.4a. After op-

timising the position of the concave mirror, the fluorescence signal was measured to be 1.28±0.04 x larger, as opposed to the 1.81x that was calculated under ideal conditions. The curvature of the glass cell may play a larger role in reflecting and distorting the path of the light as it returns toward the PMT.

Further improvements to the SNR could be achieved by swapping the filter in front of the PMT. Initially the Thorlabs Hot Mirror (see Table 2.3) was used to provide the least attenuation of the fluorescence signal, helping locate the TPT features easier before optimising the alignment of the spectroscopy apparatus. However, as shown in Fig. 3.4b, the Thorlabs 420 nm BPF provides a much better SNR, even though the signal amplitude is reduced by over 2x. It was found that blocking ambient light from equipment and overhead lights in the room from reaching the PMT was essential to yielding a good SNR on the TPT signal. The BPF provides an SNR of 115 (while the experiment is in the dark) which was roughly 3x larger than the hot mirror provides, owing to a higher suppression of scattered 778 nm light.

The spectroscopy was carried out with no magnetic shielding, and as previously discussed in Section 2.7, the polarisation of the pump beam affects the atoms sensitivity to the magnetic field, and hence switching polarisation affects both the signal amplitude and linewidth. A quarter-wave plate is placed in front of the telescope in the beam path toward the Rb cell, to excite the Rb TPT with right hand-circular polarisation from both directions (preferentially driving $\sigma^+ + \sigma^+$ transitions). Then the quarter-wave plate is swapped for a half-wave plate (with identical transmission coefficient) which preferentially drives $\pi + \pi$ transitions. The results of both measurements are compared in Fig. 3.5. In this case, the $\sigma^+ + \sigma^+$ polarisation scheme provides a significantly stronger and narrower signal (2x narrower).

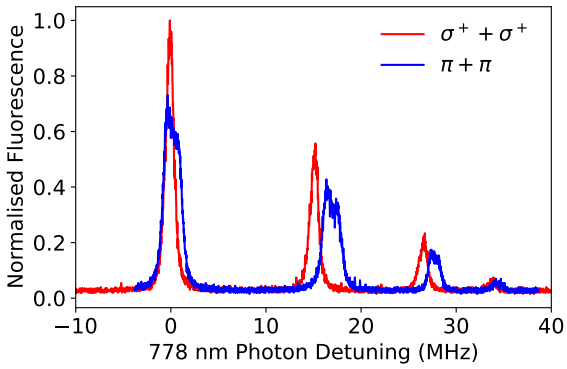

Figure 3.5: A quarter-wave plate is placed in the beam path toward the Rb cell, to drive $\sigma^+ + \sigma^+$ TPTs (yielding ∼1 MHz FWHM), and then swapped for a half-wave plate to compare the signal while driving $\pi + \pi$ transitions (yielding ∼2 MHz FWHM).

The magnetic broadening is a result of Earth's background field of $\sim 0.45 \pm 0.05$ Gauss. The factor of ∼2 difference to the magnetic broadening using the two polarisa-

tion schemes is proportional to the factor of 2 difference between the upper and lower limits of the ^{87}Rb reference TPT quoted in Section 2.7. While it is difficult to put an exact figure on the linewidth broadening to magnetic fields, the difference in linewidths suggests we are able to more cleanly drive $\sigma^+ + \sigma^+$ transitions than we can drive $\pi + \pi$ transitions in this particular magnetic field orientation.

The differences in the relative spacing between the ^{87}Rb hyperfine features using the two polarisation schemes, is a result of each hyperfine state having slightly different sensitivity to their offset in magnetic fields. Typically, the separation between the ^{87}Rb TPT outermost hyperfine features is used to convert the x-axis of the data from scan time to frequency. The accuracy of this conversion plays a role in measuring the linewidth of each feature in the spectrum, and therefore the accuracy can be affected by the changing magnetic field. Based on calculations of the maximum offset of each hyperfine transition in magnetic fields up to 1 Gauss, it is possible to estimate that the time-frequency conversion factor of the spectra will have a maximum variation of $\pm 5\%$ as long as the background magnetic field is < 1 Gauss.

In Fig. 3.6, we compare experimental data of the Rb TPT reference signal with the estimated fluorescence signal model. The fluorescence model relies on both the excitation rate and fluorescence collection efficiency calculations described in Sections 2.4 and 2.8, where the experimentally measured concave mirror enhancement has been substituted in place of the theoretical enhancement factor. Once the signal amplitude of the $F = 2 \rightarrow F' = 4$ hyperfine feature is estimated from the model, the spacing and relative amplitude of the rest of the hyperfine features are set according to measurements by [34]. Using $I_{av} \simeq 10$ W/cm^2 (average intensity of forward- and counter-propagating 778 nm beams) yields a total 420 nm fluorescence power of 1.5 μW, of which we expect 44 nW to be detected by the PMT, using the hot mirror filter.

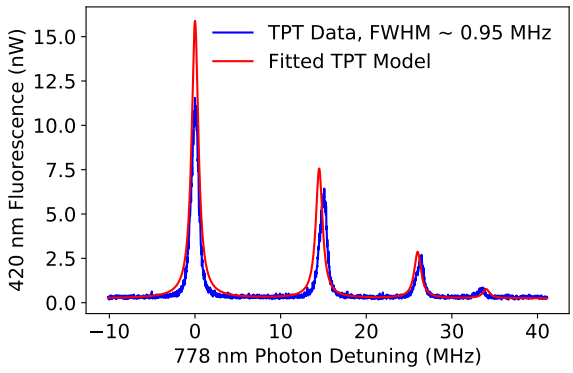

Figure 3.6: Rb TPT spectroscopy data, obtained by scanning the ECDL frequency with a sawtooth signal, repeating at a rate of 60 Hz. The Rb cell is heated to 100 °C, and a pump beam of $I_{av} \simeq 10$ W/cm^2 is applied using the $\sigma^+ + \sigma^+$ polarisation scheme. Using the experiment parameters, the fluorescence signal is estimated (shown in red) and compared with the data.

Using the frequency separation between the TPT features to calibrate the x-axis

of the signal spectrum from scan time to frequency, the FWHM of the F = 2 → F' = 4 reference TPT measures 0.95 MHz. This ∼2.8x broader than the natural linewidth, and is a result of ∼218 kHz transit-time broadening (for a $1/e^2$ radius of 0.33 mm), with the remaining 396 kHz excess broadening, attributed to laser linewidth and magnetic broadening. From Fig. 3.6, the measured signal fluorescence amplitude was 11.6 nW. This is significantly lower than the model predicts, and we must consider that the transition broadening will result in a ∼ proportional reduction to the signal amplitude. If the modelled fluorescence signal amplitude is reduced by the broadening factor of 2.8x, then we get a fluorescence amplitude of 15.7 nW, which is much closer to the measured amplitude. The modelled signal is compared to the measured signal after applying this factor, under the crude approximation that all of the broadening mechanisms are Lorentzian. This is not entirely true for the Zeeman broadening, as can be seen in Fig. 2.7. The relative amplitude of the other hyperfine features is notably different than expected, which is owing to the differing sensitivity of the hyperfine TPTs to magnetic fields using this polarisation scheme.

Accurate spectroscopy data could be acquired while scanning the laser frequency at repetition rates of 60 Hz, but when monitored on timescales of few seconds to several minutes, the laser frequency was prone to significant drift as well as FM noise at 50 Hz. Even drifts of 1 MHz/s can make it both difficult to lock the laser initially and can also carry the laser frequency beyond the lock range relatively quickly. The Fabry-Perot modes exhibited a much lower drift rate than the ECDL frequency (compared to the TPT signal features), allowing it to be used to estimate the laser frequency drifts without being significantly impacted by the Fabry-Perot drifts. The Fabry-Perot was used extensively to identify and tackle sources of the ECDL FM noise. The laser frequency drift was measured by scanning the Fabry-Perot cavity length, while the laser was left alone then measuring how far the Fabry-Perot mode had moved along the scan time/frequency axis every 10 seconds. An example of the ECDL drift measurement is shown in Fig. 3.7.

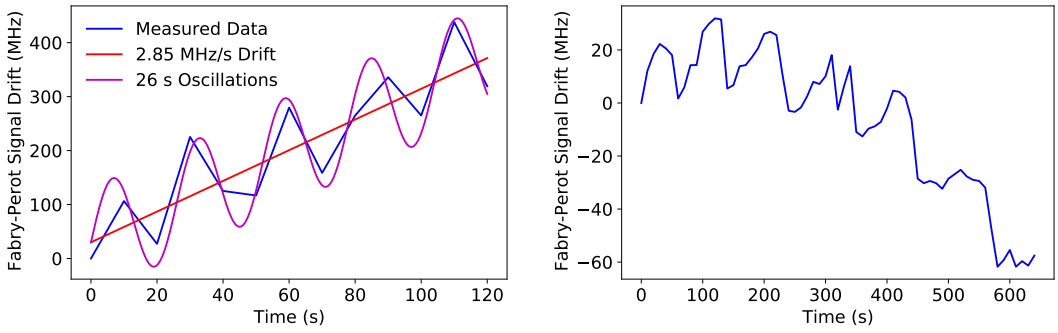

(a) *(b)*

Figure 3.7: (a) Initial ECDL drift measurement, highlighting periodic oscillations and a steady drift. (b) ECDL Drift measurement after improving the housing temperature stability. As the laser drift is reduced the measurement will be limited by drift of the Fabry-Perot cavity length.

When the ECDL temperature was unstable or not fully settled, (e.g. after the insulating enclosure of the ECDL had been removed and put back) the drift could be quite significant, as shown in Fig. 3.7a. The oscillations are indicative of the temperature PID control gain being too high and feedback itself inducing oscillations. Once the temperature control had been re-tuned and allowed to stabilise for half a day, the 26 second period oscillations were less pronounced and the long-term drift much lower as shown in Fig. 3.7b. The improvements were enough to allow the laser to remain within the limited range of the lock feedback.

3.2.3 Generating an Error Signal and Feedback to Laser

Once the ECDL was stable and the reference Rb D2 TPT signal had been characterised and optimised, the next step was to set up some feedback to the ECDL and initiate a frequency lock. This would not only give an indication of the stability that the lock to the optical reference could provide, but also help diagnose any more underlying issues in the laser and apparatus stability required to keep the lock stable. Fig. 3.8 shows the required electronic stages for locking the ECDL to the TPT signal.

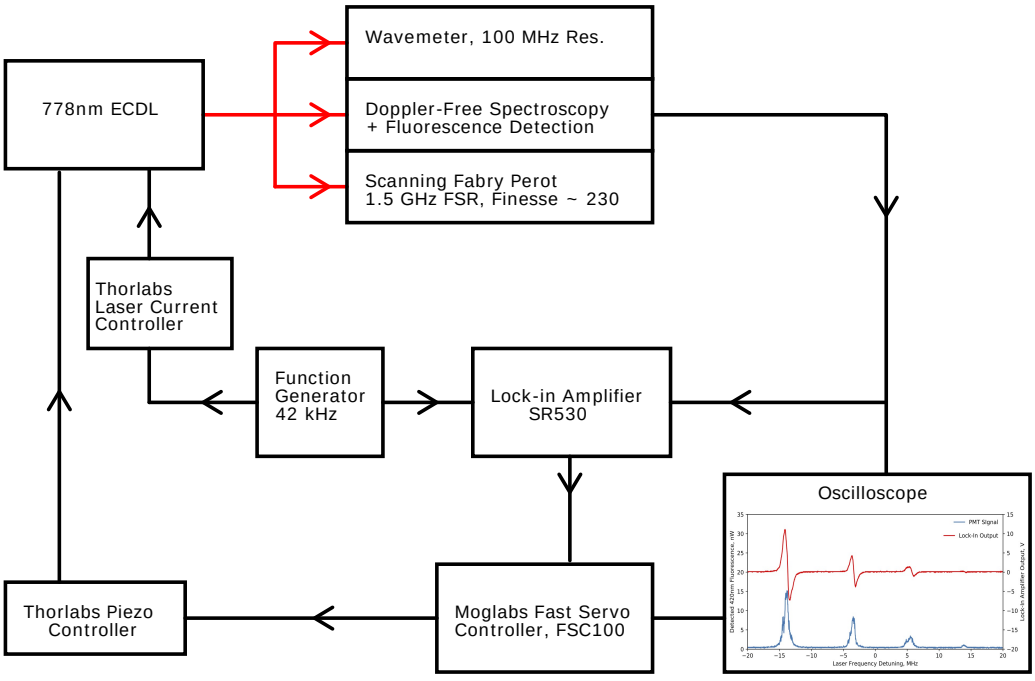

Figure 3.8: This diagram shows all of the apparatus required to lock the ECDL to the fluorescence signal using only feedback to the ECDL piezo. The oscilloscope image insert shows a typical scan across the TPT features with error signal simultaneously recorded, while the piezo is swept at a rate of 10 Hz.

As shown in Fig. 3.8, a 42 kHz modulation signal is applied to the ECDL current, with an appropriate modulation depth less than the linewidth of the TPT feature. The

modulation is picked up on the TPT 420 nm fluorescence signal by the PMT. The signal is then demodulated in to an error signal by a lock-in amplifier (SR530). The integration time of the lock-in amplifier is set to 1 ms. The phase of the reference signal on the lock-in amplifier is then adjusted until the error signal reaches minimum amplitude and then shifted 90° to yield the maximum SNR on the error signal. The Error signal SNR being the ratio of peak to peak signal amplitude over the peak to peak background noise. An error signal, with SNR typically around 150 is then fed in to a Moglabs Fast Servo Controller (FSC100), which allows for PID control of separate feedback signals to slow (piezo tuning) and fast (diode current) laser frequency control. Due to interfacing issues with applying the fast feedback to the Thorlabs Laser controller, only the slow feedback to the piezo could be used, with a bandwidth up to 50 Hz (limited by the FSC100 circuitry).

Before engaging the lock feedback, the laser is scanned over all of the TPT hyperfine features, to generate and save a trace of the PMT signal and its accompanying error signal, for later use in calibrating the error signal frequency noise. The piezo sweep voltage is then offset to shift the zero-crossing of the error signal for the reference TPT to the centre of the piezo scan range. The scan range and rate is then reduced until the amplitude of the error signal reaches its maximum and a switch is flipped on the servo controller to engage the lock. A second trace of only the reference TPT fluorescence and error signal (Fig. 3.9) is then saved again for allowing conversion of error signal noise to frequency noise. The gain on the error signal is then tuned by increasing it until periodic oscillations were induced in the feedback loop, then reduced to just below the gain where these oscillations disappear.

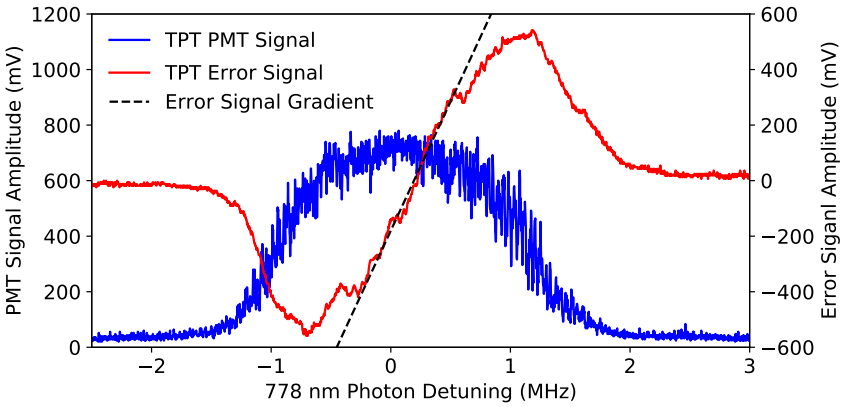

Figure 3.9: The fluorescence signal and corresponding error signal of the reference hyperfine TPT are acquired with a piezo scan rate of 10 Hz and narrow scan range so as to record the maximum error signal amplitude. The error signal zero-crossing gradient in this case is 1.1 kHz/mV. The TPT feature linewidth is broader than in Fig. 3.6, due to 50 Hz FM laser noise, picked up at slow scan rates.

When locked, the error signal may be recorded over long periods, showing fluctua-

tions in the stability of the lock, as various sources of noise perturb the lock (see Fig. 3.10a). This parameter gives a reasonably good indication of the quality of the lock, and can allow us to estimate the frequency stability of the ECDL by converting the amplitude of these fluctuations in voltage, to frequency. Using a pre-calibrated frequency axis in Fig. 3.9, we can determine the slope of the error signal as it crosses the x-axis, in terms of MHz/mV. This slope can then be used to convert small scale (within the linear region of the error zero-crossing) error signal noise during the lock to frequency noise or lock stability. This yields estimated fluctuations of the frequency reference of less than $\pm$ 200 kHz while continually locked for periods longer than an hour, as shown in Fig. 3.10a.

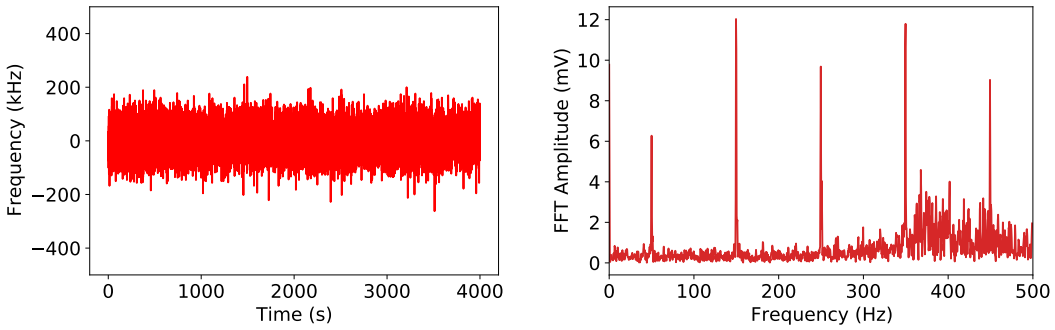

(a) *(b)*

Figure 3.10: (a) The locked error signal noise converted to frequency noise. The maximum deviation is less than the Rb TPT natural linewidth, but could be much better than this. (b) FFT of some typical error signal noise, predominantly with 50 Hz electrical noise features.

At this stage, carrying out a fast Fourier transform (FFT) helps identify periodic noise components at short time-scales less than a second. From the FFT of the error signal in Fig. 3.10, we can see noise components at 50 Hz, as well as higher harmonics of 50 Hz. This is likely the same FM noise which is broadening the fluorescence signal beyond 0.9 MHz FWHM. Since the piezo feedback bandwidth for maintaining the lock is limited to 50 Hz, it appears that the noise is not fully compensated for. Another feature highlighted by the FFT is the broadband lump around 400 Hz. This may be attributed to acoustic noise or vibrations coupling in to the ECDL, and is also beyond the bandwidth of the lock feedback.

It was possible to estimate what size of frequency drifts the lock was compensating for by directly monitoring the voltage being fed to the ECDL piezo during the lock. This voltage could be converted to frequency drift though prior measurements of the applied piezo voltage Vs frequency shift, using the Fabry-Perot to measure the frequency shift. Fig. 3.11a shows the approximate frequency drift correction of the ECDL during the same lock as the corresponding error signal from Fig. 3.10a. On short time-scales the measurement shows the feedback compensating for $\simeq$ 26 second oscillations. On long time-scales there appear to be frequency drifts of the same magnitude as seen in Fig.

3.7b.

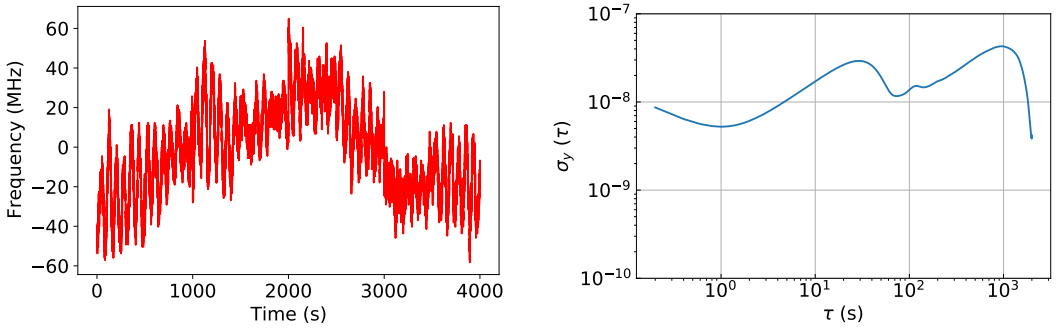

(a) *(b)*

Figure 3.11: (a) The feedback signal applied to the ECDL piezo during the lock data in Fig. 3.10a, is converted from voltage to approximate laser frequency tuning, yielding a rough estimate of how unstable the ECDL frequency is over an hour. (b) The overlapping Allan deviation of the data set in (a) as fractional frequency noise. This is essentially the ECDL's unlocked/free-running stability.

3.2.4 Rb TPT Frequency Lock Results

We can convert the frequency noise, to fractional frequency noise (dividing by 385.285 THz) and plot the overlapping Allan deviation (OADev). The OADev should continually follow a downward slope if the frequency is absolutely stable. In Fig. 3.11b, we can see that the OADev of the estimated ECDL drift does not continually follow a downward slope as τ increases. This OADev plot also shows some peaks which correspond to the period of the oscillations in the frequency drift data of Fig. 3.7. Now we can plot the overlapping Allan deviation for the error frequency noise, as shown in Fig. 3.12, which can then be compared to Fig. 3.7 to determine how much improvement there is to the ECDL frequency stability while locked to the reference TPT.

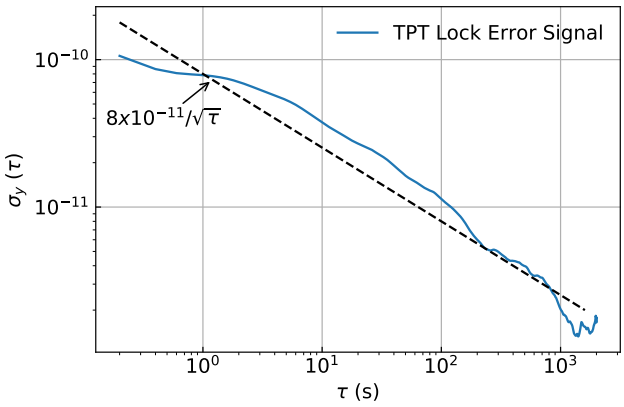

Figure 3.12: The overlapping Allan deviation corresponding to the error noise data shown in Fig. 3.10. A line with a slope of $8 \times 10^{-11}/\sqrt{\tau}$ is plotted indicating the actual short-term stability at 1 second and the expected trend if only white frequency noise were present.

The OAdev in Fig. 3.12 indicates that the laser is now around 2 orders of magnitude more stable (at 1 second) than when it is unlocked. We can see that the OADev roughly follows the $8 \times 10^{-11}/\sqrt{\tau}$ slope showing that the dominant noise source is white frequency noise. The long-term stability (at 10^3 s) reaches 2×10^{-12}. Frequency stability in this range is already close to the stability which a typical commercial microwave atomic clock can achieve [23, 76]. In Section 1.3, we briefly discussed the ultimate limit of an AFR stability in terms of the shot noise limit. For the fluorescence from a 23 mm long, 0.44 mm wide beam of Rb atoms at 100 °C, the atom number should be around 5.8 $\times 10^9$, of which we are detecting roughly 0.091 $\times 10^9$. This then sets the shot-noise limited frequency stability given by Eq. 1.5 at 1 s to around 9×10^{-14}, which is still several orders of magnitude below the current stability.

However, this is by no means an absolute frequency stability measurement, as the data presented here only shows us the relative stability of the laser to the atomic frequency. A true stability measurement should be made relative to another atomic clock, GPS timing signal or another more stable optical frequency reference. To be able to achieve this however, will require the frequency to be stepped down, using an optical frequency comb to a standard 10 MHz timing signal or similar range frequency. There is clearly room for improvement, as the stability achieved here is still at least an order of magnitude less stable than that achieved by the miniaturized optical atomic clock from Z.L. Newman et. al. [33] and the compact optical atomic clock from K.W. Martin et. al. [31]. It is anticipated that a transition from using a 778 nm ECDL to using a frequency-doubled 1556 nm telecoms laser will vastly improve the frequency stability as well as robustness of the system. Telecoms lasers typically have linewidths of around 10 kHz, and are practically insensitive to vibrations.

3.3 Ti:Sapphire Rb TPT Spectroscopy

The Ti:Sapphire laser [77] has been a valuable tool in the field of spectroscopy for decades now, because of its very wide tuning range of around 400 nm and typically narrow linewidth. Owing to its narrow linewidth and high power output in the range of 778 nm, it has been used in the past for spectroscopy of the Rb TPTs [34, 67]. This Ti:Sapphire laser system is however too large, and lacks the required tunability/feedback using an analog signal to be considered for use in a portable atomic frequency reference. Therefore it is only used here to verify that the TPT spectroscopy apparatus is not adding any unexpected noise to the Rb TPT signal.

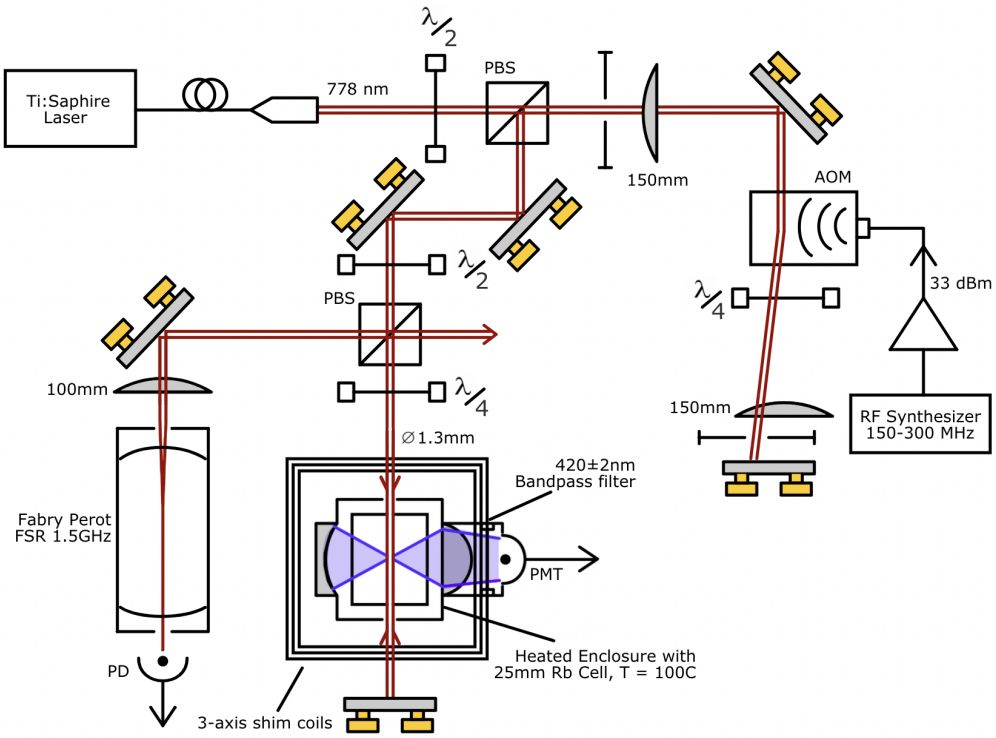

Figure 3.13: Rb TPT spectroscopy optics board, with some modifications from Fig. 2.10. These include: a double-pass AOM for fast modulation and scanning of the 778 nm photon detuning, removal of telescope to maintain a wider beam and reduce the transit-time broadening and the implementation of Helmholtz coil pairs along each axis around the vapour cell allows for cancellation of local magnetic fields. The fluorescence collection scheme is unchanged.

This particular Ti:Sapphire laser is quoted with an intrinsic linewidth of approximately 15 kHz, and is pre-locked to a stable optical cavity within the laser system to reduce frequency drift. Up to 200 mW from the Ti:Sapphire laser is fibre-coupled to the optics breadboard shown in Fig. 3.13. For this measurement a few modifications to the TPT spectroscopy optics board had been made. The first of these was the installation of a double-pass AOM (Acousto-optic Modulator), allowing fast, repeatable 778 nm detuning scans, and also making it easier to switch between using different lasers. The double-pass implementation of the AOM, enables scanning of the optical frequency without affecting the resulting beam angle used for spectroscopy. Additionally, there is twice the scan range using this arrangement, compared with a single-pass setup, leading to a 300 MHz scan range. Beam power is lost by using this stage, and the double-pass transmission efficiency is $\sim$ 55 - 60 % across a 120 MHz wide scan range at 778 nm. Around 50% of the 778 nm optical power is lost via the double-pass AOM stage, before the beam is directed toward the Rb vapour cell.

The second modification was the placement of square Helmholtz coil pairs (shim coils) around each axis of the 25 mm Rb vapour cell. These were required to cancel out large local magnetic fields, now present after relocating the (somewhat mobile)

spectroscopy breadboard to the location of the Ti:Sapphire laser. Using a MEMS magnetometer (LSM303DLH) placed on top of the Rb cell oven, the local magnetic field strength was measured to be approximately -0.9 Gauss. The axial components of this field were approximately:

Field component	Strength (Gauss)
z (horizontal along beam axis)	+ 0.25
x (horizontal perpendicular to beam axis)	+ 0.25
y (vertical)	- 1.4
total	- 0.9

Table 3.1: Magnetic fields within < 3 cm of the Rb cell midpoint measured using the 3-axis LSM303DLH magnetometer.

This strength of field caused a noticeable broadening of the TPT features, and reduction in their amplitude (Fig. 3.14). The current to each shim coil pair was adjusted until the maximum signal amplitude and minimum linewidth were measured on the TPT signal. Once the TPT signal was at maximum, the magnetometer was used to confirm that the total field strength along each axis of the coil was roughly zero ($< \pm$ 0.05 Gauss). After compensating for the local magnetic field, the FWHM of the $F = 2 \rightarrow F' = 4$ hyperfine TPT feature was reduced from $\simeq$ 1.8 MHz to 433 kHz (shown in Fig. 3.14). The remaining broadening corresponds to a transit-time broadening of 77 kHz, leaving the rest ($\simeq$ 22 kHz) attributed to the Ti:Sapphire laser linewidth, which is quoted to possess a minimum of 15 kHz, but has not been directly measured. The 778 nm photon detuning was scanned relatively fast (3 MHz/ms) so as to reduce any laser noise to a minimum.

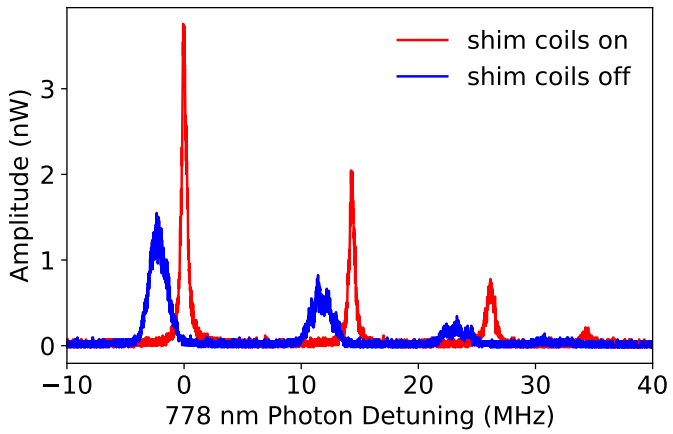

Figure 3.14: ^{87}Rb TPT spectrum using the Ti:Sapphire laser and magnetic field compensation (red trace) compared with resulting spectrum immediately after switching off the shim coils (blue trace).

Taking the difference in the ^{87}Rb TPT reference linewidth with and without the

magnetic field compensated for, tells us that ~ 1.363 MHz of the width corresponds to magnetic broadening. This figure is close to the lower estimate of the broadening which is attributed to the magnetic field: 0.9×1.4 MHz/Gauss $= 1.26$ MHz. The offset of the reference TPT, is not a result of laser drift, since the Ti:Sapphire laser was locked to an internal reference cavity during the scans which were taken < 10 s apart from each other, to reduce possible laser drift to a minimum. The measured offset for the magnetic field present in Fig. 3.14 is -2.18 MHz, which can only be this large if we are predominantly driving $\sigma^+ + \sigma^+$ transitions. At -0.9 Gauss $\times$ 2.1 MHz/Gauss (quoted from Section 2.7), we can expect a maximum line centre offset of - 1.89 MHz shift. Therefore the magnetic field could be slightly higher in the centre of the Rb cell than was measured, or some laser frequency drift has occurred in between the scans.

In the absence of a magnetic field, the Rb TPT spectrum data should provide a closer match to the fluorescence signal model outlined in Section 2.8. A data set using the $\sigma^+ + \sigma^+$ polarisation scheme and an intensity of 2.4 W/cm^2 was obtained. In Fig. 3.15 this data is compared with the signal model. The model again relies on the measured enhancement factor provided by the concave mirror on the opposite side of the vapour cell to the PMT, and also employs a fitting factor to broaden the linewidth and reduce the amplitude proportionally. In this case, the fitting factor 434/334 (ratio of the measured linewidth over the natural linewidth). The resulting model plotted in Fig. 3.15 provides a close match to the data, with the hyperfine feature spacing matching the that which is quoted in [56]. The predicted fluorescence signal of the tallest hyperfine feature ($F = 2 \rightarrow F' = 4$) matches the model very closely. However there are some discrepancies in the relative amplitude of the rest of the hyperfine features, and this may be a result of the atoms having too short an interaction time with the 778 nm beam.

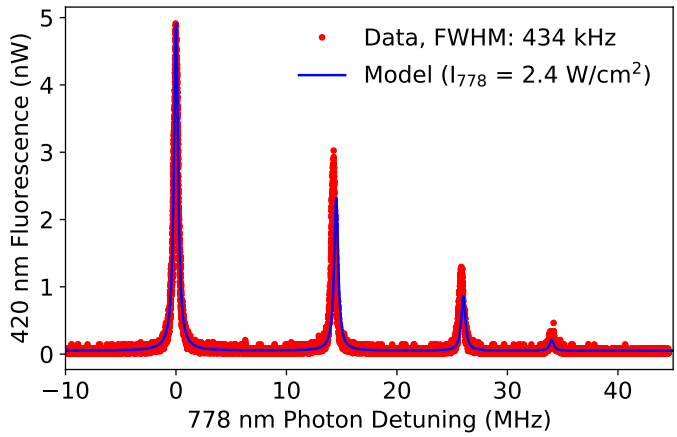

Figure 3.15: ^{87}Rb TPT spectrum, using $1/e^2$ beam radius of 0.65 mm and average counter-propagating beam power of 31.5 mW. The 778 nm detuning is scanned using the AOM with a 50 Hz saw-tooth waveform. The data is compared with the fluorescence signal model outlined in Section 2.8, providing a close match after dividing the amplitude by the ratio of the measured FWHM over the natural linewidth (434/334).

The Rb TPT should be practically insensitive to the AC-Stark shift, owing to the large detuning of 1 THz from the intermediate transitions (discussed in Section 2.5). To make sure of this, scans of the Rb TPT spectrum were taken at increasing 778 nm power (intensity), then a Lorentzian profile is fitted to the $F = 2 \rightarrow F' = 4$ feature of each spectrum. The fitted linewidth at each intensity is plotted in Fig. 3.16a, showing no measurable increase in the FWHM after increasing the intensity by almost 10x. In Fig. 3.15 the fitted signal amplitude matches the expected ${I_{778}}^2$ dependency trends. Due to the lack of any broadening effect while increasing the beam power, the repeated measurements of the linewidth are used to calculate an error on the linewidth measurement, yielding 434 ± 35 kHz.

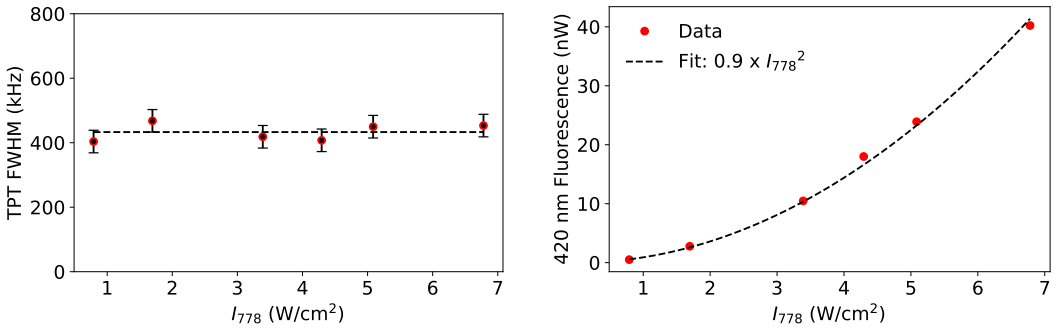

(a) *(b)*

Figure 3.16: (a) FWHM measurements of the ^{87}Rb $5S_{1/2}, F = 2 \rightarrow 5D_{5/2}, F' = 4$ *TPT as a function of increasing intensity. No change in linewidth is measured and the average measured linewidth (dashed line) was 434 ± 35 kHz. (b) Fluorescence signal amplitude measured as a function of the intensity following trends proportional to* ${I_{778}}^2$.

3.4 Chip-scale Rb TPT Spectroscopy

Following the first commercial chip-scale atomic clocks (CSACs) [20, 78], there has been a rapidly growing interest in using silicon wafer manufacturing techniques to fabricate miniature components for atomic clocks [22]. CSACs which are currently used in commercial applications predominantly operate by performing CPT (coherent population trapping) spectroscopy in Cs vapour cells [21, 79]. A CPT atomic clock relies on the phase stabilisation of a modulation frequency applied to the spectroscopy laser (current modulated VCSEL in this case). The modulation generates two optical fields separated by the ground-state hyperfine frequency separation of 9.192 GHz for Cs (and 6.834 GHz for Rb). This enables both ground state hyperfine levels to be coherently coupled to a single excited state, generating a very narrow EIT (electromagnetically-induced transparency) signal when resonant (otherwise known as a dark line, for the absence of fluorescence) [80]. The local oscillator generates the modulation frequency, and feedback from spectroscopy steers the local oscillator to maintain the CPT resonance frequency, hence this type of CSAC can be categorised as a microwave atomic

clock. The physics package for the Microsemi CSAC has been reduced to a size of <1 cm^3, draws around 30 mW of power to run, and yet can provide a short-term Adev stability of $< 2 \times 10^{-10}$ at 1 s and long term stability of $< 1 \times 10^{-11}$ at 100 s [20].

Optical atomic frequency references have much greater scope to achieve orders of magnitude improvement in both long and short-term stability. One group has already demonstrated a market-ready compact optical frequency reference using a 780 nm DFB laser performing frequency modulation spectroscopy of the Rb D2 transition in a miniature vapour cell [81, 82].

The above-mentioned CSACs all use chip-scale (1-2 mm^2) Si photodiodes (PD) for detection of the atomic signal. The considerably more bulky PMTs required for detection of the Rb TPT have held back the development of a chip-scale Rb TPT optical frequency reference. However, the release of the μPMT from Hamamatsu, has greatly aided research groups at NIST in their work towards chip-scale frequency references [30] and optical atomic clocks at 778 nm [33]. The transition of such devices from optical frequency references to atomic clocks is enabled by using chip-scale microresonators to generate optical frequency combs on a chip. A second research group has already demonstrated a prototype rubidium optical atomic clock at 795 nm using an optical frequency comb generated in a high-Q whispering gallery mode (WGM) microresonator - all of which fits within a 5 x 6 x 1.2 cm physics package [83]. This system has yet to achieve superior short-term stability, but performs very well in long-term stability, approaching 3×10^{-13} at 10,000 s. Such a system could be easily adapted to lock to the $\simeq$ 1500x narrower Rb TPT line and demonstrate competitive stability characteristics to high quality microwave atomic clocks. Besides long-term frequency stability, other desirable characteristics for chip-scale atomic clocks, particularly for space-born applications [84], include:

- Low vibrational sensitivity
- Low power consumption
- Quick warm-up times
- Fully autonomous

In the following two sections we will investigate the suitability of a chip-scale 778 nm DFB laser, and also a miniature Rb cell fabricated from a Silicon wafer. Both devices are currently prototypes, and early experimental data will help inform the required improvements for further generations of the device to perform high-resolution atomic spectroscopy. The ultimate goal is to be able to fabricate both the laser and spectroscopy apparatus on to the same platform using chip-scale semiconductor fabrication techniques.

3.4.1 DFB Laser Rb TPT Spectroscopy

A DFB employs frequency-selective feedback, similar to the use of the diffractive grating of an ECDL laser. However the DFB laser achieves frequency-selective feedback through a Bragg grating structure etched in to or on the surface of the laser diodes active area. The DFB laser can achieve even narrower linewidths (e.g. < 10 kHz at 10 μs [85]) than an ECDL laser without the vibrational sensitivity of the external optics. The micro-fabrication process of the DFB laser also allows for the implementation of nano-structures like waveguides, which can improve spatial filtering of the laser mode. DFB lasers are often used in telecoms applications at 1530-1560 nm, owing to their exceptional frequency stability allowing for higher rates of data encoding. An added advantage of chip-scale lasers is that they have smaller thermal masses yielding a quicker response to temperature changes and hence achieve more precise temperature stabilisation and control.

Researchers at The University of Glasgow have been developing their own micro-fabricated DFB laser [86, 87] (example shown in Fig. 3.17a). This DFB laser employs a 0.4 mm length waveguided cavity above the laser diodes active region. Running along either side of the waveguide cavity are Bragg-grating structures, which in this case have chirped grating depths along the cavity length. This property of the Bragg grating spatially varies the coupling strength of incident light and effectively reduces the round-trip phase shift of light in the cavity to zero, providing an easier alternative to the usual methods used to reduce the round-trip phase shift. The laser has been able to achieve a linewidth of around 100 kHz (at 100 ms timescales), and as low as 3 kHz linewidth (at μs timescales). This laser has already proven suitable for spectroscopy of the single-photon Rb D2 transitions, without any issues being highlighted.

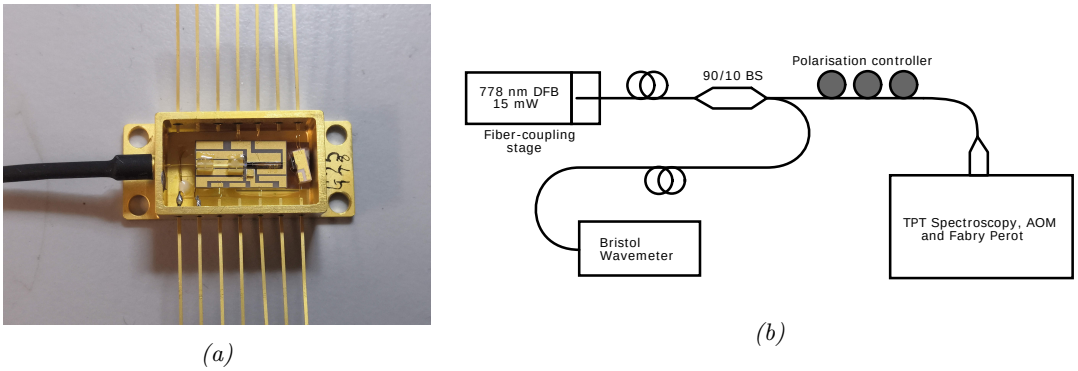

(a) (b)

Figure 3.17: (a) A 780 nm DFB laser fabricated at Glasgow University fitted within a fibre-coupled butterfly package (b) DFB laser frequency monitoring and polarisation control in between the laser output and the spectroscopy apparatus.

The DFB laser chip used in this case was able to output up to 30 mW optical power at 778.1 nm. However, the coupling efficiency between the chip laser output and fibre tip was not able to be increased above 50%, meaning only around 15 mW was

available. However, the fibre-coupling was required to transfer the laser output from a temperature-stabilised platform to the spectroscopy optics breadboard, and provides the added benefit of ensuring a Gaussian beam for spectroscopy. As shown in Fig. 3.17b, a fibre pick-off for monitoring the laser frequency and polarisation controller are also part of the fibre link.

The fibre-coupled light from the 778 nm DFB laser was connected to the spectroscopy board version which included the double-pass AOM stage (as shown in Fig. 3.13). However the magnetic field compensation coils had not been set up around the Rb cell at this stage of the experiments. Owing to the limited coupling efficiency of the lasers output and further losses incurred at the AOM, only 6-7 mW of 778 nm power was deliverable to the Rb cell. To improve the chances of measuring a clean signal using such low optical power, the beams $1/e^2$ radius was reduced to 0.22 mm, yielding an intensity of 4 W/cm^2 and the Rb cell temperature was increased to 110 °C. A small amount of laser power is directed to the Fabry-Perot, for checking the lasers mode is clean, and stable. Once the DFB laser is internally temperature-tuned near the Rb TPT resonance, the scanning AOM then picks up a continuous scan of either the 87 or 85 Rb hyperfine features (shown in Fig. 3.18).

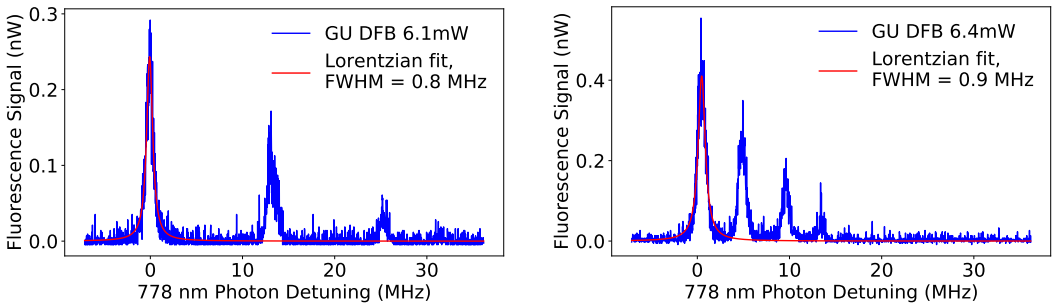

Figure 3.18: (a) ^{87}Rb TPT and (b) ^{85}Rb TPT spectra, using an AOM to scan the DFB laser frequency and a 25 mm length Rb cell heated to 110 °C. Lorentzian profiles are fitted to multiple spectra like this one to make sure the fitted linewidths were consistent.

The measured signal for the ^{87}Rb TPT is shown in Fig. 3.18a. An example of the ^{85}Rb TPT spectra was also recorded (Fig. 3.18b), for the sake of being able to provide a higher SNR at such low pump intensity. We find the DFB laser able to resolve the ^{87}Rb F = 2 $\rightarrow$ F' = 4 reference TPT with a very similar linewidth to that measured on the same timescale using the ECDL in Section 3.2. The DFB laser packaging was not able to fully enclose the chip laser, greatly reducing its temperature stability. This meant that fast scans of the laser frequency at a typical 50 Hz scan rate (3.3 MHz/ms) were required to record the TPT spectra without significant laser drift and other FM laser noise adding distortions to the TPT spectra.

To overcome some of the signal noise, the TPT signal linewidth was measured by

fitting Lorentzian profiles to the reference TPT for each isotope, with an uncertainty arising from fitting to repeated data sets. The linewidth was consistently broader for the ^{85}Rb TPT than for the ^{87}Rb TPT. This is owing to the continued presence of a background magnetic field, which was measured to be at the level of Earth's local magnetic field: 0.45±0.05 Gauss. In this case, the transit-time broadening is expected to be 0.322 MHz, leaving just 0.146 MHz of linewidth broadening remaining to be accounted for. Assuming the minimum amount of magnetic sensitivity of $\Delta f_B = 1.4$ MHz/Gauss (only $\sigma^+ + \sigma^+$ transitions being driven), then this would suggest only 0.1 Gauss is aligned with the beams axis through the Rb cell, and that the contribution from the laser linewidth does not appear to be adding significant noise to the measured linewidth of the Rb TPT reference. The measured FWHM is close to that measured using the ECDL laser, which is a promising step towards being able to work with the smaller and more robust 778 nm DFB laser.

In a publication from 2005, S. Kraft et al.[88] also demonstrate results of Doppler-free spectroscopy of the reference ^{87}Rb TPT using a 778 nm DFB laser. Their results yielded a minimum TPT linewidth of 1.5-2 MHz while scanning their laser frequency at rates up to 463 MHz/ms. At reduced scan speeds of 23 MHz/ms, the fitted linewidth was quite wide at 4-5 MHz. The authors attribute this broadening to laser jitter noise, rather than laser linewidth. The DFB laser used in this study, provides a much better resolution of the Rb TPT hyperfine features at even slower scan rates.

Optical feedback from the spectroscopy apparatus did once again appear as an issue when using this laser, but was quickly dealt with. Temperature fluctuations of the DFB laser prevented spectra from being accurately recorded at slower scan rates. There was also signs that the laser frequency would continually hop by ±10-20 MHz at intervals of around 1 second. The reason for this was suspected to be digitised current stabilisation by the laser driver. Even using different current drivers, it was not possible to record a TPT signal while current tuning the laser. Owing to this issue and the developmental nature of the laser at this stage, the DFB laser does not have the required frequency stability to lock to the reference Rb TPT. However the narrow-linewidth operation of the laser and small scale would clearly benefit an integrated optical TPT reference.

3.4.2 MEMS Cell Spectroscopy

Another step on the route to a commercial atomic frequency reference is the production of cheap atomic vapour cells. Traditional glass-blown vapour cells are still very expensive and time-consuming to manufacture. The ability to fabricate multiple devices at once using silicon wafer micro-fabrication processes, allow for mass production of miniature vapour cells. In this section we test a prototype micro-fabricated Rb cell, which has been recently-developed at the University of Glasgow (pictured in Fig. 3.19a). The micro-fabricated Rb cell is essentially a $\simeq$ 1.5 mm-thick silicon wafer, with

two holes etched through it - one 3 mm diameter hole for optical access to the sample and a smaller hole conjoined by a narrow channel to the first, containing a rubidium pellet. The cell is sealed under vacuum by a borosilicate glass layer on either side, using anodic bonding [22]. In order to activate the Rb pellet after the cell is sealed, a high power laser is focused on to the pellet, allowing the release of Rb vapour from the pellet through the process of laser ablation.

Due to reduced optical access to the micro-fab Rb cell, the PMT must be moved from the side-on detection position, to detect fluorescence on the axis of the pump beam through the vapour cell (similar to the technique used in [30]). The on-axis detection scheme is made possible using the hot mirror filter (see table 2.3) to retro-reflect the 778 nm pump back through the Rb cell, while passing the fluorescence toward the PMT with $> 85\%$ transmission. A 25 mm convex lens collects the transmitted fluorescence and directs it through a BPF ($> 45\%$ transmission), to the PMT. A schematic of this detection scheme is shown in Fig. 3.19b. The fractional solid angle is limited by the effective radius of the convex lens and its distance from the atoms, yielding a fraction of 0.107. However, further optical losses (At the filters, lens, cell window and PMT aperture) reduce the fraction of collected fluorescence to 0.021.

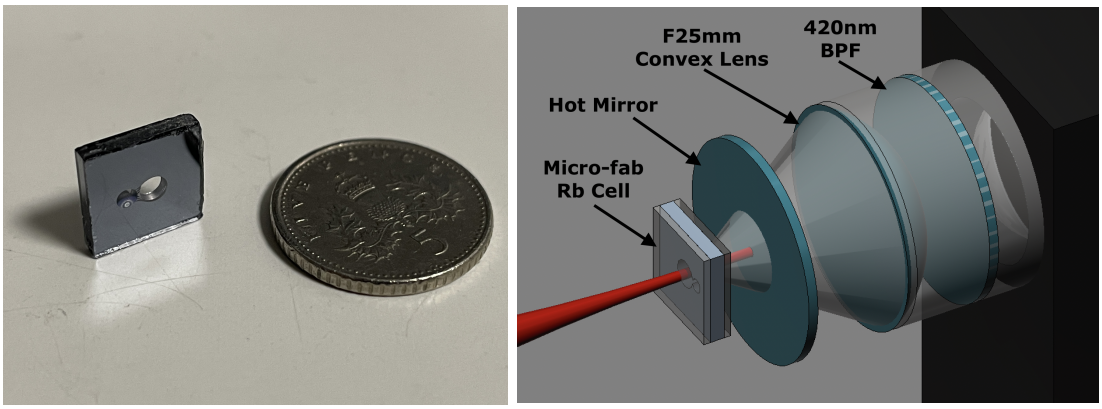

(a) *(b)*

Figure 3.19: (a) The micro-fabricated miniature Rb cell (b) A hot mirror filter in this TPT fluorescence detection scheme allows the PMT to be in line with the pump beam, providing a high reflectivity at 778 nm and $> 85\%$ transmission at 420 nm.

A new and more compact oven was designed to house the micro-fabricated Rb cell and detection apparatus. The oven was 3D-printed using the same material and technique as described in Section 2.8.2. Once again the oven enclosure features ports to secure lens tubes for the telescope and fluorescence detection optics. As shown in Fig. 3.20a, the 3D-printed oven is relatively compact and well-insulated. Two miniature, high-power resistors and a thermistor are placed in contact with separate silicon walls of the Rb cell. Insulation wool is filled in around the Rb cell to secure it and speed up the warm-up time. PID temperature control of the oven was implemented using a home-made driving circuit, controlled from an Arduino. Fig. 3.20b shows an example

of the quick oven warm-up time to around 100 °C, reaching a stability of $< \pm 0.3$ °C in less than 5 minutes.

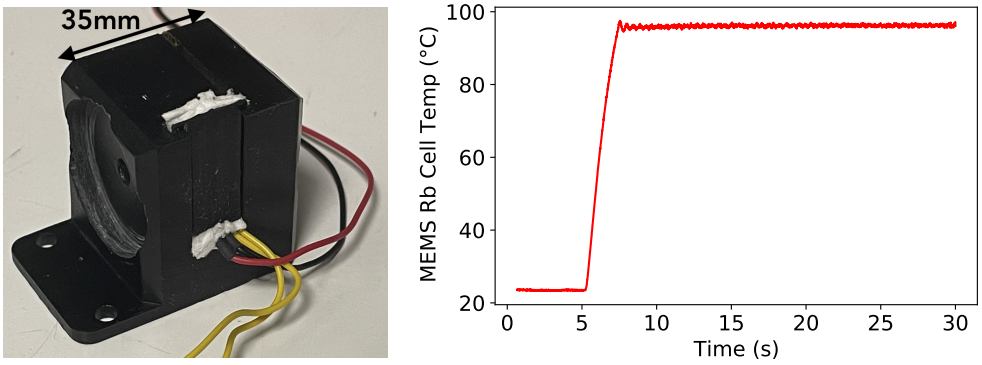

(a) *(b)*

Figure 3.20: (a) Compact 3D-printed oven housing for the micro-fab Rb cell. A side-door enables access to insert the Rb cell and heating electronics. (b) Typical warm-up time of less than 5 minutes to reach the 100 °C operating temperature for spectroscopy.

The Rb cell enclosure is mounted on a beam splitter alignment stage, which allows for adjustment of the retro-reflecting hot mirror angle along with the enclosure itself. Switching from a vapour cell with a 23 mm path length, to a cell with just a 1.5 mm path length provides an extra challenge for maintaining a detectable fluorescence signal ($\simeq$ 15x less atoms in the beam path). To compensate for fewer atoms, the beam radius was initially reduced to a $1/e^2$ radius of $w_0 = 27\mu$m, thus resulting in a pump intensity of $\simeq 480$ W/cm^2 using an average of 11 mW 778 nm power from the frequency-doubled telecoms laser (see Section 4.3.3). The 778 nm laser frequency is scanned using a double-pass AOM on the spectroscopy optics board (same apparatus as shown in Fig. 3.13, but with no magnetic shielding in use).

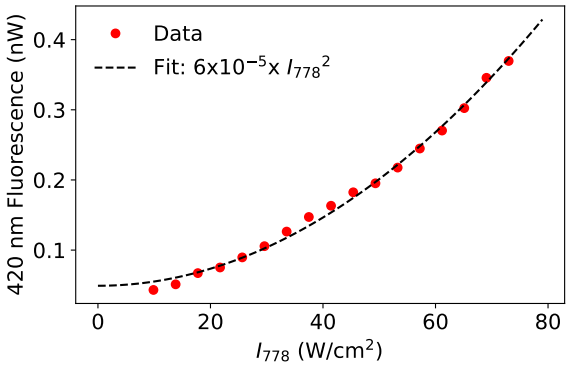

Figure 3.21: The 778 nm beam intensity is increased by adjusting the beam power, and we observe the TPT signal to rise proportionally to $I_{778}{}^2$.

As shown in Fig. 3.21, the TPT fluorescence signal begins to yield a discernible

signal (SNR $>$ 2) using $\simeq$ 10 W/cm^2. By comparison, an SNR of around 115 was possible using the 25 mm Rb cell detection scheme and the same pump beam intensity. Even at such a high pump intensity as 480 W/cm^2, the signal amplitude is much lower than was obtained using the 25 mm cell. Besides amplitude reduction corresponding to spectral broadening, coalescing of Rb droplets on the cell window (coldest point of the cell) may also be responsible for blocking some of the fluorescence signal. The non-linear scaling of the TPT excitation rate with I^2, should enable a signal 4x larger by using 2x more 778 nm power, which is reflected in the trends of the TPT signal Vs intensity in Fig. 3.21.

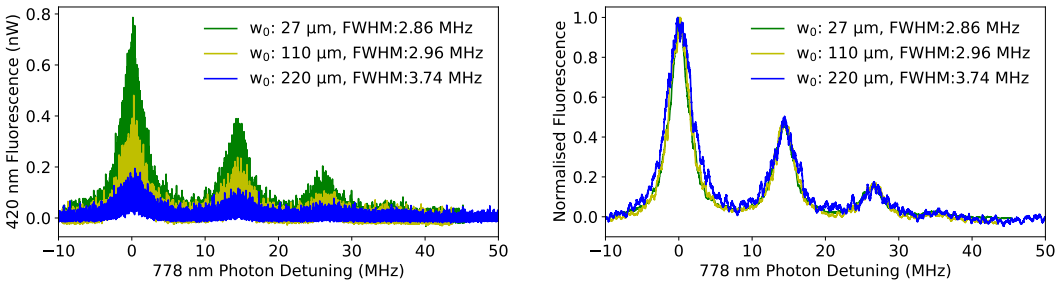

(a) *(b)*

Figure 3.22: (a) Scans of the ^{87}Rb reference TPT signal, comparing the measured FWHM linewidth using different beam widths (Beam power kept constant). (b) Example of the scan signals after they are normalised and low-pass filtered, revealing the wide linewidth is not limited by Δf_{tt}.

The resulting TPT signal for the narrow beam waist and intensity of 450 W/cm^2 is shown by the green data in Fig. 3.22a. The wide linewidth of the green trace in Fig. 3.22a is not particularly surprising, owing to an estimated transit-time broadening, Δf_{tt} = 2.62 MHz for the 27 μm beam waist. The measurement was repeated using beam waists, of w_0 = 110 and 220 μm to try and reduce the effects of Δf_{tt}. The 220 μm beam, should reduce Δf_{tt} to just 0.32 MHz, however the measured TPT signal FWHM did not appear to change significantly as Δf_{tt} was reduced. In each case, the reference TPT signal FWHM was measured by applying a low-pass filter to the TPT signal data and then fitting a Lorentzian profile to extract the FWHM from the fitting parameters. The unchanging FWHM is clear to see from the normalised low-pass filtered signals in Fig. 3.22b. Compared to the $<$ 1 MHz signal linewidth which could be measured using the same laser and the 25 mm Rb glass cell, the broadening could not be attributed to laser noise. The broadening is much wider than can be attributed to the presence of Earth's magnetic field, and more localised magnetic fields due to high current in the heater resistors were ruled out by taking spectroscopy data immediately after switching the heaters off. It is possible that collisional broadening is responsible for the wide signal, due to the presence of gaseous contaminants released during the activation of the Rb pellets. As discussed in Chapter 5.6 of Frequency Standards by F. Riehle [89],

the Rb atoms de-excite prematurely when they collide with the contaminants, limiting the interaction time of the beam with each atom, in a similar fashion to transit-time broadening.

However, there is still room to achieve stronger fluorescence signals by adjusting the oven design to improve optical access to the Rb cell and by reducing optical losses through the filters. Additionally, a cold mirror filter could be placed in front of the beam entering the Rb cell (illustrated in Fig. 3.23). This would improve the detection efficiency by reflecting fluorescence propagating away from the PMT back toward the detector, while transmitting the pump beam in to the cell. Micro-fab Rb cells such as this one are still in the early phases of development and the process for etching the holes is limited to a thickness of about 2 mm of silicon, severely limiting the potential to scale up the TPT signal strength using this technique. However, it is possible to micro-fabricate deeper cells using a water-jet to cut the holes through the silicon wafer. Such a technique is demonstrated in [90] for a micro-fabricated Rb cell, with a 6 mm path length, and would yield a significantly larger signal. Improvements to the signal linewidth are feasible by placing materials like graphite or a non-evaporable getter (NEG) which absorb contaminants inside the cell, and also by increasing the channel length between the Rb pellet chamber and the main chamber of the cell.

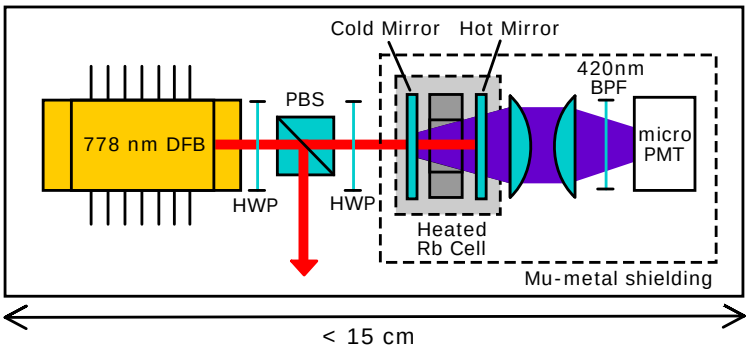

Figure 3.23: Illustration of a miniaturised Rb TPT optical frequency reference system, using the H12404 microPMT instead of the larger H7827-002 PMT currently used. PBS = Polarising beam splitter, HWP = Half-wave plate, BFP = Bandpass filter.

With further improvements to the stability and tuning of the chip-scale DFB laser, and using the deeper Rb cell described in [90], it should be possible to generate a clean TPT signal to lock the DFB laser. Both the 778 nm DFB laser and TPT signal detection could easily fit on a compact platform, as illustrated in Fig. 3.23. This platform could then be entirely or partially cased in magnetic shielding and possibly even temperature stabilised to achieve the best performance. Such a package could be used to demonstrate a lock of the DFB laser to the optical frequency reference, and act as a stepping stone toward integrating the optical system on to a fabricated waveguide silicon platform. On an integrated platform, as is described in [91], it would then be

possible to couple the referenced 778 nm beam to an optical comb-generating micro-resonator, fabricated on to the platform allowing conversion of the optical frequency to a high stability clock output. Much of the foundation toward a chip-scale system incorporating micro-resonators has already been established at NIST [33].

Chapter 4

Rb TPT Spectroscopy Using Frequency-Doubled Telecom-band Lasers

4.1 Introduction

Over the past several decades, communication networks have gradually progressed to using optical carrier frequencies to enable higher data transmission rates. The industrial demand for optical telecommunications has stimulated the development of robust optical sources with a high spectral purity (i.e. single-mode operation, low noise, and narrow-linewidth). Fibre-optic data transmission operates over a particular band of the near infra-red (NIR) region of the electromagnetic spectrum, which is between 1260 nm to 1625 nm, and is divided into five wavelength bands referred to as the O-, E-, S-, C- and L-bands. Today, optical fibres achieve the lowest attenuation over long distances using the C-band (conventional band), covering the range 1530-1565 nm. C-band telecom lasers are currently used in conjunction with WDM (Wavelength-Division Multiplexing) and EDFA (Erbium-Doped Fibre Amplifier) technology, to establish high-speed optical communication between cities as well as for under-sea, intercontinental optical communication systems.

Telecoms lasers often quote very narrow linewidths, < 10 kHz [92–94], which can achieve a free-running, short-term fractional frequency noise (precision) in the range of $\times 10^{-10}$, with comparable form-factor to microwave oscillators of the same quality. Telecoms lasers typically achieve such a precise frequency by using DFB (distributed feedback) or DBR (distributed Bragg Reflector) architectures which employ microfabricated structures within the lasing cavity improve frequency-selective feedback to the cavity. Telecoms lasers are advantageous for resolving narrow atomic transitions, but also their compact, rugged designs make these lasers well suited for portable spec-

troscopy applications. For these reasons telecoms lasers are a lucrative seed laser choice for use in a portable atomic clock, and have already been tested in a lab-based Rb TPT clock system with promising results in 2018 by K. W. Martin et al. [31].

In the following chapter, we will cover the characterisation and use of a telecoms laser, along with the frequency-doubling PPLN stage required to convert the telecoms laser to 778 nm. The 778 nm light is then tested for use with the Rb TPT reference transition, before moving on to work with a frequency-doubled, telecoms optical frequency comb laser in Chapter 5.6.

4.2 Second Harmonic Generation in PPLN

4.2.1 Frequency-Doubling Crystals

Second Harmonic Generation (SHG) crystals such as Lithium Niobate ($LiNbO_3$) play a very useful role to convert telecoms laser wavelengths (1530 - 1565 nm) to the 776 - 780 nm range of frequently-used rubidium transitions [95]. SHG crystals are already widely integrated into many laser pointers for converting invisible light from a 1064 nm laser diode, to an easily visible 532 nm output (using KTP - potassium titanyl phosphate crystal). There are now many quantum-sensing rubidium experiments which rely on SHG crystals to convert wavelengths from robust and compact telecoms lasers to 780 nm, improving the reliability of their laser systems [96–98]. For these rubidium based systems, a periodically-poled $LiNbO_3$ (PPLN) crystal (see Fig 4.1) is typically used to convert 1560 nm to 780 nm, generating second harmonic optical powers up to 11 W [92]. An increasing number of PPLN crystal manufacturers are now offering fiber-coupled PPLN packages, allowing easy integration with fiber-coupled telecoms laser systems.

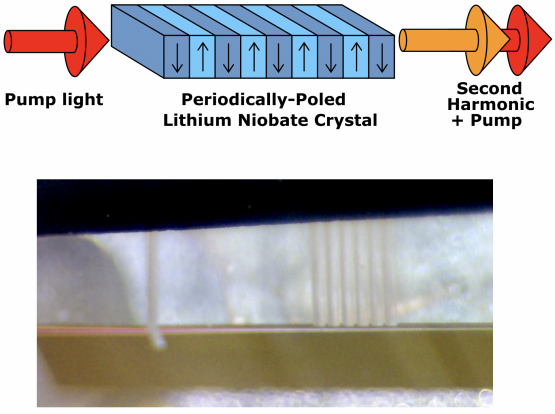

Figure 4.1: (top) Illustrative diagram of the poling structure in PPLN. (bottom) Microscope image of 5 identical ridge waveguides etched in to the Covesion PPLN crystal, to which the pump light can be coupled.

Periodic-poling of the crystal (as shown in Fig. 4.1) allows for quasi-phase-matching of the pump field to the second harmonic field, enabling much higher conversion efficiency using longer crystals. The non-linear characteristics of second harmonic generation enable the second harmonic conversion efficiency, η_{SHG}, to increase proportionally to the pump intensity, I_{pump}. For this reason, η_{SHG} is often quoted in %/W. In recent years, PPLN crystal manufacturers have begun etching waveguides in to the crystals [99], like those shown in Fig. 4.1. This provides an enhancement to η_{SHG}, by maintaining a constant high pump intensity along the whole length of the crystal.

4.2.2 Second Harmonic Generation Theory

There has been a significant amount of work carried out to model the process of second harmonic generation in a crystal medium following the first experiments in the early 1960's by Franken et al. [100, 101]. Full derivations of the theoretical conversion efficiency, and phase-matching behaviour of non-linear crystals can be found in textbooks [102, 103]. To help understand the differences between CW SHG and pulsed SHG, which will be discussed in later chapters, we will include some of the relevant SHG theory here.

Let us consider a pump beam of frequency f_m, and amplitude E_0 entering a non-linear medium along an axis z, with an electric field of the form:

$$E_P = E_0 e^{i2\pi f_m t + \phi} \tag{4.1}$$

As light propagates within the non-linear medium, two photons at the frequency of the pump electric field are able to interact with each other to create sum and difference frequencies. In the specific case of second harmonic generation, these two interacting photons are equal, and the electric field at the second harmonic, E_{SH} will be proportional to the square of the pump field.

$$E_{SH} \propto {E_P}^2 \tag{4.2}$$

In a non-linear crystal this interaction between the pump photons occurs as a result of the polarisation response of the crystal lattice. Owing to dispersion in the crystal medium, the pump photons will eventually generate second harmonic photons which are out of phase with those produced at earlier sections of the crystals, causing destructive interference. SHG at any single point in the crystal is also not going to be 100% efficient in practice, and the conversion efficiency is determined by the material properties of the crystal. To take in to account the polarisation response and properties of the crystal, we must consider the coupled amplitude (CA) equation for two electric fields: E_1 and E_2, interacting to generate a third electric field, E_3:

$$\frac{\delta E_3}{\delta z} = -\frac{i\,\omega_3}{2}\sqrt{\frac{\mu_0}{\epsilon_0 {n_3}^2}}\,d\,E_1 E_2 e^{i\Delta k z} \tag{4.3}$$

This expression is part of a set of 3 CA equations, which model the change in amplitude of each of the 3 interacting electric fields, derived in Chapter 8 of the Photonics textbook by A. Yariv and P. Yeh [103]. In the above equation, ω_3 is the sum frequency of pump fields E_1 and E_2, μ_0 is the permeability of free space, and ϵ_0 the permittivity of free space. The constant d, is known as the non-linear coefficient (used here in SI units of F/V) and is a property of the crystal. The refractive index of the frequency for E_3 in the crystal is denoted by n_3. The exponential term $e^{i\Delta k z}$ in Eq. 4.3 varies between 1 and -1 depending on how closely the pump frequency matches the phase-matching frequency of the crystal. Δk is the wavevector mismatch, and when $\Delta k = 0$ the coupling between the fields reaches its maximum. Δk can also be thought of as a measure of the difference in the propagation velocities of the pump and SH fields within the crystal, resulting from dispersion. We can calculate Δk using the refractive index values for the pump and SH fields within the crystal:

$$\Delta k = \frac{1}{c}[\omega_1(n_3 - n_1) + \omega_2(n_3 - n_2)] \tag{4.4}$$

For the case of second harmonic generation, the resultant field is pumped by photons of equal frequency ($\omega_1 = \omega_2$), and the above Eq. 4.4 reduces to:

$$\Delta k = \frac{2\omega_P}{c}(n_{SH} - n_P) \tag{4.5}$$

Values for the refractive index of $LiNbO_3$ can be calculated using formulas from [104], which are based on the Sellmeier equation. For 1556 nm and its second harmonic 778 nm these are the ordinary refractive indices $n_P = 2.2109$ and $n_{SH} = 2.2580$.

Equation 4.3 may also be used to model sum frequency generation (SFG) and difference frequency generation (DFG) from non-equal pump photons. By setting $E_1 = E_2 = E_P$, and $E_3 = E_{SH}$, the coupled amplitude equation yields the changes in amplitude of the second harmonic field, as a function of the propagation distance, through the crystal. To find the SH amplitude after a certain distance, L through the crystal, Eq 4.3 must be integrated over the range z = 0 to z = L (assuming $E_{SH} = 0$, at z = 0 and negligible depletion of the pump electric field during the interaction). This results in the following expression:

$$\Delta E_{SH}(L) = -\frac{\omega_{SH}}{2}\sqrt{\frac{\mu_0}{\epsilon_0 {n_{SH}}^2}}\,d\,{E_P}^2\frac{e^{i\Delta k L} - 1}{\Delta k} \tag{4.6}$$

Due to the difference in refractive indices of the pump and SH in bulk $LiNbO_3$, $\Delta k >> 0$ and the SH and pump fields go in and out of phase through the length of the

crystal, as they propagate at different velocities. This prevents the second harmonic power from building up through the length of the crystal. The distance required for the fields to become π out of phase is known as the coherence length, L_c. The coherence length can be calculated using the relationship:

$$L_c = \frac{2\pi}{\Delta k} \tag{4.7}$$

In Fig. 4.2 the CA model is implemented to model the behaviour of the second harmonic electric field in a $LiNbO_3$ crystal. The first oscillation of the SH amplitude is shown, reaching a maximum at $L_c/2$, where $L_c = 16.52\ \mu m$.

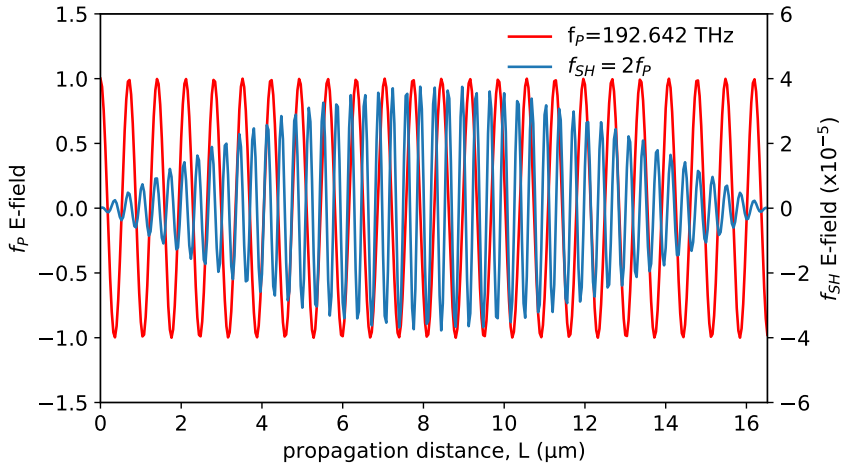

Figure 4.2: Simulation of a non-phase-matched pump electric field of 22 mW and beam radius = 4.5 μm, propagating in bulk $LiNbO_3$ crystal (with $d = \epsilon_0 \times 14$ pm/V), and the SH field generated by that pump field. Both y-axis scales are normalised to the amplitude of the pump E-field. The SH field grows and diminishes over the distance L_c due to the phase-mismatch between pump and SH fields, preventing SH power from building up.

To prevent the SH field from diminishing, a process known as periodic poling of the crystal can be implemented during manufacturing, which effectively flips the direction of the polarisation response to the pump field at regular intervals of $L_c/2$. This prevents a phase mismatch of $> \pi$ from building up throughout the crystal, and allows the second harmonic power to continue to accumulate, with behaviour known as quasi-phase-matching (QPM). Periodic poling is an artificially induced quality of the crystal structure, and it should be noted that phase-matching can also be achieved using the naturally occurring effect of bi-refringence in certain crystals such as KDP [105].

Quasi-phase matching behaviour of the SH field amplitude through a PPLN crystal can be approximated by first calculating the integrated CA equation (Eq. 4.6), for the pump frequency which the PPLN is phase-matched. Evidently $\Delta k >> 0$, and the SH field oscillates. To model phase-matched periodic poling, we can carry out a cumulative sum of the SH field amplitude, allowing the SH amplitude to build up in steps of $L_c/2$

through the crystal, as shown in Fig. 4.3.

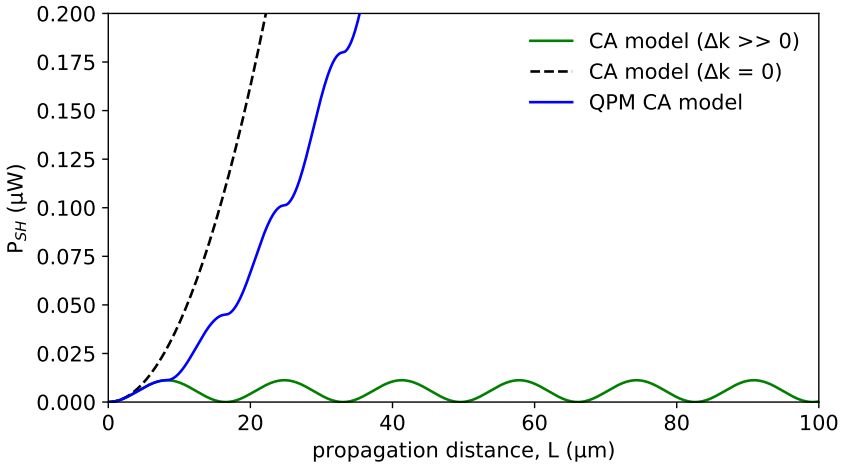

Figure 4.3: Simulations using Eq 4.6, comparing the behaviour of the second harmonic amplitude for a pump which is: phase-matched in bulk $LiNbO_3$ crystal (black dashed), non-phase-matched in bulk $LiNbO_3$ crystal (green), and quasi-phase-matched in a PPLN crystal (blue). Each of the simulations use the same pump field, and non-linear coefficient used for Fig. 4.2.

In most practical uses of a PPLN crystal it is not necessary to determine the behaviour of the second harmonic field during propagation, so we will now only consider how the SH intensity is measured at the end of a crystal of length, L. Therefore we can adapt Eq 4.6, to yield results in terms of intensity rather than electric field, using the relationship:

$$I_m = \frac{1}{2}\sqrt{\frac{\epsilon_0 n_m^2}{\mu_0}}|E_m|^2 \tag{4.8}$$

By inserting $|\Delta E_{SH}|$ in to Eq. 4.8, and also re-expressing E_P in terms of intensity, the CA equation is converted to the following expression for the second harmonic intensity:

$$I_{SH} = 2\left(\frac{\mu_0}{\epsilon_0}\right)^{3/2}\frac{{\omega_P}^2 d^2}{n_{SH}\,{n_P}^2}{I_P}^2 L^2 \frac{2(1-\cos(\Delta k L))}{(\Delta k L)^2} \tag{4.9}$$

This can then be re-expressed as the following, which highlights the sinc^2 behaviour of phase-matching in SHG processes:

$$I_{SH} = 2\left(\frac{\mu_0}{\epsilon_0}\right)^{3/2}\frac{{\omega_P}^2 d^2}{n_{SH}\,{n_P}^2}{I_P}^2 L^2 \left(\frac{\sin(\Delta k L/2)}{\Delta k L/2}\right)^2 \tag{4.10}$$

Equation 4.10 is accurate under the assumptions that the crystal is a lossless medium, and that the conversion efficiency is not high enough to significantly reduce the available pump power while propagating within the medium (also known as pump

depletion). As mentioned before, the dependence of the second harmonic intensity on ${I_P}^2$ and L^2, can make the conversion process vastly more efficient using a longer crystal and a high pump intensity. This equation can be applied to both bulk and PPLN crystals to map out how the conversion efficiency changes as we depart phase-matching conditions. However, when using Eq. 4.10 for PPLN crystal, an effective non-linear coefficient is used, accounting for the reduction in SH power for QPM compared with perfect phase-matching. This effective non-linear coefficient is sometimes quoted by crystal manufacturers, and will be at least a factor of $2/\pi$ less than the bulk crystal non-linear coefficient, which shows up in Fig. 4.3, as the relative propagation distance required to reach the same power assuming perfect phase-matching Vs QPM. Additionally, Δk should be re-expressed, so as to be used relative to the Δk value for the phase-matching frequency of the crystal, $\Delta k_{PM}(\omega_{PM})$:

$$\Delta k_{PPLN} = 2[\Delta k_{PM}(\omega_{PM}) - \Delta k(\omega_P)] \tag{4.11}$$

The factor of 2 accounts for the doubling up of any phase-mismatch during the two phase-reversals of each poling period.

As the pump power (intensity) is increased, the conversion efficiency increases proportionally to pump power, until the conversion efficiency is high enough to significantly deplete the pump field amplitude during propagation. In Chapter 8 of [103], a function for the pump depleted conversion efficiency is derived from the coupled amplitude equation, yielding the expression:

$$\eta_{SHG}(\%) = tanh\left(\sqrt{\frac{2\mu_0\omega_P^2}{\epsilon_0 n_P n_{SH}}}d|E_P|L\right)^2 \tag{4.12}$$

For the purposes of fitting pump depletion trends to experimental data, it will suffice to use a $\tanh^2$ function which is only dependent on the pump power and a fitting factor, C.

$$\eta_{SHG}(\%) = tanh\left(\sqrt{C \times P_{pump}(W)}\right)^2 \tag{4.13}$$

Fig. 4.4, implements Eq. 4.10 and 4.12, to demonstrate the difference in behaviour. The pump depletion model does not allow the conversion efficiency to increase above 100%, yielding more realistic behaviour at high pump powers.

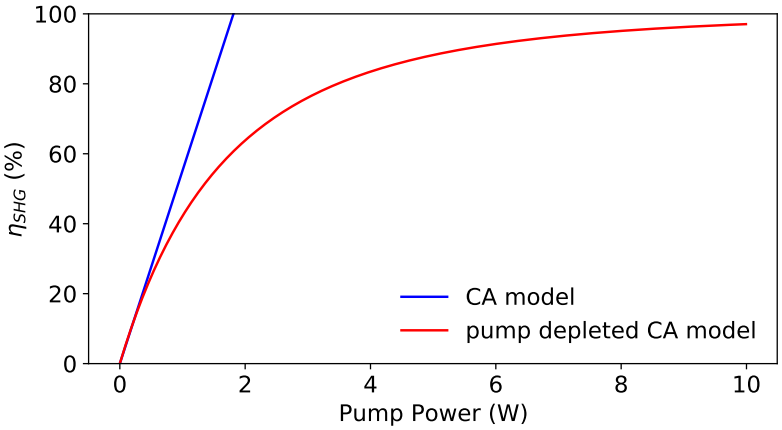

Figure 4.4: Absolute SHG conversion efficiency comparing calculations using Eq. 4.10 with the pump depleted output calculated using Eq. 4.12.

In the following sections, the theoretical models of PPLN SH conversion efficiency help to confirm that the crystal is set up optimally, and diagnose any unusual behaviour which is experimentally observed.

4.3 Rb TPT with a Frequency-doubled CW Telecoms laser

4.3.1 1556 nm CW Laser System

As described at the start of the chapter, there are a number of advantages, in terms of reliability and size, to using a telecoms seed laser. For this experiment we use a packaged external cavity laser from Pure Photonics (pictured in Fig. 4.5). This laser can tune from 1528 to 1565 nm, while outputting up to 22 mW of fibre-coupled output power and a typical intrinsic linewidth of < 10 kHz according to its spec. sheet. The laser power and operating wavelength are set using a computer to send serial control commands to an on-board control system which can adjust the laser temperature and current. The laser frequency can be modulated externally using an analogue control signal to an internal PZT (piezo-electric transducer) which adjusts the laser cavity length. This enables an analogue 120 MHz tuning range at rates up to 100 kHz.

Figure 4.5: Pure Photonics PPCL550 tuneable telecoms laser with fiber output. The laser package is very compact, with a length of less than 10 cm.

The 22 mW output power from this laser is not enough to get more than 0.25 mW of 778 nm SH output from the PPLN, therefore requiring amplification of the 1556 nm power before the PPLN. For this we use an Erbium-doped Fiber Amplifier (EDFA), from Keopsys (CEFA-C-PB-HP-PM-30-NL1-OM1-M102-FA-FA). This EDFA accommodates fiber-coupled input and output, and can deliver up to 2 W optical power. In theory, this should allow generation of up to 1 W of 778 nm power.

Using the Pure Photonics laser as a seed for the EDFA, the optical spectrum of the EDFA output was measured using a HP 86140A Series Optical Spectrum Analyser (OSA). In the optical spectrum shown in Fig. 4.6, the background noise suppression ratio is measured to be at least 45 dB (± 2 nm of the seed wavelength). Furthermore, increasing the seed power helps suppress the background noise by an extra 4 dB. If the spectral noise from the EDFA gain pedestal is too high, then the conversion efficiency of the PPLN will be reduced.

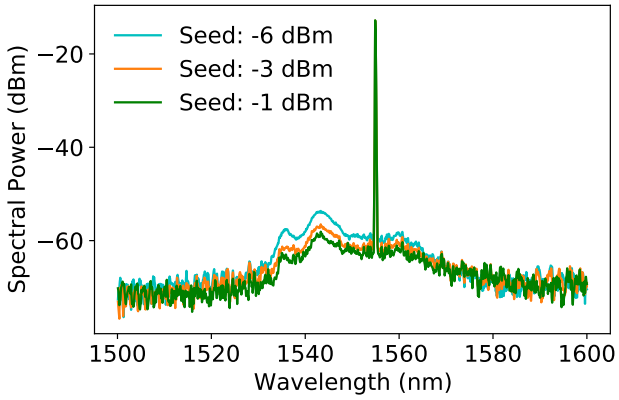

Figure 4.6: OSA data of the EDFA output shows a good background suppression noise around the amplified 1556 nm seed wavelength. The background noise across the range 1530-1570 nm corresponds to the EDFA gain profile.

4.3.2 CW SHG Characterisation

The Covesion waveguide PPLN crystal used in this experiment (WG-SHG1560-40)[106] has a length of 40 mm with a poling period of 18.5 μm, and are quoted on their datasheet as achieving $\eta_{SHG} = 47\%/\text{W}$ for the range 778-780 nm. The waveguides (pictured in Fig. 4.1) in the crystal are 9 μm wide, and require the beam to be focused to the same width to reach a typical coupling efficiency of 70%. The crystal is housed inside an oven on top of a 3-axis translation stage. The pump beam is focused to a spot size of $w_0 \simeq 4.5$ μm and aligned on to the waveguide which yields the highest conversion efficiency. For characterisation and general use, the PPLN output is re-collimated, and a long-pass beam splitter separates the two output wavelengths. Fibre-coupling the 778 nm output, both filters out remaining pump light and ensures a Gaussian beam profile for spectroscopy. The SHG stage apparatus is shown in Fig. 4.7.

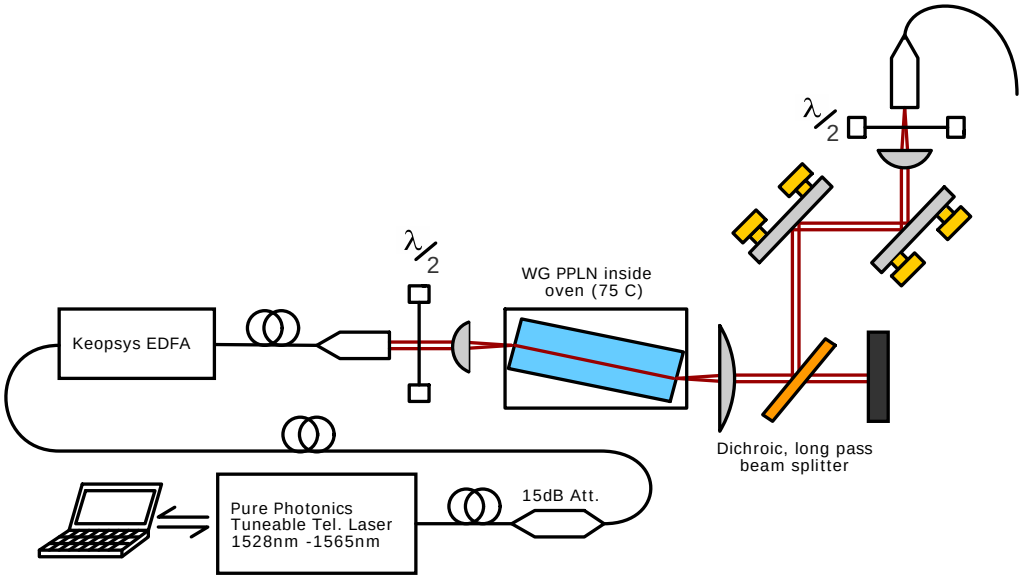

Figure 4.7: Apparatus for aligning and coupling the pump beam to the PPLN crystal, and then fiber-coupling the output to spectroscopy.

For characterisation of the SHG stage, the PPLN was heated to a temperature of 75 °C to phase-match a pump wavelength of 1556 nm. An oven controller from Covesion regulates the temperature to $< \pm 0.1$ °C. The crystal is positioned within the oven at an angle to the incoming beam (as shown in Fig. 4.7), to minimise reflections at the entry facet of the crystal and prevent the occurrence of optical etalons between the input and output surfaces of the crystal [99]. The polarisation of the pump beam is set to be vertically polarised to match the optic axis for the ordinary refractive index as it enters the PPLN, allowing for type-0 phase-matching to take place (meaning the pump and SH fields have the same polarisation). Then using a low pump power of 22 mW, the

alignment to the waveguide was adjusted to attain the maximum SH power on a silicon photodetector at the output of the PPLN. Next the PPLN temperature was fine-tuned to reach the peak conversion efficiency. By scanning the pump wavelength, as shown in Fig. 4.8a, the expected sinc^2 function phase-matching behaviour is observed. This measurement yields a peak conversion efficiency of $\simeq 55\%/\text{W}$ with a FWHM conversion bandwidth of $\simeq 0.3$ nm. The conversion efficiency is inclusive of the coupling loss to the waveguide. In Fig. 4.8a, Eq. 4.10 is compared with data, providing a close match in spectral width and amplitude when using a fitting factor of 0.45 applied to the effective non-linear coefficient (issued by the PPLN manufacturer) of 1.239×10^{-22} F/V and using 22 mW pump power.

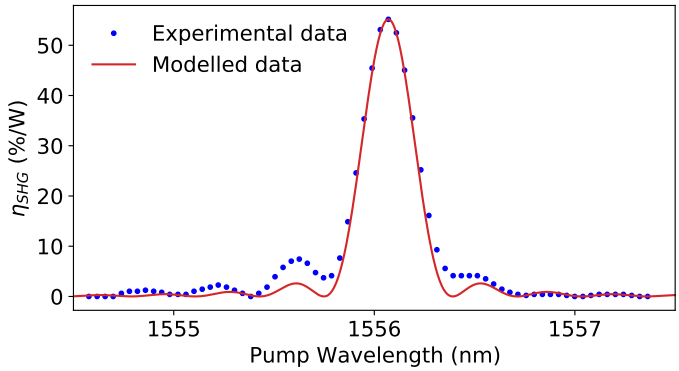

(a)

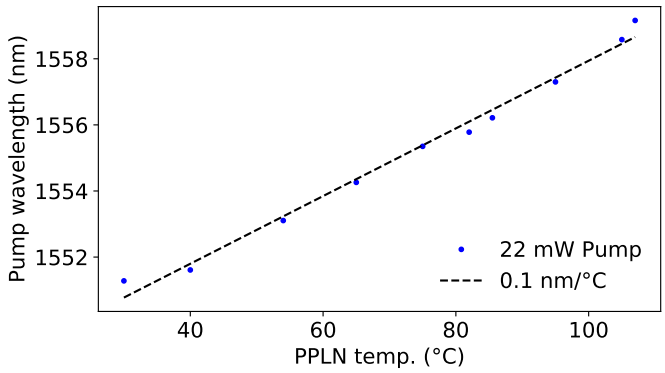

(b)

Figure 4.8: (a) Scanning the pump wavelength using 22 mW, reveals a peak SHG conversion efficiency of 55%/W (0.266 mW) at a PPLN temperature of 75 °C. Measured data is compared with the behaviour of the modelled data using Eq. 4.10 to confirm the FWHM conversion bandwidth of 0.3 nm. (b) Example characterisation of the PPLN temperature tuning coefficient for one of the PPLN waveguides.

The Covesion WG PPLN will also permit similar conversion efficiencies to 780 nm when heated to 105 °C. Characterisation of the PPLN wavelength conversion range, and temperature tuning coefficient is attained by shifting the pump wavelength and then adjusting the PPLN temperature until the maximum conversion efficiency is achieved.

The results have been plotted in Fig. 4.8b, and a fitted linear slope reveals a tuning coefficient of $\simeq 0.1$ nm/°C. While there was not expected to be any difference in poling period between the five waveguides, the phase-matching temperature for 1556.2 to 778.1 nm was observed to vary by a few degrees in each waveguide.

The peak conversion efficiency of the data in Fig. 4.8a corresponds to an absolute conversion efficiency of 1.2% at 22 mW pump power. In Fig. 4.9 the measured absolute conversion efficiency can reach a maximum of $\simeq 25$ % as the pump power/intensity is increased. Following the trends of the pump depletion model, the conversion efficiency rises linearly, while the pump power is low, but reaches a plateau when using pump powers of >600 mW.

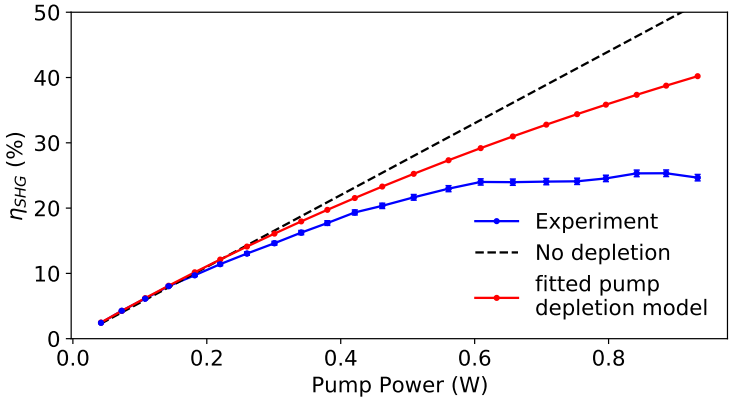

Figure 4.9: Measured conversion efficiency against pump power compared with the model from Eq. 4.13. Both CA and pump depletion models match experimental data relatively closely up until 200 mW pump power. The pump depletion model of Eq. 4.13 is fitted using the fitting parameter $C = 0.6$, so as to allow the closest fit at low pump powers.

The PPLN characterisation shown here matches the characterisation data issued from Covesion for the device, including reaching a value of 47%/W at 300 mW pump power. This confirms that the PPLN is set up properly, and reaching its best performance. Discrepancies between the modelled and experimental data in Fig. 4.8a, are likely to have arisen from imperfections in the periodic poling of the crystal. If the temperature is not completely uniform through the PPLN crystal, then there will be further reductions in conversion efficiency from ideal, stemming from the same issue of poling period variations. Evidence for variations in the poling period are also indicated by the asymmetry of the pump wavelength tuning data shown in Fig. 4.8a.

A measurement of the 778 nm output relative intensity noise (RIN) was carried out by coupling all of the PPLN output directly to a DET10A2 Thorlabs photodiode, and measuring the signal amplitude on an oscilloscope for a period of up to 2 hrs. There is some vibrational sensitivity of the alignment of the pump to the PPLN waveguide, introducing RIN noise but without pushing RMS noise above 0.2%. The 778 nm output maintains this RIN stability level both on short-time scales and long time scales, as

shown in Fig. 4.10. The output RIN stability of the EDFA is quoted to be capable of 0.05 % RMS.

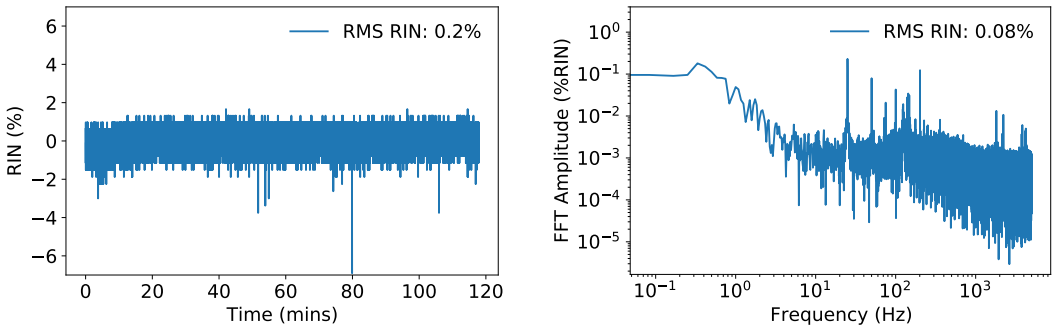

(a) *(b)*

Figure 4.10: (a) Long-term PPLN output power stability over 2 hours. (b) FFT of short-term PPLN output stability recorded over 12 min. The FFT data is normalised w.r.t. the measurement bandwidth.

The short-term RIN may still be lower than measured here, since the noise limit on these measurements is set by the baseline noise of the oscilloscope. In Fig. 4.10b, there is evidence of mains electrical noise, with components 25 Hz, and upwards at multiples of 25 Hz. The same noise components remain when using the seed laser as a pump without the EDFA, and also do not appear on oscilloscope background noise measurements. Therefore the mains electrical noise is likely coupling in to measurements through the Pure Photonics seed laser. In terms of RIN noise levels there is nothing here which we expect to degrade the Rb TPT spectroscopy signal.

The characterisation process highlighted an unexpected issue for the WG PPLN, causing the behaviour shown in Fig. 4.11. This behaviour is largely undocumented and will briefly be discussed before moving on. It is possible for electrostatic charge to build up on the surface of the crystal when its temperature is adjusted over a wide range. Although there is no available documentation on the mechanism for this effect, we suspect this to occur during temperature-induced contraction of the crystal, which generates an electrostatic charge build-up on or within the PPLN due to the piezo-electric effect (known to be a property of $LiNbO_3$ [107]). This charge would then affect the polarisation response of the crystal, leading to changes in the phase-matching behaviour. This occurred, several times in our case when switching the crystal temperature between 105 °C and 75 °C, to switch from using a 1560 to 1556 nm pump laser. The impact of the charge build-up causes the tuning behaviour to deviate from a sinc^2 function and appears to yield a peak conversion efficiency at several wavelengths (see Fig. 4.11a). The phase-matching wavelength appears to wander around, causing power fluctuations over the course of an hour, as shown in Fig. 4.11b, and reducing long-term power stability. The solution to this issue, requires a method to discharge the crystal. This was carried out, in the first instance, by shining a deep UV lamp on to

the crystal for several minutes, which returned the PPLN tuning behaviour back to a normal sinc^2 function as shown in Fig. 4.11a. Later the discharging could be achieved more easily by ramping up the pump laser power to around 1 W for 10-20 mins before running an experiment with the PPLN. This was only necessary after switching between using the PPLN for 1560 and 1556 nm conversion. More examples of this behaviour are included in Supp. Fig. S3.

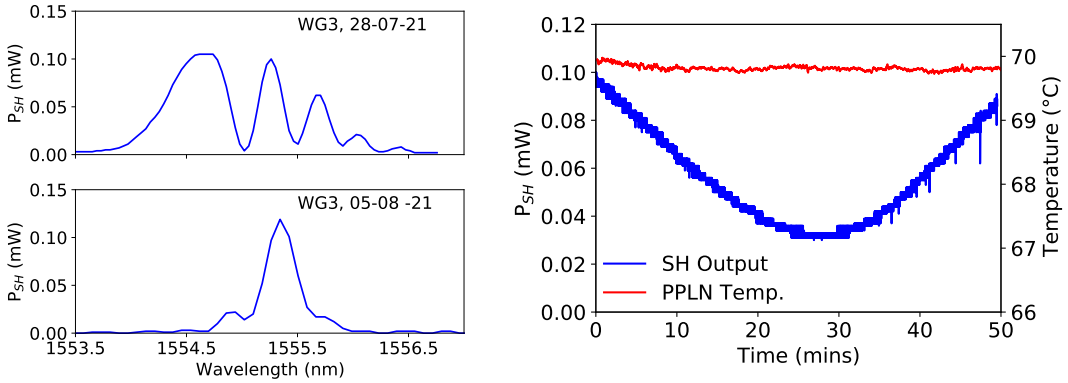

(a) *(b)*

Figure 4.11: (a) Example of odd PPLN tuning behaviour while scanning pump wavelength, compared with behaviour under same conditions after discharging the PPLN crystal with a UV lamp. (b) Continuous monitoring of the SH power and PPLN oven temperature shows the SH power to vary, without any correlation to changes in PPLN temperature.

This effect differs from the photo-refractive effect in PPLN documented by other researchers [108, 109], which occurs when a high laser power mobilises charge carriers within the crystal, altering the polarisation response. This effect typically causes the phase-matching wavelength to drop slightly lower at given PPLN temperature, and is something we observe when running the PPLN with pump powers above 500 mW, usually requiring the PPLN temperature to be adjusted by 1-2 °C. The photo-refractive effect, may account for the deviations in measured behaviour at high pump powers from the pump depletion model in Fig. 4.9.

4.3.3 Rb TPT Spectroscopy with a Frequency-Doubled CW Telecoms Laser

The fibre-coupled output of the SHG stage is connected to the Rb TPT spectroscopy apparatus described in Chapter 2.8. In practice, to deliver $\simeq$ 50 mW at 778 nm to the Rb vapour cell required $\simeq$ 500 mW of 1556 nm power to the PPLN at a SHG conversion efficiency around 20%. Further 778 nm power losses were incurred during fibre-coupling. The PPLN waveguide output was somewhat vertically elongated, and suffered clipping on the edge of the oven casing before it was collimated. This led to a poor fibre-coupling efficiency of only around 49%, relying on the fibre itself to clean up

the beam profile, while sacrificing a possible fibre-coupling efficiency of around 70%.

The telecoms laser frequency was tuned to the ^{87}Rb F = 2 → F' = 4 TPT excitation frequency via computer control (down to 1 MHz resolution), which was cross-checked using a wavemeter. A function generator is then used to scan the laser with a saw-tooth signal via its piezo tuning port and begin searching for the TPT. As mentioned already, the analogue tuning range is ≃ 120 MHz, however at the second harmonic this range doubles (along with the laser frequency), to ≃ 240 MHz. The telecoms laser frequency is well calibrated and possesses low-drift, which made it very easy to get the Rb TPT features within the scan range. In Fig. 4.12, an example scan of the hyperfine features of the ^{87}Rb TPT is shown, using a 49 mW, $w_0 = 220$ μm radius beam, incident on the Rb vapour cell at 100 °C.

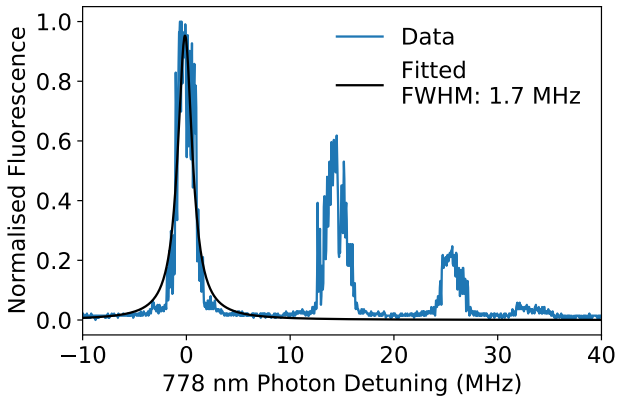

Figure 4.12: A slow scan at 23 MHz/ms over the hyperfine features of the ^{87}Rb TPT, under the conditions described above. A Lorentzian is fitted to 3 data sets like this to determine an average fitted FWHM of 1.66 ±0.05 MHz.

The hyperfine TPT features shown in Fig. 4.12 are quite wide, with the F = 2 → F' = 4 measuring a FWHM of 1.7 MHz. This is almost double the 0.9 MHz linewidth measured using the ECDL, and points toward an issue with the laser itself since no other parameters of the spectroscopy have been altered since the ECDL was used. The dominant contributions to the measured linewidth are the same as before: $\Delta f_0 = 334$ kHz, $\Delta f_{tt} = 322$ kHz, and assuming the magnetic broadening component is no larger than for TPT spectroscopy using the ECDL. The features are not just wide, but also noisy and posses a more rectangular profile than Lorentzian, indicating frequency noise during scans. The telecoms laser can operate in a mode where its frequency dithers at a rate of 888 Hz, to allow it to calibrate its frequency. Normally the lasers dither mode is switched off for any spectroscopic measurements. However there might be other stabilisation feedback loops which cannot be deactivated such as RIN feedback. RIN stabilisation however is not expected to contribute any FM noise to the laser, and the RIN stability at the vapour cell was measured to be no more than ±1.5% on time scales up to 10 minutes.

Fortunately, the telecoms laser could scan at rates up to 100 kHz. To investigate the laser FM noise further, the laser was scanned at faster rates to try and scan faster across the TPT hyperfine features than the noise was occurring. The scan rate was increased in order to eliminate the FM noise occurring during slower scan rates. The Rb TPT scans shown in Fig. 4.13, demonstrate progressively narrower FWHM, and less jitter noise. The middle scan at 275 MHz/ms appears to jump during the first feature, leaving a jagged profile. The fastest scan rate shown in Fig. 4.13, at 333 MHz/ms yields a measured FWHM of just 0.8 MHz. The line-shape of the features are much less noisy for this scan rate, but still they are not perfectly Lorentzian, and appear asymmetric. This asymmetry is likely to be stemming from magnetic broadening, Δf_B, at normal levels of Earth's magnetic field. Asymmetric broadening due to the magnetic field arises from using circular polarisation, rather than linear polarisation to pump the TPT.

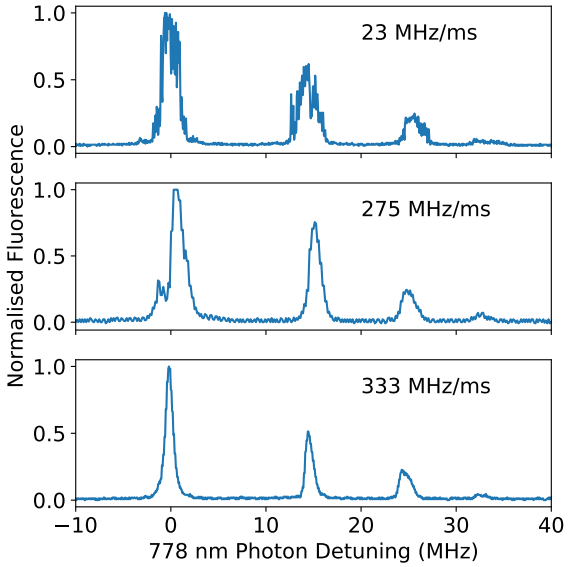

Figure 4.13: The scan rate was increased in order to eliminate the FM noise occurring during slower scan rates. The measured FWHM of the tallest hyperfine feature in each case, in order from top to bottom these were: 1.71 MHz, 1.52 MHz and 0.84 MHz. The detection bandwidth for these measurements is limited to the PMTs bandwidth of 200 kHz.

The reduction in signal noise at faster scan rates indicates the FM noise is originating from the laser. To help confirm this, it was possible to couple the 1556 nm output of the laser directly to a 25 cm confocal Fabry-Perot cavity, yielding the transmission data shown in Fig. 4.14 whilst the laser frequency is scanned using its internal piezo. In Fig. 4.14, the inset highlights the presence of periodic as well as non-periodic oscillations. The noise on the transmission feature has typical characteristics of FM noise rather than AM noise owing to its larger amplitude on the sides of the feature. The same noise was not visible when detecting transmission of a different laser at 1560 nm with this optical cavity.

An FFT of the transmission data in Fig. 4.14, showed the presence of a noise component in the region of 100 ± 10 kHz, which was the second highest-level noise component after low-frequency and DC components of the FFT spectrum. The most steady of the oscillations shown in the inset of Fig. 4.14 appear to have a period corresponding to around 100 ± 10 kHz.

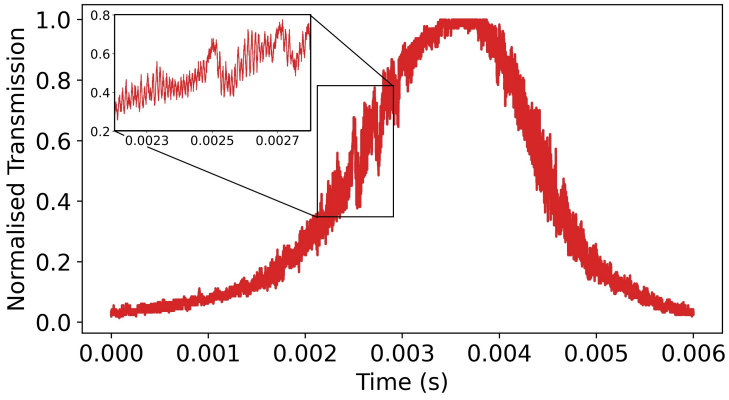

Figure 4.14: The 1556 nm Pure Photonics laser is run at full power and directly coupled to a 25 cm Confocal Fabry-Perot Cavity. The laser frequency is scanned over the cavity mode by applying a 25 Hz saw-tooth signal to its internal piezo. A Thorlabs DET10C2 photodiode records the transmission from the cavity during the scan, picking up what appears to be high frequency FM noise during the scan.

4.4 Frequency-Locking to the Rb TPT

Initially, a frequency lock of the Telecoms laser to the Rb TPT hyperfine reference transition was attempted using a similar feedback apparatus as for the ECDL lock (see Fig. 3.8). However, this proved difficult owing to the FM noise on the Rb TPT signal. The linewidth of 1.7 MHz for the slow scan implies that the FM noise dithers the signal frequency as much as 0.4 MHz either side of the lasers centre frequency. This amount of FM noise makes it almost impossible to manually scan the laser frequency to near the zero-crossing of the Rb TPT error signal. Even if the lock could be initiated, the FM noise would immediately tune the laser frequency outside the bandwidth of the lock.

While the FM laser noise prevented a direct lock to the reference transition, the seed laser is able to handle piezo feedback up to 100 kHz, as well as the available locking electronics. It was therefore possible to lock to the 7 MHz-wide, scanning Fabry-Perot transmission feature (cavity mode), and if the FM noise falls within the FWHM of the mode then a lock can be maintained, eliminating the FM noise. Following this, it would then be possible to scan the Fabry-Perot cavity length, causing a shift of the cavity mode frequency, allowing the laser to excite the reference transition, while following the mode. If successful, a second feedback loop could be implemented to lock

the Fabry-Perot cavity and hence the laser to the reference transition. The apparatus for locking the telecoms laser to the Fabry-Perot mode is shown in Fig. 4.15, and uses the same technique as we used for locking the ECDL to the Rb TPT. As we could only modulate the telecoms laser via piezo feedback, a summing circuit combines the modulation signal with the feedback signal and allows switching between a scan signal and feedback to help navigate to the lock point.

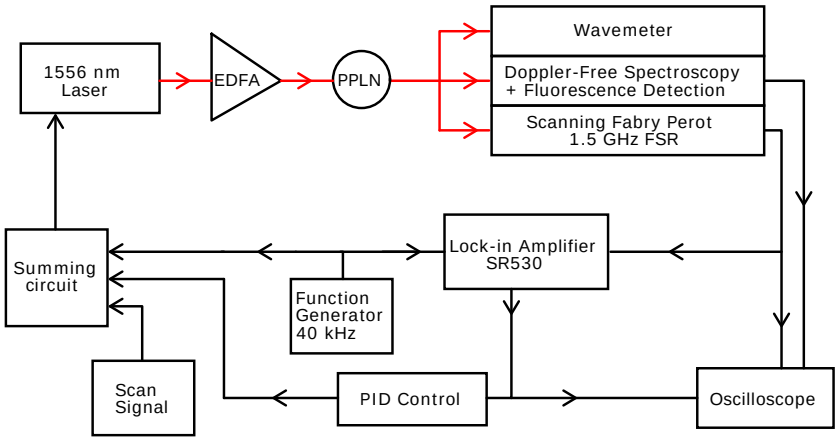

Figure 4.15: Apparatus for locking the 1556 nm CW telecoms laser to a Fabry-Perot mode in order to pre-stabilise the laser, and enable lower noise scans over the Rb TPT hyperfine features. Red lines indicate optical paths, and black are electrical paths.

Once the apparatus was ready for the lock, the laser frequency was adjusted to be resonant with the Rb TPT signal, and then the Fabry-Perot cavity length adjusted to also provide resonance with the laser. This allowed for the FM laser noise to be simultaneously picked up on both resonance signals at once (while no modulation was applied), as shown in Fig. 4.16. Both signals demonstrate fluctuations which are synchronised with a period of about 100 kHz, confirming the presence of the FM noise.

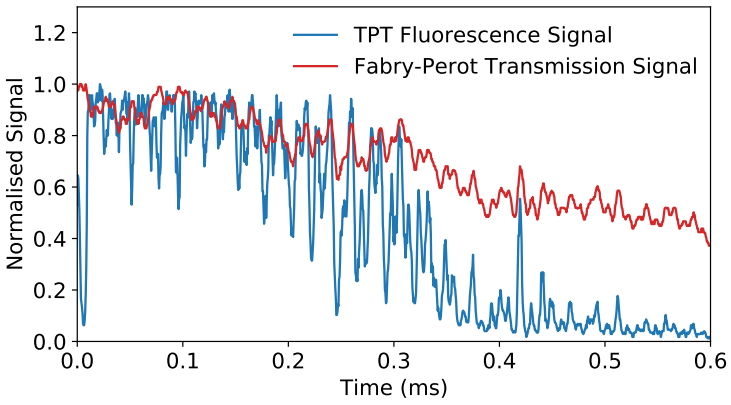

Figure 4.16: Synchronised fluctuations in the Rb TPT fluorescence signal and Fabry-Perot transmission signal. The fluctuations show that the problem is common to the laser frequency itself, and indicates the noise is occurring at a rate of ∼ 100 kHz.

After locking the telecoms laser to the Fabry-Perot mode, Fig. 4.17, shows the resulting lock stability in terms of the transmission signal. While locked, the cavity length is scanned to pull the laser frequency across the Rb TPT hyperfine features. The resulting scan shows the same noise as we observed before appearing on the features, with only a marginal reduction in the laser linewidth.

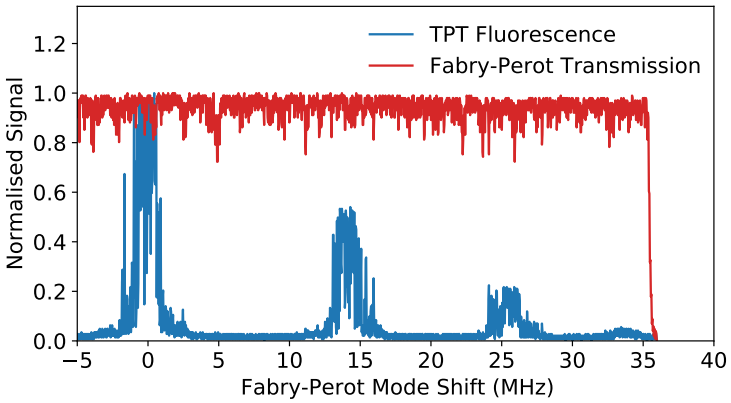

Figure 4.17: Observation of the Rb TPT features while the laser is locked to the Fabry-Perot mode. The Fabry-Perot lock stability can be gauged by how closely the transmission signal stays near its peak level.

Even after pushing the modulation frequency up to the limit of the feedback electronics at around 100 kHz, the FM noise was still just beyond the range of the equipment to be able to compensate for. It appeared that there were no easy options left to measure the long-term stability of the telecoms laser while locked to the Rb TPT, as there was also the unforeseen issue of the telecoms laser drifting beyond the 120 MHz range over which the piezo could scan. Without compensating for the FM noise, it is unlikely the lock would demonstrate any better stability than we achieve with the ECDL system. The telecoms laser had however been useful for optimising CW conversion efficiency through the PPLN stage, and this would provide a basis for comparison as we switch to using an optical frequency comb for the next stage of the work.

Chapter 5

Rb TPT with a Frequency-Doubled Optical Frequency Comb

5.1 Introduction

One of the main applications for an Rb TPT optical frequency reference is in a portable atomic clock [33]. However, current methods for converting the optical reference frequency to a clock signal are still relatively complex. Earlier, in Section 1.5, we discussed the use of the Optical Frequency Comb (OFC) to convert an optical frequency reference to an optical atomic clock. So far, we have taken the approach of using a frequency-doubled 1556 nm CW laser, to deliver 778 nm output power and laser linewidth comparable to the Ti:Sapphire laser, but with reduced size and complexity. However, the CW telecoms laser frequency reference still requires to be mixed with an output from a separate, self-referenced OFC laser to generate a useful clock timing signal (e.g. 10 MHz TTL or 1 pps). In the case of a two-photon (or more) excitation, it is possible to use an OFC laser to drive the transition, without reducing the SNR or causing transit-time broadening [110]. A frequency-doubled OFC laser could potentially be used to drive the two-photon transition and simultaneously seed a self-referenced frequency comb, reducing the complexity of a two-photon optical atomic clock. As mentioned in [67], the non-linear dependence of the frequency-doubling conversion efficiency additionally yields an enhancement factor proportional the number of modes (N) in the OFC spectrum. Such an improvement in efficiency could eventually allow the system to operate without requiring an EDFA to boost optical power.

There have been a number of studies of the Rb TPT using OFC lasers, such as the mode-locked Ti:Sapphire laser. One such study was conducted here in the physics department of the University of Strathclyde, in 1996 by M. Snadden et al. [67]. The pub-

lication demonstrates high-resolution measurements of the weakly-excited, two-photon transition, recording linewidths < 500 kHz. In this case, the main advantage to using the 778 nm OFC was to provide high power levels and a narrow linewidth compared with other 778 nm CW lasers of its time. Rb TPT spectroscopy using OFCs has led to further high accuracy measurements of atomic properties and time evolution measurements of excitation schemes [68, 111].

Within the last decade, a research group from Peking University, Beijing demonstrated the use of a frequency-doubled 1556 nm OFC laser with a thermal Rb TPT optical frequency reference [69, 70, 112]. They use an Erbium-fibre femtosecond laser, with a wide spectral bandwidth, > 4 nm (after frequency-doubling). The wide bandwidth of their OFC laser allows modes either side of the central resonant mode at 778 nm to simultaneously step-wise excite the Rb TPT (780 + 776 nm), boosting the TPT signal strength by 2-3x in theory [112]. Step-wise resonant excitation additionally makes the transition more sensitive to the AC-Stark shift (see Section 2.5). In the research group's 2015 publication, they manage to demonstrate a fractional frequency stability of 8×10^{-12} at 1 s and 4.3×10^{-13} at 1000 s for the OFC, while referenced to the Rb TPT.

This technique however generates elevated levels of Doppler-broadening resulting from the frequency difference of the photons taking part in the step-wise excitation. Compensating for this issue adds extra complexity and has led the group to use a magneto-optical trap (MOT) to cool the atoms and eliminate Doppler-broadening fully [113]. By contrast, in this section we will be using a frequency-doubled telecoms OFC with a narrow spectral bandwidth (< 0.25 nm @ 778 nm) that does not allow the OFC modes to excite the Rb TPT step-wise, and hence reduces much of the extra apparatus required to achieve a Doppler-free signal. Under ideal conditions, the OFC can deliver a narrow linewidth, low vibrational sensitivity and additional telecoms applications of the frequency reference, while achieving the same Rb TPT excitation rates as a CW telecoms laser, using less seed laser power.

Compared with a single mode, CW laser, there are a number of subtle differences to carrying out TPT spectroscopy with an OFC laser. In order to provide a foundational understanding of which characteristics of an OFC laser are important for this particular application, the following section will provide some background theory of how OFC lasers operate. We then demonstrate that the OFC laser meets the required specifications, such as low phase-noise between the comb modes, with analysis of the frequency-doubling conversion efficiency helping confirm this. Finally the OFC laser is used for spectroscopy of the Rb TPT, which combined with knowledge from the prior sections, allows for a deeper analysis of the suitability of this laser for such an application.

5.2 Principles of an Optical Frequency Comb Laser

An optical frequency comb (OFC) is a type of laser, which outputs a spectrum of multiple, equally-spaced laser modes/frequencies, hence its spectrum resembles the profile of a hair comb. Typically the modes of an OFC have a frequency spacing ranging from 10's of MHz to THz, which occur continuously over a range of up to several hundreds of THz [114, 115]. In the ideal OFC spectrum (Dirac Comb function), the modes span out over an infinite spectral range, and are all of equal amplitude. However, real devices output modes over a limited range known as the spectral bandwidth, which we will denote BW_{OFC} for use in equations. The spectral bandwidth is the frequency span over which all modes are above half of the maximum amplitude of the modes. The number of modes which fit within the spectral bandwidth is denoted as N. When all of the OFC modes are in phase with one another, the laser output forms regular pulses with a typical peak optical power (P_{peak}) on the order of N times greater than the lasers average optical power (P_{av}). The pulses arise from the coherent superposition of the electric fields of each mode. The spacing between the OFC modes is denoted as f_{rep} (the repetition rate), because this value also corresponds to the rate at which the OFC pulses occur, as shown in Fig. 5.1.

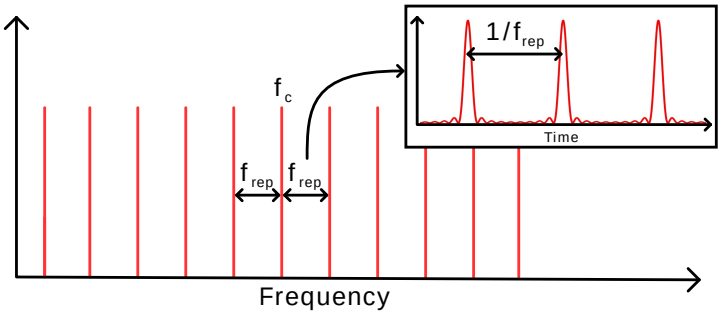

Figure 5.1: The ideal frequency comb spectrum. The modes of the comb form around the unmodulated centre frequency of the comb, f_c, and are each separated by the repetition rate of the comb laser, f_{rep}. The insert demonstrates how the mode spacing corresponds to the period between pulses.

If we are to extend the spectral bandwidth of the OFC to include a larger N, the peak amplitude of the pulses increases and the pulse width narrows proportionally to conserve the same total power within the area of the pulse. Hence the ratio of $\mathrm{P}_{peak}/\mathrm{P}_{av}$, pulse width (FWHM), and the pulse duty cycle (ratio of pulse width to the period between pulses) all vary proportionally to N. This can be demonstrated by simulating the total electric field of the pulses. A model of the pulses is created by way of a summation over the electric field of N laser modes, occurring at frequencies, f_m:

$$f_m = f_c + m \times f_{rep} \tag{5.1}$$

Where m is an integer denoting the position of the mode with respect to f_c, for which values of m are limited to:

$$m = \{-(N-1)/2 \; ... + (N-1)/2\} \tag{5.2}$$

For which m increases in steps of 1. For example, if N = 7, then m = -3,-2,-1,0,+1,+2,+3. To keep the notation simple, we will only consider OFCs with an odd number of modes, so that f_c always sits at m = 0. The total electric field of the OFC, $E_{OFC}(t)$ is then obtained by a summation over all of the modes within the spectral bandwidth as such:

$$E_{OFC}(t) = E_0 \sum_{m=-(N-1)/2}^{(N-1)/2} e^{i2\pi f_m t} \tag{5.3}$$

Where the electric field amplitude corresponds to the average optical power being equally split between all of the modes, so that $E_0 \propto \sqrt{P_{av}/N}$. To model the measurable optical power in the pulses, we can skip converting the power in each mode to E_0 and back again, and re-express the pulse model as:

$$P_{OFC}(t) = \frac{P_{av}}{N} \left| \sum_{m=-(N-1)/2}^{(N-1)/2} e^{i2\pi f_m t} \right|^2 \tag{5.4}$$

We can determine from Eq. 5.4, that at times when all of the modes align to form a pulse, the summation term within the square brackets equals N, and the peak power of the pulse can be estimated as:

$$P_{peak} = P_{av} \times N \tag{5.5}$$

Simulations of the OFC pulses, using Eq. 5.4 are plotted in Fig. 5.2 for increasing values N. The pulses appear to have a solid area because of the rapid oscillations of the electric field within the pulse envelope. In the case of an OFC with a flat spectral profile like that shown in Fig. 5.1, the pulse envelope may be modelled using a $sinc^2$ function [116]. Additionally, one can introduce phase noise in to the simulation, which leads to broadening of the pulse width, reduction in peak amplitude, and asymmetrical pulse shapes.

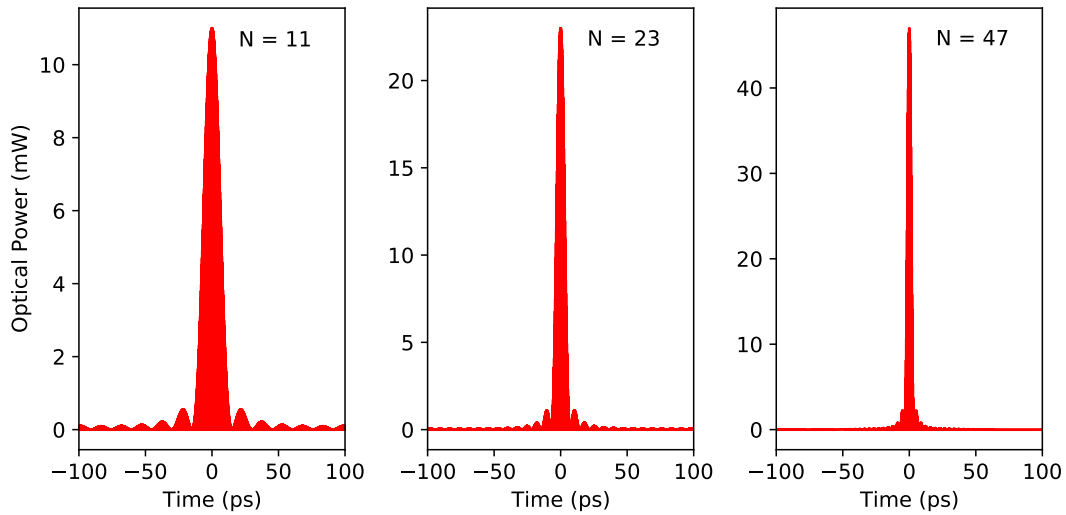

Figure 5.2: Example OFC pulse simulations for a laser with P_{av} = 1 mW, f_c = 192.642 THz, and f_{rep} = 6 GHz, while we add more modes to the OFC spectral bandwidth. The pulse amplitude increases proportionally to the number of modes, while the pulse width increases proportionally to the spectral bandwidth.

Over the past 20 years of developing the optical frequency comb, many different methods of generating an OFC spectrum from a single mode laser have emerged. Some examples of commonly-used methods, and their applications include:

1. Mode-locked lasers (MLLs) - Generate wide-bandwidth frequency combs, with femto-second pulses and 10's to 100's of MHz f_{rep}. They are often used in combination with a non-linear fiber stage for generating, octave-spanning frequency combs for optical frequency measurement applications requiring self-referencing of the comb spectra [35].

2. Laser coupling to whispering gallery modes (WGM) in micro-resonators [78] - Generates a Kerr Soliton comb, with repetition rates in the range of 100's of GHz, easily yielding octave-spanning comb spectra. OFCs using micro-resonators are able to be fabricated directly on to a chip-scale semiconductor platform [117], and have been demonstrated for use as a self-referenced OFC [33, 39].

3. Laser propagation through "Highly Non-Linear Fiber" (HNLF) - A technique yielding similar comb characteristics to MLLs, and typically used to broaden the range of modes in an MLL or WGM comb spectrum [39].

4. Electro-optic comb generators [114] - Using an electro-optic modulator (EOM) to phase modulate the laser, allows for easy tuning of f_{rep} in the 10's of GHz range. Currently, their most common applications lie in multi-channel optical communication systems, relying on the EOM to easily control the frequency spacing between the channels and encode data to each frequency at a high bit-rate [118].

5. Gain-switching Laser [119, 120] - Direct amplitude modulation of the laser power, allowing easily tunable f_{rep} up to 10's of GHz, and pico-second pulse widths. useful for providing a spectrally flat range of modes. Used to facilitate DWDM (Dense Wavelength Division Multiplexing) allowing the transmission of multiple signals in both directions along a fibre, greatly increasing data transmission rates [47].

In the following sections, we will be using an OFC laser of the final type described. This laser is designed with applications toward DWDM systems, and advanced modulation techniques. So far the DWDM channel spacing has typically been limited to 100 GHz, to ensure the frequency of the individual seed lasers on each channel do not cross paths as their frequency drifts. New DWDM devices are aiming for narrower spacing at 12.5 GHz [121] and below [47]to increase the data transmission capacity. One method for reducing the drift between the channels is to use an single OFC laser to provide a fixed spacing between all of the channels. However, if the central frequency of the OFC were to drift, so would all of the channels (modes of the OFC) drift with it. Hence, if we can reference the telecoms OFC to an atomic reference frequency, then long-term drifts will be reduced, and enable narrower channel separations.

5.3 OFC Laser Characterisation

The OFC laser used in this section is a prototype version of a C-band, telecoms LYRA-OCS-1000 laser system from Pilot Photonics. The laser system design is an externally-injected, gain-switched OFC laser and is geared toward operating as a seed laser for high-bandwidth, telecoms applications such as DWDM [122]. According to the developers, the laser is also designed to be used for advanced modulation formats to extend the data transmission rates, including quadrature phase-shift keying and polarisation division multiplexing (PDM) [123]. An OFC laser operating as the transmitter in such systems must meet certain requirements, including high side mode suppression ratio (SMSR), high wavelength stability, flexible channel spacing, spectral flatness and high phase coherence. These properties are highly advantageous for our application.

5.3.1 Operation and Control

This OFC laser typically outputs a 60 - 70 GHz-wide spectral bandwidth around 1556 nm, with a fixed average optical output power of 2.3 - 2.5 mW_{av} (fibre-coupled). The linewidth of the OFC modes is around 300 kHz and while there is little to no drift between each of the modes, the OFC spectrum as a whole, demonstrates drifts of < 1 GHz/day [124]. The number of OFC modes within the spectral bandwidth can vary depending on the value of f_{rep} (supplied externally from an RF source), which unlike other types of OFC, is quite widely tunable from 2 GHz up to 10 GHz. To achieve

such operating characteristics, the design of the OFC is comprised of two laser diodes integrated on to a chip. The first LD (Fabry-Perot laser) outputs a wide linewidth, and is operated near its threshold current, then directly current-modulated at f_{rep} (gain-switching) to generate a series of modes. The second LD (tuneable laser) has a narrow-linewidth, widely-tunable 1556 nm output, which is allowed to provide optical feedback to the first LD, using for example a circulator (shown in Fig. 5.3). Due to the optical feedback, the FP laser is able to injection-lock [125] to the tuneable lasers frequency, transferring the narrow linewidth, and stability of the tuneable laser to the OFC modes, and extending the spectral bandwidth of the OFC [124, 126]. Injection-locking the OFC to the tuneable laser additionally improves the SMSR of the OFC and allows extra control over the spectral flatness of the comb modes within the bandwidth [127]. The system design is illustrated in Fig. 5.3b, which all fits in to a small and rugged package shown in Fig. 5.3a.

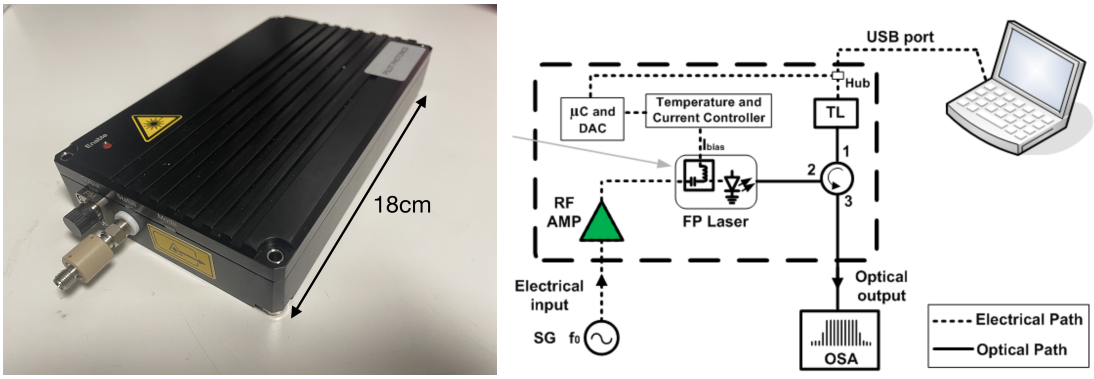

(a) (b)

Figure 5.3: (a) Image of the relatively compact OFC laser module. The output is fibre-coupled, and the RF frequency is supplied from an external source. (b) Illustrative diagram of the lasers operation from [124]. Abbreviations: FP = Fabry Perot, TL = Tuneable Laser, µC = Micro-controller, and SG = Signal Generator, OSA = Optical Spectrum Analyser.

As with many telecoms lasers, this OFC device is designed to be set up and operated from a computer. The centre wavelength and comb spectral profile of the laser may be fine-tuned via the computer interface, by adjustments to the laser temperature and current of both LDs. Any external tunable RF source can be connected to the laser to allow it to generate a comb output. However, any noise attributed to the RF source will be transferred to the comb modes, reducing the phase coherence between the modes. For the purposes of this experiment, a Keysight RF synthesizer (N5183B MXG) is used to ensure low noise between the comb modes and a wide tuning range for f_{rep}.

The full OFC spectrum may be tuned by about ± 0.2 nm without destabilising the injection-lock, by controlling the OFC LD's current or temperature. However the individual mode frequencies can also be tuned by adjusting f_{rep}, enabling faster scan rates of an OFC mode, than the computer control over the OFC LD's current or

temperature allows. The OFC laser may also be operated with the RF source switched off. For initial characterisation, the fibre output of the OFC laser was connected directly to an optical spectrum analyser (HP86140A) with the RF source switched off, and compared with the RF source switched on as shown in Fig. 5.4.

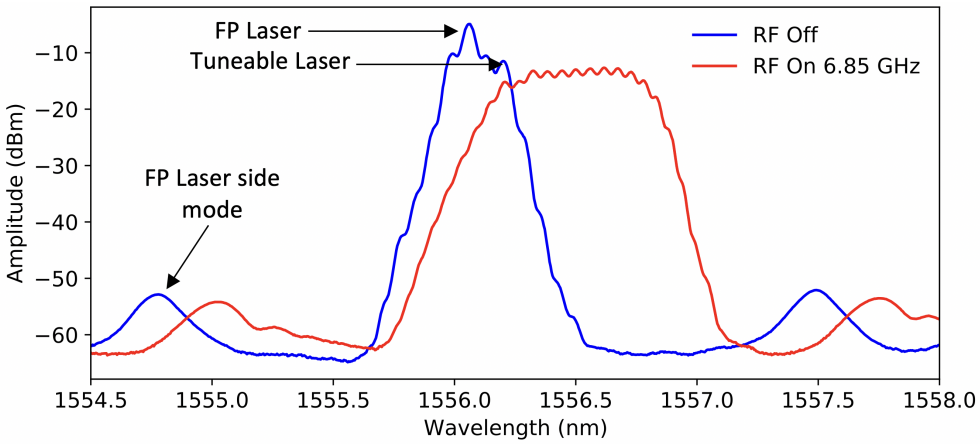

Figure 5.4: Comb Spectral profiles observed on an OSA, comparing RF input off and on. The spectral resolution of this OSA is about 9 GHz at 1556 nm, which is just enough to resolve the individual modes when f_{rep} is near 7 GHz. The centre frequency, f_c can be identified as the comb mode directly below the TL laser after the RF signal is switched on.

While the RF source is switched off, some degree of injection-locking of the FP laser to the TL laser wavelength can be observed over a narrow range, as the TL laser is tuned near the FP laser wavelength. In Fig. 5.4, we can see separate peaks for the output of both LDs. Once there is sufficient spectral overlap between the two LD frequencies, then the coupling for injection-locking may occur, and in Fig. 5.4, this only occurs after the RF source is switched on. The strength of attraction (pulling) of one laser to another nearby laser mode is dependent on both the spectral amplitude and the frequency offset of the pulling laser mode [125, 128]. The circulator, allows feedback to occur from the TL to the FP diode, but not the other way around.

The mode directly below the indicated TL laser peak is essentially the central mode, f_c of the comb spectrum, and can be identified as the mode of the OFC which does not shift when f_{rep} is adjusted up or down. In the case of this particular method for generating the comb spectrum, the majority of the generated modes lie to one side of the central mode. The one-sided characteristic of this OFC spectrum is attributed to the fact that only modes generated while the current is above threshold are emitted while the laser is being gain-switched above and below the threshold current. Suppressed side-modes of the FP laser can also be seen in Fig. 5.4 approx. 1.3 nm (160 GHz) either side of the FP laser peak (corresponding to the $\sim$ 0.3 mm FP laser cavity length [126]).

By adjusting the RF power to the laser it is possible to reduce or increase the spectral bandwidth, as shown in Fig. 5.5. At the maximum RF power which the

FP laser could handle (P_{RF} = 27 dBm) the spectral bandwidth (FWHM of full OFC profile) is approx. 0.57 nm (70 GHz). On the linear amplitude scale used in Fig. 5.5, the spectral flatness across the modes in the OFC bandwidth is clear to see. For the SHG characterisation and Rb TPT spectroscopy, the RF power was reduced from 27 dBm by 1-2 dBm, depending on the value of f_{rep}, so as to maintain a fixed bandwidth of 62 GHz. This had the added advantage of bringing the midpoint of the comb profile closer to the Rb TPT excitation wavelength of 1556.213 nm.

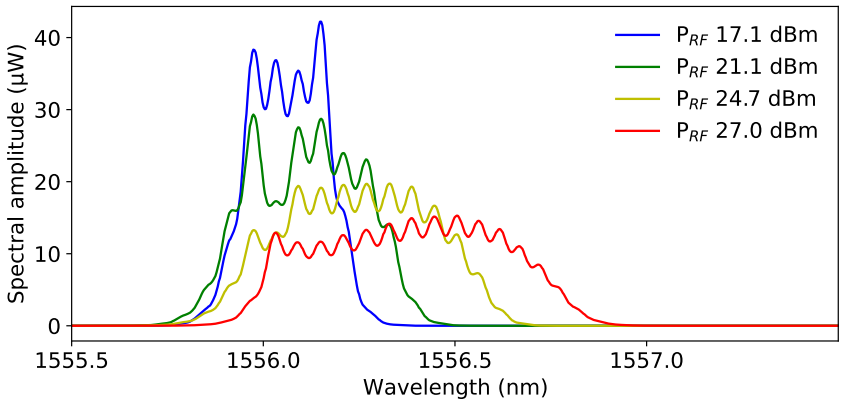

Figure 5.5: The spectrum of the OFC laser output with f_{rep} = 7 GHz is compared on the OSA, for increasing RF power levels. As the RF power increases, so does the spectral bandwidth.

5.3.2 OFC Pulse and Mode Stability

Ensuring low phase noise between the OFC modes is an important factor for this experiment. Excessive phase noise between the modes will lead to poor phase-matching for SFG in the PPLN crystal, hence reducing the effect of the OFC to provide an enhanced conversion efficiency. Low phase noise is also necessary to ensure coherent mixing of different modes to excite the Rb TPT. It is possible to assess the phase noise between the modes by directly measuring the optical pulse shape of the OFC output. In time-domain simulations of the comb pulses using Eq. 5.3 random phase offsets were applied to each mode of the comb to simulate phase noise. The simulations revealed measurable amounts of the pulse power ($>$ 10% of P_{peak} in this case) beginning to spread in to the region between the pulses for average phase noise levels above $\sim$ 200 mRads.

To measure individual pulses, the OFC laser was fibre-coupled to a 20 GHz bandwidth optical detector of a Wide-Bandwidth Oscilloscope (WBO) (Infiniium DCA Agilent 86100B). This has both optical and electrical inputs, allowing simultaneous measurement of the RF signal supplied to the OFC and the optical pulses from the output. A trigger from the RF source is required to observe the optical pulses on the WBO, so that it can build up a trace of the pulses from multiple sweeps across the time axis. If there is phase noise occurring in between the sweeps, then this will manifest as a

broadening of the pulses. For the pulse measurements, the spectral bandwidth of the OFC was kept constant at $\mathrm{BW}_{OFC} = 62 \pm 2$ GHz. From this parameter the pulse width can be calculated using the following relationship:

$$\Delta t_{pulse} = \frac{1}{BW_{OFC}} = \frac{t_{rep}}{N} \tag{5.6}$$

This leads to an estimated value for $\Delta t_{pulse} = 16.1 \pm 0.6$ ps. Unfortunately the optical detector response time is too slow to make accurate measurements of a pulse width on this scale, and may also lead to a corresponding reduction in amplitude of the pulses.

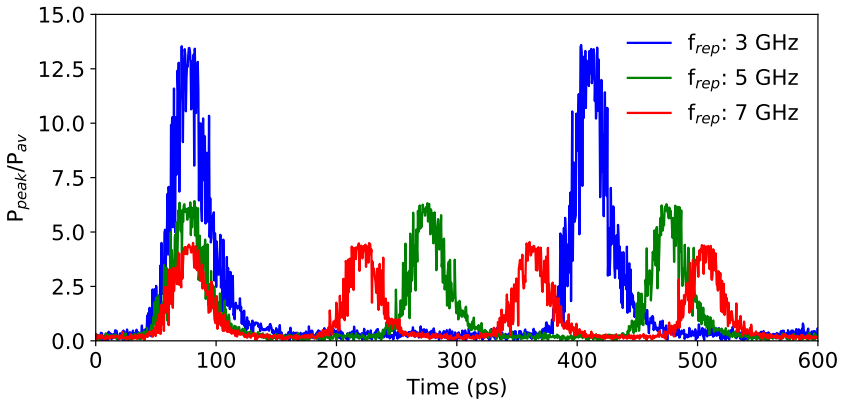

Figure 5.6: Direct measurement of OFC pulses on the WBO, with the amplitude normalised to the measured average optical input power. f_{rep} is adjusted to 3, 5 and 7 GHz, while maintaining a fixed spectral bandwidth of 62 ± 2 GHz. The pulse traces are the product of multiple sweeps across successive pulses. Noise on the edges of the pulse profile represent the average noise between pulses as the data of successive sweeps are overlapped.

In Fig. 5.6, the amplitude of the pulses is plotted as a ratio of the pulse power over the average measured power. Comparing the pulses at several different values of f_{rep} confirms that the pulse amplitude increases proportionally to the number of modes within the OFC bandwidth. The absence of noise underneath the profile of each pulse is a good indication of low phase noise between the pulses themselves, and hence low noise between the modes. The pulses can be seen to increase in amplitude and decrease in their duty cycle as f_{rep} is adjusted from 7 to 3 GHz. The increased pulse amplitude is a result of more modes fitting within the spectral bandwidth at lower f_{rep}. The measured pulse width from the data is $\simeq 30 \pm 3$ ps for all 3 values of f_{rep} that were measured, with the pulse peak amplitude reduced by roughly the same amount as the pulsed broadening. Such characteristics are indicative of the limitations of the detectors response time.

To confirm that the phase noise between the comb modes was not significant, we can measure the linewidth of the RF beat notes formed as the OFC modes interfere

with one another. This produces an optical beat note at f_{rep}, $2\times f_{rep}$, $3\times f_{rep}$ ... etc. The linewidth of the beat notes indicates the magnitude of phase noise between the modes, as documented in an earlier journal publication on the OFC laser [126]. In the publications documenting the OFC laser, the RF beat note measurements yield FWHM linewidths of < 10 Hz, limited by the measurement device resolution. Our measurements while using the OFC demonstrate equally narrow linewidths for both of the beat notes at f_{rep} and $2\times f_{rep}$, as shown in Fig. 5.7. Detection of higher harmonics of the f_{rep} beat note indicate that modes separated by $\Delta N > \pm 1$ are also coherent with one another. Higher beat notes than $2\times f_{rep}$ were beyond the measurement bandwidth of the spectrum analyser.

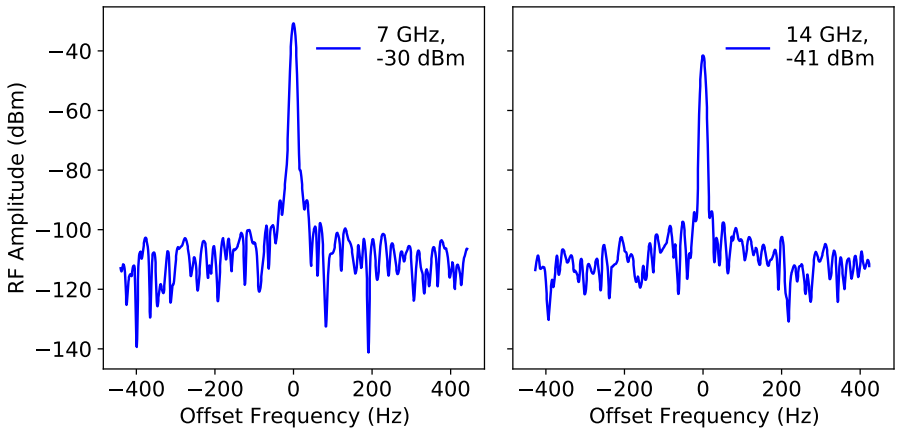

Figure 5.7: RF spectrum traces (∼10 Hz resolution bandwidth) of the OFC mode beat notes while f_{rep} = 7 GHz. The measured FWHM linewidth of the RF beat notes at f_{rep} and $2\times f_{rep}$ is equivalent to the measurement resolution, confirming the noise is at least below 10 Hz.

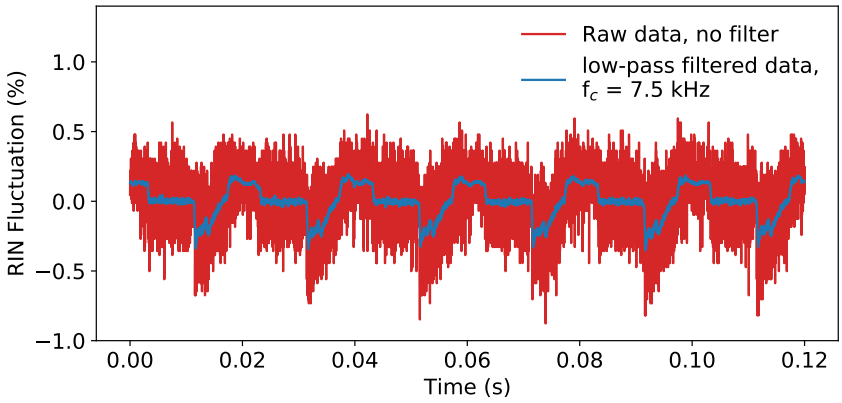

Figure 5.8: The relative optical intensity noise (RIN) of the OFC output recorded on a photodiode. The RMS noise is < 0.2 %, which is within acceptable levels. A Low-pass filter is applied to the RIN data (cut-off frequency, f_c = 7.5 kHz), revealing oscillations with a 0.02 s period (50 Hz), likely corresponding to some AC to DC filtering, or another kind of electrical noise.

Last of all, a measurement of the RIN (relative intensity noise) fluctuations was

taken to make sure there were no drifts in the OFC output power. Long-term intensity fluctuations were observed to be negligible ($< 0.2\%$ RMS), however the measurement picked up some periodic short-term fluctuations, which are shown in Fig. 5.8. The short-term noise shows repeating oscillations with a period of approx. 0.02 s (50 Hz) which may be attributed to incomplete AC-DC filtering of mains electrical power sources. By applying a moving average type low-pass filter to the RIN data, it is possible to resolve more detail of the periodic fluctuations, but the signal shape doesn't match any source we could identify.

5.4 Frequency-Doubled OFC Characterisation

Considering that an OFC laser produces pulses with a peak intensity of N times higher than its average power, one might expect the non-linear, I^2 dependence of the frequency-doubling conversion efficiency to lead to an enhancement factor of N^2 over a CW pump laser. However, the presence of the extra modes in the pump spectrum gives rise to SFG (sum frequency generation) as well as SHG conversion. SFG conversion generates twice the number of modes in the SH spectrum compared with the pump spectrum, leading to a wider spectral bandwidth and hence reduces the pulse width. When we account for the duty cycle ($\propto N$) and compare the average SH output power from an OFC laser with that of a CW laser we should have an overall enhancement factor of N x η_{SH} (%/W). Through characterisation of the SH OFC we will determine in this section if we can achieve such a level of enhancement.

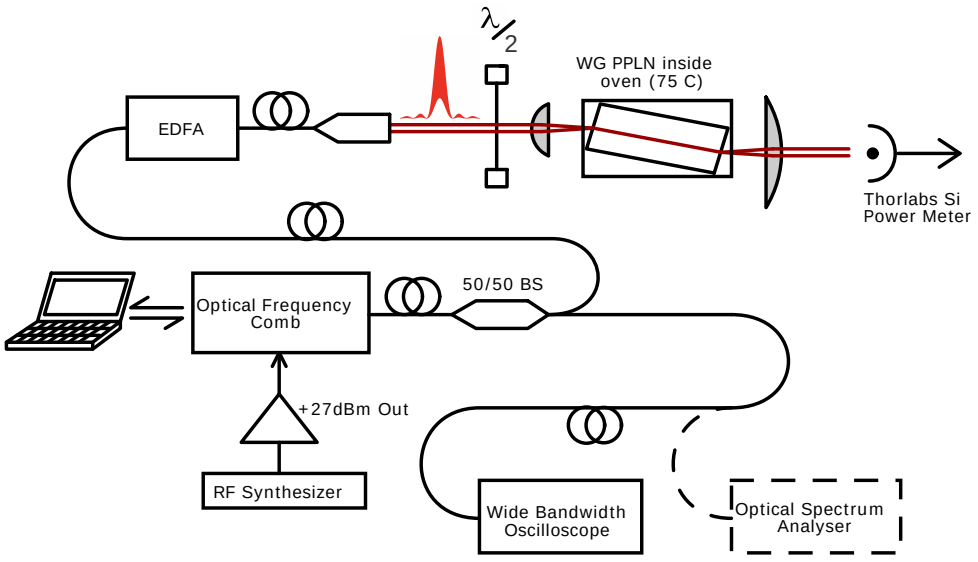

Figure 5.9: Diagram of apparatus used for characterisation of the SHG conversion of the OFC. A fibre-coupled 50/50 beam splitter (BS) allows continuous measurement of the spectral and temporal profile of the OFC output, before amplification through the EDFA (Erbium-Doped Fibre Amplifier).

The OFC laser was fibre-coupled to the PPLN stage that was previously used for the CW laser, in order to generate the 778 nm 2nd harmonic of the OFC which would be required for spectroscopy of the Rb TPT. As shown in Fig. 5.9, the fibre-coupled OFC laser output is first of all split, allowing the OFC spectral profile and pulse shape to be easily monitored, while the rest of the OFC output is amplified through the EDFA before being fibre-coupled to the PPLN stage.

5.4.1 Measurement of OFC Second Harmonic Conversion Efficiency

To confirm that the enhancement factor to η_{SH} is dependent on the number of modes within the comb bandwidth, we vary f_{rep} to change the number of modes which fit inside the bandwidth. However the gain of the RF amplifier in between the RF synthesizer and the OFC varies across the f_{rep} range of 3-8 GHz. This means that the OFC laser diode parameters and the RF power had to be adjusted for each value of f_{rep} to maintain a constant spectral amplitude, bandwidth and midpoint of the OFC spectrum. Besides this, the OFC laser parameters are tuned to ensure the midpoint of the comb spectrum is at the Rb TPT reference frequency while keeping the internal tuneable and FP lasers tightly injection-locked (to yield the best possible uniformity across the comb modes). The resulting spectral profiles for each value of f_{rep} are shown in Fig. 5.10.

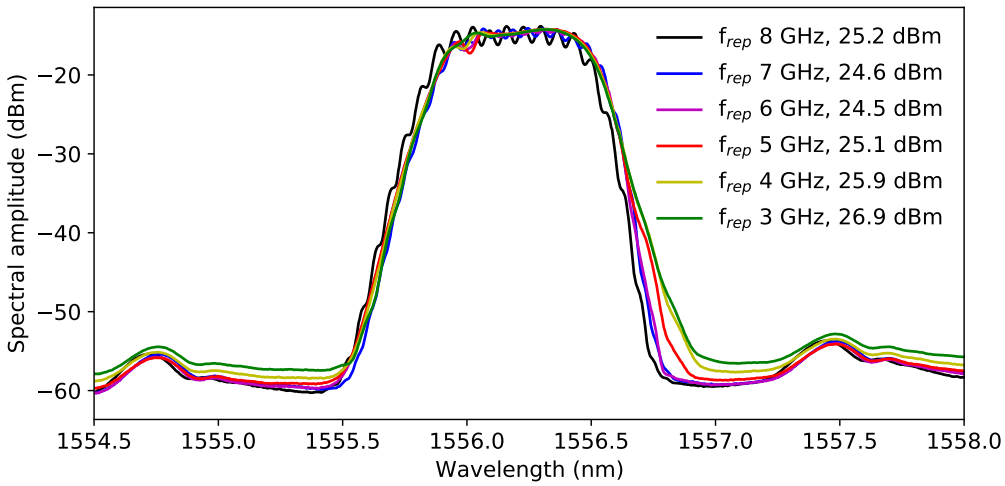

Figure 5.10: Spectral profiles of the OFC output for each f_{rep} value used in SHG characterisation, acquired using an OSA. The closely overlapping spectral profiles demonstrate that the spectral bandwidth (∼ 62 GHz), comb midpoint of 1556.213 nm, and spectral amplitude remain constant as f_{rep} changes.

The comb laser was then amplified through the EDFA to a power level of 50 mW. The PPLN temperature was adjusted (± 0.1 °C) for each measurement in order to achieve the maximum conversion efficiency. The conversion efficiency was measured using the average power detected at 778 nm by a Thorlabs power meter (S130C), directly after the PPLN output. The power meter is insensitive to light at 1556 nm,

preventing any transmitted pump power from contributing to the measurement. In Fig. 5.11 we demonstrate the effect of using higher values of f_{rep} and hence larger N to increase the conversion efficiency, while the average pump power remains constant at 50 mW.

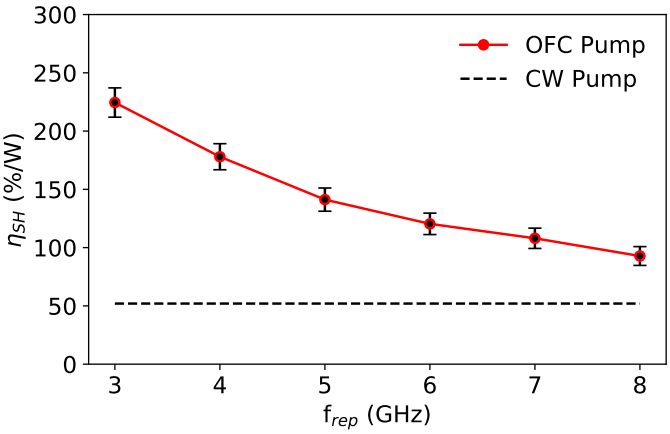

Figure 5.11: OFC conversion efficiency to the second harmonic as a function of f_{rep}. A pump power of 50 ± 1 mW is used for both CW and OFC measurements, which in the CW case yields 52%/W (dashed line). Errors are calculated based on ± 1 mW pump and ± 0.1 mW SH power measurement errors, yielding an error of ±5.3%/W × $\sqrt{P_{SH}}$.

The results in Fig. 5.11 demonstrate an enhanced SH conversion efficiency for the OFC beyond that of the CW laser (52%/W), but not as much as N × 52%/W. For example, at f_{rep} = 8 GHz, N = 8 ± 1, and theoretically 416 %/W should be attainable. In practice, we only achieve 93%/W, and the highest conversion efficiency recorded, using f_{rep} = 3 GHz was 224 ± 12 %/W, where in theory, 1040 %/W should be possible (based on N = 20). Across the whole range of f_{rep}, the measured conversion efficiency is only about 20% of the predicted conversion efficiency.

It will be necessary to generate higher levels of optical power at 778 nm for spectroscopy, therefore the conversion efficiency is characterised as a function of pump power in Fig. 5.12. As the pump power is increased, the higher conversion efficiency of the OFC will cause the absolute conversion efficiency (P_{SH}/P_{pump}) to be subject to pump depletion at a faster rate. This trait is most easily seen in the 0 - 300 mW range of Fig. 5.12. The advantage of the OFC is clearly much more obvious at lower pump powers.

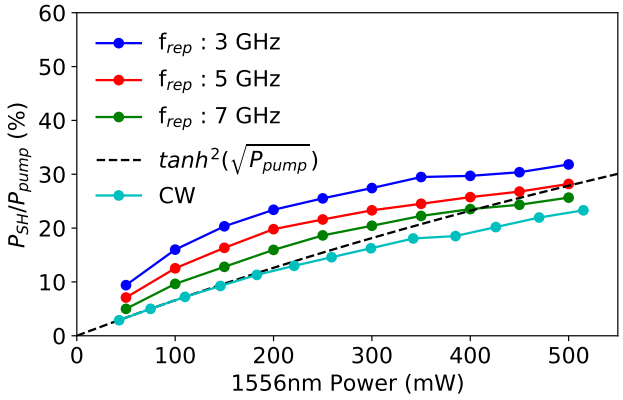

Figure 5.12: Absolute conversion efficiency Vs average pump power of the OFC for several values of f_{rep}. Compared with the CW measurements, pump depletion causes the OFC curves to plateau sooner owing to the higher conversion efficiencies. The dashed line of the pump depletion model is fitted to the CW data.

5.4.2 Measurement of OFC Second Harmonic Spectrum and Pulses

To investigate the cause for reduced SH conversion efficiency, measurements of the spectral and temporal properties of the OFC SH output at 778 nm were taken. First of all, the spectral bandwidth of the OFC SH is measured on the OSA and determine the number of modes in the SH spectrum. Then the SH pulses were recorded on the WBO to check if they are clean and have a pulse width corresponding to the measured bandwidth. Spectra obtained on the OSA for the 778 nm OFC SH at f_{rep} = 3 and 7 GHz are shown in Fig. 5.13.

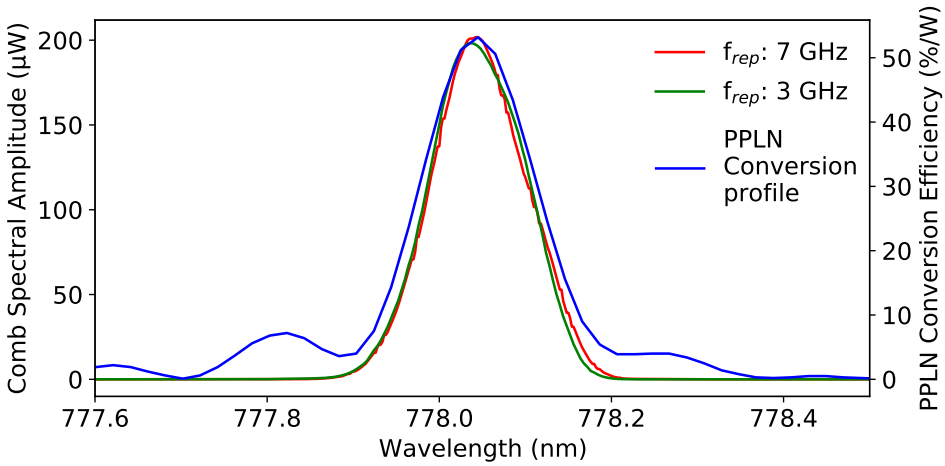

Figure 5.13: OSA spectrum of the OFC SH profiles using f_{rep} = 3 and 7 GHz. When compared with the FWHM of the measured PPLN phase-matching bandwidth from Fig. 4.8a, both the shape and width of the OFC SH profiles appear quite similar.

The spectral bandwidth of the OFC SH, measured from Fig. 5.13 is 66 ± 2 GHz

at 778 nm, and has changed its profile to reflect that of the phase-matching profile. The SH spectral bandwidth measures about the same bandwidth as the pump bandwidth, however as mentioned earlier, the bandwidth should be double, and this aspect implies that the pump comb was only 33 GHz wide. Indeed, 33 GHz is quite close to the acceptance bandwidth of this PPLN, which is 37 ± 2 GHz from previous measurements. This behaviour indicates that frequency-doubling of pump modes outside the PPLN phase-matching bandwidth is not occurring. The PPLN conversion bandwidth increases inversely proportionally to the PPLN length. This aspect of the OFC conversion process was unfortunately not considered when purchasing the PPLN crystal, which was initially to be used with a CW laser.

Next, the SH pulses were measured to ensure that the 778 nm pulses were still clean. To measure the 778 nm SH pulses it was not possible to use the internal optical detector of the WBO, and instead a fibre-coupled, ultra-fast photodetector with a DC-30 GHz bandwidth at 778 nm (Thorlabs DXM30AF) was used. The signal output from the photodetector was then recorded on to a 50 GHz bandwidth electrical input to the WBO to observe the pulses shown in Fig. 5.14.

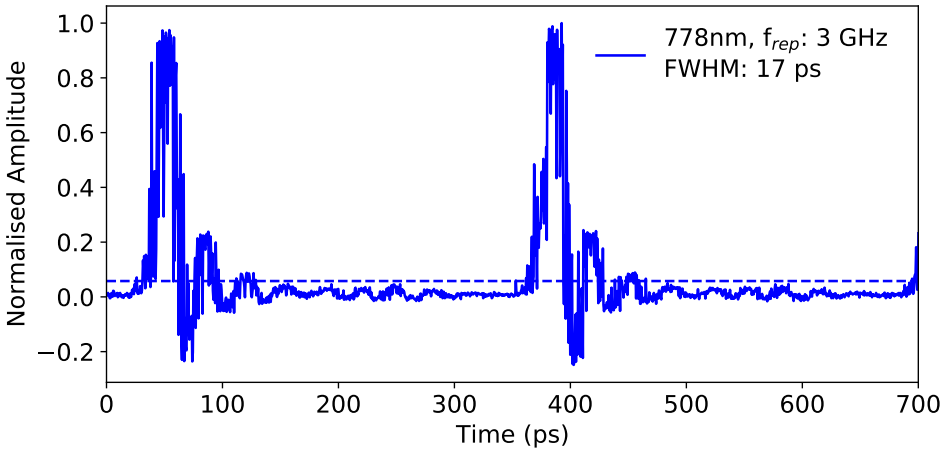

Figure 5.14: Pulse measurement using Thorlabs DXM30AF, 26 GHz BW photodetector for the 2nd harmonic of the OFC laser. The dashed line indicates the average power level of the OFC 2nd harmonic, relative to the peak power, yielding a P_{peak}/P_{av} ratio of 17.

The OFC SH pulses at 778 nm appear just as clean as the measurement of the 1556 nm pulses, indicating a low level of phase noise between the modes. There is a rippling effect after each of the pulses, giving rise to negative fluctuations in the signal. This is an artefact of the detectors limited response time to a quick change in power. The FWHM of the main peak, before any ripples, is taken to be the real FWHM of the pulse. The FWHM of the 778 nm pulses measures 17 ± 0.4 ps, which is within a few ps of the 15.2 ps FWHM expected for 66 GHz bandwidth, and may still be limited by the response time of the detector. This is a good sign that there is little to no phase noise or phase offset between the modes of the OFC SH. The P_{peak}/P_{av} ratio for the

778 nm pulses yields a value of 17, when we expect the ratio to be around 22 (based on how many 3 GHz modes can fit in the 66 GHz bandwidth). The first reason for the P_{peak}/P_{av} ratio measuring lower than expected, is likely because all of the modes are assumed to be the same amplitude. However, this is clearly no longer the case after the bandwidth-limited conversion. The second reason may be due to the pulse occurring close to the response limits of the detector.

For now, the spectral bandwidth measurements from the OSA are a more direct estimate of the OFC SH bandwidth, and can also be used to estimate how many modes are fitting within the limited phase-matching bandwidth of the PPLN. Before moving on to use the 778 nm SH OFC for spectroscopy, the next section aims to estimate the OFC laser SH conversion efficiency under the conditions where the pump OFC bandwidth is wider than the phase-matching bandwidth of the PPLN. Considering that the OFC second harmonic is generated through a combination of SHG and SFG, this is not quite so simple to estimate based on just the number of modes that fit within the PPLN bandwidth.

5.5 Conversion-Bandwidth Limited Frequency-Doubling Using an OFC

To build a model of the limited PPLN conversion efficiency using an OFC of a wider spectral bandwidth (BW_{OFC}) than the PPLN phase-matching bandwidth (BW_{PM}), let us first look at how the SH spectrum of the OFC would appear under ideal conditions. The second harmonic conversion process is proportional to the product of two identical electric fields, which in the case of an OFC, yields the second harmonic electric field of the form:

$$E_{SH-OFC}(t) \propto E_0^2 \sum_{m=-(N-1)/2}^{(N-1)/2} e^{i2\pi(f_c+mf_{rep})t} \times \sum_{m=-(N-1)/2}^{(N-1)/2} e^{i2\pi(f_c+mf_{rep})t} \tag{5.7}$$

The multiplication of the two fields results in the interaction of all modes with each other. Each of the modes can undergo SHG to create a spectrum of modes with 2x f_{rep} spacing, but additionally they can undergo SFG, leading to modes with f_{rep} spacing in the resulting spectrum. Due to there being more ways for modes to interact to form the second harmonic through SFG, than through SHG, the SFG process contributes more to the spectral power at each resulting mode. Let us now compare the pulses and resulting spectrum of the pump and second harmonic assuming 100% conversion efficiency. Fig. 5.15 shows a simulation for a pump OFC of N = 5, f_{rep} = 5 GHz, and an average pump power of 5 mW, which is then compared to its second harmonic.

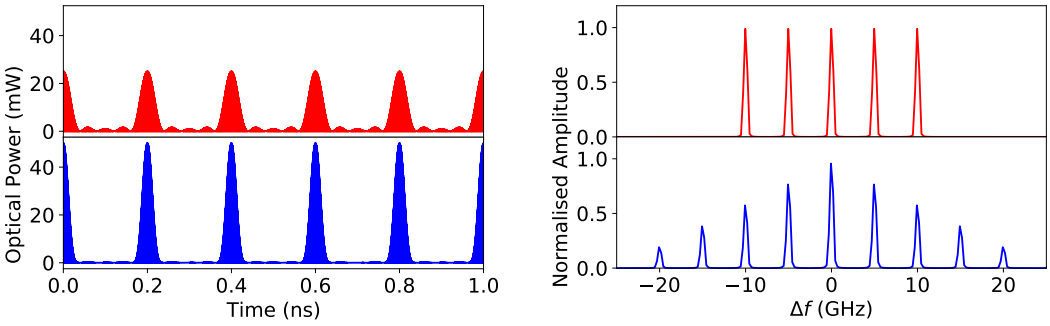

(a) *(b)*

Figure 5.15: (a) Eqs. 5.3 and 5.7 are used to simulate the pulses of an OFC (red) and its second harmonic (blue) using N = 5, equal amplitude modes, with f_{rep} = 5 GHz, and an average pump power of 5 mW (b) Shows the FFT of the simulated SH OFC pulses. The pyramidal distribution comes as a result of different modes combining through SFG, for which the central SH mode has the largest number of possible mode combinations (equal to N), and hence the largest amplitude.

The resulting spectrum of the SH OFC in Fig. 5.15 demonstrates that the relative amplitude of the OFC modes now lie in a pyramidal distribution around the central mode of the comb. There are now 2N-1 total modes in the spectrum, and the outermost modes are 1/N x the amplitude of the central mode. Each pair of modes closer to the centre has a relative amplitude of (N-$|m|$)/N, with m corresponding to the modes of the SH OFC. Arising from the increase in the number of modes from N to 2N-1, the SH OFC pulses have $\sim$ 2x P_{peak}/P_{av} compared to the pump OFC, as seen in the time domain graph of Fig. 5.15a. However, the pulse repetition rate remains the same, as well as the average power of the OFC in this particular simulation. A similar approach to modelling the resulting SH electric field is taken in a study by D. Wei et. al [129]. They also note the presence of low frequency E-field components including the beat notes between all of the modes, which we observe in our simulation, and which is also measured when the OFC laser is coupled to a fast photodetector (see Fig. 5.7).

In reality, frequency-doubling is not 100% efficient, owing to the material properties of the conversion crystal, and also due to imperfect phase-matching of the pump field. When the pump laser has a wide spectrum of modes at differing frequencies, only one mode at a time may be perfectly phase-matched. The rest of the modes will suffer from dispersion within the crystal and slip out of phase with each other as they propagate, leading to a lower conversion efficiency. As mentioned earlier in section 4.2.2, SHG is a simplified case of SFG and conversion efficiencies for both processes may be derived from the same coupled amplitude equation (Eq. 4.3). Following from this, the PPLN phase-mismatch term (Δk_{PPLN}) is exactly the same when converting to an SFG mode as if it were to result from SHG involving two equal modes combining to form the resulting SFG mode. To reduce the complexity of implementing a model of the OFC SH conversion efficiency, a summation over all possible SH modes is implemented, each with a weighted conversion efficiency proportional to the number of SFG interactions

which may form the SH mode. Hence the calculation for the SH intensity of the full pump OFC spectrum is:

$$I_{SH-OFC} = \sum_{m=-N}^{N} \left[\frac{N - |m|}{N} \times I_{SH}(f_c + m\frac{f_{rep}}{2}) \right] \tag{5.8}$$

To implement the model we assume the OFC has a flat spectral profile resembling the one shown in Fig. 5.15b, and the average optical power of the OFC is split equally between the modes within the spectral bandwidth: $P_m = P_{av}/N$. The model assumes that the middle mode of the pump OFC is aligned with the peak phase-matching frequency of the PPLN, with an equal number of modes either side. The next step is to determine N for the pump OFC based on the measured spectral bandwidth and f_{rep}. Using these parameters of the pump OFC, the frequency of all resulting 2N-1 second harmonic modes may be determined, and we can then simply calculate the individual SHG conversion efficiency (applying Eq. 4.10) from a corresponding set of pump modes. To factor in the effects of SFG, the pump intensity for Eq. 4.10 is set equal to the sum of the intensity of all of the real modes (totalling P_{av} instead of P_m). This is entirely true for the central mode of the pump OFC, because there are N ways which the OFC modes may combine to generate the central mode SH. However, before the summation of the resulting series of intensities for each mode, we account for the reduced number of SFG interactions forming each mode further away from the middle mode by applying the weighting factor of $(N - |m|)/N$ corresponding to each mode, m.

To match this model to the characterisation data, we calculate Eq. 5.8 for a range of values of f_{rep}, and then convert the result to η_{SH} (%/W) to compare with the data presented in Fig. 5.11. The measured spectral bandwidth of 62 GHz at 1556 nm is used. N is calculated as the closest odd number to the spectral bandwidth divided by f_{rep}. The average pump power of the OFC is set to P_{av} = 50 mW. The intensity is calculated for a $1/e^2$ radius of 4.5 μm while the beam is coupled to the waveguide with a 70% coupling efficiency. We then use the same non-linear coefficient multiplied by a 0.45 fitting factor, as used in Fig. 4.8a to fit the CW pump wavelength scan data to a model of the PPLN conversion efficiency. The centre frequency, f_c is chosen to be 192.642283 THz, and is assumed to be at the centre of the comb, leaving an equal number of modes either side. This frequency is then assumed to be perfectly phase-matched to the PPLN.

Fig. 5.16 demonstrates that the model follows the trends of the measured values of η_{SH} for the OFC ($<$ 30% of η_{SH} error across all data). The error between the model and measured η_{SH} for the OFC increases from $\sim$ 22% toward 30% as f_{rep} is decreased. This error is partly down to the assumption that the OFC spectrum is perfectly flat, when there is really a variation in amplitude between the modes, and some additional power in modes outside the bandwidth which are not accounted for.

The model is primarily aimed at demonstrating the OFC conversion efficiency trends as f_{rep} is adjusted, and it performs well in this respect.

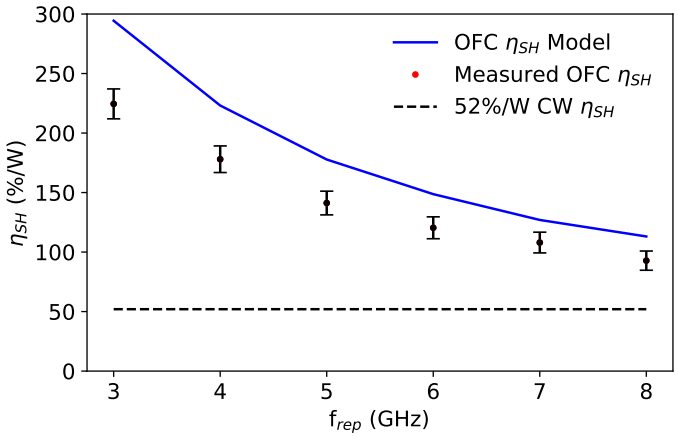

Figure 5.16: OFC SH conversion efficiency as a function of f_{rep}, comparing measured data with the modelled behaviour, using Eq 5.8 and P_{av} = 50 mW.

Matching the model to the data is only half the battle of making sure this approach is valid. To improve the confidence in the model, we ensure that it meets several test conditions. The first is that $\eta_{SH} = 52$ %/W when only one mode fits within the PPLN conversion bandwidth. Secondly, that the conversion efficiency rises to a maximum of N× 52 %/W when all OFC modes fit within the conversion bandwidth. Third, that increasing the OFC spectral bandwidth >> 62 GHz, while f_{rep} is constant, and hence allowing more modes to be present outside the PPLN phase-matching bandwidth does not affect the calculated η_{SH} for the OFC.

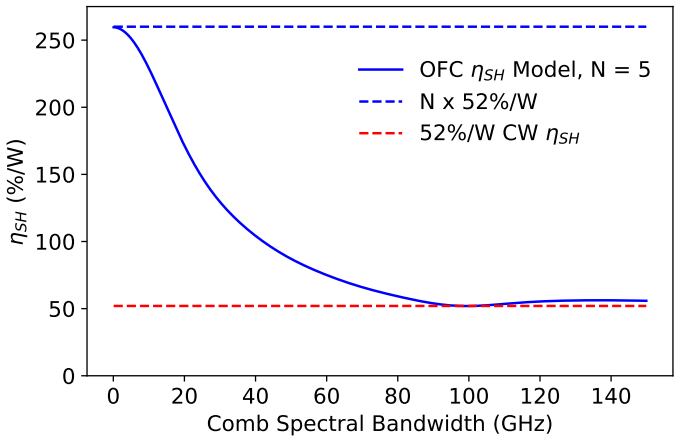

Figure 5.17: Modelled OFC SH conversion efficiency (using Eq. 5.8) as a function of comb spectral bandwidth. The mode number is fixed at N = 5, and are equally spaced across the OFC bandwidth as it changes.

In Fig. 5.17 we show the model being tested to these limits, by creating an OFC

with a fixed mode number of N = 5, and then varying the OFC spectral bandwidth and hence f_{rep} so that the modes are always equally spaced across the OFC bandwidth. It is worth noting from Fig. 5.17 that no matter how far apart the modes either side of the mode which is phase-matched to the PPLN become, they all still contribute to the SFG process with perfect phase-matching.

In the case of the PPLN used here, the PPLN phase-matching bandwidth, BW_{PM} is about 0.3 nm /38 GHz at 1556 nm, which is quite narrow due to the 40 mm crystal length. Decreasing the crystal length, L provides a larger BW_{PM}, owing to the presence of L in the $sinc^2$ term of Eq. 4.10. However, the conversion efficiency is also proportional to L^2, rapidly lowering the conversion efficiency as we decrease L. In Fig. 5.18, we compare our model for η_{SH} while varying the PPLN crystal length. The plot gives an indication of how much shorter the crystal would have be to accommodate an OFC with $BW_{OFC} = 66$ GHz while providing the maximum enhancement factor over a CW laser. We find that the enhancement factor begins to drop below 95% of its maximum after L = 4 mm ($BW_{PM} \simeq 338$ GHz). However, if the maximum conversion efficiency takes priority over maintaining or extending BW_{OFC}, then there is still a clear benefit to the conversion efficiency at longer L.

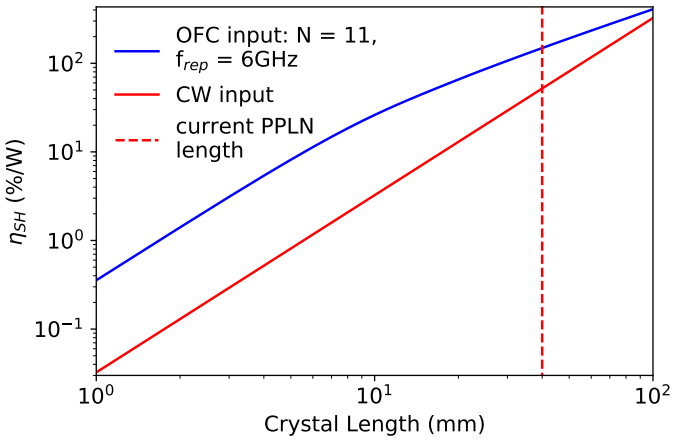

Figure 5.18: The PPLN conversion efficiency is modelled as a function of the crystal length, using Eq. 5.8, demonstrating the length range (0 - 4 mm), where an OFC of $BW_{OFC} = 66$ GHz demonstrate the highest enhancement above a CW input. At 1 mm, $BW_{PM} \simeq 1.35$ THz, which reduces to $\simeq 135$ GHz for a length of 10 mm.

The results from this section provide enough confidence that η_{SH} of this particular OFC cannot be pushed much higher. The model has provided a useful method for determining the SH conversion efficiency of an OFC under non-ideal conditions. We are unaware of any other study at present that compares modelled and experimental data for the SH conversion efficiency of an OFC over a wide range of values of N. This has been made possible by the OFCs widely tuneable f_{rep}.

5.6 Rb TPT Spectroscopy with an OFC Laser

Besides the absorption of two equal photons from a single resonant mode, the excited $5D_{5/2}$ state of the Rb TPT can be reached via the interaction of any two OFC modes which are oppositely detuned from resonance, in a similar process to SFG in the PPLN. This increases the probability of excitation beyond that of a single mode which is directly on resonance with the Rb TPT. However, since the average power of the laser is divided between all of the OFC modes, the TPT excitation rate is equivalent to the CW excitation rate, once the modes combine. Unfortunately the Rb TPT does not benefit from the same enhancement factor available for the frequency-doubling process. This is because the transitions narrow natural linewidth of 334 kHz prevents the widely GHz-range spaced modes of this OFC to be simultaneously resonant (the TPT linewidth is analogous to the 36 GHz-wide PPLN bandwidth). As discussed in [67, 110], the maximum excitation rate will only occur while the modes of the OFC are perfectly coherent with each other. Measurements of the 778 nm SH OFC pulses confirm the resulting phase stability is not measurably impacted by the limited phase-matching bandwidth of the PPLN.

When the Rb TPT is excited through the sum of two oppositely-detuned counter-propagating OFC modes, the Doppler-shift will no longer fully cancel out. This issue is first discussed in [110], and one can easily derive an approximation of the laser bandwidth-related broadening (Δf_{LBW}, based on the frequency difference between two modes at either side of the FWHM of the OFC bandwidth, from Eq. 2.2:

$$\Delta f_{LBW} = v_p \times \frac{{BW_{OFC}}^2}{c} \tag{5.9}$$

Where, v_p is the most probable velocity of the thermal atoms (in this case 100°C) and c is the speed of light in vacuum. In the case of the 778 nm OFC used here, BW_{OFC} $\simeq$ 62 GHz, and this yields a value of $\Delta \mathrm{f}_{LBW}$ = 55 kHz, which is relatively small compared with the natural linewidth. However for a wide-bandwidth OFC required to simultaneously excite the Rb TPT step-wise (780nm + 760 nm) and at 778 nm, the bandwidth at 778 nm must be at least 2 THz, leading to $\Delta \mathrm{f}_{LBW}$ = 1.8 MHz. Such a broadening of over 5x the natural linewidth outweighs the enhancement of the 2-3x higher excitation rate which is achievable by enabling step-wise excitation [112], without additionally cooling the atoms in a MOT.

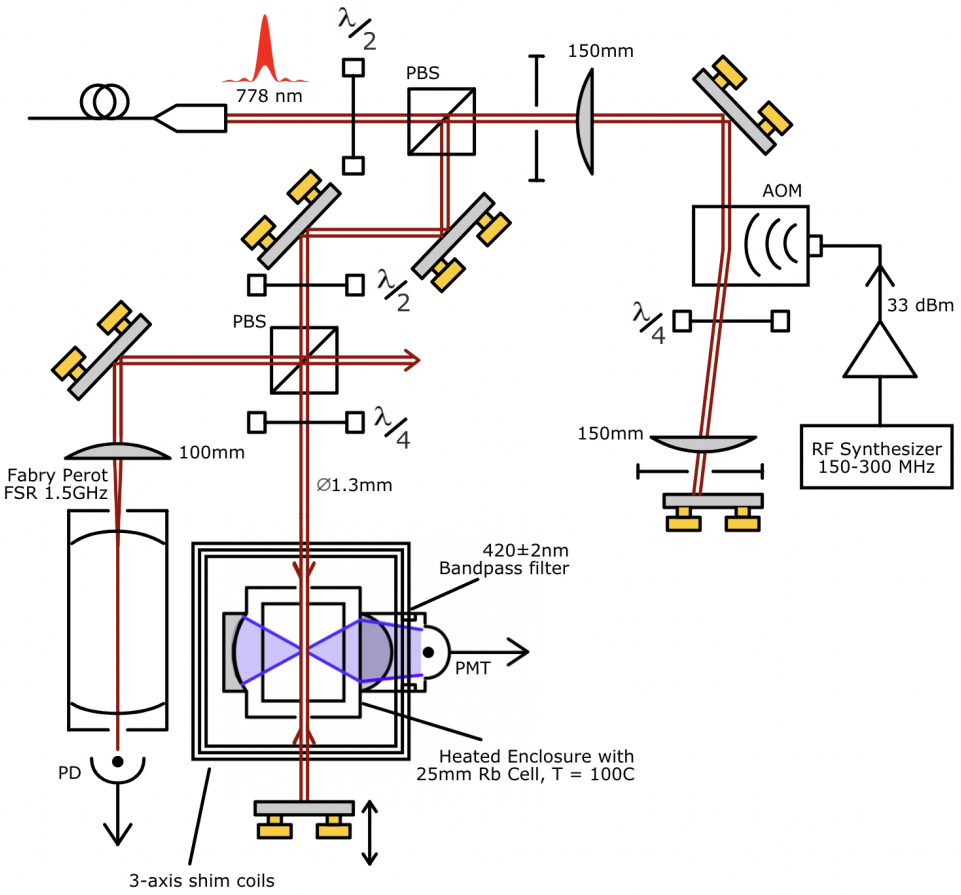

Figure 5.19: Rb TPT Spectroscopy apparatus used for measuring the fluorescence signal from the Rb TPT using the OFC laser. The apparatus features: a double-pass AOM to allow fine-resolution scans of the entire OFC spectrum, a Fabry-Perot to enable fine resolution (∼ 7 MHz) of the SH OFC spectrum, and the magnetically shielded, Doppler-free Rb TPT spectroscopy apparatus.

The apparatus used for the OFC-pumped Rb TPT signal characterisation is shown in Fig. 5.19. Following the narrow-linewidth measurements of the Rb TPT (< 500 kHz) using the Ti:Sapphire laser in Section 3.3, the same apparatus and conditions were set up to ensure minimal broadening of the TPT signal. This includes the cancellation of the local magnetic field, and avoiding focusing the pump beam in to the Rb cell. The beam is set to a 0.65 mm $1/e^2$ radius, ensuring transit-time broadening is no more than 109 kHz. However, this OFC laser is quoted with an intrinsic linewidth of $\sim$ 300 kHz, limiting the minimum measurable linewidth to $\sim$ 750 kHz, depending on the actual linewidth of the laser.

It is possible to scan the OFC modes across the TPT resonance by applying a small FM modulation to f_{rep}. However, in this case, the control over f_{rep} was not fine enough to properly resolve the hyperfine transition profiles, and so the double-pass AOM in the spectroscopy apparatus was used to allow finer, and more stable scanning of the OFC frequency.

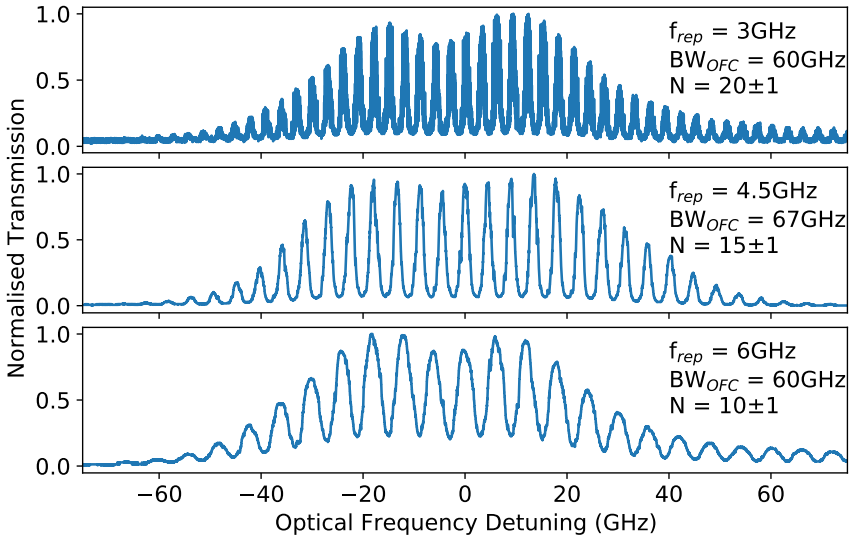

Figure 5.20: Spectral profiles of the 778 nm SH OFC, measured using a scanning Fabry-Perot. The frequency axis for each data set is approximately calibrated using the f_{rep} spacing of the modes in each profile.

The Fabry-Perot was used to check exactly how many modes there are in the 778 nm SH OFC spectrum, and also to check that laser frequency is scanning continuously. The Thorlabs SA200 scanning Fabry-Perot achieves a 7 MHz FWHM spectral resolution, enabling one to resolve the individual modes at f_{rep} = 3 GHz, which was not possible before. The FSR of the Fabry-Perot is 1.5 GHz wide, which only continuously covers a small range of the full OFC spectrum. However, all modes present within the OFC will show up on a single scan of the FSR (which is really scanning the whole laser spectrum simultaneously in overlapping 1.5 GHz sections), but it can be difficult to tell which mode is which. To make it easier to observe the modes in the correct order, f_{rep} is set to be equal to, or a multiple of the FSR of the cavity, causing all of the modes to appear at the same point in the scan range. By then applying a small detuning of f_{rep} from the multiple of the FSR, the modes cease to overlap and become separated in the Fabry-Perot spectrum by the value of the detuning, while retaining their original spectral order. This measurement allows for us to calculate the spectral bandwidth of the 778 nm OFC by counting the number of modes. Due to the constraint of maintaining f_{rep} as a multiple of the FSR, OFC spectra with f_{rep} of 3, 4.5 and 6 GHz were chosen to compare the Rb TPT signal against. The resulting SH OFC profiles measured with the Fabry-Perot are shown in Fig. 5.20.

One significant difference between CW and pulsed Doppler-free spectroscopy, which is discussed briefly in previous work on frequency comb TPT spectroscopy [69, 70], is the overlapping of the pulses within the Rb cell. In order to maximise the signal strength, the optical path distance to the retro-reflecting mirror on the other side of

the Rb cell was adjusted to ensure that the comb laser pulses were overlapping at the middle of the Rb cell as shown in Fig. 5.21a. Due to the relationship of the distance between optical pulses (D_{pulse}) with f_{rep}, the mirror position had to be changed for each value of f_{rep} used. At f_{rep} = 6 GHz, $D_{pulse} \simeq$ 50 mm. The measurement in Fig. 5.21b, demonstrates the Rb TPT fluorescence signal ranging between minimum and maximum, and returning to exactly the same level after extending optical path of the pulses by 50 mm.

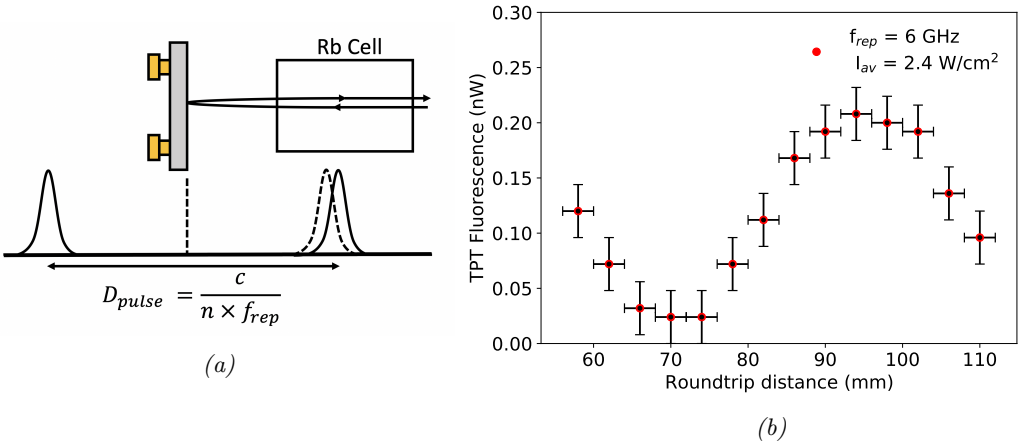

Figure 5.21: (a) Illustration of the relationship between f_{rep} and the optical path distance between pulses (D_{pulse}). The position of the mirror is adjusted to change the overlap of the pulses within the Rb cell. (b) Fluorescence signal as a function of the roundtrip distance from the midpoint of the Rb cell to the mirror. The error bars correspond to peak-to-peak background noise of the signal, and to ± 2 mm accuracy for adjusting the roundtrip distance.

After, setting the mirror position to generate the strongest signal, alignment of the counter-propagating beams was fine-tuned, and the magnetic field compensation adjusted to increase the signal amplitude further. The resulting Rb TPT signal obtained while using OFCs of f_{rep} = 3, 4.5 and 6 GHz are shown in Fig. 5.22. To obtain the signal, a mode at the midpoint of the OFC spectrum is tuned to resonance with the Rb TPT, so that there is a symmetrical distribution of modes either side of the directly resonant mode, and then the AOM is used to scan the OFC spectrum with a 9 Hz sawtooth signal. The average intensity, I_{778}o of the counter-propagating beams has been set to $\sim$ 2.4 W/cm^2 so that the Rb TPT signal amplitude can be directly compared with data obtained in Fig. 3.15 using the Ti:Sapphire laser. The only condition for the Rb TPT excitation that has changed being that I_{778} is now split among 10 - 20 modes which must combine with opposite detuning to excite the transition. We expect signal strength from the Rb TPT will remain constant while changing N, so long as the average intensity of the OFC remains constant.

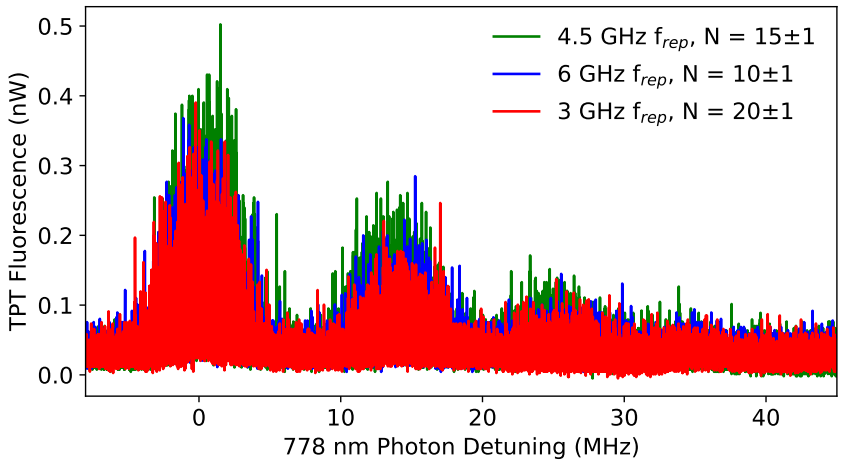

Figure 5.22: The frequency of the OFC is scanned across the Rb TPT hyperfine features, while using an average intensity of 2.4 W/cm^2 to excite the transition. The maximum signal amplitude appears relatively constant as we expect, when comparing OFC lasers with an increasing number of modes. Some unexpected rapid oscillations feature within the transition profile.

The raw Rb TPT fluorescence signal in Fig. 5.22 is very noisy, regardless of being well above the baseline noise levels, and also yields a much lower amplitude than the same intensity from the Ti:Sapphire laser ($\sim$ 13x lower). When the data is run through a filtering function (moving average), the shape and width of the hyperfine profiles becomes a bit clearer, as shown in Fig. 5.23. The Rb TPT signal maximum appears to be staying roughly constant, while N is changed. There are however clear signs of excess broadening on the Rb TPT signal resulting in a FWHM of $\sim$ 5 MHz. This is significantly wider than the expected signal linewidth of roughly 750 kHz, which is based on an assumed linewidth for the laser rather than any direct measurement.

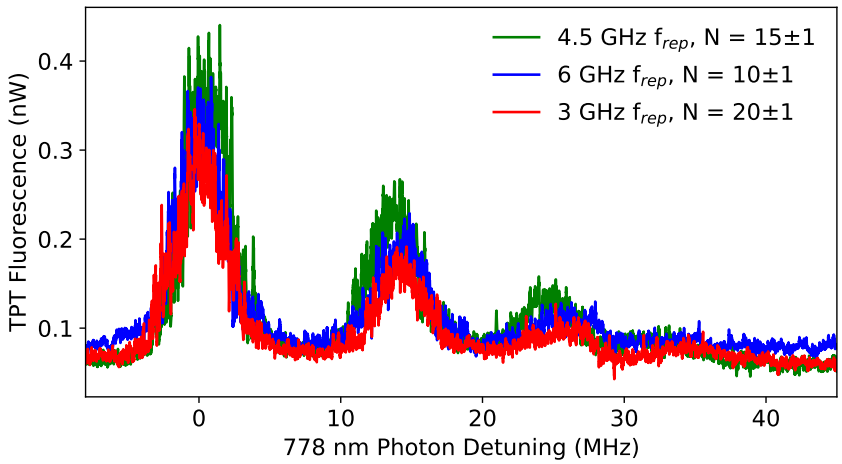

Figure 5.23: A moving average is applied to the same data from Fig. 5.22, to reveal some detail on the shape and FWHM of the transition profiles.

There could be several reasons for the reduced amplitude. Let us first rule out the possibility that the weak signal is resulting from the power in only a single OFC mode being on resonance with the Rb TPT. At best (for f_{rep} = 6 GHz), a single resonant mode will contain $\sim 1/10^{th}$ of I_{av}, and result in a signal $\sim$ 100x less than the CW fluorescence amplitude of 5 nW. Furthermore, it follows that the increase in N from 10 to 20 modes will then result in a lower signal from a single mode, or else yield a signal of twice the strength if the enhancement is taking place. The signal is clearly stronger than if only a single mode were on resonance with the Rb TPT.

5.7 Diagnosis of Issues with the OFC Laser

Owing to the OFC generation technique for this laser, each mode is considered to essentially be CW, with the pulses arising from the coherent superposition of the modes. However, the fact that the signal broadening and amplitude reduction are on a similar scale is indicative of broadening corresponding to a limited interaction time with the laser at the excitation frequency. The cause of this may be that either FM fluctuations or AM fluctuations are affecting the OFC spectrum as a whole, but previous results have already demonstrated the AM/RIN noise of the laser is relatively low. The rapid peak-to-peak fluctuations within the profile of the Rb TPT hyperfine transitions therefore instead indicate laser FM noise. Unlike the FM jitter noise observed using the CW telecoms laser (see Figs. 4.13 and 4.14), scanning the OFC frequency at faster rates up to 1 kHz, did not reduce the noise, indicating the noise occurs at a much faster rate. The source of the FM noise was easily separated apart from anything related to f_{rep}, by measuring the laser spectrum for both the FP and TL diode modes while operating in CW mode with the RF source disconnected. An example of the noise on the FP laser mode is shown in Fig. 5.24.

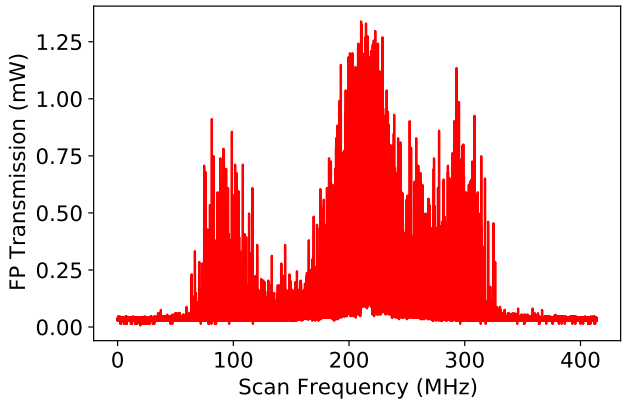

Figure 5.24: Scanning Fabry Perot measurement of the FP laser mode reveals details of the FM noise while running in CW operation. The same attributes could be seen for the modes from both internal diodes of the OFC laser. Noisy side-bands with variable offsets can be seen either side of the main transmission peak

Higher bandwidth measurements up to 0.35 GHz require using a smaller gain for the photodiode picking up the Fabry-Perot transmission signal and therefore compromise on the SNR, but still enabled a good resolution of the the FM noise characteristics. In this case, the bandwidth was limited by the $\sim$ 1 ns response time of the PD used to detect the transmission signal (Thorlabs DET10A2). The same peak-peak fluctuations that were detected in the Rb TPT signal also persisted in the higher bandwidth Fabry-Perot measurements. With such a noisy signal it is difficult to approximate the FWHM of the laser mode, but it is evidently wider than the 7 MHz FWHM of the Fabry-Perot modes. Additionally the OFC laser in CW mode possesses noisy side bands, as shown in Fig. 5.24 which occurred with variable offsets in the region of 100 MHz from the main mode.

The presence of the noisy side-bands indicate quite a large peak-peak modulation depth/noise of around $\pm$ 100 MHz. By stopping the Fabry-Perot scan while on the side of the main mode, the FM noise was monitored more closely for 120 μs. A short segment of this measurement, shown in Fig. 5.25a, reveals that the CW laser mode is scanning over the 7 MHz FWHM Fabry-Perot transmission profile in less than 0.5 μs. This measurement could then be processed with an FFT, to reveal more information on the rate of the modulation occurring. In Fig. 5.25b, we compare the background noise from the transmission photodiode to the transmission signal to tell apart artefacts of the detector noise from the laser noise. Predominantly we see typical laser noise, dropping off with a 1/f dependency toward higher frequencies. The relatively low amplitude additional components around 200 MHz may correspond to an FM modulation which gives rise to the $\pm$ 100 MHz side-bands indicated in Fig. 5.24.

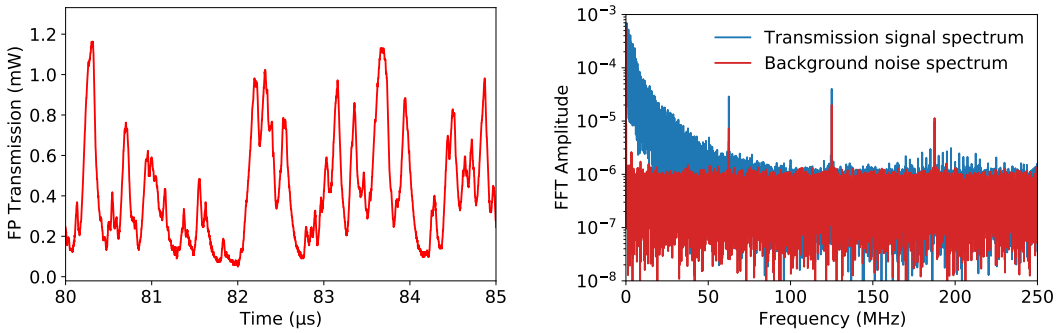

(a) *(b)*

Figure 5.25: (a) An example section of the typical Fabry-Perot transmission signal noise, while neither the OFC laser (running in CW mode) or Fabry-Perot (FP) are scanning. This indicates the laser frequency can be drifting from the peak (∼1.2 mW) of the 7 MHz FWHM Fabry-Perot transmission profile to the base at very fast and variable rates (b) FFT of transmission data (normalised to the measurement bandwidth) showing presence of additional frequency components around 200 MHz while the laser is running, compared with transmission signal when switched off.

The FM noise which is being generated on the central frequency of the OFC prevents

any analysis of the stability of the laser while locked to the Rb TPT. However there is a clear advantage to the frequency-doubling efficiency using the OFC instead of a CW laser. The advantage is at its greatest when the comb modes are narrowly spaced, and the PPLN is running with low input power/conversion efficiency to reduce the effects of pump depletion. If a single PPLN stage were to be used for self-referencing the OFC using its second harmonic, and providing light to excite the Rb TPT, then a wider bandwidth of the 778 nm OFC would be advantageous. In such a case, we then need to consider ways to avoid Doppler broadening arising from step-wise excitation of the Rb TPT. This can be done either using the PPLNs phase-matching bandwidth, or by placing a < 3 nm wide band-pass filter in the 778 nm beam path to spectroscopy.

There is a silver-lining to the discovery of the rapid FM noise on this particular laser. With such wide-band frequency noise on the order of 10's of MHz that is demonstrated in Fig. 5.24, it would normally not be possible to detect any of the hyperfine features of the Rb TPT. As such the increased background noise levels in Fig. 5.22, are likely the Rb TPT signal generated by the single mode interaction of the laser with the transition. However, the interaction of the OFC modes cancels out, to some extent, the noise of the laser to be able to resolve all of the hyperfine features with roughly 5 MHz linewidths. It is clearly disadvantageous to use a noisy laser for applications such as an optical frequency reference. However, to the best of our knowledge, a study on the impact of FM laser noise from an OFC laser on spectroscopy of a narrow-linewidth transition has not been carried out before.

Chapter 6

Low-Drift Optical Cavity for Laser Pre-Stabilisation

6.1 Introduction

Referencing a laser to a narrow atomic transition such as the Rb TPT provides excellent long-term stability, reducing the phase-noise of the laser proportionally to the linewidth and the SNR of the transition signal. However, Sections 4.3.3 and 5 have highlighted the difficulty of engaging a lock to the Rb TPT signal in the presence of high-frequency FM laser noise, with FM modulation depths significantly wider than the Rb TPT signal linewidth. In this case, it is necessary to pre-stabilise the laser, prior to spectroscopy of the transition.

In contrast to atomic transitions, an optical cavity can be designed to provide a transmission signal at any chosen optical frequency, with a linewidth chosen by the user to be wider than the FM noise of the laser requiring pre-stabilisation, and hence feedback of sufficient bandwidth to compensate for the FM noise. Furthermore, while signal stability of atomic transitions begin to degrade when driven at laser powers beyond the transition saturation intensity (discussed in Chapter 5.6 of [89]), limiting the achievable SNR, optical cavities are not prone to the same limitation. Transmission signals with a high SNR and negligible short-term frequency noise are easily producible from an optical cavity. By Pre-stabilising a noisy laser to a scanning optical cavity, we can drastically reduce the linewidth and FM laser noise. Unfortunately, an optical cavity is much more sensitive to environmental perturbations like temperature fluctuations than atoms are. For example, temperature changes can expand the length of the optical cavity by enough to cause the frequency of a cavity mode to drift beyond the tuning range of a laser. This would lead to a disruption of the lock feedback, as well as reducing the locked lasers mid- to long-term stability (a standard Thorlabs scanning FPI can typically drift several GHz over a few hours). We investigate the use of a com-

bination of metals with opposite coefficients of thermal expansion (CTE) to maintain a fixed separation of the mirrors of the cavity, and reduce its sensitivity to temperature fluctuations.

6.1.1 Introduction

An optical cavity (also known as an optical resonator) refers to a configuration of two or more mirrors in between which light reflects back and forth retracing the same path as it does so [130]. The light trapped within the cavity naturally generates standing waves between the mirrors. The mirrors used to form the cavity are typically not 100% reflective, allowing some light to enter and exit the cavity. When the wavelength of the light entering the cavity fits within the cavity round-trip length an integer number of times, constructive interference occurs within the cavity, increasing the transmitted output power from the cavity. Resulting from this, one will observe a spectrum of transmission features occurring at regular intervals when scanning the laser wavelength, like the data shown in Fig. 6.1. The amplitude and spectral width or the transmission signals vary proportionally to the quality factor of the resonator cavity, as well as with the alignment of the laser to the transverse spatial modes of the cavity. By contrast with spectra generated by atomic transitions, the optical cavity spectrum may be tuned to be resonant with a laser of any wavelength, making it extremely versatile.

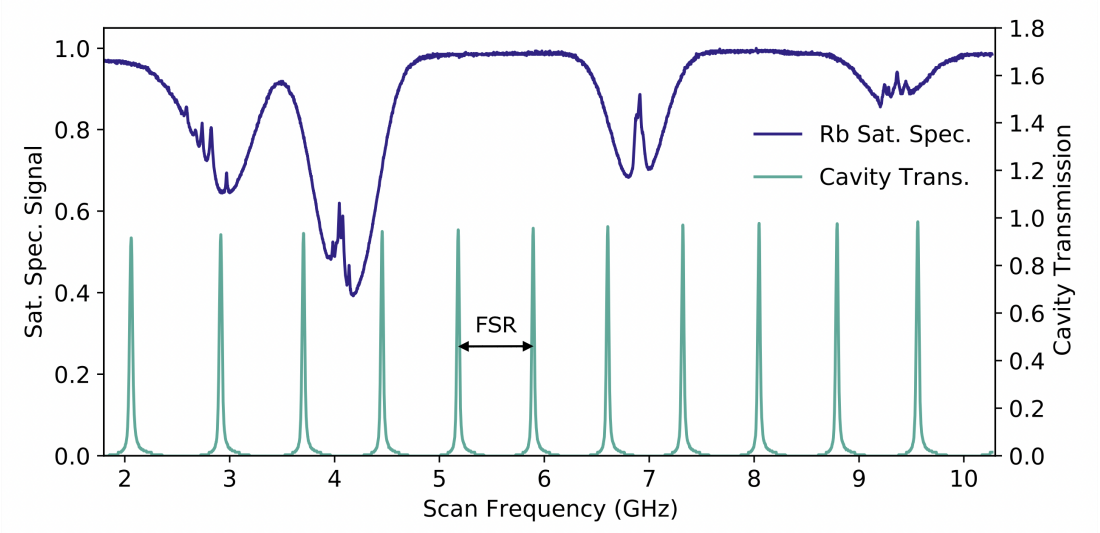

Figure 6.1: A 780 nm laser is frequency scanned, and its beam path is split, using one path to generate a signal from saturable absorption spectroscopy of rubidium D2 transitions and the other to simultaneously interact with an optical cavity. The cavity acts as a reference to approximately calibrate how far the laser has scanned each time a transmission is measured. The FSR between each mode is 750 MHz.

One particularly common type of optical cavity is the Fabry-Perot Interferometer (FPI), named after its inventors, who first proposed its use for spectral analysis of

monochromatic light in 1899 [131]. Nowadays, an FPI is typically made using two mirrors with a piezo transducer forming part of the material separating the two mirrors, allowing the cavity length to be finely scanned over a small range. This generates a spectrum of the cavity modes in the same way scanning the laser wavelength does. Besides providing a signal to lock a laser to, FPIs are a useful tool in the lab for analysis of the spectral qualities of a laser. The spectral separation between each mode of the FPI spectrum, known as the free spectral range (FSR), is easily calculated using the cavity length, and thus the spectrum can be used to calibrate how far the laser scans. This is useful in the context of atomic spectroscopy for determining the measured separation between transitions, like the spectra shown in Fig. 6.1.

The main drawback of using the optical cavity as a frequency reference is the difficulty with which one can define the absolute frequency of a mode without first knowing the frequency of the laser. Hence a narrow atomic transition is normally more useful to lock a laser when the absolute frequency is required. It is possible to incorporate qualities of both types of frequency references together by first locking a tunable laser to a scanning FPI mode, and then locking the cavity mode to an atomic transition using feedback to the FPI length.

A frequency lock to an optical cavity can be made to provide long-term frequency stability, reducing not only the frequency noise, but also the phase noise of a laser [132]. This level of stability is required to prepare a laser as a local oscillator for optical lattice atomic clocks which reference to the ^{87}Sr $1S_0$–$3P_0$ transition [133, 134], as well as for resolving sub-Hz linewidth optical transitions, such as those used in stored ion clocks [135]. Optical cavities achieve this level of stability primarily by operating in a vacuum, and using thermally insensitive materials such as ULE Corning glass, or fused silica as a spacer between the mirrors to eliminate the temperatures effects entirely. ULE (ultra low expansion) materials demonstrate a very low coefficient of thermal expansion (CTE), often with the ability to tune the CTE to near zero, by adjusting its temperature. The CTE is defined as the fractional length change, per degree:

$$CTE = \frac{\Delta L}{L}\frac{1}{\Delta T} \tag{6.1}$$

The CTE is typically quoted in ppm/°C, and ULEs are capable of achieving 0.001 ppm/°C [135]. ULE material is expensive, and difficult to manufacture or modify, so standard scanning FPIs like those from Thorlabs, typically use Invar. Invar is a metal alloy with the lowest CTE of any currently available metal (see Fig. 6.2); measuring between 1.6 and 6 ppm/°C. Recently a new type of metal alloy has become commercially available. This metal is known as Allvar, and quotes a negative CTE, meaning that it actually contracts as the temperature rises, as shown below in Fig. 6.2.

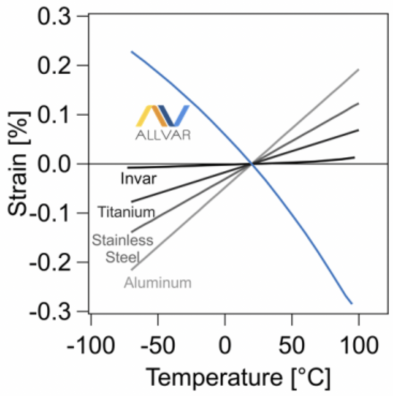

Figure 6.2: The strain (proportional to expansion of the metal) is compared for different metals and alloys as the temperature is adjusted away from room temperature. All metals expand with temperature, but Allvar (a Titanium-based alloy), has been fused with other compounds in such a way that the alloy demonstrates a negative CTE along one of its axis, while maintaining a positive CTE perpendicular to this axis. Image source: allvaralloys.com

By pairing together sections of Invar and Allvar in the correct ratio to separate the cavity mirrors we can cancel out the expansion of Allvar with the contraction of Invar, reducing the cavities change in length during a temperature change to near zero. The CTEs of Invar and Allvar both demonstrate some temperature dependency (Indicated by the slight curve on the lines plotted in Fig. 6.2). This enables the ability to pick the ratio so as to allow the CTE zero-crossing to occur at a specific temperature and stabilise the cavity to this temperature, greatly reducing the extent of long-term drifts of the cavity resonances. At this point in time there are no known examples of Allvar being incorporated in to a low-drift optical cavity. However there has been research so far in to its use in creating low expansion mounts for telescope optics. Therefore allowing them to be operated in space, where equipment is subject to extreme temperature variations, which can lead to misalignment issues of optics [136]. Recent high-precision measurements of air pressure changes have been reported using an Invar Fabry-Perot interferometer measurement technique [137]. These publications highlight the value of using a metal spacer when very accurate temperature stabilisation is required for the air within the cavity. The benefit of using metal over ULE being to reduce thermal gradients across the cavity body, and with a higher thermal conductivity allowing quicker stabilisation of small temperature changes.

In general, ULE cavity optical references claim that thermal and vibrational noise ultimately limits the frequency stability of the cavity [132, 138]. An added benefit to metal spacers over ULE material, is superior thermal conductivity, which helps to reduce thermal gradients across the mass of the spacer material, and increase the bandwidth of temperature stabilisation feedback. Additionally, metals tend to have higher young's modulus than typical ULE materials, which is a key factor when it comes to tackling the remaining vibrational sensitivity of an optical cavity [137, 139].

6.1.2 The Confocal Optical Cavity

Although many stable geometries of optical cavity mirror arrangements have been explored, the confocal cavity arrangement (shown in Fig. 6.3) is highly favoured for its insensitivity to misalignment. The confocal cavity consists of two plano-concave mirrors, with the same radius of curvature (ROC). Stable cavity modes are realised when the mirrors are spaced apart by L = ROC, allowing the focii of both mirrors to meet in the middle of the cavity at ROC/2. In addition to the central TEM_{00} mode which the laser beam may couple to along the central axis, the beam may also couple to higher order transverse modes, when entering offset from the central axis, as shown in Fig. 6.3.

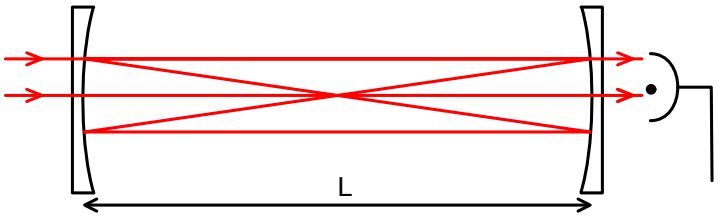

Figure 6.3: Illustration of the round-trip path a beam takes when entering on and off axis in a confocal cavity. A photodiode opposite a coupled laser detects a transmission when the laser is resonant with a cavity mode.

Once aligned with one of the transverse modes of the cavity, the laser frequency (or cavity length) may be scanned to couple to the longitudinal modes of the cavity to generate the transmission spectrum. Each of the longitudinal modes are spectrally separated by the free spectral range (FSR), which is equal to the inverse of the time it takes light to propagate a full round trip between the cavity mirrors and return to the point it started. A beam perfectly aligned to the central axis of the confocal cavity will excite the fundamental transverse mode, with round-trip path length of 2L, yielding an FSR of:

$$FSR = \frac{c}{2nL} \tag{6.2}$$

In equation 6.2, c/n is the speed of light in the medium between the two mirrors. However, any parts of the input beam which do not enter exactly on the central axis of the cavity, couple with higher-order transverse modes which occur with a round-trip path length of 4L, therefore with an FSR:

$$FSR = \frac{c}{4nL} \tag{6.3}$$

Only under the conditions of L = ROC, for the confocal cavity, do all of the higher order

transverse modes occur with the same FSR. When aligning a beam to the cavity, the chances of coupling to a cavity resonance are greatly improved by the presence of the many stable higher order transverse modes. Additionally the higher order transverse modes of the confocal cavity are less sensitive to angular misalignment with the central axis of the cavity. Both of these characteristics make this type of optical cavity much easier to obtain a transmission signal from.

The maximum transmission of the peaks which are shown in Fig. 6.1 occur when the laser frequency, f_{laser} is equal to the frequency of a longitudinal cavity mode, f_m, which correspond to an integer number, N_m, $\times$ FSR. This leads to the expression for the resonance frequency with the higher order confocal cavity modes:

$$f_m = \frac{N_m c}{4nL} \tag{6.4}$$

In practice it is difficult to align a cavity without either the cavity scanning its length or the laser scanning its frequency over a range of at least one FSR. This ensures you will couple to the longitudinal modes, acquiring a signal which can then be optimised with alignment to the transverse modes. A lens may also be used to focus the beam in to the cavity, which reduces coupling of the laser to higher transverse modes, increasing the amplitude of the transmission signal.

6.1.3 Cavity Mode Frequency Stability

While the modes in an optical cavity at any one moment in time will always be perfectly evenly spaced apart by an FSR, the exact value of the FSR and consequently the absolute frequency of the modes can drift on longer time scales. From Eq. 6.4, it is evident that the only two variable parameters determining the frequency of a mode with a given number are the cavity length, L and the the refractive index, n. We will determine the effect of changes to each of these variables individually.

By, assuming n stays constant, and then differentiating Eq. 6.4 w.r.t. L, we find the sensitivity of f_m to changes in cavity length:

$$\frac{\delta f_m}{\delta L} = -\frac{N_m c}{4nL^2} \tag{6.5}$$

This can be simplified by now re-substituting f_m in to the equation:

$$\Delta f_m(\Delta L) = -f_m \frac{\Delta L}{L} \tag{6.6}$$

The negative signage tells us that the frequency of the laser must decrease to track a given cavity mode as the the cavity length increases. The primary cause of changes in the cavity length, are temperature fluctuations inducing expansion or contraction of

the cavity spacer. Under the approximation that the CTE is constant for the change in temperature, we can re-express Eq. 6.6 in terms of a temperature change of the spacer material, ΔT_{spacer} and the CTE of the spacer:

$$\Delta f_m(\Delta T_{spacer}) = -f_m \times CTE \times \Delta T_{spacer} \tag{6.7}$$

Changes in the refractive index of the air between the cavity mirrors, are predominantly dependent on: temperature, pressure, humidity and the wavelength of light in the air. The Ciddor equation can be used to calculate the refractive index under different conditions, using an online app from NIST: `https://emtoolbox.nist.gov/Wavelength/Ciddor.asp`. We can follow a similar derivation as for the length change for the effect of a change in the refractive index, assuming the cavity length is constant:

$$\Delta f_m(\Delta n) = -f_m \frac{\Delta n}{n} \tag{6.8}$$

In this instance, n may be treated as 1 without affecting the calculated shifts by any practically measurable amount. By separately calculating Δn, for a small change in each of: air temperature in °C, pressure in Pa, and humidity in %, one can calculate a combined mode frequency sensitivity in MHz to changing air conditions:

$$\Delta f_m(\Delta n) = -1.02 \times \Delta P_{air} + 347.35 \times \Delta T_{air} + 3.65 \times \Delta H_{air} \tag{6.9}$$

Equation 6.9 is essentially an approximation of the Ciddor equation, calculated at 780.241 nm, assuming the refractive index varies linearly with each parameter. The coefficients for pressure and humidity are relatively constant ($< \pm 0.01\%$) over the ranges measured in this experiment. However the temperature coefficient varies slightly with temperature, causing $< \pm 2\%$ over the range 20-40°C. The number quoted above is for a temperature of 30°C, and varies linearly from this value with a gradient of -1.58 (MHz/°C)/°C.

Using an environmental sensor such as the Bosch BME280 [140], one can measure pressure (± 0.2 Pa), temperature (± 0.005 °C) and humidity (± 1%) simultaneously, and therefore accurately determine the shift in the cavity mode frequency due to changes in the refractive index. Fig 6.4 shows an example of pressure and temperature trends over a 16 hour period. Example humidity trends are not shown here, because indoors, they tend to be relatively constant ($\pm 1\%$) over a 24 hour period.

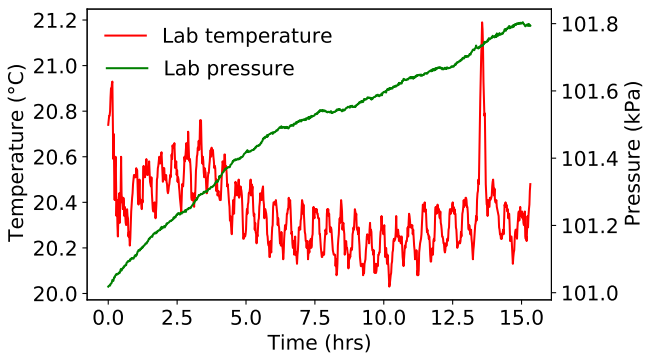

Figure 6.4: An example 16 hour pressure and temperature log in the lab where the experiment was run, using the BME280 sensor. Temperature data shows typical oscillations corresponding to AC unit cooling cycles every 25 mins, whilst the pressure changes occur independently of temperature, increasing by nearly 800 Pa in this period.

As mentioned at the end of Section 6.1.1, there are other mechanisms which impact the stability of f_m, which ULE cavities are sensitive to. However, for this investigation, the measurement techniques used will not be sensitive enough to pick these up over the effects of the environmental perturbations described above.

6.2 A Metal Optical Cavity with Zero-Crossing CTE

6.2.1 Invar Cavity CTE Measurement

The starting point of this investigation was to characterise a 100 mm long, Invar metal, confocal cavity. The length of the cavity is adjustable, to aid the alignment of the cavity, and has been set to ensure that all of the higher order modes overlap with an FSR corresponding to Eq. 6.3. The plano-concave mirrors at either end have radii of curvature = 100 mm, and a measured reflectivity, R $\geq$ 96% at 780 nm. Using these specifications, the cavity is expected to have an FSR of 750 MHz, Finesse of 38, and a FWHM linewidth of 20 MHz. Even with such a wide linewidth, it would be possible to stabilise a locked laser to $\leq$ the Rb TPT linewidth given the transmission signal has a large enough SNR.

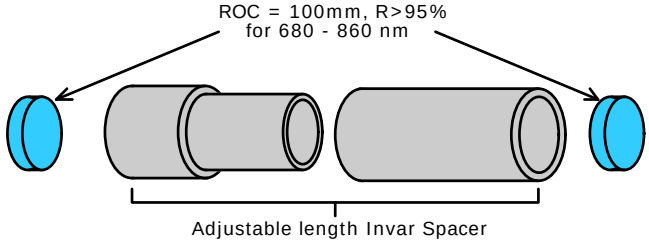

Figure 6.5: Assembly of the original, adjustable-length, Invar confocal cavity

The Invar CTE can be accurately measured by raising the cavity temperature, and tracking how far the cavity modes shift to determine the change in the Invar length between the mirrors. For this measurement, the cavity was heated by 10 °C in an insulated oven on the lab bench, and the mode shifts were recorded for 3 hours while the cavity temperature stabilised. A slow heating rate was chosen to allow uniform expansion across the full length of the Invar metal. To track the mode frequency shift, a tuneable frequency-doubled telecoms laser with 780 nm output was used to scan across the cavity modes and establish a lock to a cavity mode. It is then possible to track the change in the mode frequency as the laser frequency tracks the cavity mode and measure the laser frequency on a wavemeter down to an accuracy of ± 0.1 GHz. The apparatus used for the measurement is shown in Fig. 6.6. The frequency-doubled telecoms laser was chosen for this experiment, owing to its long term stability (low drift) and wide scan range using the FM modulation port. Two thermistors in contact with the cavity metal near either end were used to measure the changes in temperature, and ensure less than a 0.5 °C differential during the heating cycle.

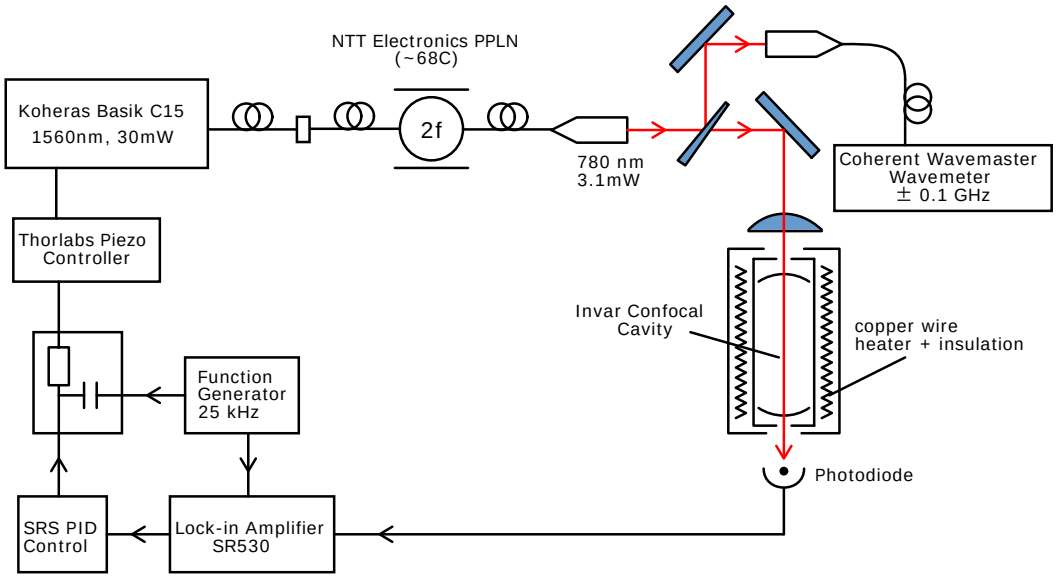

Figure 6.6: Apparatus used to track the drift of the cavity mode, while the cavity is being heated. The laser frequency is modulated at 25 kHz. The FM modulation is picked up on the cavity transmission signal, and demodulated by the lock-in amplifier to create an error signal. A filter combines the modulation signal and the feedback error signal which are fed to the piezo modulation port of the 1560 nm laser.

The changes in laser frequency were recorded from the wavemeter approximately every 10 minutes, until both the temperature and the wavemeter readings had stabilised. After the raw data was acquired, the effect of the change in air temperature to the refractive index ($\Delta f_m/\Delta n$) was subtracted from the measured frequency shifts using Eq 6.9, and assuming the pressure and humidity are roughly constant (±50 Pa and 0.5% R.H.) over the measurement duration. The experiment was repeated 3 times

with increasing temperature ranges, yielding consistent results of the CTE each time. Fig 6.7 shows an example of the Invar CTE measurement across the widest temperature range of these 3 measurements.

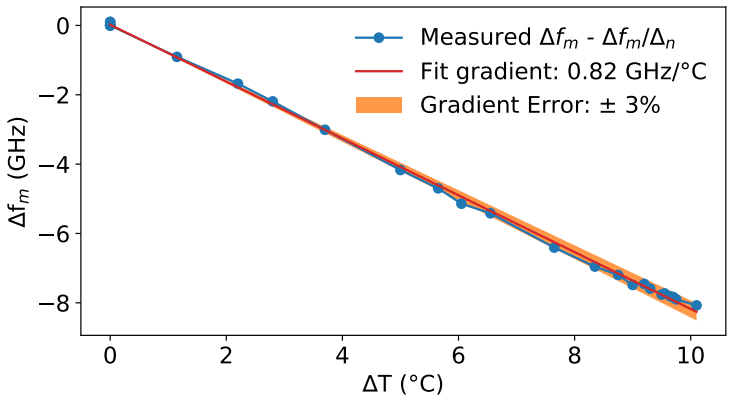

Figure 6.7: The CTE measurement highlights the sensitivity of the mode frequency to temperature changes (23-33 °C) of Invar. Shifts corresponding to the change in refractive index of air during the temperature increase have been subtracted. The ± 3% CTE gradient error is calculated based on sensor and measurement uncertainty contributions.

Using the gradient $\Delta f_m/\Delta T$ from the data shown in Fig 6.7, the CTE can be determined using Eq 6.7. This yielded a CTE value of 2.13 ppm/°C ± 3%, where the tolerance of 3% corresponds to the frequency and temperature measurement uncertainty contribution to the fitted gradient. This measured value sits within the expected range quoted elsewhere for Invar. Additionally the results of Fig 6.7 show that over the full temperature range, the measurements follow a roughly linear trend, indicating uniform heating of the cavity. Using the measured Invar CTE, it is now possible to accurately estimate how much Allvar would be required to cancel out the expansion of Invar. Each section of Allvar comes pre-characterised with an exact CTE analysis. For the section at hand this was given as -26.4 ± 2 ppm/ °C at 25 °C. The length of Invar which is required to replace with Allvar is calculated using the formula:

$$L_{Allvar} = 100\ mm \times \left| \frac{CTE_{Invar}}{CTE_{Allvar}} \right| \tag{6.10}$$

This yields a required length, $L_{Allvar} = 8.14 \pm 0.75$ mm for compensating Invar expansion at room temperature. This then leaves $L_{Invar} = 91.86 \pm 0.75$ mm. However, in Fig. 6.2, the Allvar CTE can be seen to vary slightly with temperature. With temperature control of the cavity, this means one can tune the CTE of the Allvar after it is put in place. Considering this, excess Allvar was used - 10 mm instead of 8.14 mm, so that it was possible to observe the CTE turning from positive to negative a few degrees above room temperature. This enables easier temperature tuning and more stable feedback around the CTE turning point.

6.2.2 Modifying The Cavity With Allvar

To incorporate the Allvar section in to the cavity length, the Invar cylinder had to have a small section cut out near the middle of the cavity length. A specially designed bracket, shown in Fig. 6.8a serves the purpose of holding the independent sections of Allvar and Invar flush against each other, using the least amount of extra metal in between the sections. It it important to make sure that the Invar and Allvar sections are in direct contact at all times during their expansion and contraction. The aluminium screws which secure the sections together, are the most likely component to prevent free-expansion/contraction of the sections, by holding the sections apart as the Allvar contracts. To avoid this happening, the screws are secured in place with Belleville spring washers, the placement of which is indicated in Fig. 6.8b. These washers can allow the screws to extend without loosing the tension on the brackets, so as to keep the sections held firmly together. A specific torque of 0.565 Nm (5 In/Lbs) was applied to each set of washers (6 used with each screw).

(a)

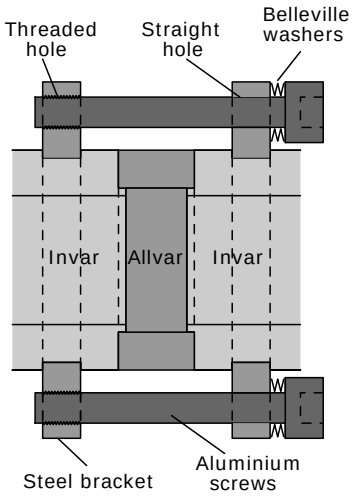

(b)

Figure 6.8: (a) Image of modified Invar cavity with the Allvar section appearing as the darker metal in between the brackets. As the cavity remains adjustable in length, a black lens tube clamp is used to secure the length of the cavity. (b) A cross-section of the brackets show how they are embedded in to the surface of the Invar sections.

6.2.3 Invar-Allvar Cavity CTE Measurement

With the addition of Allvar in to the cavity, the previous method for measuring the CTE of Invar would no longer be accurate to track the reduced range of frequency shifts in the cavity. To improve on the resolution of Δf_m, the wavemeter frequency reference ($\pm$ 100 MHz) was swapped for a measurement scheme which measures the cavity mode shift relative to a reference transition in rubidium, allowing a much higher resolution.

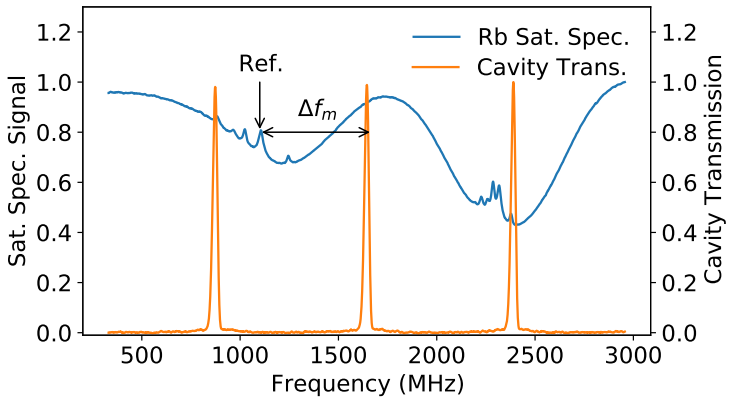

Figure 6.9: Simultaneously acquired Rb Sat. Spec and cavity transmission signals allow tracking of the separation between the indicated reference transition and cavity mode frequency.

To reference Δf_m, the ^{87}Rb D2 $5S_{1/2}, F = 2 \rightarrow 5P_{3/2}, F' = 2/3$ crossover transition at 384.228 THz [141], was chosen (indicated in Fig. 6.9). The Rb reference signal was measured using saturable absorption spectroscopy (Rb sat. spec.). The Rb reference signal and cavity transmission signals are acquired simultaneously using the apparatus shown in Fig. 6.10, and a narrow linewidth laser which continuously scans a 3 GHz range.

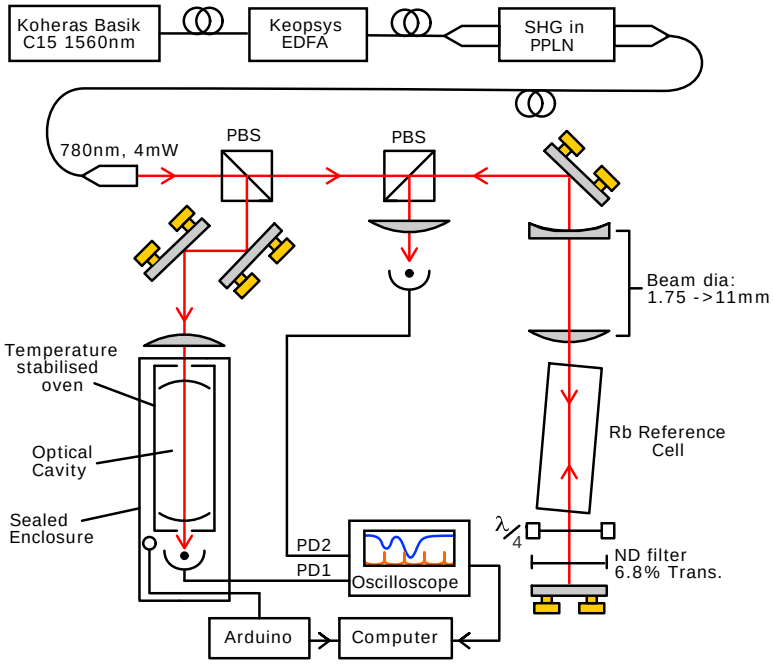

Figure 6.10: (a) The apparatus for measuring the Rb sat. spec. signal and cavity transmission signal. A 100 mm convex lens focuses a beam into the cavity, improving the coupling to a single transverse mode of the cavity. Roughly half the 780 nm power is directed to saturable absorption spectroscopy. PD1 (Cavity Trans.) and PD2 (Rb Sat. Spec.) record the the data shown in Fig. 6.9.

The process for determining Δf_m involves computer analysis of the signals to track the drift. Similar techniques have been implemented for other low-drift Fabry-Perot cavity measurements [142, 143]. Once the data is acquired, the process is as follows:

- Traces of both cavity and sat. spec. signals are saved from the oscilloscope once per minute for the duration of the experiment using LabView to automate data acquisition
- At the end of the experiment, the data is processed by a Python script, which does the following, and has been illustrated in Fig. 6.11:
    1. Low-pass filtering removes noise in the data to improve fitting reliability
    2. Fit Gaussian profiles to the Doppler-broadened absorption features of the ^{87}Rb spectrum and subtract the fit from the data, leaving the reference transition as the highest point in the Rb sat. spec. data and allowing its location in the scan to be easily identified by a peak identification algorithm
    3. Peak identification algorithm then returns location of all peaks in cavity transmission data
    4. A new file stores the time difference from the Rb ref peak to each of the transmission peaks, the amplitude of each of the transmission peaks and the time location of the Rb reference peak at each consecutive minute of the experiment
- The oscilloscope data time axis can be converted to a frequency scale using the cavity FSR as a calibration reference, to then determine Δf_m in frequency

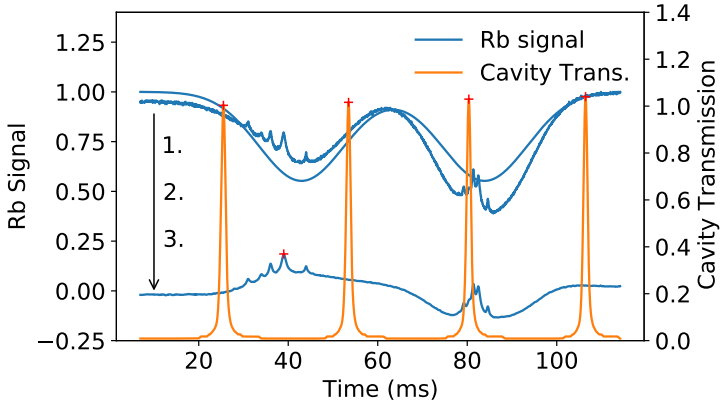

Figure 6.11: Example processing of Rb Sat. Spec. data, showing the results of steps 1,2 and 3 described above.

The above method, enables a resolution of Δf_m down to $\simeq \pm 2.5$ MHz, which is predominantly limited by the time-scale resolution of the scan, as well as the SNR of the

measurement and FWHM of both the reference transition and transmission peaks. The analog version of this method, would be an optical heterodyne measurement between two separate lasers individually locked to the reference transition and cavity mode. This would require quite a bit of extra equipment by comparison to the method described above, and the extra spectral resolution gained by this method is not necessary for this investigation.

As noted in several publications on low-drift ECDL designs, changes in pressure cause the largest variations in the stability of the refractive index within the optical cavity [144]. The ideal solution to this issue is to hermetically seal the cavity itself, however this was impractical due to time-constraints. Instead, the experiment was placed inside a sealed waterproof enclosure to prevent random pressure fluctuations. Any remaining changes in pressure, temperature and humidity were logged using several sensors inside the enclosure. This allowed for the removal of cavity mode frequency shifts related to changes in the refractive index of air during post-processing of the measurements. As shown in Fig. 6.12, the enclosure was modified with a window to let the laser beam enter the cavity, and electrical connections for the transmission photodiode, heater coils, and environmental sensors. Careful application of Torrseal and silicone sealant around connectors and window, preserved the air-tightness of the enclosure.

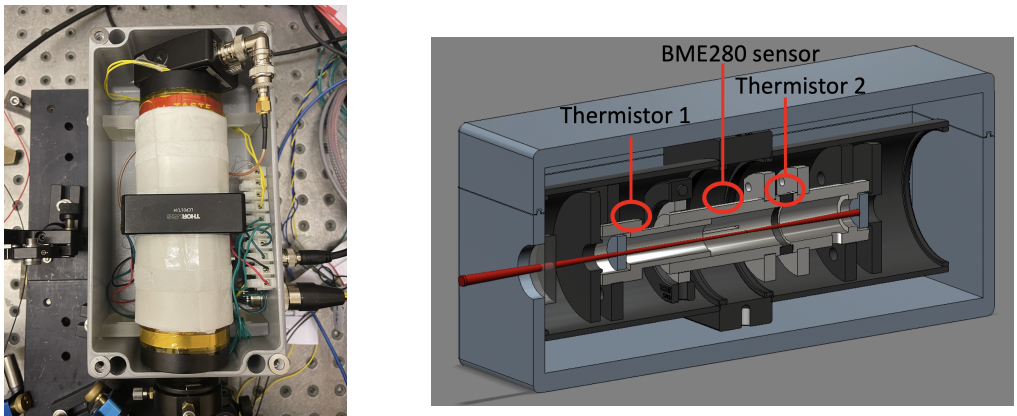

(a) (b)

Figure 6.12: (a) View inside enclosure, showing connections to the sensors and the photodiode which detects the cavity transmission. A neoprene rubber ring provides an airtight seal around the lid (IP66 waterproof rating). (b) Cross-section of enclosure oven and cavity, showing the placement of three separate sensors for monitoring conditions and stabilising the oven temperature.

An Arduino MKR Zero is used to log data from the two NTC thermistors (AYN-MF59-104F-3950FB) as well as the BME280 sensor (shown in Fig. 6.12). A voltage regulator is used in conjunction with the Arduino supply voltage to power the sensors, and oversampling is implemented within the Arduino code, to reduce the NTC thermistor RMS noise to $\pm$ 0.03°C, without reducing the sensor bandwidth below 1 Hz. The

Arduino MKR zero has an SD card slot to log data, and also a 10-bit DAC, which is used for PID feedback to the oven, allowing temperature stabilisation using the sensor readings.

The enclosure was tested for leaks in pressure by switching on the oven heaters while the enclosure was sealed. This causes the pressure to quickly rise proportionally to the average enclosure temperature, up to a level above the lab's ambient air pressure (measured by an external pressure sensor). If the box is sealed properly, then the pressure will stay at the elevated level indefinitely. Correlations between the enclosure pressure and average temperature indicate the enclosure is isolated from the external conditions on the short term, and the volume of air inside is fixed. Using the combined gas law, and conditions of 100,000 Pa (1 atm) and 20 - 30 °C, the correlation between the pressure and temperature should be around 335±5 Pa/°C.

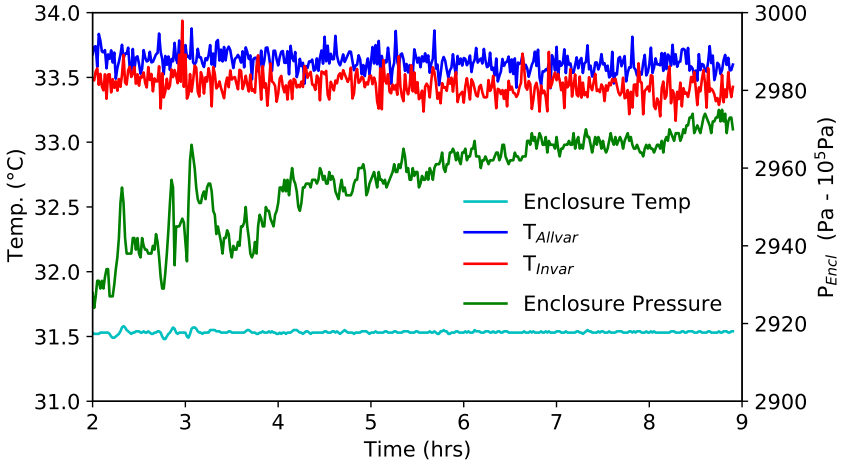

Figure 6.13: Logged data, after allowing 2 hours for the cavity to stabilise to 33.5 °C. Different positions within the enclosure were tested for locating the BME280 sensor including outside the oven, where it is located for this data set. This is the reason for the 2 °C difference in temperature between the 3 temperature readings. The BME280 temperature readings have considerably less noise, owing to oversampling on the sensor chip, and its own low-noise electronics. Although the pressure changes immediately to any changes in temperature within the enclosure, the long settling time of the pressure indicates the time it takes for the whole enclosure to reach thermal equilibrium.

The stability which the pressure was able to reach was intrinsically linked with the stability of the enclosure temperature. For example, a ± 5 mK temperature stability would result in a < ± 2 Pa stability. The oven temperature could reach a stability of ± 5 mK (the resolution of the BME280 temperature sensor) after a few hours stabilisation time (see Fig. 6.13). After 12 hours of stabilisation to the set-point, the fluctuations in the enclosure air pressure across a 1 hour span were reduced below ± 2 Pa, confirming ± 5 mK temperature stability. However, on longer time-scales, changes in the external lab temperature would cause the heater coils to run hotter or colder to stabilise the oven temperature, causing the average temperature and hence the pressure of the enclosure

to fluctuate. Additionally, there are thermal gradients throughout the enclosure due to the constant heat dissipation through the external walls (for example the temperature difference between the 3 temperature sensors in Fig. 6.13). However, the enclosure pressure will stabilise very quickly to be the same at all points in the enclosure.

Using the improved accuracy to track Δf_m, and compensating for changes in the refractive index, it was now possible to measure the combined CTE of the Invar-Allvar cavity spacer. This involved a process of slowly increasing the cavity temperature by 1 °C and allowing it to stabilise for around 1 hour until the RMS fluctuations in Δf_m reduced below 5 MHz while measured over 15 minutes. Once Δf_m and the temperature were stable, the air pressure, temperature and humidity inside the oven were logged from the BME280 sensor. Using the Ciddor equation calculator, the change in refractive index was estimated, and the corresponding mode frequency shift, Δf_n, was subtracted from Δf_m, yielding the shift resulting solely from the change in cavity length. In Fig. 6.14a it is possible to observe the expected turning point behaviour of the cavity. From the starting temperature of 24 °C, the Allvar CTE dominates the length change, yielding an overall contraction in the cavity length as the temperature rises. A turning point in the CTE showed up at about 28 °C. As the cavity temperature rises higher to 31 °C it begins to show an overall expansion, with the Invar CTE now dominating.

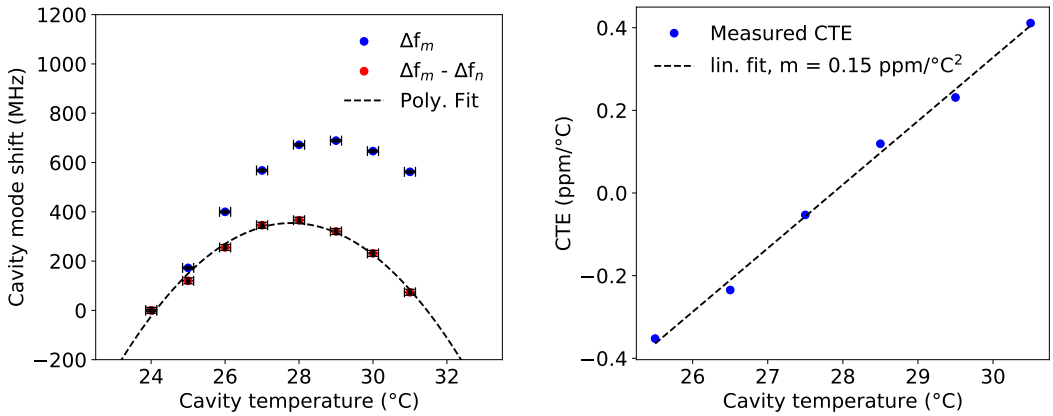

Figure 6.14: (a) Raw data from CTE measurement, comparing before and after compensating for refractive index changes using the Ciddor equation. The adjusted cavity mode shift is fitted with a 2nd order polynomial. (b) The cavity spacer CTE is estimated from the $\Delta f_m - \Delta f_n$ data in (a) using Eq. 6.7.

The trends in Fig. 6.14a demonstrate the total range of the measured cavity mode shifts during the CTE zero-crossing temperature measurement. However, Fig. 6.14b, shows that it is possible to linearly tune the cavity CTE from around -0.4 to +0.4 ppm/°C over a 5 °C range. The zero-crossing of the CTE is found to be 27.80 ± 0.15 °C, using 10 mm of Allvar and 90 mm of Invar. Based on typical oven temperature fluctuations of ± 0.005 °C, measured using the BME280 sensor, it would be possible to

achieve a CTE < 0.001 ppm/°C. This is around 2000 × lower than the measured CTE for Invar.

6.3 Optical Cavity Frequency Reference Stability

The CTE zero-crossing temperature tuning of the Invar-Allvar cavity was put to the test by monitoring the long-term stability (> 1 hour) of the cavity while it was temperature stabilised to approximately the CTE zero-corssing temperature. Long-term stability measurements were carried out using the same apparatus and procedure described and shown in Section 6.2.3. An example data set of the cavity mode stability over 5 hours is shown in Fig. 6.15. During the measurement, the cavity mode frequency drops -170 MHz, corresponding to a settling of the air pressure. The slow change in pressure is likely resulting from the gradual shift in temperature of the walls of the enclosure as they thermalise, even though the oven temperature is stable over this period. Gradual pressure stabilisation in the first 12 hrs of the measurement are fairly typical, like that shown in Fig. 6.13. Using the sensor measurements from within the oven and Eq. 6.9, we estimate the change in refractive index, and remove the corresponding shifts in the cavity mode, $\Delta f_n(P,T,H)$ from the measured Δf_m. This yields a reasonably accurate estimate of what one can expect in terms of drift if the cavity is hermetically sealed inside of the oven. The process of removing refractive index related drifts helps to identify residual drifts of the cavity mode that correlate with other measured parameters. A straight line was fitted to the compensated mode stability data, from which the gradient yields an estimate of the residual drift rate at +0.3 MHz/hr over the 5 hour data set.

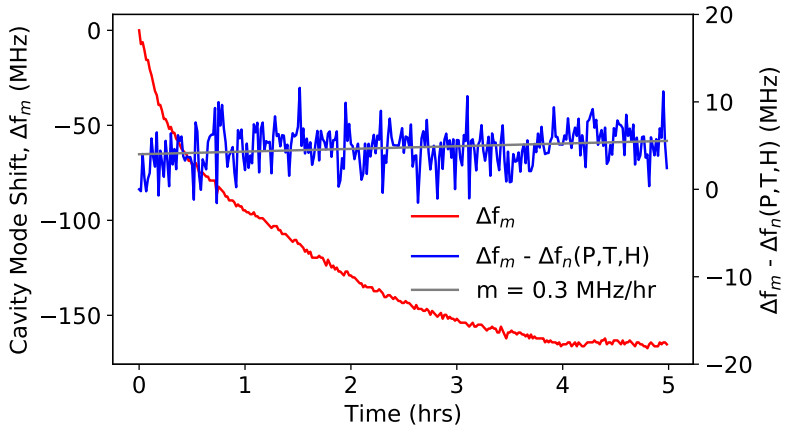

Figure 6.15: 5 hour long-term stability measurement after already allowing time for the cavity enclosure temperature stabilise to 27.8 °C for approximately 5 hours.

After 5 hours the total residual drift in Δf_m is below the ± 2.5 MHz Δf_m measurement resolution, making it hard to be completely certain the drift is not an artefact

of the fitting process or sensor calibration drift. A longer measurement was required to determine the extent of any residual drifts which are present, and whether there is a periodicity to the changes in Δf_m. The measurement duration was extended to several days (64 hours), while stabilised at 27.8 °C, to better understand the extent of the residual drift of the cavity mode frequency. These results are plotted below in Fig. 6.16.

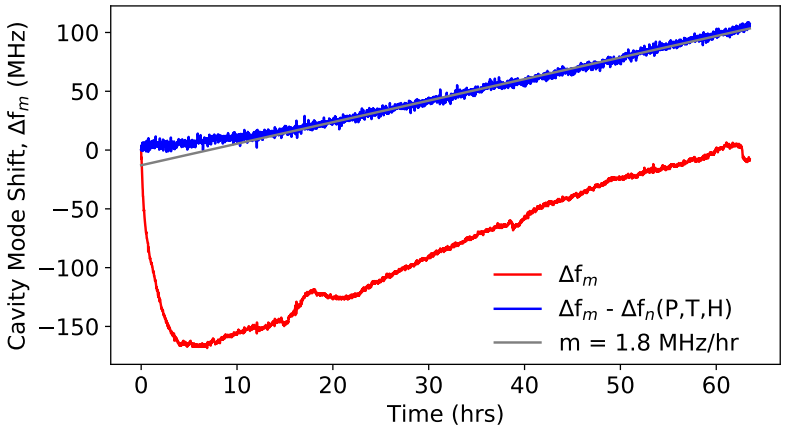

Figure 6.16: 64 hour drift measurement, with 5 hours allowed for the cavity temperature to stabilise to 27.8 °C prior to the measurement. A steady drift is revealed on time scales > 12 hours.

In Fig. 6.16, the refractive index compensated data, $\Delta f_m - \Delta f_n(P, T, H)$ appears to be stable for the first 5-10 hours as before, but then a steady linear drift of approximately +1.8 MHz/hr sets in for the rest of the measurement. Whilst such a definite linear drift is undesirable, this range of drift (1-2 MHz/hr) is as good as the stability achieved by other Fabry-Perot optical cavities seeking to demonstrate low drift outside vacuum conditions [145, 146]. External cavity diode laser systems are also good examples of optical cavities which are normally operated outside of vacuum conditions and suffer frequency drift related to thermal fluctuations. Such ECDL systems have typically demonstrated drift rates in the 1-2 MHz/hr range over long time scales [144, 147, 148]. Graphs of all of the logged data during the 64 hour cavity mode stability measurement can be found in supplementary Fig. S1 and S2.

The residual linear drift could result from several possible causes:

1. Slow pressure leak in enclosure (pressure dropping steadily towards external pressure).

2. Drift in BME280 temperature sensor calibration, leading to an undetected drift in the oven temperature.

3. Drift in BME280 pressure sensor calibration, affecting the compensation for changes in refractive index.

4. Out-gassing of materials within the heated enclosure.

5. Ageing of spacer or mirror glass, leading to a slow linear expansion (creep) of mirror separation [139].

The first of these possible causes could be ruled out by comparing the residual drift with the stabilised enclosure air pressure lower and then higher than room pressure. This would cause the residual drift gradient to switch from positive to negative when the two measurements are compared. No change in gradient could be seen for this test. Drift in the internal calibration of the BME280 temperature sensor, would have to be in the range of $\simeq$ 0.3 °C to induce a total drift of $\simeq$ 100 MHz. A sensor calibration offset on this scale should be easy to spot when compared with the measurements from the two NTC thermistors, however this is not evident. Furthermore an undetected drift in temperature of this scale would induce a pressure change of $\simeq$ -100 Pa, unless the pressure sensor calibration is drifting. A drift in the calibration of the BME280 pressure sensor would not be as obvious, with no second reference on the internal air pressure besides the behaviour of the cavity mode itself. For the residual drift to be correlated to pressure calibration drifts, the calibration would have had to drift by $\simeq$ -100 Pa. A second BME280 pressure sensor which monitors lab air pressure typically measures an offset of $\simeq$ 130 Pa difference in the same environment. This offset has remained approximately the same $\pm$ 5 Pa over months of using the two sensors, with the sensors also maintaining the same offset when compared with local with local weather station measurements.

The fourth possible cause put forward above is the potential for compounds in the enclosure with a low melting point, to release vapours, or additionally for some water in the enclosure to vaporise gradually while the cavity is heated. Such compounds in the enclosure, for example could be silicone sealant, Kapton tape, or thermal paste. Evaporation of any compound to a vapour or gas phase will cause an increase in pressure, and may also register an increase in the humidity sensor reading. Both pressure and humidity readings showed a gradual decreasing trend over the duration of the stability measurement, making it highly unlikely that this is the cause of the residual drift.

The fifth suspected reason for the residual drift is owing to a material property of the spacer between the mirrors, commonly described as creep. Creep is a gradual, steady shrinking of the spacer typically discussed for optical cavities using Zerodur [149, 150]. If creep is occurring in the cavity spacer or mirror material, then the residual drift rate of $\simeq$ 43 MHz/day would infer a fractional cavity length change of $\simeq$ -0.1×10^{-6}/day. Measurements of the Zerodur creep rate, in terms of fractional length change, have typically been quoted around -8×10^{-11}/day to -2×10^{-9}/day [149]. It is most likely that the residual drift we measure is on too large a scale to be attributed to material creep.

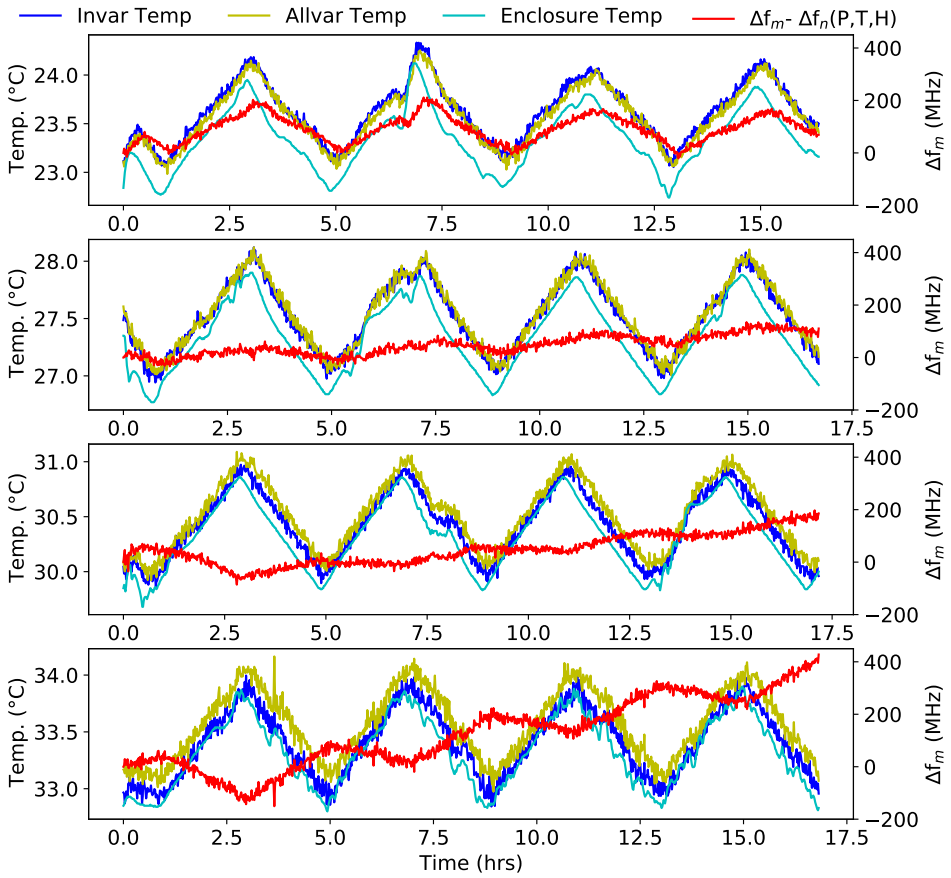

Figure 6.17: Test of cavity thermal sensitivity to changes in length at 4 different temperatures (23,27,30 and 33 °C). After approx. 5 hours stabilising to each set-point, a saw-tooth modulation is applied to the set-point to slowly vary the temperature by 1 °C. All 3 temperature measurements from within the oven are plotted to check the temperature is changing uniformly. The cavity mode sensitivity to thermally induced length shifts at each temperature has been plotted by subtracting off refractive index related shifts for each data point.

To help determine the root of the residual drift, we compared the hysteresis of the cavity mode shifts corresponding to the CTE, at various temperatures. This set of measurements should additionally demonstrate the changing magnitude and sign of thermal sensitivity below and above the CTE zero-crossing temperature. The resulting plots in Fig. 6.17 show the mode shift owing to length fluctuations ($\Delta f_n(P,T,H)$ subtracted off) following the changing temperature very closely. This is especially obvious for the 23 °C set-point. The results at 23 °C are promising for demonstrating the use of the thermal conductivity of the metal and their ability to expand and contract to the same length over multiple heating cycles. As the temperature is increased we see the amplitude of the oscillations in Δf_m reducing, and the oscillating response of Δf_m w.r.t. temperature is inverted by 30 °C, indicating the determination of the CTE zero-

crossing temperature definitely lies within the range of 27 - 31 °C. Most notably, there is clearly a positive drift on top of the oscillations at most of the set-points, and the magnitude of this drift appears to grow as the temperature rises. These measurements highlight that the issue is temperature-related, however we are still unable to determine what exactly is generating the residual drift.

6.4 Discussion of Results

While it was possible to demonstrate the Invar-Allvar combination of metals to yield a low, zero-crossing CTE, it was not possible to demonstrate an improvement to the frequency stability beyond the standard set by other groups mentioned above. However, based on the the Invar-Allvar combination CTE measurement, it is expected that under vacuum conditions, this cavity could demonstrate competitive levels of stability to a ULE cavity, at a lower price, and easier manufacturing processes. For reference, Thorlabs currently sell an off-the-shelve ULE cavity (XM-ORC), which currently costs £59,580, and quotes a linear drift rate of 0.54 kHz/hour. To compare the frequency stability of this optical cavity with that of the ECDL locked to the Rb TPT in Section 3.2, the data from Fig. 6.16 is converted to the overlapping Allan deviation, and plotted in Fig. 6.18. The sampling interval for this measurement was set to 60 s (lower limit of 20 s). The OADev beyond 60 s shows trends which begin to deviate from white FM noise (dashed line), but continue to average down to 100 s for the un-adjusted data set before becoming unstable on longer time-scales. On the other hand, the refractive index compensated data averages down to 1000 s, before a very linear frequency drift carries the stability away.

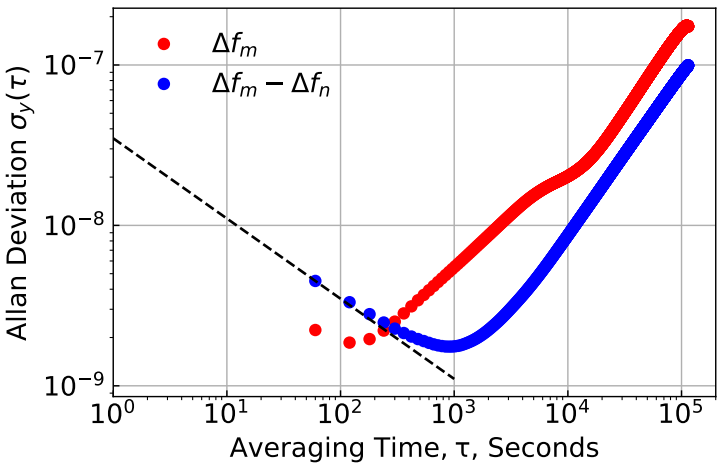

Figure 6.18: Data from 6.16 with a 60 s sample interval is converted to fractional frequency fluctuations using the Rb ref. transition frequency, and the corresponding overlapping Allan deviation is computed. A slope of $3.5\times10^{-8}\tau^{-0.5}$ is fitted to intersect the first data point, and estimate the stability at 1s, assuming white frequency noise is the dominant noise source.

Further work on this project aims to hermetically seal, or evacuate the cavity to achieve a stable refractive index, and benefit from the CTE zero-crossing temperature of the cavity spacer to create a truly stable optical cavity. Such an optical cavity could either be implemented as a less expensive and more compact optical reference option for stabilising lasers, or as a cavity of an ECDL. In the case of using this cavity for an optical frequency reference or to pre-stabilise a laser for applications in the work discussed in previous chapters, it would be logical to use different concave mirrors to yield a higher finesse. Additionally, it may be possible to compensate for the CTE of a piezo mounted within the cavity length, allowing the cavity to scan its length without compromising thermal sensitivity. By leaving the cavity open to the air, the insensitivity to temperature induced changes in the length make changes in the refractive index much easier to spot, potentially proving advantageous for applications in Fabry-Perot cavity refractometry and pressure measurements.

Chapter 7

Conclusion

7.1 Summary of Findings

The findings from this thesis add to a history of over 50 years worth of research utilising Doppler-free spectroscopy of the Rb two-photon transition. In Chapter 2 we discuss various aspects of Rb TPT spectroscopy which affect the amplitude of the fluorescence signal we can measure. Towards making the spectroscopy apparatus more compact, we have explored the use of a light-weight, 3D printed material for an Rb vapour cell oven that can continuously operate in the region of 100 - 150 °C.

An external cavity diode laser at 778 nm is then used in Chapter 3 to demonstrate that the spectroscopy apparatus is capable of providing a stable frequency lock to the Rb TPT. The lock could be maintained for periods of several hours with an Allan deviation following a trend of $8 \times 10^{-11}/\sqrt{\tau}$ down to a fractional frequency stability of 2×10^{-12} at 1000 seconds. Using a narrow-linewidth Ti:Sapphire laser and adding some magnetic field compensation to the spectroscopy apparatus, we demonstrate a linewidth measurement of 434 ± 35 kHz for the $^{87}Rb\ 5S_{1/2}, F = 2 \rightarrow 5D_{5/2}, F' = 4$ TPT.

We then explored the use of chip-scale equipment, using the compact spectroscopy apparatus to demonstrate the suitability of a chip-scale DFB 778 nm laser for an optical frequency reference. This work has led to several publications (see Section 0.1) using the Rb TPT spectroscopy results to benchmark the stability of the DFB laser. The DFB laser possesses short-term stability comparable to the ECDL, but lacked the means to implement a frequency lock. Such a laser is intended for integration on to a single semiconductor platform accommodating both the laser and miniature spectroscopy apparatus. To further this goal, we designed a miniature, 3D-printed, heated spectroscopy apparatus, which allowed us to characterise the TPT signal from a 1 mm thick, silicon-fabricated Rb cell. The apparatus achieved rapid warm-up times of less than 5 minutes and potential for increased fluorescence collection efficiency,

compared with a longer vapour cell. The Rb TPT signal from this vapour cell however, was excessively broad at $\sim$ 2 MHz, due to the presence of contaminants in the cell, making it not worthwhile to pursue a frequency-lock with this particular Rb cell.

Newly-developed telecoms-based optical frequency comb lasers intended for DWDM applications provide a compact solution for turning an optical frequency reference in to an optical atomic clock, by combining the spectroscopy laser and optical frequency comb in to a single source. Chapter 4 initially demonstrates the characterisation of a PPLN frequency-doubling stage, required to transfer the telecoms wavelength lasers to 778 nm, using a CW telecoms laser. Due to the reduced vibrational sensitivity of the telecoms laser, over the ECDL, an attempt is made to achieve a more stable frequency lock to the Rb TPT, but could not maintain a lock due to high frequency internally-generated noise on the telecoms laser output. In Chapter 5 the CW laser was then replaced with an OFC telecoms laser, which demonstrated >2x higher PPLN conversion efficiency compared to the CW laser, while delivering up to 30 mW of 778 nm light. The 778 nm OFC was then used to excite and resolve the $^{87}Rb\ 5S_{1/2}, F = 2 \rightarrow 5D_{5/2}, F' = 4, 3, 2, 1$ hyperfine TPT signals, which were of strong enough amplitude to demonstrate coherent interaction of all OFC modes. Yet the signal amplitude was lower than ideal and the linewidth broadened to $\sim$ 5 MHz, due to the presence of high frequency FM noise within the OFC laser.

Finally, Chapter 6, demonstrates the implementation and characterisation of Allvar metal to create a low-drift optical cavity for the proposes of providing high bandwidth, short-term stabilisation for a laser. Using a combination of Allvar and Invar metal to space apart the cavity mirrors, we demonstrate thermally tunable expansion characteristics. The coefficient of thermal expansion (CTE) can be tuned overall negative, positive and most notably < 0.001 ppm/°C, while stabilising the cavity to a temperature of 27.8 ± 0.005 °C. The long-term cavity mode stability of the cavity was measured while referenced to one of the $^{87}Rb\ 5S_{1/2} \rightarrow 5P_{3/2}$ 780 nm transitions, yielding drifts of 0.3 MHz/hr on time-scales up to 5 hrs (after subtracting off pressure-correlated frequency shifts). However, on longer time scales of several days ($> 1 \times 10^5$ s), there was a clear drift mechanism of 1.8 MHz/hr. The source of this drift is still unclear. The applications are toward a full metal high finesse optical cavity which enters the same frequency stability regime as a ULE cavity, and allows pre-stabilisation of lasers for spectroscopy of narrow-linewidth optical transitions. The all-metal spacer lends itself to allow reduced thermal gradients as well as more responsive temperature stabilisation.

7.2 Future Work

The further development of a compact Rb TPT spectroscopy apparatus, like that which is illustrated in Fig. 3.23, would make a useful step toward a fully portable Rb TPT

reference and eventually an atomic clock. Either a laser such as the DFB laser could be mounted to the spectroscopy platform, or instead a fibre-coupling input could allow different lasers to be easily and quickly tested against each other on the path toward a fully integrated referenced laser system. While the DFB could in principle provide enough 778 nm power to achieve a stable lock to the Rb TPT reference signal, the extra commercial applications of working with a 1556 nm OFC laser are lucrative. The 1556 nm OFC laser which is used here, shows a promising improvement in frequency-doubling efficiency over the CW 1556 nm laser. Developing the apparatus in a modular design, with fibre-coupling in between reduces the complexity of diagnosing issues that may arise from misalignment, and enables easier upgrades to the apparatus during the development stage.

Ultimately a system using a 1556 nm OFC laser could have its output split (after optical amplification) in to two optical paths. The first path would feed in to the PPLN, generating the second harmonic for Rb TPT spectroscopy and additionally for mixing with the octave spanning OFC. The second path could use HNLF or another super-continuum generation techniques to widen the OFC spectral bandwidth to 1 octave. Thereafter it would be recombined with the OFC second harmonic to detect and stabilise the carrier-envelope offset, f_{ceo} in the beat-note of the two 1556 nm OFC beam paths. Once the OFC laser has feedback to stabilise both f_{ceo} and its modes are locked to the signal from Rb TPT spectroscopy, then a portion of light from the octave-spanning OFC can be sampled for detection of f_{rep}, and hence a clock output, as well as an optical output at a wide range of wavelengths. The optical output could even be tuned to any frequency in between the modes by including and Electro-optic modulator at the output beam path. The applications of such a type of device are very wide ranging, covering applications in astronomy, DWDM devices, optical atomic clocks, navigation and many more applications [35].

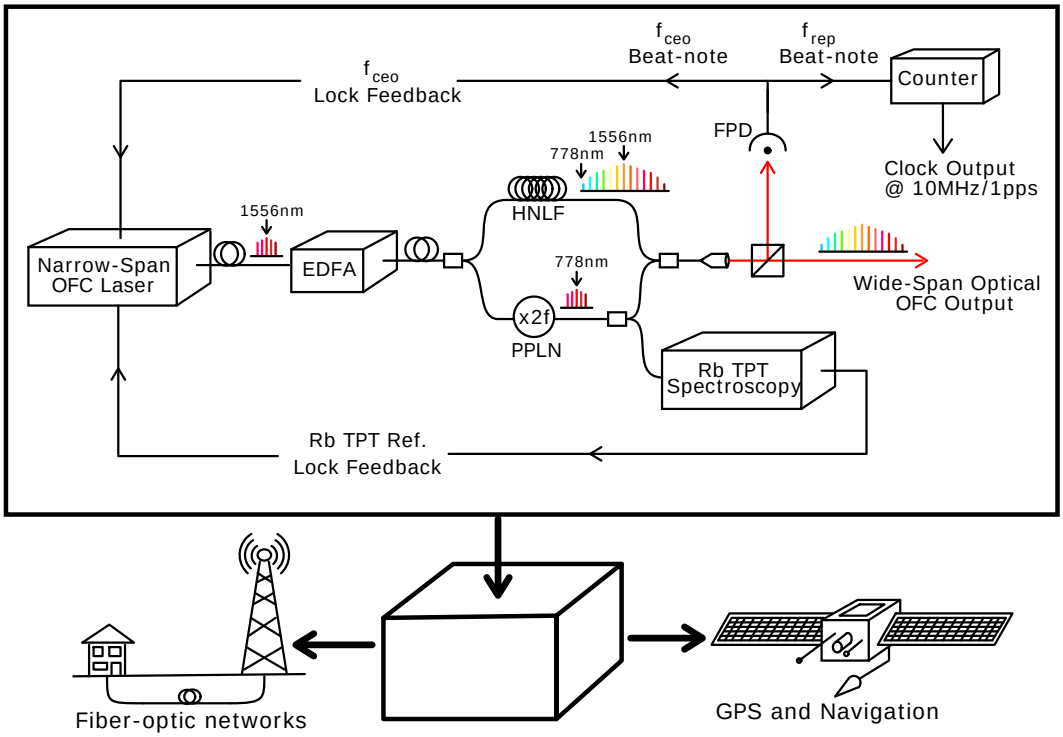

Figure 7.1: Basic layout for an optical atomic clock which operates using a single narrow-spanning OFC laser. Fibre-coupling would be preferred to improve vibrational stability. It is conceivable that a system of this design could fit inside of a 19" Rack mount casing, with the rest of the feedback and control electronics taking up an extra two rack mount cases. Integration of all of the electronics parts of the system would reduce the size further. As discussed, the potential applications of the system are wide-ranging. Abbreviations: EDFA = Erbium-doped Fibre Amplifier, HNLF = Highly Non-linear Fibre, PPLN = Periodically-poled Lithium Niobate.

If the noise of an OFC laser were negligible (< 10 kHz), then the spectroscopy platform will likely limit the frequency stability of such a system. Increasing fluorescence collection efficiency from the vapour cell, in order to reduce the required laser intensity should be a priority. Additionally Rb-Rb collisional shifts can be minimised by achieving higher levels of temperature stabilisation using the chip-scale apparatus. The simplicity of the system described above is a major advantage for SWaP (Size, Weight and Power) constraints. Yet by combining all of these parts on to a photonic integrated chip platform (like that which is discussed in the publications for the DFB laser used in Section 3.4.1) would enable significant steps toward a chip-scale device optical atomic clock, greatly improving the SWaP of the system. The simplicity of Rb TPT Doppler-free spectroscopy lends itself to chip-scale fabrication techniques.

Bibliography

[1] R. Hide and J. O. Dickey. "Earth's variable rotation". In: *Science* 253 (1991), p. 629.

[2] R. R. Rohr. *Sundials: History, theory, and practice*. Courier Corporation, 2012.

[3] J. D. North. "The astrolabe". In: *Scientific American* 230 (1974), p. 96.

[4] O. Neugebauer. "The Early History of the Astrolabe. Studies in Ancient Astronomy IX". In: *Isis* 40 (1949), p. 240.

[5] C. Audoin and B. Guinot. *The measurement of time: time, frequency and the atomic clock*. Cambridge University Press, 2001.

[6] B. W. Parkinson. "Origins, evolution, and future of satellite navigation". In: *Journal of Guidance, Control, and Dynamics* 20 (1997), p. 11.

[7] L. Maleki and J. Prestage. "Applications of clocks and frequency standards: from the routine to tests of fundamental models". In: *Metrologia* 42 (2005), S145.

[8] M. Takamoto, I. Ushijima, N. Ohmae, T. Yahagi, K. Kokado, H. Shinkai, and H. Katori. "Test of general relativity by a pair of transportable optical lattice clocks". In: *Nature Photonics* (2020), p. 1.

[9] W. J. Riley. *Handbook of frequency stability analysis*. US Department of Commerce, National Institute of Standards and Technology ..., 2008.

[10] V. Gerginov and K. Beloy. "Two-photon optical frequency reference with active ac Stark shift cancellation". In: *Physical Review Applied* 10 (2018), p. 014031.

[11] A. D. Ludlow, M. M. Boyd, J. Ye, E. Peik, and P. O. Schmidt. "Optical atomic clocks". In: *Reviews of Modern Physics* 87 (2015), p. 637.

[12] S. R. Jefferts, T. P. Heavner, T. E. Parker, and J. H. Shirley. "Nist cesium fountains: current status and future prospects". In: *Time and Frequency Metrology*. Vol. 6673. 2007, p. 667309.

[13] N. Nemitz, T. Ohkubo, M. Takamoto, I. Ushijima, M. Das, N. Ohmae, and H. Katori. "Frequency ratio of Yb and Sr clocks with 5×10^{-17} uncertainty at 150 seconds averaging time". In: *Nature Photonics* 10 (2016), p. 258.

[14] R. Bondarescu, A. Schärer, A. Lundgren, G. Hetényi, N. Houlié, P. Jetzer, and M. Bondarescu. "Ground-based optical atomic clocks as a tool to monitor vertical surface motion". In: *Geophysical Journal International* 202 (2015), p. 1770.

[15] V. Formichella, J. Camparo, and P. Tavella. "Influence of the ac-Stark shift on GPS atomic clock timekeeping". In: *Applied Physics Letters* 110 (2017), p. 043506.

[16] T. Dass, G. Freed, J. Petzinger, J. Rajan, T. J. Lynch, and J. Vaccaro. *GPS clocks in space: Current performance and plans for the future*. Tech. rep. ITT Industries Aerospace Clifton NJ Communications Div., 2002.

[17] P. Waller, F. Gonzalez, S. Binda, D. Rodriguez, G. Tobias, A. Cernigliaro, I. Sesia, and P. Tavella. *Long-term performance analysis of GIOVE clocks*. Tech. rep. European Space Agency Noordwijk (Netherlands), 2010.

[18] J.-M. Danet, O. Kozlova, P. Yun, S. Guérande, and E. De Clercq. "Compact atomic clock prototype based on coherent population trapping". In: *EPJ Web of Conferences*. Vol. 77. EDP Sciences. 2014, p. 00017.

[19] S. Kang, M. Gharavipour, C. Affolderbach, F. Gruet, and G. Mileti. "Demonstration of a high-performance pulsed optically pumped Rb clock based on a compact magnetron-type microwave cavity". In: *Journal of Applied Physics* 117 (2015), p. 104510.

[20] P. Cash, W. Krzewick, P. Machado, K. R. Overstreet, M. Silveira, M. Stanczyk, D. Taylor, and X. Zhang. "Microsemi chip scale atomic clock (CSAC) technical status, applications, and future plans". In: *2018 European Frequency and Time Forum (EFTF)*. IEEE. 2018, p. 65.

[21] H. Zhang, H. Herdian, A. T. Narayanan, A. Shirane, M. Suzuki, K. Harasaka, K. Adachi, S. Goka, S. Yanagimachi, and K. Okada. "ULPAC: A miniaturized ultralow-power atomic clock". In: *IEEE Journal of Solid-State Circuits* 54 (2019), p. 3135.

[22] J. Kitching. "Chip-scale atomic devices". In: *Applied Physics Reviews* 5 (2018), p. 031302.

[23] Microchip. *Microchip 5071A Cesium Primary Time and Frequency Standard Specifications*. `https://www.microchip.com/en-us/products/clock-and-timing/components/atomic-clocks/atomic-system-clocks/cesium-time/5071a`. Date accessed: 28-08-2022.

[24] S. R. Systems. *PRS10 — Low phase noise Rb oscillator*. `https://thinksrs.com/products/PRS10.htm`. Date accessed: 10-12-2022.

[25] H. Packard. *Caesium Beam Clock 5061A*. `https://www.opweb.de/english/company/Hewlett_Packard/5061A`. Date accessed: 10-12-2022.

[26] E. Technologies. *Space-Qualified Rubidium Atomic Frequency Standard Clocks*. `https://www.excelitas.com/product/space-qualified-rubidium-atomic-frequency-standard-clocks`. Date accessed: 10-12-2022.

[27] S. Dynamics. *cRb-Clock*. `https://spectradynamics.com/products/crb-clock/`. Date accessed: 10-12-2022.

[28] J. Stuhler, M. A. Hafiz, B. Arar, A. Bawamia, K. Bergner, M. Biethahn, S. Brakhane, A. Didier, J. Fortágh, M. Halder, et al. "Opticlock: Transportable and easy-to-operate optical single-ion clock". In: *Measurement: Sensors* 18 (2021), p. 100264.

[29] S. Koller, J. Grotti, A. Al-Masoudi, S. Dörscher, S. Häfner, U. Sterr, C. Lisdat, et al. "Transportable optical lattice clock with 7×10^{-17} uncertainty". In: *Physical review letters* 118 (2017), p. 073601.

[30] V. Maurice, Z. L. Newman, S. Dickerson, M. Rivers, J. Hsiao, P. Greene, M. Mescher, J. Kitching, M. T. Hummon, and C. Johnson. "Miniaturized optical frequency reference for next-generation portable optical clocks". In: *Optics Express* 28 (2020), p. 24708.

[31] K. W. Martin, G. Phelps, N. D. Lemke, M. S. Bigelow, B. Stuhl, M. Wojcik, M. Holt, I. Coddington, M. W. Bishop, and J. H. Burke. "Compact optical atomic clock based on a two-photon transition in rubidium". In: *Physical Review Applied* 9 (2018), p. 014019.

[32] L. A. Mallette, P. Rochat, and J. White. "An introduction to satellite based atomic frequency standards". In: *2008 IEEE Aerospace Conference*. IEEE. 2008, p. 1.

[33] Z. L. Newman, V. Maurice, T. Drake, J. R. Stone, T. C. Briles, D. T. Spencer, C. Fredrick, Q. Li, D. Westly, B. R. Ilic, et al. "Architecture for the photonic integration of an optical atomic clock". In: *Optica* 6 (2019), p. 680.

[34] F. Nez, F. Biraben, R. Felder, and Y. Millerioux. "Optical frequency determination of the hyperfine components of the 5S 1/2 $\rightarrow$ 5D 3/2 two-photon transitions in rubidium". In: *Optics Communications* 102 (1993), p. 432.

[35] S. A. Diddams. "The evolving optical frequency comb". In: *JOSA B* 27 (2010), B51.

[36] J. N. Eckstein, A. I. Ferguson, and T. W. Hänsch. "High-resolution two-photon spectroscopy with picosecond light pulses". In: *Physical Review Letters* 40 (1978), p. 847.

[37] S. A. Diddams, D. J. Jones, J. Ye, S. T. Cundiff, J. L. Hall, J. K. Ranka, R. S. Windeler, R. Holzwarth, T. Udem, and T. W. Hänsch. "Direct link between microwave and optical frequencies with a 300 THz femtosecond laser comb". In: *Physical review letters* 84 (2000), p. 5102.

[38] H. S. Margolis. "Optical frequency standards and clocks". In: *Contemporary Physics* 51 (2010), p. 37.

[39] J. D. Jost, T. Herr, C. Lecaplain, V. Brasch, M. H. Pfeiffer, and T. J. Kippenberg. "Counting the cycles of light using a self-referenced optical microresonator". In: *Optica* 2 (2015), p. 706.

[40] T. Quinn. "Practical realization of the definition of the metre (1997)". In: *Metrologia* 36 (1999), p. 211.

[41] R. Felder, D. Touahri, O. Acef, L. Hilico, J.-J. Zondy, A. Clairon, B. de Beauvoir, F. Biraben, L. Julien, F. Nez, et al. "Performance of a GaAlAs laser diode stabilized on a hyperfine component of two-photon transitions in rubidium at 778 nm". In: *Laser Frequency Stabilization and Noise Reduction*. Vol. 2378. SPIE. 1995, p. 52.

[42] C. Edwards, G. Barwood, H. Margolis, P. Gill, and W. Rowley. "Development and absolute frequency measurement of a pair of 778 nm two-photon rubidium standards". In: *Metrologia* 42 (2005), p. 464.

[43] A. Danielli, P. Rusian, A. Arie, M. Chou, and M. Fejer. "Frequency stabilization of a frequency-doubled 1556-nm source to the 5S 1/2 → 5D 5/2 two-photon transitions of rubidium". In: *Optics Letters* 25 (2000), p. 905.

[44] J. Bernard, A. Madej, K. Siemsen, L. Marmet, C. Latrasse, D. Touahri, M. Poulin, M. Allard, and M. Têtu. "Absolute frequency measurement of a laser at 1556 nm locked to the 5S 1/2 → 5D 5/2 two-photon transition in 87Rb". In: *Optics Communications* 173 (2000), p. 357.

[45] M. Poulin, C. Latrasse, D. Touahri, and M. Têtu. "Frequency stability of an optical frequency standard at 192.6 THz based on a two-photon transition of rubidium atoms". In: *Optics Communications* 207 (2002), p. 233.

[46] O. Terra and H. Hussein. "An ultra-stable optical frequency standard for telecommunication purposes based upon the 5S 1/2 → 5D 5/2 two-photon transition in Rubidium". In: *Applied Physics B* 122 (2016), p. 27.

[47] B. J. Chun, S. Hyun, S. Kim, S.-W. Kim, and Y.-J. Kim. "Frequency-comb-referenced multi-channel fiber laser for DWDM communication". In: *Optics Express* 21 (2013), p. 29179.

[48] O. Terra and H. Hussein. "Calibration of grating based optical spectrum analyzers". In: *Journal of Optics* 44 (2015), p. 366.

[49] Z. L. Newman, V. Maurice, C. Fredrick, T. Fortier, H. Leopardi, L. Hollberg, S. A. Diddams, J. Kitching, and M. T. Hummon. "High-performance, compact optical standard". In: *Optics Letters* 46 (2021), p. 4702.

[50] C. Perrella, P. Light, J. Anstie, F. Baynes, R. White, and A. Luiten. "Dichroic Two-Photon Rubidium Frequency Standard". In: *Physical Review Applied* 12 (2019), p. 054063.

[51] D. Sheng, A. P. Galván, and L. Orozco. "Lifetime measurements of the 5D states of rubidium". In: *Physical Review A* 78 (2008), p. 062506.

[52] M. Safronova, C. J. Williams, and C. W. Clark. "Relativistic many-body calculations of electric-dipole matrix elements, lifetimes, and polarizabilities in rubidium". In: *Physical Review A* 69 (2004), p. 022509.

[53] B. Cagnac, G. Grynberg, and F. Biraben. "Spectroscopie d'absorption multiphotonique sans effet Doppler". In: *Journal de Physique* 34 (1973), p. 845.

[54] G. Grynberg and B. Cagnac. "Doppler-free multiphotonic spectroscopy". In: *Reports on Progress in Physics* 40 (1977), p. 791.

[55] L. Hilico, R. Felder, D. Touahri, O. Acef, A. Clairon, and F. Biraben. "Metrological features of the rubidium two-photon standards of the BNM-LPTF and Kastler Brossel Laboratories". In: *The European Physical Journal-Applied Physics* 4 (1998), p. 219.

[56] F. Nez, M. Plimmer, S. Bourzeix, L. Julien, F. Biraben, R. Felder, Y. Millerioux, and P. De Natale. "First pure frequency measurement of an optical transition in atomic hydrogen: better determination of the Rydberg constant". In: *EPL (Europhysics Letters)* 24 (1993), p. 635.

[57] C. Schwob, L. Jozefowski, B. De Beauvoir, L. Hilico, F. Nez, L. Julien, F. Biraben, O. Acef, J.-J. Zondy, and A. Clairon. "Optical Frequency Measurement of the 2S - 12D Transitions in Hydrogen and Deuterium: Rydberg Constant and Lamb Shift Determinations". In: *Physical Review Letters* 82 (1999), p. 4960.

[58] P. K. Kumar and M. Suryanarayana. "Precision two-photon spectroscopy of alkali elements". In: *Pramana* 83 (2014), p. 189.

[59] F. Biraben, B. Cagnac, and G. Grynberg. "Observation of the 3S-5S two-photon transition in sodium vapor without Doppler broadening, using a CW dye laser". In: *Physics Letters A* 49 (1974), p. 71.

[60] D. A. Smith and I. G. Hughes. "The role of hyperfine pumping in multilevel systems exhibiting saturated absorption". In: *American Journal of Physics* 72 (2004), p. 631.

[61] O. Heavens. "Radiative transition probabilities of the lower excited states of the alkali metals". In: *JOSA* 51 (1961), p. 1058.

[62] C. J. Foot et al. *Atomic physics*. Vol. 7. Oxford University Press, 2005.

[63] D. A. Steck. *Quantum and atom optics*. University of Oregon, 2007.

[64] D. A. Steck. *Rubidium 87 D-line data*. `http://steck.us/alkalidata` (revision 2.2.1). Date accessed: 01-11-2019.

[65] S. Wang, J. Yuan, L. Wang, L. Xiao, and S. Jia. "Investigation on the monochromatic two-photon transition spectroscopy of rubidium by using intensity modulation method". In: *Journal of the Physical Society of Japan* 87 (2018), p. 084301.

[66] M. Zhu and R. W. Standridge. "Optical frequency standard for optical fiber communication based on the Rb 5S $\rightarrow$ 5d two-photon transition". In: *Optics Letters* 22 (1997), p. 730.

[67] M. J. Snadden, A. Bell, E. Riis, and A. I. Ferguson. "Two-photon spectroscopy of laser-cooled Rb using a mode-locked laser". In: *Optics Communications* 125 (1996), p. 70.

[68] I. Barmes, S. Witte, and K. S. Eikema. "High-precision spectroscopy with counterpropagating femtosecond pulses". In: *Physical Review Letters* 111 (2013), p. 023007.

[69] J. Wu, D. Hou, Z. Qin, X. Dai, Z. Zhang, and J. Zhao. "Erbium fiber laser-based direct frequency comb spectroscopy of Rb two-photon transitions". In: *Optics Letters* 38 (2013), p. 5028.

[70] S. Zhang, J. Wu, Y. Zhang, J. Leng, W. Yang, Z. Zhang, and J. Zhao. "Direct frequency comb optical frequency standard based on two-photon transitions of thermal atoms". In: *Scientific Reports* 5 (2015), p. 15114.

[71] W. Demtröder. *Laser spectroscopy*. Vol. 2. Springer, 1982.

[72] F. Biraben, M. Bassini, and B. Cagnac. "Line-shapes in Doppler-free two-photon spectroscopy. The effect of finite transit time". In: *Journal de Physique* 40 (1979), p. 445.

[73] Formlabs. *High Temp Resin V2 Datasheet*. `https://printparts.com/datasheets/High-Temp-Datasheet.pdf`. Date accessed: 2022.

[74] L. D. Turner, K. Weber, C. Hawthorn, and R. E. Scholten. "Frequency noise characterisation of narrow linewidth diode lasers". In: *Optics Communications* 201 (2002), p. 391.

[75] A. Daffurn, R. F. Offer, and A. S. Arnold. "A simple, powerful diode laser system for atomic physics". In: *arXiv preprint arXiv:2104.06019* (2021).

[76] I. F. Products. *IQD presents its new atomic clock ICPT-1*. `https://www.iqdfrequencyproducts.com/news/2020/11/25/iqd-presents-its-new-atomic-clock-icpt-1/`. Date accessed: 28-08-2022.

[77] W. Koechner and M. Bass. *Solid-state lasers: a graduate text*. Springer Science & Business Media, 2006.

[78] S. Knappe, V. Shah, P. D. Schwindt, L. Hollberg, J. Kitching, L.-A. Liew, and J. Moreland. "A microfabricated atomic clock". In: *Applied Physics Letters* 85 (2004), p. 1460.

[79] R. Vicarini, M. A. Hafiz, V. Maurice, N. Passilly, E. Kroemer, L. Ribetto, V. Gaff, C. Gorecki, S. Galliou, and R. Boudot. "Mitigation of temperature-induced light-shift effects in miniaturized atomic clocks". In: *IEEE Transactions on Ultrasonics, Ferroelectrics, and Frequency Control* 66 (2019), p. 1962.

[80] N. Belcher, E. E. Mikhailov, and I. Novikova. "Atomic clocks and coherent population trapping: Experiments for undergraduate laboratories". In: *American Journal of Physics* 77 (2009), p. 988.

[81] A. Strangfeld, S. Kanthak, M. Schiemangk, B. Wiegand, A. Wicht, A. Ling, and M. Krutzik. "Prototype of a compact rubidium-based optical frequency reference for operation on nanosatellites". In: *JOSA B* 38 (2021), p. 1885.

[82] A. Strangfeld, B. Wiegand, J. Kluge, M. Schoch, and M. Krutzik. "Compact plug and play optical frequency reference device based on Doppler-free spectroscopy of rubidium vapor". In: *Optics Express* 30 (2022), p. 12039.

[83] L. Maleki, A. Savchenkov, V. Ilchenko, W. Liang, D. Eliyahu, A. Matsko, D. Seidel, N. Wells, J. Camparo, and B. Jaduszliwer. "All-optical integrated rubidium atomic clock". In: *2011 Joint Conference of the IEEE International Frequency Control and the European Frequency and Time Forum (FCS) Proceedings*. IEEE. 2011, p. 1.

[84] L. A. Mallette, J. White, and P. Rochat. "Space qualified frequency sources (clocks) for current and future GNSS applications". In: *IEEE/ION Position, Location and Navigation Symposium*. IEEE. 2010, p. 903.

[85] H. Virtanen, T. Uusitalo, M. Karjalainen, S. Ranta, J. Viheriälä, and M. Dumitrescu. "Narrow-linewidth 780-nm DFB lasers fabricated using nanoimprint lithography". In: *IEEE Photonics Technology Letters* 30 (2017), p. 51.

[86] E. Di Gaetano and M. Sorel. "Design of chirped-coupling sidewall Bragg gratings for narrow linewidth distributed feedback lasers". In: *Optics Letters* 44 (2019), p. 1642.

[87] E. Di Gaetano, S. Watson, E. McBrearty, M. Sorel, and D. Paul. "Sub-megahertz linewidth 780.24 nm distributed feedback laser for 87 Rb applications". In: *Optics Letters* 45 (2020), p. 3529.

[88] S. Kraft, A. Deninger, C. Trück, J. Fortágh, F. Lison, and C. Zimmermann. "Rubidium spectroscopy at 778–780 nm with a distributed feedback laser diode". In: *Laser Physics Letters* 2 (2004), p. 71.

[89] F. Riehle. *Frequency standards: basics and applications*. John Wiley & Sons, 2006.

[90] S. Dyer, P. F. Griffin, A. S. Arnold, F. Mirando, D. P. Burt, E. Riis, and J. P. McGilligan. "Micro-machined deep silicon atomic vapor cells". In: *Journal of Applied Physics* 132 (2022), p. 134401.

[91] K. Gallacher, P. F. Griffin, E. Riis, M. Sorel, and D. J. Paul. "Silicon nitride waveguide polarization rotator and polarization beam splitter for chip-scale atomic systems". In: *APL Photonics* 7 (2022), p. 046101.

[92] S. Sané, S. Bennetts, J. Debs, C. C. Kuhn, G. McDonald, P. Altin, J. Close, and N. Robins. "11 W narrow linewidth laser source at 780nm for laser cooling and manipulation of Rubidium". In: *Optics Express* 20 (2012), p. 8915.

[93] C. Spiegelberg, J. Geng, Y. Hu, Y. Kaneda, S. Jiang, and N. Peyghambarian. "Low-noise narrow-linewidth fiber laser at 1550 nm (June 2003)". In: *Journal of Lightwave Technology* 22 (2004), p. 57.

[94] F. Kéfélian, H. Jiang, P. Lemonde, and G. Santarelli. "Ultralow-frequency-noise stabilization of a laser by locking to an optical fiber-delay line". In: *Optics letters* 34 (2009), p. 914.

[95] J. P. McGilligan, P. F. Griffin, R. Elvin, S. J. Ingleby, E. Riis, and A. S. Arnold. "Grating chips for quantum technologies". In: *Scientific reports* 7 (2017), p. 1.

[96] Y. Awaji, K. Nakagawa, M. De Labachelerie, M. Ohtsu, and H. Sasada. "Optical frequency measurement of the H 12 C 14 N Lamb-dip-stabilized 1.5-μm diode laser". In: *Optics Letters* 20 (1995), p. 2024.

[97] R. Matthey, W. Moreno, F. Gruet, P. Brochard, S. Schilt, and G. Mileti. "Rb-stabilized laser at 1572 nm for CO2 monitoring". In: *Journal of Physics: Conference Series*. Vol. 723. IOP Publishing. 2016, p. 012034.

[98] A. Hinton, M. Perea-Ortiz, J. Winch, J. Briggs, S. Freer, D. Moustoukas, S. Powell-Gill, C. Squire, A. Lamb, C. Rammeloo, et al. "A portable magneto-optical trap with prospects for atom interferometry in civil engineering". In: *Philosophical Transactions of the Royal Society A: Mathematical, Physical and Engineering Sciences* 375 (2017), p. 20160238.

[99] S. A. Berry, L. G. Carpenter, A. C. Gray, P. G. Smith, and C. B. Gawith. "Zn-indiffused diced ridge waveguides in MgO: PPLN generating 1 watt 780 nm SHG at 70% efficiency". In: *OSA Continuum* 2 (2019), p. 3456.

[100] P. Franken, A. E. Hill, C. e. Peters, and G. Weinreich. "Generation of optical harmonics". In: *Physical Review Letters* 7 (1961), p. 118.

[101] P. Franken and J. Ward. "Optical harmonics and nonlinear phenomena". In: *Reviews of Modern Physics* 35 (1963), p. 23.

[102] R. W. Boyd. *Nonlinear optics*. Academic press, 2020.

[103] A. Yariv and P. Yeh. *Photonics: optical electronics in modern communications*. Oxford University Press, 2007.

[104] M. J. Weber. *Handbook of optical materials*. CRC Press, 2018.

[105] P. Maker, R. Terhune, M. Nisenoff, and C. Savage. "Effects of dispersion and focusing on the production of optical harmonics". In: *Physical Review Letters* 8 (1962), p. 21.

[106] Covesion. *Technical guide*. `https://www.covesion.com/en/resource-type/technical-guide/`. Date accessed: 10-03-2022.

[107] Y. Kojima, Y. Fujiwara, S. Yamada, and N. Wakatsuki. "Chip crystal resonator with load capacitors". In: *38th Annual Symposium on Frequency Control*. IEEE. 1984, p. 114.

[108] O. Kashin, M. Homann, V. Matusevich, F. Setzpfandt, T. Pertsch, and R. Kowarschik. "Change of the refractive index in PPLN waveguides due to the photorefractive effect". In: *Applied Physics B* 104 (2011), p. 547.

[109] V. Pecheur, H. Porte, J. Hauden, F. Bassignot, M. Deroh, and M. Chauvet. "Watt-level SHG in undoped high step-index PPLN ridge waveguides". In: *OSA Continuum* 4 (2021), p. 1404.

[110] Y. V. Baklanov and V. Chebotayev. "Narrow resonances of two-photon absorption of super-narrow pulses in a gas". In: *Applied Physics* 12 (1977), p. 97.

[111] A. Marian, M. C. Stowe, J. R. Lawall, D. Felinto, and J. Ye. "United time-frequency spectroscopy for dynamics and global structure". In: *Science* 306 (2004), p. 2063.

[112] J. Wu, D. Hou, Z. Qin, Z. Zhang, and J. Zhao. "Observation of Rb two-photon absorption directly excited by an erbium-fiber-laser-based optical frequency comb via spectral control". In: *Physical Review A* 89 (2014), p. 041402.

[113] H. Lu, J. Leng, and J. Zhao. "The Optimization of Cold Rubidium Atom Two-Photon Transition Excitation with an Erbium-Fiber Optical Frequency Comb". In: *Applied Sciences* 9 (2019), p. 921.

[114] T. Fortier and E. Baumann. "20 years of developments in optical frequency comb technology and applications". In: *Communications Physics* 2 (2019), p. 153.

[115] S. A. Diddams, K. Vahala, and T. Udem. "Optical frequency combs: coherently uniting the electromagnetic spectrum". In: *Science* 369 (2020), p. 6501.

[116] S. Liu, K. Wu, L. Zhou, G. Zhou, L. Lu, and J. Chen. "Modelling a dual-parallel silicon modulator for sinc-shaped Nyquist pulse generation". In: *IEEE Journal of Selected Topics in Quantum Electronics* 27 (2020), p. 1.

[117] H. Bao, A. Cooper, M. Rowley, L. Di Lauro, J. S. Totero Gongora, S. T. Chu, B. E. Little, G.-L. Oppo, R. Morandotti, D. J. Moss, et al. "Laser cavity-soliton microcombs". In: *Nature Photonics* 13 (2019), p. 384.

[118] F. Zhang, J. Wu, Y. Li, and J. Lin. "Flat optical frequency comb generation and its application for optical waveform generation". In: *Optics Communications* 290 (2013), p. 37.

[119] L. Shang, A. Wen, G. Lin, and Y. Gao. "A flat and broadband optical frequency comb with tunable bandwidth and frequency spacing". In: *Optics Communications* 331 (2014), p. 262.

[120] H. Ren, L. Fan, N. Liu, Z. Wu, and G. Xia. "Generation of Broadband Optical Frequency Comb Based on a Gain-Switching 1550 nm Vertical-Cavity Surface-Emitting Laser under Optical Injection". In: *Photonics*. Vol. 7. Multidisciplinary Digital Publishing Institute. 2020, p. 95.

[121] FS.com. *An Overview of DWDM Technology and DWDM System Components*. `https://community.fs.com/blog/an-overview-of-dwdm-technology-and-dwdm-system-components.html`. Date accessed: 22-02-2023.

[122] G. Jain, D. Gutierrez-Pascual, M. J. Wallace, J. F. Donegan, and P. M. Anandarajah. "Experimental Investigation of External Optical Injection and its Application in Gain-Switched Wavelength Tunable Optical Frequency Comb Generation". In: *Journal of Lightwave Technology* 39 (2021), p. 5884.

[123] M. D. G. Pascual, V. Vujicic, J. Braddell, F. Smyth, P. Anandarajah, and L. Barry. "Photonic integrated gain switched optical frequency comb for spectrally efficient optical transmission systems". In: *IEEE Photonics Journal* 9 (2017), p. 1.

[124] M. D. G. Pascual, R. Zhou, F. Smyth, P. M. Anandarajah, and L. P. Barry. "Software reconfigurable highly flexible gain switched optical frequency comb source". In: *Optics Express* 23 (2015), p. 23225.

[125] B. Razavi. "A study of injection locking and pulling in oscillators". In: *IEEE Journal of Solid-State Circuits* 39 (2004), p. 1415.

[126] M. D. G. Pascual, V. Vujicic, J. Braddell, F. Smyth, P. M. Anandarajah, and L. P. Barry. "InP photonic integrated externally injected gain switched optical frequency comb". In: *Optics Letters* 42 (2017), p. 555.

[127] P. Anandarajah, R. Maher, Y. Xu, S. Latkowski, J. O'carroll, S. Murdoch, R. Phelan, J. O'Gorman, and L. Barry. "Generation of coherent multicarrier signals by gain switching of discrete mode lasers". In: *IEEE Photonics Journal* 3 (2011), p. 112.

[128] P. Gellie, S. Barbieri, J.-F. Lampin, P. Filloux, C. Manquest, C. Sirtori, I. Sagnes, S. P. Khanna, E. H. Linfield, A. G. Davies, et al. "Injection-locking of terahertz quantum cascade lasers up to 35GHz using RF amplitude modulation". In: *Optics Express* 18 (2010), p. 20799.

[129] D. Wei and M. Aketagawa. "Analysis of the second harmonic generation of a femtosecond optical frequency comb". In: *Optical Engineering* 53 (2014), p. 122604.

[130] A. Yariv and P. Yeh. "Photonics: optical electronics in modern communications". In: Oxford University Press, 2007. Chap. 4.

[131] A. Perot and C. Fabry. "On the application of interference phenomena to the solution of various problems of spectroscopy and metrology". In: *The Astrophysical Journal* 9 (1899), p. 87.

[132] T. Kessler, C. Hagemann, C. Grebing, T. Legero, U. Sterr, F. Riehle, M. Martin, L. Chen, and J. Ye. "A sub-40-mHz-linewidth laser based on a silicon single-crystal optical cavity". In: *Nature Photonics* 6 (2012), p. 687.

[133] I. Ushijima, M. Takamoto, M. Das, T. Ohkubo, and H. Katori. "Cryogenic optical lattice clocks". In: *Nature Photonics* 9 (2015), p. 185.

[134] G. K. Campbell, A. D. Ludlow, S. Blatt, J. W. Thomsen, M. J. Martin, M. H. De Miranda, T. Zelevinsky, M. M. Boyd, J. Ye, S. A. Diddams, et al. "The absolute frequency of the 87Sr optical clock transition". In: *Metrologia* 45 (2008), p. 539.

[135] S. Webster, M. Oxborrow, S. Pugla, J. Millo, and P. Gill. "Thermal-noise-limited optical cavity". In: *Physical Review A* 77 (2008), p. 033847.

[136] J. A. Monroe, J. S. McAllister, D. S. Content, J. Zgarba, X. Huerta, and I. Karaman. "Negative thermal expansion ALLVAR alloys for telescopes". In: *Advances in Optical and Mechanical Technologies for Telescopes and Instrumentation III*. Vol. 10706. SPIE. 2018, p. 202.

[137] I. Silander, C. Forssén, J. Zakrisson, M. Zelan, and O. Axner. "An Invar-based Fabry-Perot cavity refractometer with a gallium fixed-point cell for assessment of pressure". In: *ACTA IMEKO* 9 (2020), p. 293.

[138] J. Alnis, A. Matveev, N. Kolachevsky, T. Udem, and T. Hänsch. "Subhertz linewidth diode lasers by stabilization to vibrationally and thermally compensated ultralow-expansion glass Fabry-Pérot cavities". In: *Physical Review A* 77 (2008), p. 053809.

[139] F. Riehle. "Frequency standards: basics and applications". In: John Wiley & Sons, 2006. Chap. 4.4.

[140] Bosch. *Bosch Sensor Datasheet*. `http://www.bosch-sensortec.com/products/environmental-sensors/humidity-sensors-bme280`. Date accessed: 06-03-2023.

[141] J. Ye, S. Swartz, P. Jungner, and J. L. Hall. "Hyperfine structure and absolute frequency of the 87 Rb 5P 3/2 state". In: *Optics Letters* 21 (1996), p. 1280.

[142] A. Rossi, V. Biancalana, B. Mai, and L. Tomassetti. "Long-term drift laser frequency stabilization using purely optical reference". In: *Review of Scientific Instruments* 73 (2002), p. 2544.

[143] W. Zhao, J. Simsarian, L. A. Orozco, and G. Sprouse. "A computer-based digital feedback control of frequency drift of multiple lasers". In: *Review of Scientific Instruments* 69 (1998), p. 3737.

[144] H. Talvitie, J. Åman, H. Ludvigsen, A. Pietiläinen, L. Pendrill, and E. Ikonen. "TECHNICAL NOTE Improved frequency stability of an external cavity diode laser by eliminating temperature and pressure effects". In: *Applied Optics* 35 (1996), p. 4166.

[145] E. Riedle, S. Ashworth, J. Farrell Jr, and D. Nesbitt. "Stabilization and precise calibration of a continuous-wave difference frequency spectrometer by use of a simple transfer cavity". In: *Review of scientific instruments* 65 (1994), p. 42.

[146] E. Hansis, T. Cubel, J.-H. Choi, J. Guest, and G. Raithel. "Simple pressure-tuned Fabry–Pérot interferometer". In: *Review of scientific instruments* 76 (2005), p. 033105.

[147] A. Takamizawa, S. Yanagimachi, T. Ikegami, and R. Kawabata. "External cavity diode laser with frequency drift following natural variation in air pressure". In: *Applied Optics* 54 (2015), p. 5777.

[148] E. H. Chang, J. Rivera, B. Bostwick, C. Schneider, P. Yu, and E. R. Hudson. "Low-Drift-Rate External Cavity Diode Laser". In: *arXiv preprint arXiv:2205.14149* (2022).

[149] F. Bayer-Helms, H. Darnedde, and G. Exner. "Längenstabilität bei Raumtemperatur von Proben der Glaskeramik" Zerodur"". In: *Metrologia* 21 (1985), p. 49.

[150] M. Notcutt, L.-S. Ma, A. D. Ludlow, S. M. Foreman, J. Ye, and J. L. Hall. "Contribution of thermal noise to frequency stability of rigid optical cavity via Hertz-linewidth lasers". In: *Physical Review A* 73 (2006), p. 031804.

Appendix A. Example Log of Conditions During Invar-Allvar Cavity Stability Measurement

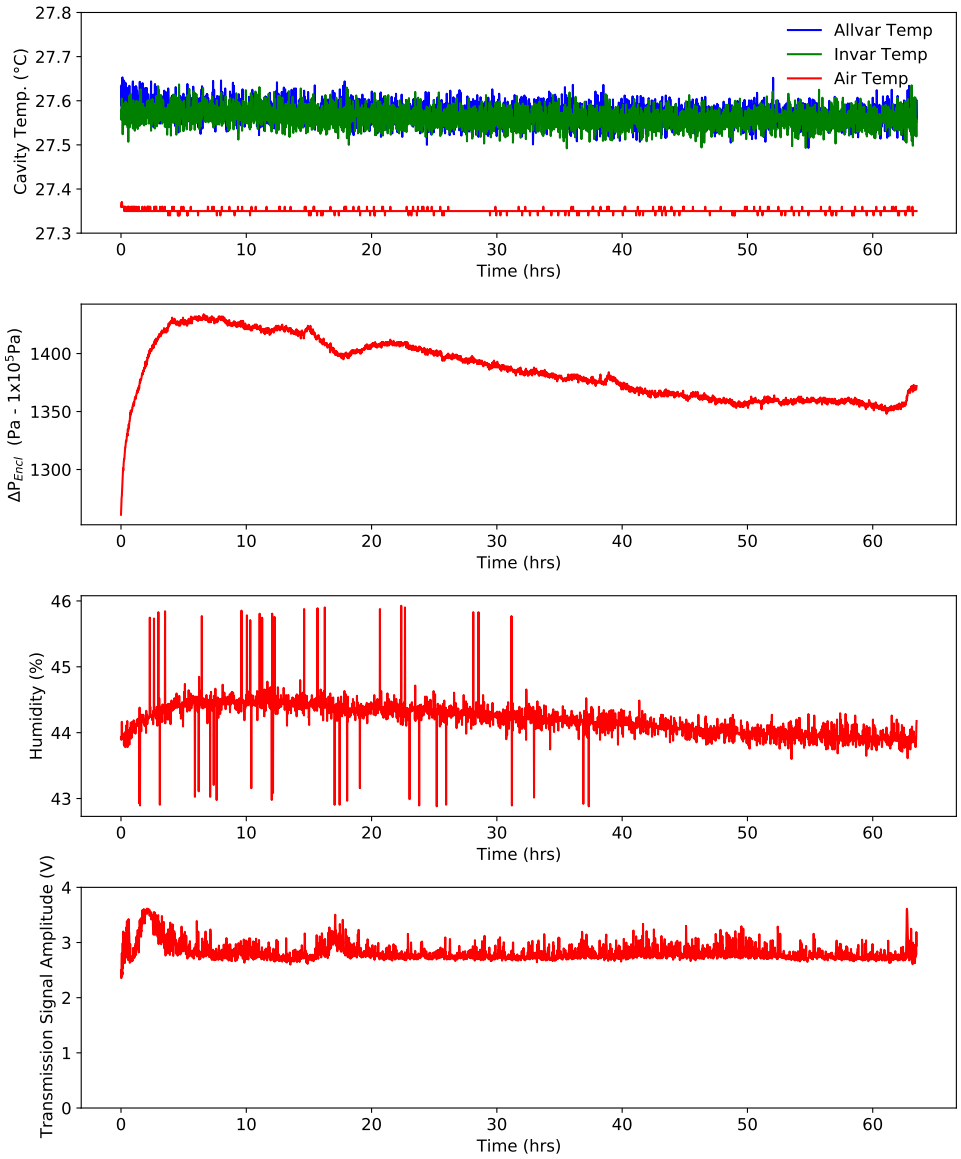

Figure S1: Continuous log of all parameters within the enclosure for the 64 hour measurement Invar Allvar cavity stability measurement.

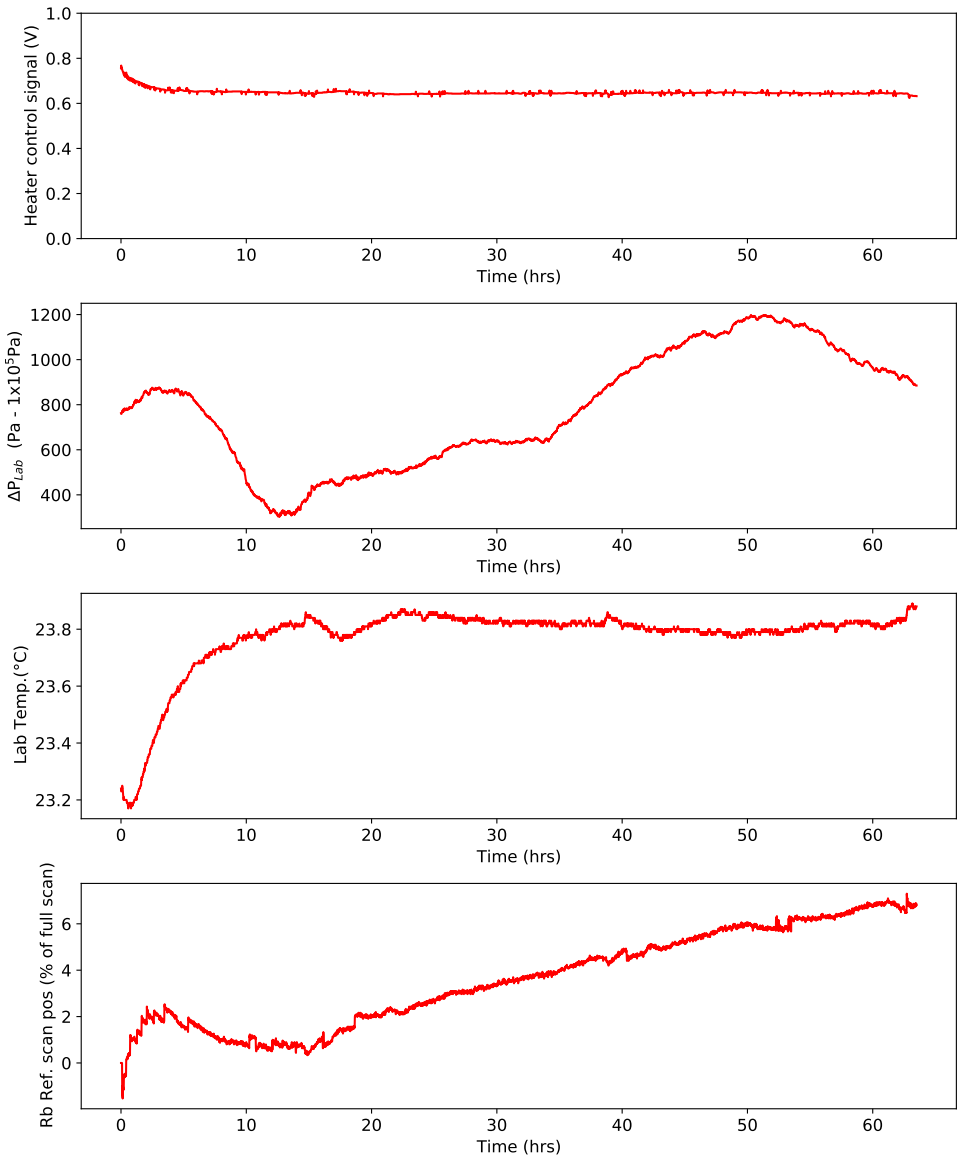

Figure S2: Continuous log of all available parameters outside the enclosure for the 64 hour measurement Invar Allvar cavity stability measurement.

Appendix B. PPLN Electrostatic Charge Build-Up Behaviour

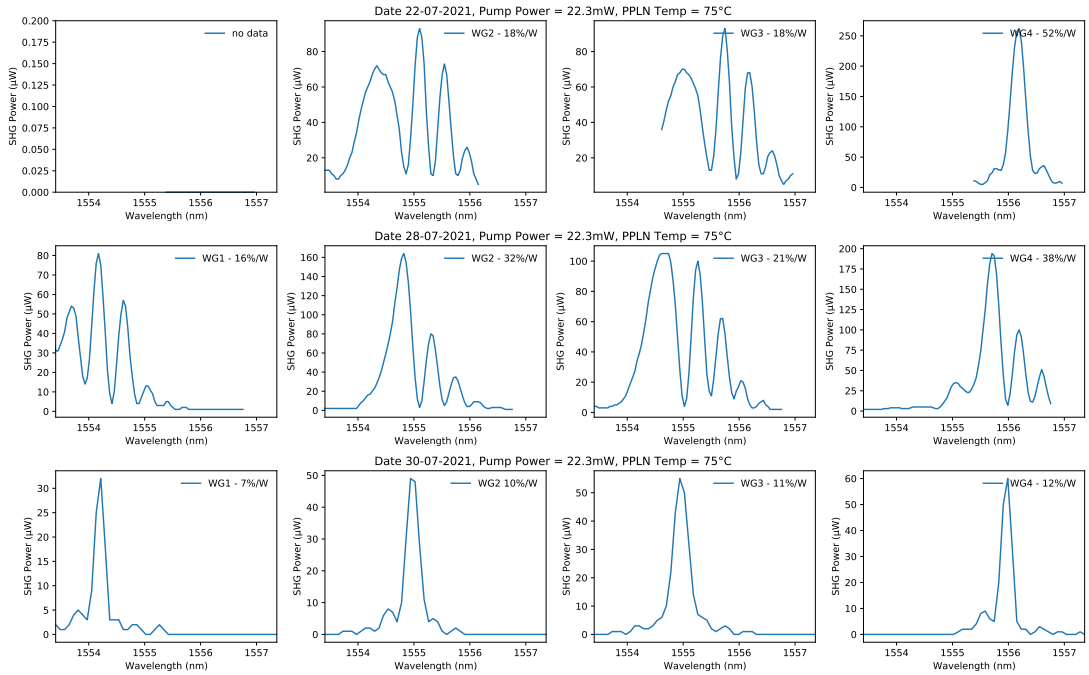

Figure S3: The Pump laser is aligned with individual PPLN waveguides, then the wavelength is scanned while the second harmonic output power is measured. Electrostatic charge on the PPLN crystal is believed to be responsible for yielding variable tuning behaviour and causing the peak conversion efficiency to shift around. The temperature of the PPLN is 75 °C for all measurements. The behaviour was observed to change day to day. The final set of plots were measured after shining a UV light on to the crystal facets.